A Tribo-dynamic solution for the flexible piston skirt and liner conjunction

B.R. Littlefair

BEng

A Thesis submitted in partial fulfilment of the requirements for the

Degree of Doctor of Philosophy of Loughborough University

Wolfson School of Mechanical & Manufacturing Engineering

Loughborough University

Loughborough

UK   November 2013

In loving memory of Lyn Littlefair

Abstract

The internal combustion engine is still at the heart of the vast majority of vehicles manufactured worldwide today. For these applications reciprocating pistons are typically employed to convert the pressures generated by internal combustion into mechanical work required by the vehicle. Of the energy supplied to the engine as a whole approximately 17% is lost by means of mechanical friction. The piston ring - liner and piston skirt - liner conjunctions contribute approximately 30% of the overall friction losses in almost equal proportions. It is, therefore, important to note that reduction in piston assembly friction would have a significant effect on the fuel consumption and, therefore, performance of engines manufactured today.

In order to reduce the effect of friction it is of critical importance that the model and predictions made alongside the design of engine components accurately represent the real in-cycle conditions encountered in practice. Much of the published research to date has excluded the effects of global thermo-elastic distortions on the lubrication of the piston skirt. In cases where this effect has been studied, it has been for relatively low engine speeds or loads on relatively stiff conjunctions. In motorsport applications the expected component lifespans are much shorter than in the usual OEM production vehicles. Reduction in component mass, particularly in reciprocating components has been at the centre of these recent gains. The effect of mass reduction coupled with the increased BMEP observed in high performance engines emphasises the importance of underlying mechanisms of lubrication.

This thesis develops the modelling methodology for piston skirt – cylinder liner conjunction for the motorsport and high performance engine applications. It presents a multi-body, multi-scale approach to the prediction of the lubrication conditions of the skirt – liner conjunction, incorporating realistic measured boundary conditions. It highlights the effect of inertial loading observed at high speeds in such applications. Using the methodology developed in this work, future improvements in friction may be accurately predicted though the use of the modular boundary and component contributions used throughout. Crucially though, the models created have been scrutinised and verified using instantaneous ultrasonic film thickness measurements non-invasively from the conjunction.

One of the key findings of the thesis is that the component stiffness profiles have a significant effect on the dynamics of the piston assembly. The shape of the conjunction at a given instant, and thus the contact condition, is largely governed by the interaction between the themo-mechanical distortion of the contiguous solids, as well as changes in lubricant characteristic responses. The iso-viscous elastic mechanism of lubrication has been identified as being the dominant mechanism of lubrication.

Keywords: Piston skirt lubrication, Thermo-mechanical distortion, Iso-viscous elastic, Transient elasto-hydrodynamic lubrication, Ultrasonic film thickness measurement

Acknowledgements

Table of contents

Figure List

Latin Characters

a -   In Reynolds' discretisation – contact half-length .... $[\,m\,]$

      -   Elsewhere - Distance from gudgeon pin axis to piston crown .... $[\,m\,]$

A -   Nodal deflection array .... $[\,m\,]$

b -   In Reynolds' discretisation – contact half-width .... $[\,m\,]$

      -   Distance from piston's centre of mass to piston crown .... $[\,m\,]$

c_s -   Nominal clearance .... $[\,m\,]$

c -   Speed of sound within the lubricant .... $[\,m\,s^{-1}\,]$

c_o -   Offset clearance .... $[\,m\,]$

C_c -   Crankshaft offset .... $[\,m\,]$

C_n -   Converged value in Newmarks integrator .... $[\,-\,]$

C_g -   Centre of gravity offset.. $[\,m\,]$

C_{pb} -   Gudgeon pin offset .... $[\,m\,]$

C_p -   Combined gudgeon pin and crankshaft offset $\left(C_p = C_{pb} + C_c\right)$ .... $[\,m\,]$

e_b -   Clearance between bottom end of piston skirt and cylinder liner .... $[\,m\,]$

e_l -   Piston lateral motion... $[\,m\,]$

e_t -   Clearance between top end of piston skirt and cylinder liner .... $[\,m\,]$

d -   Offset clearance in the circumferential direction .... $[\,m\,]$

D^* -   Influence co-efficient matrix .... $[\,-\,]$

E' -   Reduced Young's modulus .... $[\,Nm^{-2}\,]$

f_{con} -   Connecting rod force .... $[\,N\,]$

f_g -   Gas force .... $[\,N\,]$

f_{gg} -   Inertial force of gudgeon due to primary motion .... $[\,N\,]$

f_{gp} -   Inertial force of piston due to primary motion .... $[\,N\,]$

f_{ig} -   Inertial force of gudgeon due to secondary motion .... $[\,N\,]$

Greek Characters

α	-	Pressure-viscosity index	$[Pa^{-1}]$
β	-	Piston's rigid tilt angle	$[rad]$
β'	-	Thermal expansion coefficient of lubricant	$[K^{-1}]$
δ_h	-	Hertzian deflection	$[m]$
δ	-	General deflection	$[m]$
ε_c	-	Piston crown pressure deformation array	$[m]$
ε_{ip}	-	Positive inertial piston deformation array	$[m]$
ε_{in}	-	Negative inertial piston deformation array	$[m]$
ε_p	-	Pressure convergence criteria	$[-]$
η	-	Dynamic viscosity	$[Pa\ s]$
η_k	-	Kinematic viscosity	$[m^2s^{-1}]$
θ	-	Crankshaft torsional displacement	$[rad]$
Λ	-	Crank radius / connecting rod length ratio	$[-]$
λ	-	Film parameter	$[-]$
Ξ	-	Crank radius / offset ratio	$[-]$
ξ	-	Exponent of density temperature dependence	$[K^{-1}]$
ξ'	-	Pressure viscosity coefficient	$[-]$
ρ	-	Density	$[kgm^{-3}]$
τ	-	Shear stress	$[Nm^{-1}]$
ϕ	-	Connecting rod angle.	$[rad]$
φ_j	-	Circumferential location along the skirt	$[rad]$
ω	-	Crankshaft angular velocity	$[rad\ s^{-1}]$
ψ	-	Shear rate	$[s^{-1}]$
Ω	-	Pressure relaxation parameter	$[-]$

Sub-scripts

o -   Denotes at ambient temperature and pressure

i -   Row reference within a conjunction profile variable

j -   Column reference within a conjunction profile variable

p -   Integrator time step number in Linear Acceleration Method

q -   Iteration step in Linear Acceleration Method

Super-scripts

$\cdot$ -   First time derivative ....$[\,s^{-1}\,]$

$\cdot\cdot$ -   Second time derivative ....$[\,s^{-2}\,]$

ATS	-	Anti Thrust side
BMEP	-	Brake mean effective pressure
BTC	-	Bottom dead centre
CRF	-	Honda CRF 450r engine
DOF	-	Degree of freedom
HD	-	Hydrodynamic
EHL	-	Elastohydrodynamic
LIF	-	Laser induced fluorescence
NVH	-	Noise vibration and harshness
PCG	-	Preconditioned conjugate method
QS	-	Quasi static
TDC	-	Top dead centre
TS	-	Thrust side
WOT	-	Wide open throttle

Chapter 1.
Introduction

1.1 Background and motivation

Globally, the internal combustion engine still dominates the method of propulsion within the automotive sector. Its range, refuelling efficiency, low cost and well developed infrastructure surrounding presents significant targets for competing alternatives to achieve. These are as yet not achieved by any other automotive based propulsion alone. Other energy storage mechanisms, such as batteries and Hydrogen offer significantly smaller energy densities and often either slow re-charging times, in the case of batteries, or complex storage requirements in the case of Hydrogen. Combinations of systems (hybrids) are becoming more common and are currently in widespread production.

Over the last 15 years, the automotive sector has witnessed a number of ever increasing pressures. Continuing demands for improvement on emissions and efficiency have been imposed for each new European directive, alongside improvements for safety. Manufacturers have strived to develop cars which are attractive to both private and fleet customers through comfort, cost, reliability, performance and style improvements, whilst keeping abreast of the increasing directives and regulations.

With increasing vehicle sales in Western Europe, the European Commission has introduced a series of legislations / directives. These directives set the required levels for particulate and NOx emissions with progressive reduction in levels as shown in Figure 1.1.
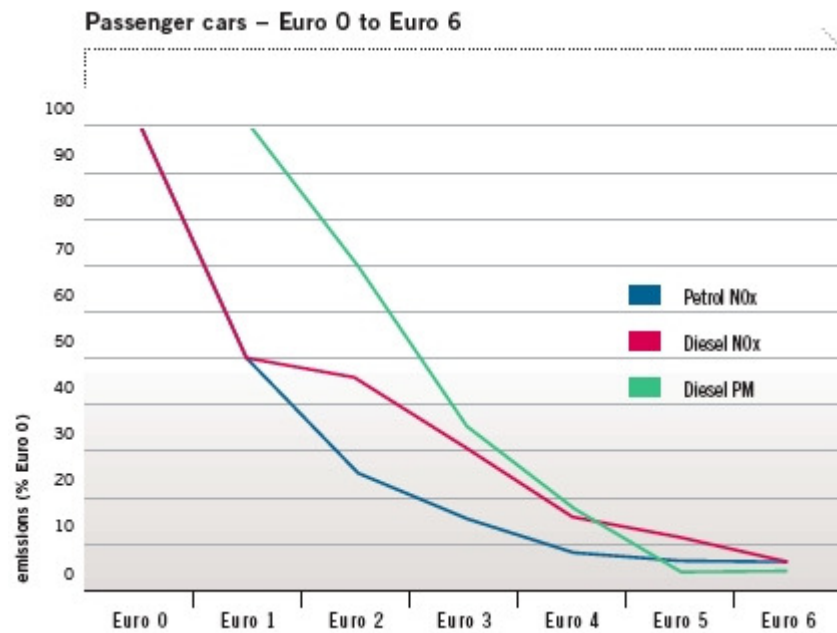
*Figure 1.1 - Euro standards emissions progression (**ACEA**)*

Legislation adopted in 2009 by the European Commission for improving fuel economy of cars aims to ensure that average manufacturer emissions do not exceed 120g CO_2/km for 65% of a manufacturer's production. This percentage rises annually to achieve 100% by 2015 with progressive fines where this is not met. This regulation has clearly driven the sights and objectives for a great number of car manufacturers, providing a real financial incentive to encourage innovation and diversification in product ranges and technologies. For some manufacturers, it has even led to changing the nature of cars in its provision in order to achieve these targets. A primary example includes Aston Martin's recent introduction of the Cygnet.

A greater need for fuel economy can be felt at national level, across manufacturers and with individual end-users. This need is translated into market trends, with increasing fuel prices and links to road tax duties as a means of mitigating CO_2 emission levels. Over the last 10 years these needs have been met mostly by manufacturers through the refinement of diesel engines, with diesel operated vehicles having a progressively greater share of sales in the UK and Europe.

Globally there are further challenges presented by some of the rapidly developing economies, such as China, with a per capita CO_2 emission of 1,500 tonnes per annum (the same figure is 20,000 tonnes for the USA). Nevertheless, the overall emission levels from China and India

are significant given their population sizes and with the increase in economic prosperity the figure for per capita CO_2 is only set to rise. Much of this rise will be produced as a result of the rapid rise in car ownership predicted for China and India, as well as for Brazil (see Table 1.1).

These developing markets are currently being presented with low cost, basic vehicles such as the Tata Nano. The Nano boasts a 624cc, 2 cylinder petrol injection engine, typically returning approximately 47 mpg; this however is at a great expense. It does not satisfy the Euro regulations by some margin and most models lack even the most basic safety features. It is however the cheapest production car of modern times at $2000 USD. (**O'Connor** (2008))

Table 1.1 - Projection of car ownership per 1,000 people (King 2007)

	India	China	Brazil	US
2000	5	7	137	480
2030	81	188	429	538
2050	382	363	645	555

In contrast to its European 'rival' the Volkswagen (VW) polo blue motion, it fairs poorly. The VW boasts an overall efficiency almost double to that of the Nano, contributable to a number of new systems. A more refined 1.2TDI engine, improved aerodynamics, regenerative braking and a start/stop system for town driving contribute to its superior efficiency. Additionally it meets and exceeds the new Euro5 directive. However this all comes at a price, at approximately £13,000 (**VW** (2010)).

Clearly road transport has revolutionised the way the world operates. In 1908 Henry Ford produced the Model T, the first mass-produced motor vehicle. Over the subsequent 100 years, road transport has radically enhanced mobility, economic prosperity and quality of life for billions of people. Typically modern cars have a higher level of equipment, improved ride quality, comfort and handling, both active and passive safety features, drastically improved reliability and a much greater useful life. These developments are primarily driven by customer expectation or governing regulation.

The impacts of these can be seen in the development history of the Mercedes C-Class; between the W201 first produced in 1982 and the Current W204 there has been

approximately a 20% increase in weight, a 30% increase in power but a reduced engine displacement from 2.0 to 1.8L. These trends are replicated across the automotive sector.

1.2 Efficiency improvements and engine development

Federal Mogul identified the losses from a typical combustion engine in an urban driving scenario (Figure 1.2). This shows that approximately 17% of the energy is dissipated as mechanical losses within the engine. These are made up of losses from piston assembly, journal and big end bearings, valve train, ancillaries and transmission. The piston assembly accounts for a sizeable proportion of the overall losses (excluding used power energy), at approximately 11%. Approximately half of the loss to the cylinder system was contributed by the ring pack. Clearly, even though the skirt contact is a relatively low loaded conjunction, it still accounts for a significant proportion of the frictional losses. It is therefore clear that a reduction in frictional losses across the board has the potential for a significant improvement.
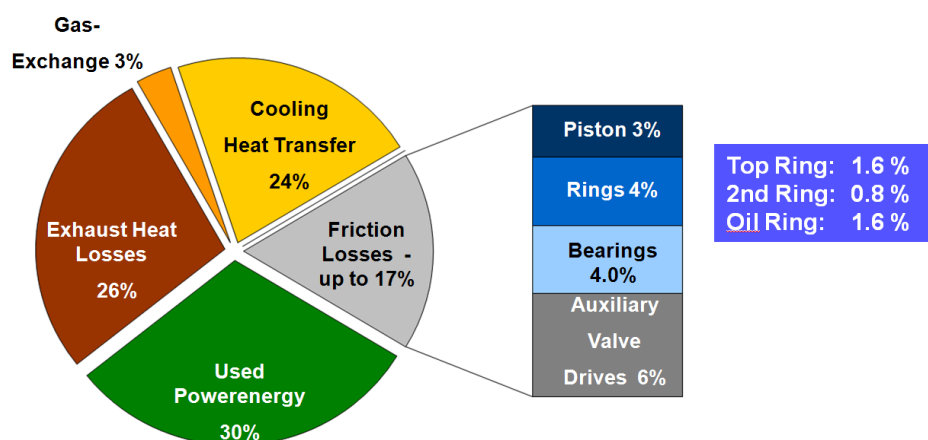
*Figure 1.2 - Combustion engine losses (**Federal Mogul**, (2012))*

For the commercial market there are many up and coming technologies that offer efficiency savings, targeting a number of overall losses or inefficiencies in a typical driving cycle. These have been identified in the King review (**King** (2007)) and a relative price for the inclusion of these has been estimated (Table 1.2).

*Table 1.2 - Possible efficiency improvements (**King**, 2007)*

Technology	Efficiency saving	Cost per vehicle (£)
Direct injection and lean burn	10-13%	200-400
Variable valve actuation	5-7%	175-250
Downsizing engine capacity with turbo charging or super charging	10-15%	150-300
Dual Clutch transmission	4-5%	400-600
Stop-start	3-4%	100-200
Stop-start with regenerative braking	7%	350-450
Electric motor assist	7%	1,000
Reduced mechanical friction components	3-5%	Negligible

The new technologies identified in Table 1.2 (many of which are included on the previously mentioned VW model) indicate significant potential improvements. The possible savings due to friction are relatively small, mainly due to the well-developed research and development knowledge in the area. It is key that the cost of modifications should be as small as possible so that the end-user is encouraged to bear the extra initial outlay set against the potential eventual benefits. The investment in tribological improvement is largely research and development; likely developments will be in geometrical improvements. Such improvements are likely to alter the manufacturing process slightly with little added cost.

Along with efficiency improvements, there are other key objectives in the development and refinement of commercial engines:

- Reduced noise with improved Noise, Vibration and Harshness (NVH) characteristics
- Reduced package space for engine installation
- Increased lifespan
- Reduced oil consumption

Achieving the aforementioned improvements can only be accomplished by careful consideration and design of lubrication systems. More specifically the role of the lubricant in separating the bodies within the piston assembly reduces friction, which in turn improves system dynamics, as well as fuel efficiency, thus indirectly improving emission levels. This is critical in avoiding major failure and achieving desired improvements. A great deal of research and development has been carried out in the area of piston tribo-dynamics, ring pack

lubrication including study of wear pattern formed on piston skirt and inside the bore or cylinder liner. The clearance between the reciprocating piston in the bore and the deformation of the former leads to the formation of a lubricant film and generation of hydrodynamic pressures in the contact conjunction (**Knoll** and **Peeken** *(1982)).* A detailed review of the research most relevant to this body of research is presented in Chapter 2.

More generally reduction of engine parasitic losses can be achieved by a combination of a number of strategies, as noted by **Blau** and **QU** (2004):

- Redesigning the engine components
- Reformulating the lubricants
- Improving methods of lubricant filtration and supply
- Reducing churning losses in fluids
- Changing the operating conditions of the engine
- Substituting more durable, low friction materials
- Altering the finish or micro-scale geometry of the bearing surface

1.3 Aims and objectives

The research being undertaken seeks to develop the fundamental understanding of the complex piston-bore / Tribo-dynamics problem, particularly under realistic "fired" engine conditions with the entailing transient behaviour.

The project aims to produce a set of validated predictive numerical tools in order to continue the development of piston-liner systems with the overall aim of improving performance through modification of the conjunction. The models will determine the effect of significant parameters in the operation of the piston skirt through a range of operating conditions.

The model will be based around a transient solution for the secondary piston dynamics. This involves the integration of inertia dynamics, coupled with a conformal contact lubrication model for piston skirt-bore/liner conjunction, employing realistic lubricant boundary conditions. This model involves the solution of Reynolds' equation to obtain generated contact pressures for lubricant film shape and thickness, determined through prediction of

conjunctional deformation (local), as well as thermo-elastic global deformation of contiguous solids (cylinder liner/bore and piston).

The validation of this model will be achieved though parallel testing using a modified Honda CRF 450R engine as its base. The numerical predictions will be validated through data acquired by direct film thickness measurement using a series of ultrasonic sensors.

The work conducted throughout this thesis is part of the wider research project Encyclopaedic, funded part by industry and part by EPSRC. The work covered in the wider project entails the development and testing of new experimental techniques and parametric studies in the effects of film thickness variation, wear and friction generation in the piston – liner system. In addition to the study of piston skirt lubrication presented here, the numerical development also includes the effects of ring lubrication, surface properties, thermal variations and surface modification.

1.4 Structure of thesis

Thus far the background details to the project and trends within the automotive industry have been explained. **Chapter 2**, a literature review, details the current design trends and the development of Tribology with its application to the piston skirt conjunction. A detailed review of elastohydrodynamic lubrication and global shape representation is also presented here.

Chapter 3 explains the kinematics and dynamics of the piston assembly. The theory of hydrodynamic lubrication and the equations derived for usage within the computational routines is shown.

The derivation of the equations of motion for the calculation of the piston's dynamic secondary motion, in a Newton-Euler form, is presented alongside the kinematic solution to the piston's primary motion.

The structure of the transient algorithm is detailed showing the constituent routines and dependencies developed within Chapters 3 and 4.

Chapter 4 details the characterisation of the piston skirt and cylinder liner. The shape, modes of distortion and methods of calculation are presented and developed through this chapter.

Chapter 5 details the experimental setup used throughout the project. The instrumentation and test procedures are presented here, along with the measured input data for the speed and load cases studied.

Chapter 6 shows results from quasi static procedures. Initial comparisons with the experimentally recorded film thickness values are presented within this chapter. The contact conditions are analysed with the fundamental mechanism of lubrication identified for the contact.

Chapter 7 presents the results of the detailed transient analysis and comparisons with experimental results for lubricant film thickness. The three dimensional motions of the piston are characterised and the influencing variables are identified and their effects illustrated.

Chapter 8 provides a conclusion from the developments throughout the project. The findings, including details of achievement of the project's aims within the wider Encyclopaedic project are detailed. The novel aspects of the work throughout are highlighted. Finally, suggestions for future work and development are discussed.

2.1 Overview and Introduction

This chapter discusses the use of pistons and presents a brief history of, it also illustrates how the fundamental design has developed. The chapter also details the history and development of the modern combustion engine and highlights the design features of the fundamental piston assembly components. An overview of the history of Tribology is provided alongside a review of the modelling and simulation literature surrounding the piston skirt – liner conjunction. Finally, a number of methods previously devloped for the direct measurement of lubricant film thickness are discussed and their relevance to the specific conjunction considered.

Pistons have been used in a number of different applications in various forms for thousands of years. The earliest known application was the piston pump of Ctesibius from Alexandria in the 2nd century BC (**Usher** (1982)). The pump exploited the successive suction and compression achieved in a pair of cylinders in order to raise fluids. In the 17th century pistons were applied to achieve propulsion in the model steam engine by Henri Papin (**Dell** (2004)**).** This was a simple external combustion engine using the expansion of steam fed into a cylinder, displacing the piston, converting the work into rotational motion by a simple connecting rod-crank assembly. Much of the early problems within the steam engine were associated with the sliding seal and the accuracy related to the manufacture of the cylinder. In order to improve the sealing and control the secondary motion, two con rods were commonly employed with direct, non-articulating coupling (piston rod) being made to the seal and a secondary connection being made to the crank coupled rod. This connection was supported on a slider, often made from brass, wood or bronze. It was this linear sliding bearing that supported the inherent side force within a crank slider mechanism. This mechanism reduced the wear on the cylinder and improved the quality of seal; it also made replacing worn parts a much simpler operation. A significant downside of such an arrangement is the length required by the mechanism. Early examples of such an arrangement are still operational today in many different forms; shown in Figure 2.1 is the example of a hydraulically driven water pump still in operation today using this arrangement.

Figure 2.1 - Piston driven water pump with two connecting rods

The internal combustion engine was first used in propulsion by Nicolaus Otto, though he was not the first to develop the idea for a 4-stroke internal combustion engine. The concept was originally proposed by Alphonse Eugène Beau de Rochas though he did not patent it. The 4 stroke cycle Otto developed encompassed 4 different strokes per cycle: intake, compression, expansion upon ignition of a fuel mixture and finally exhaust. Otto's single cylinder system used two valves allowing a pre mixed fuel-air mixture into the combustion cylinder before ignition see (Figure 2.2). He also created a simple cam-roller proportional valve operating system. Modulation of speed was achieved by regulating the air fuel mixture. (**Otto**, (1877)).
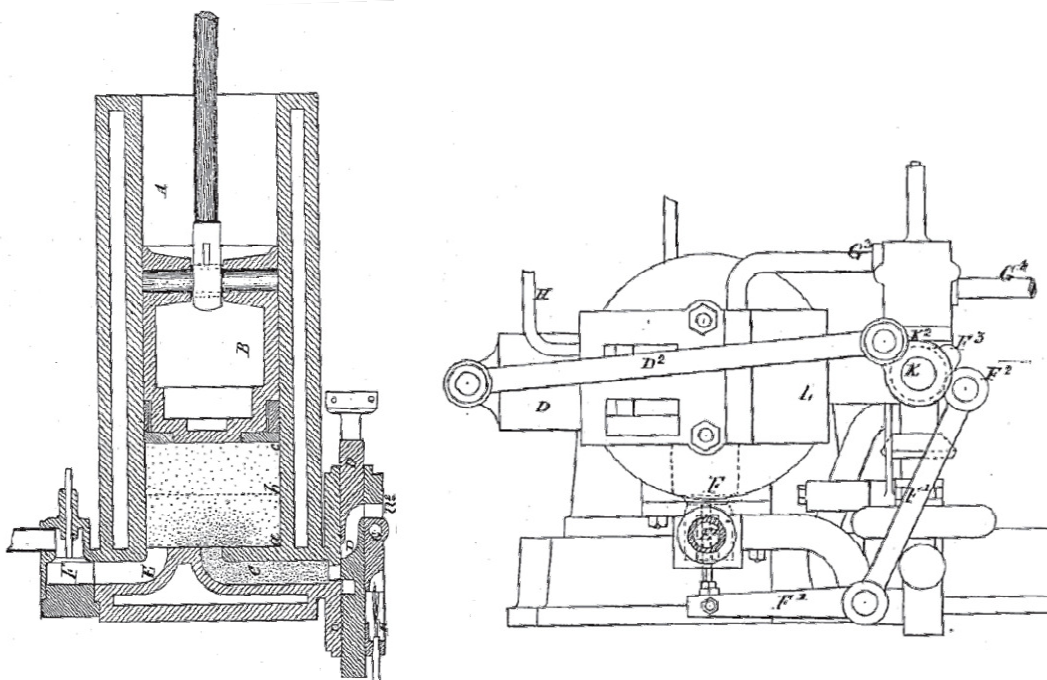
*Figure 2.2 - Ottos original patented 4 stroke design, **Otto** (1877)*

Otto's engine was a technological breakthrough of the age, which effectively founded the internal combustion engine industry and by 1890 almost 50,000 of these engines had been sold throughout the USA and Europe (**Heywood,** (1988)).

The principal of the 4-stoke internal combustion cycle has not differed from Otto's original design in over a hundred years. Today, the technology surrounding the process in all its forms has improved aspects since the initial simple Otto's engine. Of the engines available now there are two principal types; spark and compression ignition. They both utilise the same piston assembly arrangement, but employ different combustion methods and have very different NVH signatures.

2.2 Piston assembly

A modern IC engine piston assembly (Figure 2.3) is made up from the following components

        A. Piston
        B. Connecting rod
        C. Gudgeon pin
        D. Compression rings
        E. Oil control ring
        F. Cylinder liner
        G. Engine block
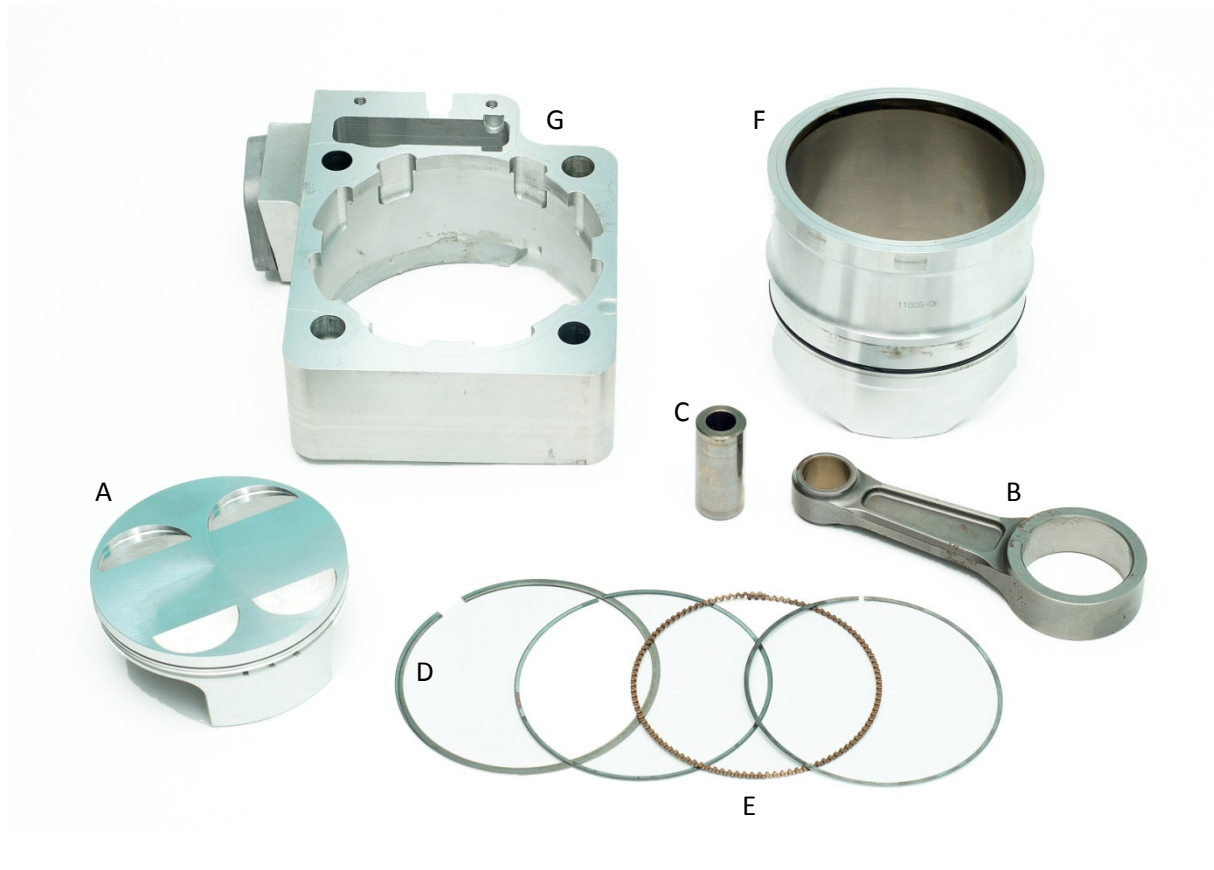
Figure 2.3 - Components of piston assembly

Pistons are designed specifically to suit the engine for which they are intended, the type and size of piston will depend on the engine's application and requirements.

Figure 2.4 - Examples of high performance engine pistons

Figure 2.4 shows two very different pistons and skirt profiles, although both are from SI engines. The RHS shows a piston from a high performance road vehicle engine, whilst that on the left belongs to a performance off-road motocross motor-sport bike engine. There is a large difference in the extent of the skirt, masses of the pistons, stiffness and number of rings. The performance off-road piston is much lighter and more flexible in order to reduce inertia and friction. These types of piston typically weigh less than 0.25 kg. They are very similar to F1 vehicle pistons, which have an expected lifespan of 450 km typically at full throttle. In road cars the designed useful life is much longer. In the case of the Aston Martin (AM) and other niche OEM vehicles a useful life corresponding to at least 200k miles is envisaged with regular oil changes and servicing. The AM piston also features an offset gudgeon pin and centre of gravity. Primary reason for having the gudgeon pin positioned eccentrically is to prevent the piston from slamming into the cylinder bore at or in the vicinity of the top dead centre (TDC). This problem is referred to as piston slap. The aim of an ideal motion of piston with offset gudgeon pin is for the piston to gently rock from side to side within the bore, thereby eliminating slapping action (**Betts,** (1997)). This motion of piston has its downside in terms of performance; this is discussed in more detail in section 3.2.

2.2.1   Current skirt design features

Pistons must be able to transfer the mechanical load to the Gudgeon pin and onto the connecting rod ensuring piston stability. At the same time, they must also withstand large thermal and mechanical stresses. They must be able to effectively distribute and transfer the heat generated through combustion in order to prevent catastrophic thermal distortion. The external shape of the piston skirt is critical in compensating for the mechanical and thermal expansion and deformations experienced. In order to achieve this objective, pistons are machined to present a 'Barrel' shape, which is the key requirement to create a hydrodynamic wedge and compensates for the temperature gradient between the top and bottom surfaces (**Kerr,** (1995)). In the circumferential direction of the piston (i.e. its periphery) the profile is an oval, where the diameter across the thrust axis is greater than over the pin axis. These are both shown in Figure 2.5. In some cases in free (unfitted into the bore) cold condition (not fired engine) the piston diameter across the thrust axis is greater than the bore, effectively pre-stressing and deforming circumferentially when it is installed into the bore (**Howell-Smith,** (2010)). The oval shape is employed to ensure that under both thermal and mechanical stresses the skirt and bore conform adequately. This conformability helps to maintain low peak pressures, a good load distribution and a coherent film, separating the contacting surfaces and keeping wear to a minimum.
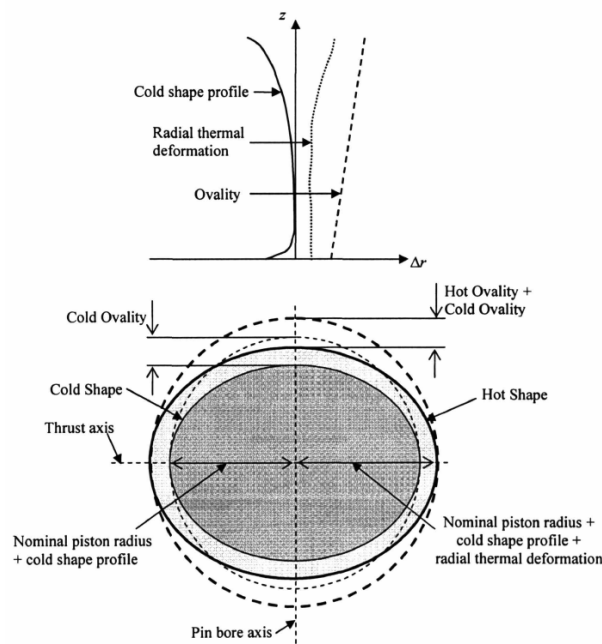
*Figure 2.5 - Barrel and ovality changes (**McClure** (2007))*

14

2.2.2 Cylinder bore and liners

The area constrained by the cylinder bore above the piston crown and below the head constitutes the variable volume combustion chamber. The liner is designed to withstand the thrust forces from the skirt. It provides the surface for the piston rings to seal against and is critical for heat transfer to the coolant. There are three main types of liners (fitted into the cylinder bore of high performance engines): dry, wet and cast in. Wet liners' interface with the engine's cooling water directly, whilst dry ones do not. The main advantage of a wet liner is its ability to draw heat away more quickly, a distinct advantage at high speed, typical of high performance engines (piston speeds of the order of 30-35 m/s at mid-span are not untypical, whereas in normal road cars these are in the range 10-20 m/s). In the case of wet liners particularly, the thermal deformation plays a large part in the conformability with both the piston rings and the skirt. As such the shape and size of the liner bores is specified with these issues in mind. The liners are generally pressed into the bore, then machined and honed to ensure the correct geometry and surface finish prior to the piston being fitted. The importance of this surface finish is discussed in section 2.7.

2.3 Tribology – A review and introduction

The science of Tribology focuses on the understanding of lubrication, friction and wear. It is a multidisciplinary subject requiring other key disciplines, including but not limited to surface topography & deformation, lubricant rheology, heat transfer, dynamics and material science. The aim of a tribology designer of a lubricated conjunction is to control the friction and wear between two contacting surfaces, whether it is through the introduction of a shearing film between two surfaces in relative motion e.g. a roller bearing, or the reduction of film maintaining contact e.g. a rubber automotive tyre.

Evidence shows that man has understood to some extent the relevance of lubrication as far back as ancient Egyptian times. Records have shown that liquids were used to reduce the friction on a sledge carrying a monument (**Dowson** (1968)), this representing a purely sliding contact. Earlier examples have been discovered such as the potters' wheels dating back to 3250 BC, employing a simple bitumen lubricated pivot hole bearing; this represents the second classical contact type, rolling.

Although in the examples above the use of oils was employed for lubrication, the mechanism of lubrication was not understood and their use was derived from empirical observations. Newton's description of viscosity in 1673 represented the first step in the evolving understanding of the lubrication mechanism; viscosity of a lubricant (in general any fluid) being its most important property in fluid film lubrication. Prior to Newton a property such as viscosity was only surmised as the resistance of a fluid to motion. In 1829 observations were made by Rennie and he discovered that the effectiveness of lubricants was related to their ability to separate sliding surfaces (**Dowson** (1968)). Beauchamp Tower (**Tower** (1883)) discovered one of the benchmarks in Tribology, substantial pressures within journal bearings. His experiments with relatively high speed lubricated brass bearings showed that the hydrodynamic film was being maintained due to the motion of the journal. Working directly from Tower's observations, Reynolds created his famous theory of hydrodynamic lubrication (**Reynolds** (1886)).

Reynolds was able to mathematically describe the phenomenon observed by Tower, when a viscous fluid is drawn into a space of decreasing height by the imposed surface velocities of the bearing elements; load carrying pressures in the oil film would be generated. The mathematical formulation is the well known Reynolds' equation, which describes the physical

wedge condition of lubricant in a narrow conjunction. Reynolds derived his formula by the simplification of Navier-Stokes equations, ignoring inertial, body and surface forces, only retaining the viscous force of the lubricant.

$$\frac{\partial}{\partial x}\left(\frac{\rho h^3}{\eta}\frac{\partial p}{\partial x}\right)+\frac{\partial}{\partial y}\left(\frac{\rho h^3}{\eta}\frac{\partial p}{\partial y}\right)=12\left(\frac{\partial}{\partial x}\left[\rho h u\right]+\frac{\partial}{\partial y}\left[\rho h v_l\right]+\frac{d\left(\rho h\right)}{dt}\right) \qquad (2.1)$$

The relationship Reynolds derived indicated that the minimum film thickness between a pair of contacting surfaces decreases proportionally to an increased load. This meant in certain cases performed by Tower, the film thickness would have been less than the surface roughness of his brass bushing. This phenomenon would have produced wear between the two surfaces and would have been clearly evident, this proved not to be the case. In 1881 Hertz had considered localised elastic deformation of ellipsoidal solids of revolution under loads which were sufficient to cause small elastic surface deformations. Hertz's localised elastic deflection obeys the conditions: $\delta_h << a << R$, where δ_h is the Hertzian deflection, a is the footprint radius in a circular point contact and R the radius of a ball in contact with a semi-infinite elastic solid. It is clear that this elastic deflection can create a small gap, which may be occupied by a film of lubricant, separating the load bearing surfaces.

In 1901 **Stribeck** (1901) performed a number of experiments on journal friction, looking at the correlation between the Co-effecient of friction, load and speed. He looked in detail at the minimum point. He summarised his results on a curve, plotting the co-efficient of friction and the film parameter, λ , where $\lambda = \dfrac{h_{\min}}{\sqrt{R_a^2 + R_b^2}}$. R_a and R_b are the rms roughness values of the two contacting surfaces. Figure 2.6 shows his curve in the form now commonly recognised, though Stribeck had not fully understood the phenomena occurring in each of the sections identified.
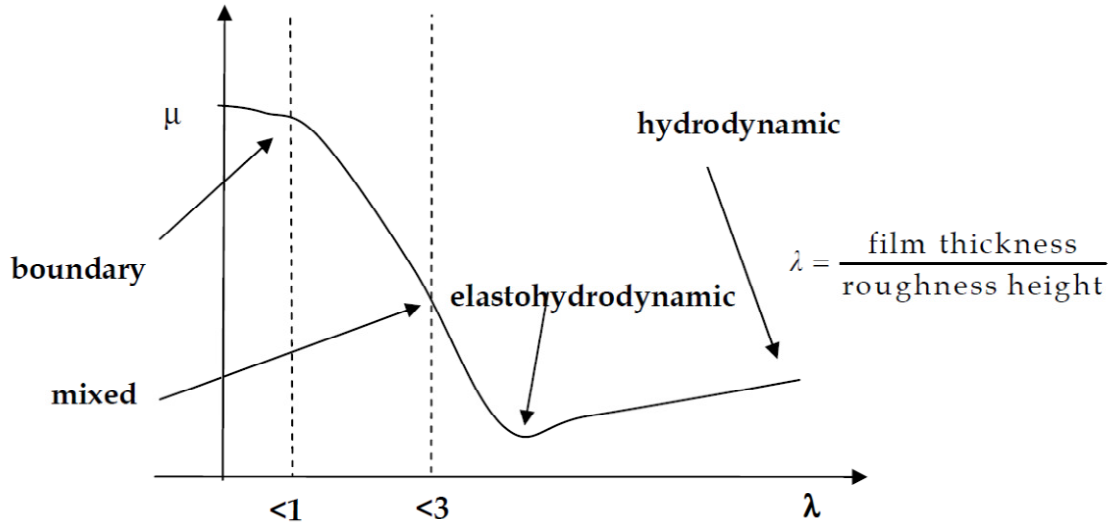
Figure 2.6 - Stribeck curve

This was realised only half a century after Reynolds' 1896 paper by Grubin based on his work with Ertel (**Grubin**, 1949). In fact, Hertz had died at the age of 27, two years prior to the Reynolds' paper. The combined hydrodynamic action of the fluid film and the elastic deformation of the contiguous surfaces were termed elastohydrodynamic lubrication (EHL).

With high loads the and absence of any wear on counterforming contacts, in particular meshing gear teeth, authors like **Peppler** (1936, 1938) and **Meldahl** (1941) calculated the elastic deflection of the lubricated surfaces, using Hertzian assumptions. Although the inclusion of this gap moved a step closer to the experimental observations, it did not fully represent the gaps measured.

Others such as **Gatcombe** (1945) had suggested that piezo-viscous action of the lubricant may be responsible for the increased load carrying capacity of concentrated counterformal contacts. This effect was also found to be insufficient to explain the observations.
The lubricant viscosity variation with pressure, generated in a narrow conjunction was appreciated by **Barus** (1893) with assumed idealised isothermal conditions as:

$$\eta = \eta_0 e^{\alpha p} \tag{2.2}$$

This relationship is now widely referred to as the Barus law. It was used by **Gatcombe** (1945) and later by **Cameron** (1952) to take into account changes in viscosity in concentrated counterformal contacts. α is the pressure-viscosity coefficient with the unit of m^2/N or $(Pa)^{-1}$, which makes the product αp dimensionless. When this product is assumed to be zero, iso-viscous behaviour is indicated; $\eta = \eta_0$. This was the solution used by Reynolds for his long roller and also later with different boundary conditions by **Sommerfeld** (1904) for his long bearing approximation. The physical interpretation for $\alpha p = 0$ is that the generated pressures do not affect the lubricant viscosity. However, it is evident that in lubricated contacts with thin films, even those of few tens of a micrometre, as present in Reynolds' time only forms part of the solution. The contact deflection predicted by the Hertzian theory works in conjunction as the pressures generated within the lubricant are within the margins used by Hertz. Therefore, a combined piezo-viscous action and localised contact deformation can explain the absence of wear at moderate to heavy loads, the phenomenon that Reynolds was searching for. Grubin called this elasto-hydrodynamics. A subsequent analysis by **Petrusevich** (1951) confirmed the **Ertel and Grubin** (1949) supposition. However, there existed the concern that the classical Hertzian pressure distribution does not conform to the continuity of flow condition. **Dowson and Higginson's** (1959) numerical solution detected a pressure spike in the vicinity of the contact exit, where a dip in the minimum film thickness was also observed. This means that the lubricant upon entering into the contact with rising pressures has a significantly increased viscosity. It becomes almost like an amorphous solid. It is pushed along by the relative motion of the surfaces and the pressure gradient in the direction of entrainment. As the pressures are reduced from the peak Hertzian value (often termed as primary pressure peak in elastohydrodynamic contacts) the lubricant viscosity also reduces dramatically. This means that locally the load carrying capacity is reduced, giving rise to a secondary pressure peak (or pressure spike or pip as this is often referred to) and a dip in the film thickness is noted (minimum exit film). The size of the secondary pressure peak and its positioning within the contact is related to the operating conditions; load and speed, the inlet meniscus (supply of lubricant), mechanical properties of contacting surfaces and bulk lubricant rheology, particularly viscosity (**Evans and Snidle**, 1982).

Patir and Cheng (1978) created a model of hydrodynamic lubrication taking into account the effects of three dimensional surface roughness. They accounted for surface heights and

distributions in a similar manner to **Greenwood and Tripp** (1970) and also considered the directional properties of artificially orientated roughness ridges. Their average flow method looked at pressure and shear induced flow across two rough surfaces and compared it to that of a 'smooth' bearing.

This forms the basis of the vast majority of literature in existence concerning lubrication predictions across a wide array of applications (**Jalali-Vahid** (2000), **Grimble** (2009) and **Balakrishnan** (2002))

2.4 Numerical studies into Piston skirt lubrication

One of the first papers, reporting a simulation of piston skirt lubrication was undertaken by **Li et al** (1981) on a large V-8 spark ignition engine. The secondary motion of the piston was solved without taking a lubrication film into consideration. The results showed that the location of the gudgeon pin has a critical influence on the secondary piston dynamics. The results obtained showed that the location of the gudgeon pin axis has a direct influence upon the piston skirt to cylinder liner friction. The solution of the second order differential lateral accelerations was ignored and the analysis was carried out to obtain a repeated cyclic pattern. The clearance and viscosity of the lubricant were also found to be important as a result of this simplistic analysis.

Knoll and Peeken (1982) were one of the first to employ a lubrication solution to their study. They generated a hydrodynamic solver and applied it to a motorised engine. They identified that the following factors influence the secondary piston dynamics:

- Gas and inertia forces
- Piston clearance
- Offset of gudgeon axis
- Hydrodynamic friction and bearing forces at the gudgeon pin and piston skirt
- Elastic deformation during impact of the piston on the cylinder liner wall

They calculated a series of secondary motions, negating the effect of viscous damping by the lubricant. Their study also identified the improvement from the introduction of non cylindrical skirt geometry, something that is incorporated into most pistons made at present.

Li et al (1987) performed an EHL analysis of the liner-skirt conjunction of a motored engine, with particular emphasis on the axial profile. Using a two-dimensional Reynolds solver with a thermally deformed profile they solved the secondary motion of the piston and predicted the skirt power for two different skirt profiles. They emphasised the advantages of using a barrel-shaped piston skirt, enabling the skirt to carry load in both the upward and downward stroke directions whilst still maintaining a converging wedge, encouraging lubricant entrainment. A numerical analysis to compare the hydrodynamic lubrication of a conventional piston with that of an articulated piston in a large engine was undertaken by **Dursunkaya** and **Keribar** (1992). The articulated piston skirt design was found to give rise to larger tilt angle of the crown about the gudgeon pin when compared with that of a conventional piston. Therefore, the articulated skirt travelled more parallel to the liner than the rigid skirt.

Liu et al (1998) integrated the two dimensional Reynolds solver with surface roughness effects, based on the **Greenwood and Tripp** (1970) method. They solved the dynamics considering the inertia of the piston and gudgeon in a fired engine using the Newton-Euler method. However they used a rigid skirt profile, simulating with both linear and parabolic profiles. They also investigated the effect of piston offset and 'nominal clearance'.

Balakrishnan (2002) investigated a number of scenarios: a high pressure compression ignition engine and a high performance spark ignition F1 engine. He included the inertial effects in the same method as **Liu** and **Xie** (1998), using a fired arrangement with experimentally obtained combustion pressures. Measured profiles along the thrust line were employed with a cold circumferential fit, which was later improved with the incorporation of thermal expansion on the piston using the finite element method. An improved conformability resulted which showed lower pressures and thicker films and a higher load bearing capacity. This change in conformability is key design feature in modern high performance engines. High performance pistons are actively designed to conform to each other by a combination of skirt bending and thermal expansion. Much of the design improvements in this area by industry have been empirically based (**Balakrishnan** (2005)).

Balakrishnan developed his work on the contact conformability without the inclusion of global deformation (bending) of the skirt and highlighted the necessity to include this in the future.

Guzzomi et al (2008) performed an analysis based on the optimisation of the gudgeon position. They included inertial effects from the connecting rod in addition to the piston and gudgeon as previous authors have. Little attention has been given to the effect of the lubrication of small end-gudgeon interaction. During combustion the normal load on the pin bearing can rise rapidly; combined with the poor lubrication of the pin and the articulation of the bearing, results in an additional moment which can be contributed to the motion of the piston (**Dursunkaya** (1992), **Suhara** (1997) and **McClure** (2007)).

Recent work has considered the variability of the primary motion in a dynamic form and its effect on the piston lubrication (**McFadden**, (2011)). McFadden also goes on to illustrate the effect of altering the piston skirt barrel profile in order to stabilise the piston's secondary dynamics; he does though neglect the effect of gross distortion and its resulting effect on the location of the pressure distribution

McClure (2007) developed a model of piston secondary motion incorporating component deflections using the specific adaption of finite element models in a similar method as to **Zhu** (1993). A simplistic inclusion of the rotational moment produced due to friction at the gudgeon pin bore was included. A simple oil availability, accumulation and transportation model was produced varying the oil availability through the two separate stroke directions. The surface forms, asperity interaction and tooling effects were considered and compared using a variety of models and a multi-grid approach. **Bai** (2012) developed the oil transportation method introduced by McClure but also included a series of comparisons with LIF observed film shape profiles.

2.5 Solution of deformation within tribological conjunctions

As discussed previously in section 2.3 the deflection of surfaces under hydrodynamic loads has been recognised and predicted for many years now. **Hertz** (1896) found an analytical solution defining the contact stresses for elastic bodies in contact. For a more general case of

deformation in two dimensional elastic half-space, the limits of integral, known as "singular integral equation" (**Johnson** (1985)) was employed by **Muskhelishvili** (1963) to uncouple them. An approach in solving for deflection of conforming bodies in contact (spherical or cylindrical) was provided by **Paul** and **Hashemi** (1979). Another methodology to solve for the deflection of bodies in conformal contacts is by finite element approximation **Zienkiewicz** and **Taylor** (2000). Solution for pressures due to a uniform line load along a semi infinite solid was given by **Timoshenko** and **Goodier** (1970). This analytical solution was extended to solve for pressure caused by a distributed load. In finite element, the discretisation of a continuum allows for the stress-strain relationship in an element to be expressed relative to adjacent elements by the use of shape functions. **Szabo** and **Lee** (1969) derived stiffness matrices to express the elasticity of a plane using Galerkin's method. This method has been used by a number of authors in a variety of different conditions.

The column method is a single point estimation (Figure 2.7) for deflection and requires significantly less computational time. It is not particularly well suited to soft materials (**Grimble** (2009)) but it has been successfully applied in a skirt – bore configuration and verified against Galerkins' semi-infinite solution. This yielded a small error of 5-10% (**Balakrishnan** (2002) and **Gohar** (2008)).
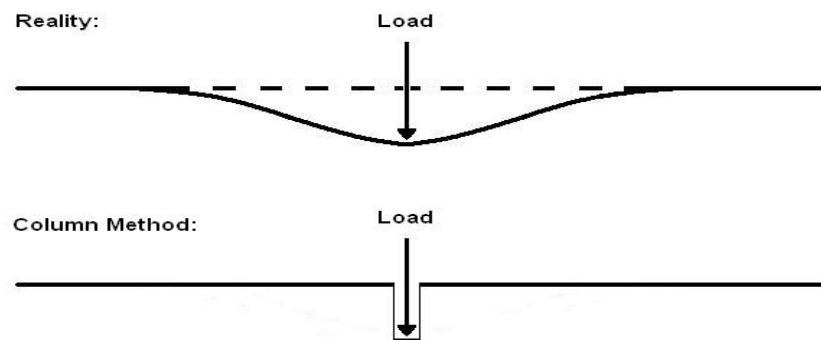
Figure 2.7 - Column method deflection compared to reality

Section 2.4 detailed the specific cases of piston skirt lubrication models, many of which used an FE derived model to form the solution to conjunction distortion. The case of localised distortion as presented here is often used when the global stiffness of the component is significantly higher than that of the material; i.e. the global component distortion is negligible

compared to the surface deformation. In the case of cam follower or gear tooth contact this case is generally valid. For the case of the piston skirt-liner conjunction the component stiffness is often low enough to induce deflection orders of magnitude greater than predicted surface distortions, as such they have a much more significant effect on the conjunction shape.

2.6 Lubricant film measurement

With the ever increasing complexity of Tribology simulations and the incorporation of a large range of physical influences, the need for precise and accurate test validification became more important. A range of techniques for measuring film thickness, most commonly for the ring conjunction have been developed over the last 40 years. The main methods in measuring film thickness are capacitance, inductance, resistance and ultrasonic. Detailed research and development is beyond the scope of the authors' research but they are briefly outlined as they are an important element of the project on a larger scale.

2.6.1   Capacitance techniques

This is based on using a miniature parallel plate capacitor between the piston ring and the cylinder bore. The sensor can be mounted to either surface and it normally consists of a small central electrode (about 0.25mm in diameter) enclosed by an insulator and hypodermic tube which acts as a screen. This does present an issue with the sensor having to be either positioned on one of the two contacting surfaces, which will change the surface properties, inertia and bulk modulus. These alterations will lead to an inaccuracy in the film thickness measurement; it does however allow easy measurement of full cycle film thickness. The technique, although relatively intrusive, it has proven durability undergoing relatively high speeds of up to 3000rpm at full load in a low to moderately powered road car engine. Measurements were made for a single sensor at mid stroke, observing a ring conjunction at 11m/s. The technique is limited to cases of full and coherent lubricant film ensuring complete surface separation. The increased conductivity potentially observed when partial asperity contact is apparent breaks down the signal, **Garcia-Atance Fatjo et al** (2013).

2.6.2 Inductance techniques

Inductance techniques work on the basis that the inductance of a circuit element, such as a wire is dependent on its proximity to magnetic material. By using an oscillating voltage supply and measuring the current lag behind the voltage signal the proximity of magnetic material (such as the cylinder liner wall or the ring) can be determined. The sensors used are typically miniature coils containing only a few windings. The experimental devices can be self-inductance, mutual-inductance or of the eddy-current type. The main problem with these sensors is that they are significantly affected by temperature changes as the temperature determines the resistance of the wire. As the temperature fluctuations within a fired engine are very large, this causes a significant problem. These sensors are significantly easier to package than the capacitance type, since they can be mounted behind the ring, as done so by **Wing** (1972), **Dow** (1983) and **Tamminen** (2006).

2.6.3 Resistive techniques

Resistive techniques simply measure the resistance of the oil film and relate this to its film thickness. It is the first documented technique of film measurement and was first done by **Courtney-Prat** (1946). The general approach involves electrically insulating the piston-ring, applying a DC voltage and using a resistance bridge circuit to detect small changes in resistance. This system works well when there is an oil film, however, when the film is sufficiently small enough for asperity contact to occur the method fails unless the liner is made of a non conducting material. **Furuhama** (1961) pinned a piston ring at one end while connecting the other end to a valve anode to measure average film thickness. The opposite of this was then done by **Saad** (2007) who measured the voltage between the piston-ring and two electrodes embedded in the cylinder wall.

2.6.4 Ultrasound techniques

Acoustic methods have been used by nature for measuring distances for many thousands of years, although this isn't a relatively new concept in engineering it is though very new tool

for measuring oil film thickness. The process is based on sending out an ultrasonic pulse and then listening to the reflected wave; the time delay and waveform received can then be used to calculate the distance travelled and the material density (and thus viscosity), as long as the accurate speed of sound in the materials is known then the distance can be accurately found.

The beauty of this technique is that it is completely un-invasive and the sensors can be mounted on the back of the ring or the outside of the cylinder liner and measure through the material. The same sensor can also be used to send and receive the signal, Figure 2.8. The only problem with the system is the data acquisition speeds involved, as the sensors need to be read many times faster than the time it takes for the wave to pass through the oil film and reflect back to the sensor. When talking of micron film thicknesses and the speeds of sound in solid metal objects the sampling speeds must reach hundreds of MHz. Research into this area has been limited, mostly due to the computational requirement posed by the necessity for high speed data collection. Nevertheless this has been used successfully and results were published (**Dwyer-Joyce** et al (2006)), the work of these authors continues within the Encyclopaedic project. This is one of the intended methods of data acquisition for measurements on both the skirt and ring.
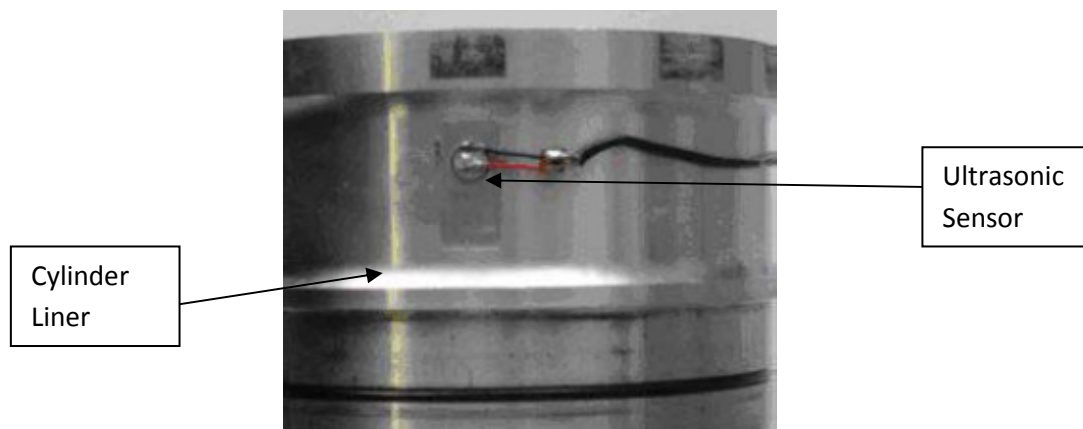
Figure 2.8 - Ultrasonic measurement of oil film thickness on a cylinder bore

2.6.5   Laser induced fluorescence (LIF) techniques

In the 1970's it was found that fluorescence of oils in ultra-violet light could be used to measure film thickness. Illuminating thin films causes them to absorb energy and then emitting this as light of a specific wavelength. It was found that the intensity of emitted light is dependent on the thickness of the layer.

Many problems with utilising this process for in engine measurements exist, not to mention the fact that either windows or fibre optics need to be embedded in the measured surfaces. A complicated laser arrangement is required with the use of lubricant dyes to enhance the fluorescence response of the oil. The system is temperature dependant and temperature compensation must be built in. The oil and dyes also suffer from photo-bleaching, which is where the fluorescence effects gradually become less sensitive to the illumination due to oil degradation. To overcome these problems many investigators use in situ calibration before and after measurements are taken. The process has been used by various researchers since Ford used it successfully with a transparent bored engine in 1980.

Most recently LIF has been used to analyse the piston skirt/liner contact. Its results lack clarity as to the three dimensional oil film profile but successfully indicate the thrust/ anti-thrust side bias the piston has through a series of strokes, **Bai** (2012). Recently **Notay** (2013) has used this technique to observe the oil ring film thickness and the effect of oil degradation on the conjunction.

2.7 Surface modification

Surface texturing is receiving an ever-increasing attention in tribological design. It was traditionally thought that improved surface quality, thereby reducing the surface roughness of mating members would improve the condition of a lubricated conjunction. Therefore, super-finishing surface treatment methods have been used, such as lapping or honing. Recent studies have shown the potential of surface modification to improve lubrication and reduce friction and wear. The honing of the cylinder liners to retain lubricant is a well known example of this. Much of the detailed research and development within the application of IC engines has concentrated on the piston compression ring (**Rahmani** (2008), **Ronen et al**

(2001)). At reversal the compression ring(s) are subjected to high loads which supported by only the squeezing action of the lubricant, as such the localised texturing at or approaching the upper compression ring reversal point is most beneficial. Figure 2.9 shows recent work detailing laser etching at these points with a non-continuous pattern to reduce the effect of blow-by. This has been shown both numerically and experimentally to reduce the friction contributed by the ring. (**Morris** et al (2013a)).

Generally the modification of surfaces with the intention of improving frictional properties involves intentionally creating undulations or minute cavities, grooves or valleys in the surface. These surface 'micro-structures' can act as micro reservoirs for lubricant, retaining lubricant which is released when needed.
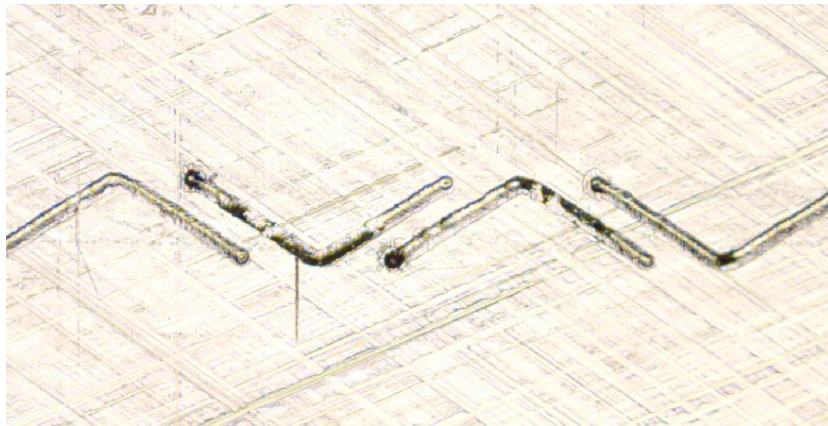
*Figure 2.9 - Magnified laser etched features on a cylinder liner, From **Morris** et al (2013a)*

Balakrishnan investigated the effects of surface modification on the skirt, the predictions included 2µm deep groves separated by 2µm distance. His results were a direct comparison with a smooth surface, They showed an increased film thickness due to the improved lubricant supply. Pressure perturbations or undulations were observed due to the localised increased film thicknesses. A comprehensive review of surface texturing is provided by **Etsion** (2010).

Chapter 3.
Piston assembly dynamics and Tribology

3.1 Overview and Introduction

This chapter derives the equations of motion for both the primary and secondary piston movements. The solution methodology for the dynamic secondary motion is given using Newmarks linear acceleration method. The second half of the chapter presents the applied Tribology technique, it highlights how Reynolds made his derivation from the Navier-Stokes equations. The specific solution routine and its 2D discretisation is also shown. Finally, the algorithm detailing the interaction between the dynamics and Tribology for the solution of the secondary dynamics is given and explained.

The majority of IC engines in production today use a traditional crank-slider mechanism at the centre of the engine, the major (and rare) exception being the Wankel rotary engine manufactured by Mazda. There are two general configurations of the crank-slider mechanism. One is where the piston centre of rotation is aligned with the crank rotation centre. This is generally referred to as the zero offset crank. When a crank or pin offset is employed a net lateral offset may be included. This can be either positive, or in the case shown in Figure 3.1, negative.

In order to predict the conditions encountered at the piston skirt-liner interface it is important to fully describe the motion of the piston relative to the cylinder bore. A fundamental influential parameter in the mechanism of lubrication is the relative velocity of the two contiguous surfaces (contact kinematics). This velocity is crucial for the adequate entrainment of lubricant into the conjunction. One of the piston skirt's primary functions within the engine is to control the three dimensional motion of the piston assembly (defined as motion not parallel to the bore surface, often referred to as the secondary motion of the piston). This includes the lateral motion of the piston relative to the cylinder bore within the confinement of its clearance as well as any tilting motion.

To describe the motion of the piston, the slider mechanism can be simplified by a 3 degree of freedom model. The three degrees of freedom are the translational motion (in the x direction), the lateral motion (in the z direction) and the tilting motion (β) in the thrust / anti-thrust

plane. In this chapter the calculation and derivation of both primary (x direction) and secondary motion (z and β) is presented. The equations derived are relative to the un-deformed cylinder bore, which is treated as the stationary reference datum.

The combined contribution of the hydrodynamic mechanism of lubrication is integral to the calculation of the secondary piston dynamics. This is developed using the well-documented Newton-Raphson low relaxation method for the solution of Reynolds equation. The formulation of this and the contributions from varying lubricant viscosity and density are also provided.

For cases of thin film, there is a chance of asperity interactions between the contiguous surfaces. This can lead to boundary friction. An approach for the calculation of boundary friction of rough surfaces is presented by **Greenwood and Tripp** (1970) for surfaces with assumed Gaussian asperity distribution. The cross-hatch honed cylinder liner surface is not necessarily Gaussian. However, plateau formed surfaces as the result of initial running-in wear have semi-Gaussian plateau roughness. This issue is further highlighted in chapter 5 (section 5.3.2). Most of the measured film thickness in this thesis is carried out at specific location, away from dead centre reversals, owing to the difficulty of positioning the ultrasonic sensors. Furthermore, the predicted film thickness throughout the engine cycle shows that a sufficient lubricant film thickness is assured, when fully flooded inlet is assumed. Therefore, there has been no need to include the effect of boundary friction.

3.2 Primary motion – Kinematic

The primary motion of the piston is defined as its pure axial translational motion along the axis if the cylinder (*x* direction).

The method presented here has been used in similar analysis by other research workers, such as **Balakrishnan** (2002), **Offner** (2000) and **Howell-Smith** (2011). The axial piston motion is assumed to be kinematic, where the piston's position, speed and acceleration can be derived from the geometry and input crank position, speed and acceleration.

A negative offset crank (Figure 3.1) is frequently incorporated into an engine design in order to reduce overall friction, as presented by **Ragot** (2007). Offset in the opposing (positive)

direction is often introduced in order to ensure adherence between the piston skirt and the liner throughout the combustion stroke and as such reduces the chance of piston lateral motion, which can result in piston slap as discussed by **Betts** (1997). This is the impact of the piston to the surface of cylinder bore. In a race engine, such as the one used in this thesis, this phenomenon is of secondary concern. Reduced overall friction is realised due to the reduction of the side force under the combustion stroke. In the Honda CRF 450R single cylinder engine, used as the basis of research study in this thesis, there is a negative crank offset of 7.68mm. The inclusion of the offset in the calculations for position, speed and acceleration is detailed below.

Initially, a constant crank angular velocity is used. In cases where a relatively small flywheel is used the crank rotational speed can vary significantly throughout the 4-stroke engine cycle. **Rahnejat** (1998) developed a comprehensive analysis of the engine order vibrations and the result of these on the primary kinematics.

Building on this, **McFadden** (2011) developed a method to derive piston's primary motions from the changing combustion pressure, considering the dynamics of engine components in a multi-body approach. The development of such a routine is beyond the scope of this research, though much of the variation predicted in primary motion from such a technique can be captured by the accurate measurement of crank velocity and effects shown from modified kinematic calculations.

3.2.1   Piston displacement calculation

The specific direction of crank offset for the Honda CRF engine is shown in Figure 3.1. Since this engine is used throughout the simulation work and experimental measurements, the primary motions are defined for this case in mind. As it is noted later, the cases of zero or positive crank offset require a very basic alteration.
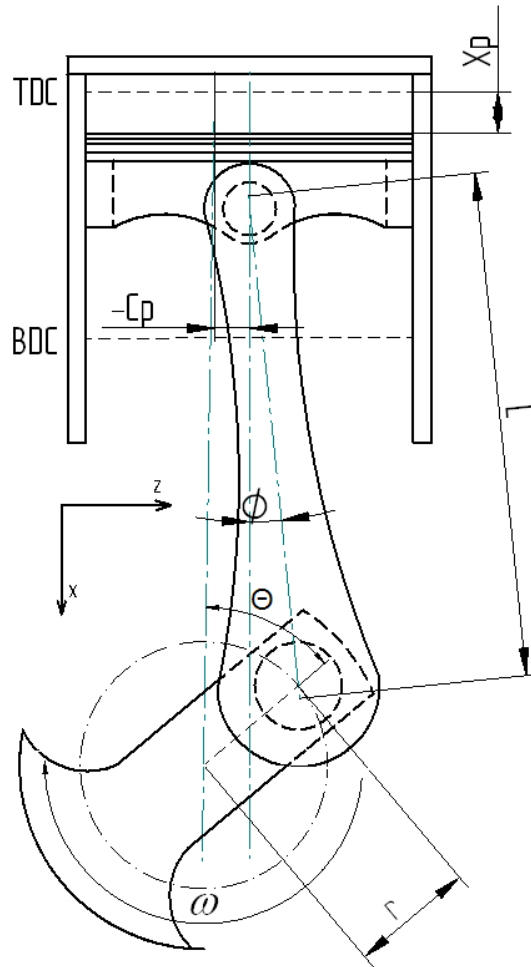
Figure 3.1 - Piston crank geometry with negative crank offset

The following dimensionless parameters are developed from the definitions embodied in Figure 3.1;

$$\Lambda = \frac{r}{l} \tag{3.1}$$

$$\Xi = \frac{C_p}{r} \tag{3.2}$$

Λ is a fixed dimensionless ratio between the crank radius and the connecting rod length, and Ξ is a fixed ratio between the crank radius and the crank offset.

Rahnejat (1998) demonstrated that engine order vibration, imbalance and the flexibility of the crankshaft contribute to engine vibration spectrum, which affects the primary piston dynamics. Considering the top dead centre (TDC) position as the origin (x=0), the piston moves from the TDC position during the crankshaft rotation reaching a maximum x displacement, commonly referred to as the bottom dead centre (BDC), before ultimately returning back to the starting point (TDC), completing a 360° crank rotation. These two positions (TDC and BDC) are referred to as the reversal points or dead centres, where there is no instantaneous speed in the axial x direction. As the result there is no relative motion of contacting solids, hence lubricant entrainment ceases momentarily. Throughout this thesis these points appear at multiples of 180° crank angle.

The angular velocity can be considered either as fixed or variable through the calculations. In either case it is calculated as.

$$\omega = d\theta / dt \tag{3.3}$$

From the case shown in Figure 3.1:

$$x_p = \sqrt{(r+l)^2 - C_p{}^2} - (r\cos\theta + l\cos\phi) \tag{3.4}$$

Substituting equations (3.1) and (3.2) into the above equation yields:

$$x_p = r\left[\sqrt{(1+1/\Lambda)^2 - \Xi^2} - (\cos\theta + \frac{1}{\Lambda}\cos\phi)\right] \tag{3.5}$$

The sign of Ξ is carried from the sign of Cp;

$$\sin\varphi = \Lambda\sin\theta + \frac{C_p}{l}\frac{r}{r} = \Lambda(\sin\theta + \Xi) \tag{3.6}$$

Transformation of equation (3.6) yields;

$$\cos \varphi = \sqrt{1 - \Lambda^2 (\sin \theta + \Xi)^2} \tag{3.7}$$

Performing a binomial power series expansion of equation (3.7) yields:

$$\cos \varphi = 1 - \frac{\Lambda^2}{2} (\sin \theta \pm \Xi)^2 - \frac{\Lambda^4}{8} (\sin \theta \pm \Xi)^4 - \frac{\Lambda^6}{16} (\sin \theta \pm \Xi)^6 - ... \tag{3.8}$$

The piston displacement can now be expressed using equation (3.9) as:

$$x_p = r \left[\begin{array}{l} A_0 + A_1 \cos \theta + A_2 \cos 2\theta + A_4 \cos 4\theta + A_6 \cos 6\theta + ... \\ +(B_1 \sin \theta + B_3 \sin 3\theta + B_5 \sin 5\theta...) \end{array} \right] \tag{3.9}$$

Where the primary cosine harmonic coefficients are:

$$A_0 = \sqrt{(1+1/\Lambda)^2} - \Xi^2 - \frac{1}{\Lambda} + \left(\frac{1}{4}\Lambda + \frac{3}{64}\Lambda^3 + \frac{5}{256}\Lambda^5 + ... \right) +$$

$$+ \frac{1}{2}(\Lambda \Xi)^2 \left(\frac{1}{\Lambda} + \frac{3}{4}\Lambda + \frac{45}{64}\Lambda^3 + ... \right) + \frac{1}{8}(\Lambda \Xi)^4 \left(\frac{1}{\Lambda} + \frac{15}{4}\Lambda + ... \right) + ...$$

$$A_1 = -1$$

$$A_2 = -\left(\frac{1}{4}\Lambda + \frac{1}{16}\Lambda^3 + \frac{15}{512}\Lambda^5 + ... \right) + \frac{3}{8}\Lambda^3 \Xi^2 \left(1 + \frac{5}{4}\Lambda^2 + ... \right) + \frac{15}{32}\Lambda^5 \Xi^4 + ... \tag{3.10}$$

$$A_4 = \left(\frac{1}{64}\Lambda^3 + \frac{3}{256}\Lambda^5 + ... \right) + \frac{15}{128}\Lambda^5 \Xi^4 + ...$$

$$A_6 = \left(\frac{1}{512}\Lambda^5 + ... \right) + ...$$

The sine coefficients, which only have value in the presence of pin offset Ξ, are given as;

$$B_1 = -\left[(\Lambda\Xi)\left(1+\frac{3}{8}\Lambda^2+\frac{15}{64}\Lambda^4+...\right)+\frac{1}{2}(\Lambda\Xi)^3\left(1+\frac{15}{8}\Lambda^2+...\right)+\frac{3}{8}(\Lambda\Xi)^3+....\right]$$

$$B_3 = \frac{1}{8}\Lambda^3\Xi\left(1+\frac{15}{16}\Lambda^2+...\right)+\frac{5}{16}\Lambda^5\Xi^3+.... \qquad (3.11)$$

$$B_5 = -\left[\frac{3}{128}\Lambda^5\Xi+......\right]$$

Typically values of Λ are less than 0.3. In this case the accuracy lost by ignoring terms above $A_2\cos 2\theta$ and $B_3\sin 3\theta$ accounts for less than 0.5% error. This simplifies equation (3.9) to:

$$x_p = r\left[A_0+A_1\cos\theta+A_2\cos 2\theta+B_1\sin\theta+B_3\sin 3\theta\right] \qquad (3.12)$$

3.2.2 Calculation of piston velocity

From equation (3.12) by differentiation the piston velocity is obtained as:

$$\dot{x}_p = v_p = \frac{dx_p}{dt} = \frac{dx_p}{d\theta}\frac{d\theta}{dt} \cong r\omega\left(A_1\sin\theta+2A_2\sin 2\theta-B_1\cos\theta-3B_3\cos 3\theta\right) \qquad (3.13)$$

The piston velocity is zero for the angle θ as multiples of π radians. These are at the piston dead centre reversals (at the TDC and BDC). The maximum velocity is found by differentiation to give the turning point (3.14) and after substitution in equation (3.13), it yields expressions for the mean piston speed as:

$$\frac{dv_p}{d\theta} = r\omega\left(\cos\theta+\Lambda\cos 2\theta\right) = r\omega\left[\cos\theta+\Lambda\left(2\cos^2\theta-1\right)\right] = 0 \qquad (3.14)$$

$$\theta_{v\max} = \cos^{-1}\left[\frac{-1+\sqrt{1+8\Lambda^2}}{4\Lambda}\right] \tag{3.15}$$

$$v_{Pm} = 2r\frac{2n}{60} = \frac{Sn}{30} \tag{3.16}$$

The maximum sliding velocity actually occurs at the piston mid-span position. The instantaneous sliding speed $\dot{x}_p$ is used to obtain the speed of entraining motion of the lubricant into the piston skirt - liner conjunction. The speed of entraining motion of the lubricant into the contact is the mean velocity of the moving surfaces. With the stationary bore/liner surface, the speed of entraining motion becomes: $\dfrac{\dot{x}_p}{2}$.

3.2.3   Calculation of piston acceleration

This is required to calculate the inertial imbalance force due to the piston's motion (discussed in section 3.3 and for the effect of inertial distortion in section 4.3.8). The primary piston acceleration can be expressed as follows:

$$\ddot{x}_p = a_p = \frac{dv_p}{dt} = \frac{dv_p}{d\theta}\frac{d\theta}{dt} = \omega\frac{dv_p}{d\theta} = r\omega^2\frac{d^2x_p}{dt^2} \tag{3.17}$$

Substituting equation (3.13) into equation (3.17) and performing differentiation yields:

$$\ddot{x}_p = -r\omega^2\left(A_1\cos\theta + 4A_2\cos 2\theta + B_1\sin\theta + 9B_3\sin 3\theta\right) \tag{3.18}$$

Again the terms above $\cos 2\theta$ (second engine order) are disregarded (as in equation (3.13)) due to their minimal influence.

3.3 Secondary motion

3.3.1   Formation of equations of motion

The secondary dynamics are dependent on the instantaneous balance of a number of forces and moments, namely the applied gas force, piston and connecting rod forces, contact forces and the resulting moments on both the thrust and anti-thrust sides. Figure 3.2 shows the free body diagram of the isolated piston with its referenced geometry, forces and moments.
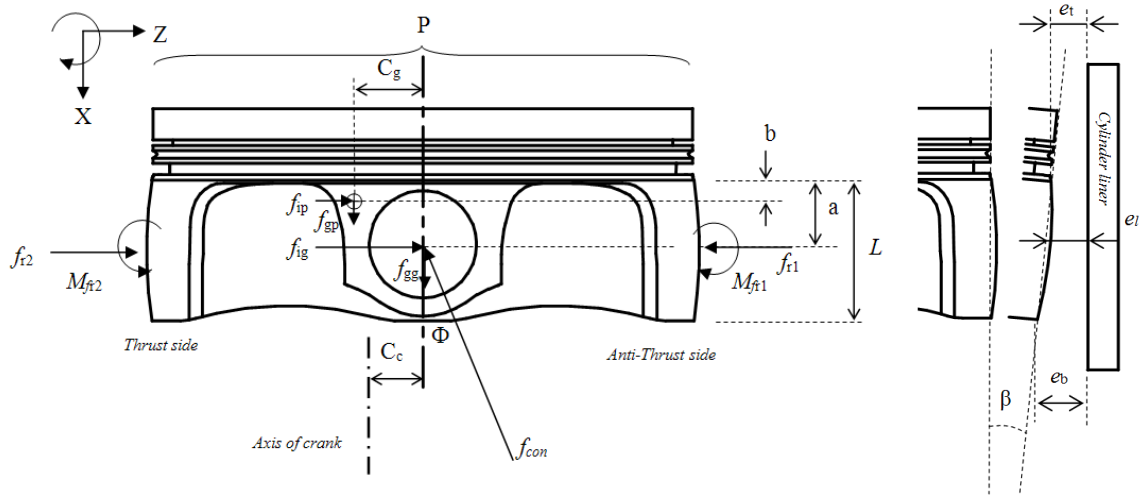
Figure 3.2 - Piston free body diagram

The force and moment equations are shown as follows, this is in line with the previous published work, including those by (**Zhu** *et al*, (1993) **Lui** *et al*, (1998), **Balakrishnan** (2005), and **Gohar** (2008)).

$$f_z = f_{ip} + f_{ig} + f_{r2} - f_{r1} - f_{con} \sin \phi \qquad (3.19)$$

$$f_x = f_{gp} + f_{gg} + f_g - f_{con} \cos \phi \qquad (3.20)$$

$$m_z = f_{ip}(a-b) + \left(f_g \times C_g \right) - \left(f_{gp} \times C_p \right) + m_c + m_{fr1} + m_{fr2} \qquad (3.21)$$

The inertial force and moment caused by the secondary motion of the piston (**Lui** *et al*, (1998)) are expressed as:

$$f_{ip} = m_p \left(\ddot{e}_t + \frac{b}{p_l}(\ddot{e}_t - \ddot{e}_b) \right)$$

(3.22)

$$f_{ig} = m_g \left(\ddot{e}_t + \frac{a}{p_l}(\ddot{e}_b - \ddot{e}_t) \right)$$

(3.23)

$$m_c = \frac{I_p}{L}(\ddot{e}_t - \ddot{e}_b)$$

(3.24)

Where using the geometric relationships, shown in Figure 3.2, the tilt of piston (β) and the lateral motion (e_l) can be substituted by the deviation of the top of the piston (e_t) and the deviation of the bottom of the piston (e_b) from its centre-line axis. These are written as:

$$e_t = e_l + a\beta$$

(3.25)

$$e_b = e_l - (L - a)\beta$$

(3.26)

Equations (3.19) and (3.20) can be used for eliminating the connecting rod force (f_{con}) and thus the contact force becomes:

$$f_z = f_{ip} + f_{ig} + f_{r2} - f_{r1} - \tan\phi \left(f_{gp} + f_{gg} + f_g \right)$$

(3.27)

The various force components in the vertical direction can be grouped together to simplify the above equation set, which yields the following expressions:

$$m_s + m_{fr1} + m_{fr2} = -m_c - f_{ip}(a-b) \tag{3.28}$$

$$f_s = f_{ip} + f_{ig} + f_{r2} - f_{r1} \tag{3.29}$$

Where:

$$m_s = (f_g \times C_g) - (f_{gp} \times C_p) \text{ and } f_s = \tan\phi(f_{gp} + f_{gg} + f_g) \tag{3.30}$$

Substituting for the inertial forces and moments into the equations of motion (3.22) and (3.23), the system dynamics can be represented in a matrix form as:

$$\begin{bmatrix} m_g\left(1-\dfrac{a}{L}\right)+m_p\left(1-\dfrac{b}{L}\right) & m_g\dfrac{a}{L}+m_p\dfrac{b}{L} \\ \dfrac{I_p}{L}+m_p(a-b)\left(1-\dfrac{b}{L}\right) & m_p(a-b)\dfrac{b}{p_l}-\dfrac{I_p}{L} \end{bmatrix}\begin{bmatrix} \ddot{e}_t \\ \ddot{e}_b \end{bmatrix} = \begin{bmatrix} f_{r1}+f_{r2}+f_s \\ m_{fr1}+m_{fr2}+m_s \end{bmatrix} \tag{3.31}$$

It is clear that a solution to this set of equations requires the evaluation of contact forces and moments: f_{r1}, f_{r2}, m_{fr1} and m_{fr2} .The calculation of these contact forces and moments are explained in section 3.5.

3.3.2   Solution of secondary dynamics

A step by step integrator is required to solve these two equations, for which the linear acceleration method, as developed by **Newmark** (1959) and adopted originally for system dynamics by **Timoshenko** (1970), is employed. It has been more recently modified to deal with contact dynamics problems by **Rahnejat** (1984).

For each equation of motion, representing a degree of freedom, 10 to 12 further equations need to be written forming a predictive-corrective iterative loop. Below a representation of the methodology is explained, constituting two blocks which will be later referred to as LAM

I and LAM II in the forthcoming flowcharts. Initial conditions must be defined before starting the iterative procedure. Due to the nature of the integrator, velocities and displacements can be set to zero initially. Following the laws of physics, where acceleration always precedes velocity, then displacement, an initial acceleration value satisfies the input requirement with these initial conditions.

There are two subscripts used (p and q) denoting integration step and iteration step respectively. p is responsible for accounting for real integration time, whereas q is the computational effort carried through the procedure. Since the algorithm requires values for initial velocities based on two previous time steps ($p-2$) in the predictor block, a set of special cases must be defined for the start of the algorithm to satisfy the initial conditions.

Predictive equations (LAM I):

If $i = 1$

Then:
$$\dot{e}_{t(p,q)} = \dot{e}_{t\_initial} + \ddot{e}_{t\_initial} \Delta t \tag{3.32}$$

$$e_{t(p,q)} = e_{t\_initial} + \left(\dot{e}_{t\_initial} + \dot{e}_t(p,q) \right) \frac{\Delta t}{2} \tag{3.33}$$

If $i = 2$

Then:
$$\dot{e}_{t(p,q)} = \dot{e}_{t\_initial} + 2 C_n \ddot{e}_{t(p-1)} \Delta t \tag{3.34}$$

$$e_{t(p,q)} = C_n e_{t(p-1)} + \left(C_n \dot{e}_{t(p-1)} + \dot{e}_t(p,q) \right) \frac{\Delta t}{2} \tag{3.35}$$

If $i > 2$

Then:
$$\dot{e}_{t(p,q)} = C_n \dot{e}_{t(p-2)} + 2C_n \ddot{e}_{t(p-1)} \Delta t \tag{3.36}$$

$$e_{t(p,q)} = C_n e_{t(p-1)} + C_n \dot{e}_{t(p-1)} \Delta t + C_n \ddot{e}_{t(p-1)} \frac{\Delta t^2}{2} \tag{3.37}$$

Corrective equations (LAM II):

If $i = 1$

Then:
$$\dot{e}_{t(p,q)} = \dot{e}_{t\_initial} + \left(\ddot{e}_{t\_initial} + \ddot{e}_{t(p,q-1)} \right) \frac{\Delta t}{2} \tag{3.38}$$

$$e_{t(p,q)} = e_{t\_initial} + \left(2\dot{e}_{t\_initial} + \dot{e}_{t(p,q)} \right) \frac{\Delta t}{3} + \ddot{e}_{t\_initial} \frac{\Delta t^2}{6} \tag{3.39}$$

If $i \geq 2$

Then:
$$\dot{e}_{t(p,q)} = C_n \dot{e}_{t(p-1)} + \left(C_n \ddot{e}_{t(p-1)} + \ddot{e}_{t(p,q-1)} \right) \frac{\Delta t}{2} \tag{3.40}$$

$$e_{t(p,q)} = C_n e_{t(p-1)} + \left(2C_n \dot{e}_{t(p-1)} + \dot{e}_{t(p,q)} \right) \frac{\Delta t}{3} + C_n \ddot{e}_{t(p-1)} \frac{\Delta t^2}{6} \tag{3.41}$$

This method assumes a linear variation of acceleration within a suitably small time step (Δt), hence its name. This is achieved by introducing certain values for the γ and β' parameters in the Newmark's original method. γ is responsible for indicating how much of the previous step acceleration is carried over for the calculation of the current velocity and displacement relationships at the end of the interval (**Newmark**, 1959), hence adding or reducing numerical damping into the system. β' controls the stability and speed with which the integrator converges and it is responsible for the type of variation of acceleration within a time step.

It has been observed that for $\beta' = \frac{1}{6}$, the acceleration varies linearly and if $\gamma = \frac{1}{2}$, there is no spurious damping, these being the normal parameters for the Linear Acceleration method. When β is modified to $\beta' = \frac{1}{4}$ the acceleration used is an average of any two consecutive time steps, a special case called the Average Acceleration Method is created. Newmark's original equations are as follows:

$$\dot{e}_{t(p)} = \dot{e}_{t(p-1)} + \left(1 - \gamma\right)\ddot{e}_{t(p-1)}\Delta t + \gamma\ddot{e}_{t(p)}\Delta t \tag{3.42}$$

$$e_{t(p)} = e_{t(p-1)} + \dot{e}_{t(p-1)}\Delta t + \left(\frac{1}{2} - \beta\right)\ddot{e}_{t(p-1)}\Delta t^2 + \beta'\ddot{e}_{t(p)}\Delta t^2 \tag{3.43}$$

It is critical that the time step size, (Δt), is controlled to a suitably small value. Having a step size that is too large for the representation of a specific phenomenon would lead to inaccuracies, lack of information or numerical instability (divergence). A significantly low value will slow down the process quite dramatically and will result in the production of unnecessary data. A Δt in the order of a few micro-seconds is typical of contact dynamic problems (**Rahnejat**, 1984).

The convergence criteria (ζ) are usually considered in terms of the acceleration, as the most rapidly changing variable out of the three quantities (e_t, $\dot{e}_t$ and $\ddot{e}_t$). Hence, convergence is deemed to be achieved if: (**Balakrishnan** (2002) and **De la Cruz** *et al* (2012))

$$\left|\frac{\ddot{e}_{t(p,q)} - \ddot{e}_{t(p,q-1)}}{\ddot{e}_{t(p,q)}}\right| \times 100 < 0.01 \tag{3.44}$$

If this criterion is not satisfied, the iteration parameter is increased by one ($q = q+1$) and the procedure is repeated. If not, all of the required values are saved and the integration step is increased ($p = p+1$).

Once the adequately converged values of $\ddot{e}_t$ and $\ddot{e}_b$ have been calculated for the given time step, the transient solution can move on a time step increment and continue until cyclic stability is maintained (dynamic instability is not present).

3.4 Lubricant Rheology

3.4.1 Density

Generally, density is a measure of mass per unit volume, with the S.I. unit kg/m^3. Specific gravity is measure as the ratio of mass of a given volume of lubricant at temperature, *t1*, with that of distilled water at temperature, *t2*. For petroleum products, the specific gravity used, is usually quoted for temperature of 15.6ºC.

3.4.1.1 Pressure dependence of Density

At low to moderate lubricant pressures the change in density resulting from pressure is relatively insignificant. In conjunctions where high pressures are encountered such as in concentrated counterformal contacts, for example that cam-tappet conjunction, where pressures are of the order of GPa the density change can be significant and needs to be taken into account.

Experimental results obtained by **Dowson *et al*** (1962) have shown that the relative change of the lubricant density due to pressure varies linearly, but not greatly in magnitude. The maximum increase in the density of lubricants due to very high pressures is found to be only 33% greater than that under atmospheric condition. This characteristic can be safely assumed for almost all lubricants. This relationship was found by **Dowson and Higginson** (1959) to be:

$$\bar{\rho} = \frac{\rho}{\rho_o} = 1 + \frac{0.6p}{1+1.7p} \tag{3.45}$$

3.4.1.2 Temperature dependence of Density

In conjunctions where external heating or ambient conditions dominate the control of temperature, the thermal expansion of the lubricant dominates the change in its density. In the case of the piston skirt, the viscous heating due to shear of the lubricant has a much less significant effect on its density. For lubricants in a conjunction with known temperature boundary conditions, equation (3.46) can be used to calculate the initial operational density.

$$\rho = \rho_o e^{\xi(T-T_0)} \tag{3.46}$$

Where ξ is the exponent of density-temperature dependence, this is typically 0.001 K^{-1} for automotive lubricants, **Stachowiak,** (2001).

3.4.2   Viscosity

Viscosity can be described as the internal resistance to flow within a fluid. Due to the hydrophilic nature of lubricant fluids, they cling to adjacent surfaces. Extending this idea to fluids flowing in a channel between a stationary and a moving plate, the bottom-most fluid layer, closest to the stationary plate remains stationary, whilst the upper-most layer, closest to the moving surface, moves along with it at velocity U_A. This is the basis of Newton's viscous flow model.
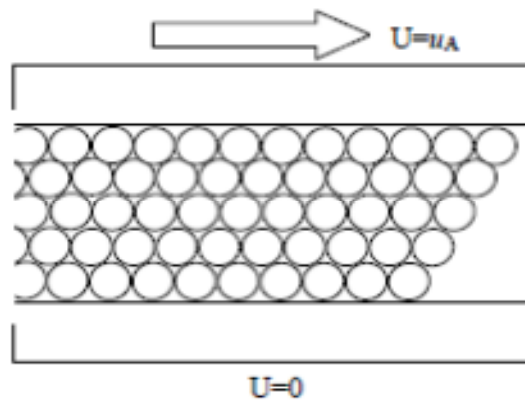
Figure 3.3 - Laminar flow in Newtonian fluids

This is illustrated in Figure 3.3. Therefore, the relationship between the velocity gradient between the layers of fluid and their displacement is known as shear rate, ψ. The velocity gradient is proportional to the shear stress, τ. In turn, dynamic viscosity, η, can be described as (a definition set by Newton in 1674):

$$\eta = \frac{\tau}{\psi}$$
(3.47)

Fluids or lubricants that exhibit the above relationship are known as Newtonian fluids. This model was proposed by **Newton** (1674) and is known as *Newtonian slow viscous action* model, in which the molecules of the fluid are considered as hard spherical and un-deformable and the flow to be slow in motion. Fluids, deviating from such behaviour, are referred to as non-Newtonian fluids. Another measure of viscosity, known as kinematic viscosity, η_k, i.e. flow in a capillary tube, is influenced by the weight of the fluid and it can be defined in terms of its density and dynamic viscosity as:

$$\eta_k = \frac{\eta}{\rho}$$
(3.48)

3.4.2.1 Temperature Influence on Viscosity

The temperature of the lubricant within a conjunction has a significant effect on the operation of lubricated components. The standard method to measure the temperature influence on viscosity is by using a capillary tube viscometer under controlled temperature conditions. By curve-fitting experimental data, the viscosity dependency on temperature is expressed (**Crouch and Cameron** (1961)) as:

$$\eta = \eta_0 e^{-\vartheta \Delta t}$$
(3.49)

The relationship between temperature and viscosity is exponential; as such the precise and accurate implementation of boundary temperature conditions is critical in calculating the true lubricant viscosity at the entry to the contact.

3.4.2.2 Pressure Influence on Viscosity

The effect of pressure on lubricant is of utmost importance where higher magnitudes of pressure are encountered, in a similar manner as the pressure effect on density. The original pressure-viscosity dependence proposed by **Barus** (1893) is:

$$\ln \frac{\eta}{\eta_o} = \xi p \tag{3.50}$$

The above equation is valid as an approximation and it is inaccurate when the pressures involved are very high (in the order of GPa) (its error becomes unacceptable). By curve-fitting experimental data, **Roelands** (1966) created the following expression to describe viscosity in terms of the pressure of lubricants under isothermal conditions:

$$\ln \eta + 1.2 = (\ln \eta_0 + 1.2)\left(1 + \frac{p}{2000}\right)^{Z_1} \tag{3.51}$$

Rearranging equation (3.51), the dynamic viscosity in terms of pressure can be written as:

$$\overline{\eta} = \frac{\eta}{\eta_0} = \exp^{(\ln \eta_0 + 9.67)(-1 + (1 + 5.1x10^{-9}p))} \tag{3.52}$$

It must be noted that in Roelands equation (3.52), the corrected lubricant viscosity is defined using three different parameters (the atmospheric viscosity (η_0), the asymptotic iso-viscous pressure (ξ) and the pressure-viscosity index (Z_1)), while in the Barus's case only the pressure-viscosity coefficient (α) is used. In effect, if the Barus's expression was employed, the exponential pressure-viscosity dependence in his equation, (3.50), can be approximated to a non-exponential dependence by the substitution of the inverse of the asymptotic iso-viscous pressure as:

$$\alpha = \frac{1}{\xi} \tag{3.53}$$

The values of the individual parameters for a given lubricant in the Roelands equation can be obtained by consulting the tables that define the lubricant properties. Pressure viscosity coefficient of lubricant can now be expressed in terms of Z_1 (**Blok** (1965)) as:

$$\xi' = Z_1(5.1x10^{-9}(\ln\eta_0 + 9.67)) \tag{3.54}$$

3.5 Elastohydrodynamic Lubrication

3.5.1   Introduction

Reynolds (1886) derived his equation based on the Navier-Stokes equation and continuity of flow condition. The assumptions and theory behind the Navier stokes equations are well understood and published throughout the last century. The specific derivation of the Reynolds' equation for use in piston skirt lubrication, based on certain assumptions, is explained in this section.

3.5.2   Reynolds Equation

In order to obtain the hydrodynamic flow equation in a narrow convergent gap, the following assumptions were made by **Reynolds** (1886):

i. The viscosity and density of the fluid are considered to be constant. This assumption holds for iso-viscous conditions, where the hydrodynamic pressures are relatively low, so that the effect of pressure on the bulk physical properties of the fluid (such as its density and viscosity) can be ignored. This enables the above equations to be simplified to:

$$\rho\Delta u = F_x - \frac{\partial p}{\partial x} + (\eta + \xi)\frac{\partial}{\partial x}\left(\frac{\partial u}{\partial x} + \frac{\partial v}{\partial y} + \frac{\partial w}{\partial z}\right) + \eta\left(\frac{\partial^2 u}{\partial x^2} + \frac{\partial^2 u}{\partial y^2} + \frac{\partial^2 u}{\partial z^2}\right) \tag{3.55}$$

$$\rho \Delta v = F_y - \frac{\partial p}{\partial y} + (\eta + \xi) \frac{\partial}{\partial y}\left(\frac{\partial u}{\partial x} + \frac{\partial v}{\partial y} + \frac{\partial w}{\partial z}\right) + \eta\left(\frac{\partial^2 v}{\partial x^2} + \frac{\partial^2 v}{\partial y^2} + \frac{\partial^2 v}{\partial z^2}\right) \qquad (3.56)$$

$$\rho \Delta w = F_z - \frac{\partial p}{\partial z} + (\eta + \xi) \frac{\partial}{\partial z}\left(\frac{\partial u}{\partial x} + \frac{\partial v}{\partial y} + \frac{\partial w}{\partial z}\right) + \eta\left(\frac{\partial^2 w}{\partial x^2} + \frac{\partial^2 w}{\partial y^2} + \frac{\partial^2 w}{\partial z^2}\right) \qquad (3.57)$$

ii. For incompressible fluids such as mineral oils the dilation term is ignored, thus:

$$\left(\frac{\partial u}{\partial x} + \frac{\partial v}{\partial y} + \frac{\partial w}{\partial z}\right) = 0 \qquad (3.58)$$

iii. Due to the small size of the element of fluid, its inertial properties are negligible, when compared to the contributions made by the shear deformation terms in the Navier-Stokes equations. Therefore:

$$\nabla u = \nabla v = \nabla w = 0 \qquad (3.59)$$

iv. The effect of body forces (such as the gravitational effect) on a fluid element is considered to be negligible. Thus:

$$F_x = F_y = F_z = 0 \qquad (3.60)$$

When the above assumptions are applied to the Navier-Stokes equations, the following special forms of the equations are obtained:

$$\frac{\partial p}{\partial x} = \eta\left(\frac{\partial^2 u}{\partial x^2} + \frac{\partial^2 u}{\partial y^2} + \frac{\partial^2 u}{\partial z^2}\right) \qquad (3.61)$$

$$\frac{\partial p}{\partial y} = \eta\left(\frac{\partial^2 v}{\partial x^2} + \frac{\partial^2 v}{\partial y^2} + \frac{\partial^2 v}{\partial z^2}\right) \qquad (3.62)$$

$$\frac{\partial p}{\partial z} = \eta \left(\frac{\partial^2 w}{\partial x^2} + \frac{\partial^2 w}{\partial y^2} + \frac{\partial^2 w}{\partial z^2} \right) \qquad (3.63)$$

v. The pressure gradient across the fluid film in the z-direction is neglected, because the lubricant film is very thin, therefore: $\frac{\partial p}{\partial z} = 0$

vi. An order of magnitude analysis can be carried out to show that the variation of velocities u and v with respect to z are large compared to all other velocity gradients. This is because of the geometry of the contact domain. Hence:

$$\frac{\partial^2 u}{\partial x^2} + \frac{\partial^2 u}{\partial y^2} = 0; \quad \frac{\partial^2 v}{\partial x^2} + \frac{\partial^2 v}{\partial y^2} = 0; \quad \frac{\partial^2 w}{\partial x^2} + \frac{\partial^2 w}{\partial y^2} + \frac{\partial^2 w}{\partial z^2} = 0 \qquad (3.64)$$

vii. The fluid film entraining velocities need not to change in the direction of entraining motion. This means that the flow is laminar (i.e. streamlined).

viii. It is assumed that no slip occurs between the solid surfaces in pure entraining motion. This means that at the boundaries between the lubricant film and the solids:

$$z = 0; \ u = u_A; \ v = v_A = 0; \ z = h; \ u = u_B; \ v = v_B = 0 \qquad (3.65)$$

where, z in the above equation represents the vertical distance (i.e. the gap measured) from a fixed datum, and u and v are the surface velocities of the solids in the x and y directions, respectively. When the above assumptions are applied to equations (3.61) to (3.63), the resulting equations are as follows:

$$\frac{\partial p}{\partial x} = \eta \frac{\partial^2 u}{\partial x^2} \qquad (3.66)$$

$$\frac{\partial p}{\partial y} = \eta \frac{\partial^2 v}{\partial z^2}$$

(3.67)

The above two equations can be integrated twice with respect to z to solve for the velocity distributions in the x and y directions, whilst employing the boundary conditions as outlined in assumption *(viii)*. Once the velocity distributions are obtained, they can be coupled with the continuity of flow equation to derive the Reynolds' equation in two dimensions as stated in (3.68).

$$\frac{\partial}{\partial x}\left(\frac{\rho h^3}{\eta}\frac{\partial p}{\partial x}\right) + \frac{\partial}{\partial y}\left(\frac{\rho h^3}{\eta}\frac{\partial p}{\partial y}\right) = 12 u_{av}\left(\frac{\partial}{\partial x}(\rho h) + v_{av}\frac{\partial}{\partial y}(\rho h) + \frac{d}{dt}(\rho h)\right)$$

(3.68)

The left-hand side terms are known as Poiseuille terms, which describe flow rate due to pressure gradients within the lubricated area. The two terms on the right-hand side are known as the Couette terms, describing the film action in a convergent gap. These terms are functions of the average velocities in entraining motion, including side-leakage. These average velocities are given as:

$$u_{AV} = \frac{u_A + u_B}{2}; \ v_{AV} = \frac{v_A + v_B}{2};$$

(3.69)

Since the lubricant entraining direction, in the case of piston sliding in the bore, is in the translation direction only, the entraining velocity in y direction can be ignored.

3.5.3 Non dimensional, finite difference approach

For the actual implementation of Reynolds equation into a numerical solution, a finite difference representation is developed. To do this, the two-dimensional conjunction is represented by a number of discreet nodes, each with a given i and j position for their x and y values, respectively. This relationship is shown in Figure 3.4, a sample position of the computational grid.
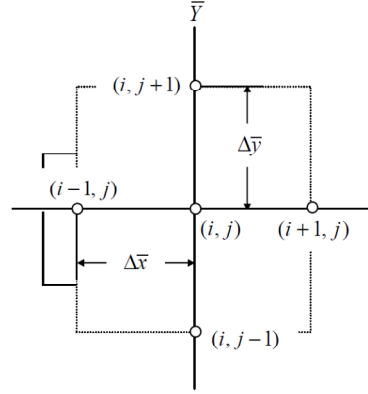
Figure 3.4 - Sample section of Reynolds computational grid with boundary nodal references

The value of function at a given point is calculated using the central difference approximation, the general form of this is given in equation 3.58. In the case of the problem presented here f(x) is Reynolds equation.

$$f'(x_0) = \frac{f(x_0 + \Delta) - f(x_0 - \Delta)}{2\Delta} \qquad (3.70)$$

The terms in equation (3.68) very significantly in terms of magnitude, pressures can be of the order of MPa, whereas lubricant films can be of the order of µm. Repetitive calculations using such large and small numbers can lead to numerical inaccuracies and in some cases instability. To overcome this, the computational variables used are non-dimensionalised using appropriate, fixed, dimensional scalars shown overleaf;

$$
\begin{cases}
X = x/b \\
Y = y/a \\
\bar{\rho} = \rho/\rho_0 \\
\bar{\eta} = \eta/\eta_0 \\
H = hR_x/b^2 = \dfrac{mm}{m^2} = [-] \\
P = p/P_h = [-] \\
\bar{t} = u_{av}t/R_x = \dfrac{\frac{m}{s}s}{m} = [-] \\
W^* = W/(E'R_x L) = \dfrac{N}{\frac{N}{m^2}m^2} = [-] \\
G^* = \alpha E'
\end{cases}
\rightarrow
\begin{cases}
x = bX \\
y = aY \\
\rho = \rho_0\bar{\rho} \\
\eta = \eta_0\bar{\eta} \\
h = Hb^2/R_x \\
p = P_h P \\
t = R_x \bar{t}/u_{av} \\
W = W^* E' R_x L \\
G^* = \alpha E'
\end{cases}
\rightarrow
\begin{cases}
dx = bdX \\
dy = adY \\
d\rho = \rho_0 d\bar{\rho} \\
d\eta = \eta_0 d\bar{\eta} \\
dh = (b^2/R_x)dH \\
dp = P_h dP \\
dt = (R_x/u_{av})d\bar{t}
\end{cases}
$$

Using these non dimensional parameters and substituting into Reynolds equation, (3.68), yields the non-dimensional form for the 2D piston skirt conjunction.

$$
\underbrace{\frac{\partial}{\partial X}\left(\frac{\bar{\rho}H^3}{\bar{\eta}}\frac{\partial P}{\partial X}\right)_{i,j}}_{A} + k^2 \underbrace{\frac{\partial}{\partial Y}\left(\frac{\bar{\rho}H^3}{\bar{\eta}}\frac{\partial P}{\partial Y}\right)_{i,j}}_{B} = \psi\left\{\underbrace{\left(\frac{\partial(\bar{\rho}HU)}{\partial X}\right)_{i,j}}_{C} + k\underbrace{\left(\frac{\partial(\bar{\rho}HV)}{\partial Y}\right)_{i,j}}_{D} + \frac{R_x}{b}\bar{\rho}S^*\right\}
$$

$$(3.71)$$

Where: $\psi = 12\dfrac{u_{av}\eta_0 R_x^2}{P_h b^3}$; $\quad S^* = \dfrac{\partial h/\partial t}{u_{av}}$ and $k = \dfrac{b}{a}$

Considering each of the terms from A – D, using the central difference method yields;

$$\frac{\partial}{\partial X}\left(\frac{\overline{\rho}H^3}{\overline{\eta}}\frac{\partial P}{\partial X}\right)_{i,j} =$$

$$= \frac{1}{\Delta X}\left[\left(\frac{\overline{\rho}H^3}{\overline{\eta}}\frac{\partial P}{\partial X}\right)_{i+\frac{1}{2},j} - \left(\frac{\overline{\rho}H^3}{\overline{\eta}}\frac{\partial P}{\partial X}\right)_{i-\frac{1}{2},j}\right] = \left(\frac{\overline{\rho}H^3}{\overline{\eta}}\right)_{i+\frac{1}{2},j}\frac{P_{i+1,j}-P_{i,j}}{\Delta X^2} - \left(\frac{\overline{\rho}H^3}{\overline{\eta}}\right)_{i-\frac{1}{2},j}\frac{P_{i,j}-P_{i-1,j}}{\Delta X^2} =$$

$$= \frac{1}{2\Delta X^2}\left[\left(\frac{\overline{\rho}H^3}{\overline{\eta}}\right)_{i+1,j} + \left(\frac{\overline{\rho}H^3}{\overline{\eta}}\right)_{i,j}\right]\left(P_{i+1,j}-P_{i,j}\right) - \frac{1}{2\Delta X^2}\left[\left(\frac{\overline{\rho}H^3}{\overline{\eta}}\right)_{i,j} + \left(\frac{\overline{\rho}H^3}{\overline{\eta}}\right)_{i-1,j}\right]\left(P_{i,j}-P_{i-1,j}\right) =$$

$$\rightarrow \boxed{A} = \frac{1}{2\Delta X^2}\left[\left(\frac{\overline{\rho}H^3}{\overline{\eta}}\right)_{i,j} + \left(\frac{\overline{\rho}H^3}{\overline{\eta}}\right)_{i-1,j}\right]P_{i-1,j} - \frac{1}{2\Delta X^2}\left[\left(\frac{\overline{\rho}H^3}{\overline{\eta}}\right)_{i+1,j} + 2\left(\frac{\overline{\rho}H^3}{\overline{\eta}}\right)_{i,j} + \left(\frac{\overline{\rho}H^3}{\overline{\eta}}\right)_{i-1,j}\right]P_{i,j} +$$

$$\frac{1}{2\Delta X^2}\left[\left(\frac{\overline{\rho}H^3}{\overline{\eta}}\right)_{i+1,j} + \left(\frac{\overline{\rho}H^3}{\overline{\eta}}\right)_{i,j}\right]P_{i+1,j}$$

$$(3.72)$$

$$\frac{\partial}{\partial Y}\left(\frac{\overline{\rho}H^3}{\overline{\eta}}\frac{\partial P}{\partial Y}\right)_{i,j} =$$

$$= \frac{1}{\Delta Y}\left[\left(\frac{\overline{\rho}H^3}{\overline{\eta}}\frac{\partial P}{\partial Y}\right)_{i,j+\frac{1}{2}} - \left(\frac{\overline{\rho}H^3}{\overline{\eta}}\frac{\partial P}{\partial Y}\right)_{i,j-\frac{1}{2}}\right] =$$

$$= \frac{1}{2\Delta Y^2}\left[\left(\frac{\overline{\rho}H^3}{\overline{\eta}}\right)_{i,j+1} + \left(\frac{\overline{\rho}H^3}{\overline{\eta}}\right)_{i,j}\right]\left(P_{i,j+1}-P_{i,j}\right) - \frac{1}{2\Delta Y^2}\left[\left(\frac{\overline{\rho}H^3}{\overline{\eta}}\right)_{i,j} + \left(\frac{\overline{\rho}H^3}{\overline{\eta}}\right)_{i,j-1}\right]\left(P_{i,j}-P_{i,j-1}\right) =$$

$$\rightarrow \boxed{B} = \frac{1}{2\Delta Y^2}\left[\left(\frac{\overline{\rho}H^3}{\overline{\eta}}\right)_{i,j} + \left(\frac{\overline{\rho}H^3}{\overline{\eta}}\right)_{i,j-1}\right]P_{i,j-1} - \frac{1}{2\Delta Y^2}\left[\left(\frac{\overline{\rho}H^3}{\overline{\eta}}\right)_{i,j+1} + 2\left(\frac{\overline{\rho}H^3}{\overline{\eta}}\right)_{i,j} + \left(\frac{\overline{\rho}H^3}{\overline{\eta}}\right)_{i,j-1}\right]P_{i,j} +$$

$$\frac{1}{2\Delta Y^2}\left[\left(\frac{\overline{\rho}H^3}{\overline{\eta}}\right)_{i,j+1} + \left(\frac{\overline{\rho}H^3}{\overline{\eta}}\right)_{i,j}\right]P_{i,j+1}$$

$$(3.73)$$

$$\boxed{C} = \left(\frac{\partial(\overline{\rho}HU)}{\partial X}\right)_{i,j} = (1-\beta_x)\frac{(\overline{\rho}HU)_{i+1,j}-(\overline{\rho}HU)_{i,j}}{\Delta X} + \beta_x\frac{(\overline{\rho}HU)_{i,j}-(\overline{\rho}HU)_{i-1,j}}{\Delta X}$$

$$(3.74)$$

$$\boxed{D} = \left(\frac{\partial(\overline{\rho}HV)}{\partial Y}\right)_{i,j} = (1-\beta_y)\frac{(\overline{\rho}HV)_{i,j+1}-(\overline{\rho}HV)_{i,j}}{\Delta Y} + \beta_y\frac{(\overline{\rho}HV)_{i,j}-(\overline{\rho}HV)_{i,j-1}}{\Delta Y} \quad (3.75)$$

The residual function can be expressed using these terms as;

$$
\begin{aligned}
F_{i,j} = \frac{1}{2\Delta X^2} & \left\{ \begin{array}{l} \left[\left(\dfrac{\bar{\rho}H^3}{\bar{\eta}}\right)_{i,j} + \left(\dfrac{\bar{\rho}H^3}{\bar{\eta}}\right)_{i-1,j} \right] P_{i-1,j} - \left[\left(\dfrac{\bar{\rho}H^3}{\bar{\eta}}\right)_{i+1,j} + 2\left(\dfrac{\bar{\rho}H^3}{\bar{\eta}}\right)_{i,j} + \left(\dfrac{\bar{\rho}H^3}{\bar{\eta}}\right)_{i-1,j} \right] P_{i,j} \\[2ex] + \left[\left(\dfrac{\bar{\rho}H^3}{\bar{\eta}}\right)_{i+1,j} + \left(\dfrac{\bar{\rho}H^3}{\bar{\eta}}\right)_{i,j} \right] P_{i+1,j} \end{array} \right\} + \\[3ex]
+ \frac{k^2}{2\Delta Y^2} & \left\{ \begin{array}{l} \left[\left(\dfrac{\bar{\rho}H^3}{\bar{\eta}}\right)_{i,j} + \left(\dfrac{\bar{\rho}H^3}{\bar{\eta}}\right)_{i,j-1} \right] P_{i,j-1} - \left[\left(\dfrac{\bar{\rho}H^3}{\bar{\eta}}\right)_{i,j+1} + 2\left(\dfrac{\bar{\rho}H^3}{\bar{\eta}}\right)_{i,j} + \left(\dfrac{\bar{\rho}H^3}{\bar{\eta}}\right)_{i,j-1} \right] P_{i,j} \\[2ex] + \left[\left(\dfrac{\bar{\rho}H^3}{\bar{\eta}}\right)_{i,j+1} + \left(\dfrac{\bar{\rho}H^3}{\bar{\eta}}\right)_{i,j} \right] P_{i,j+1} \end{array} \right\} - \\[3ex]
- \psi \frac{1}{\Delta X} & \left\{ (1-\beta_x)\left[(\bar{\rho}HU)_{i+1,j} - (\bar{\rho}HU)_{i,j} \right] + \beta_x \left[(\bar{\rho}HU)_{i,j} - (\bar{\rho}HU)_{i-1,j} \right] \right\} - \\[2ex]
- k\psi \frac{1}{\Delta Y} & \left\{ (1-\beta_y)\left[(\bar{\rho}HV^*)_{i,j+1} - (\bar{\rho}HV^*)_{i,j} \right] + \beta_y \left[(\bar{\rho}HV^*)_{i,j} - (\bar{\rho}HV^*)_{i,j-1} \right] \right\} - \psi \frac{R_x}{b}(\bar{\rho}S^*)_{i,j}
\end{aligned}
\tag{3.76}
$$

3.5.4 Solution of Reynolds equation with a modified low relaxation Newton-Raphson method.

The Newton Raphson method is an approach used for finding the approximate solution to non-linear differential equations. This is ideal for the solution of the highly non-linear, second order partial differential Reynolds equation. It uses a truncated Taylor series expansion limited to the first order terms for a given equation in the following form;

$$
f(X_{n+1}) = f(X_n) + f'(X_n)(X_{n+1} - X_n) + \varepsilon_r
\tag{3.77}
$$

For a multi variable function, $f(x,y)$, the above Taylor series can be expanded into a series of terms forming a truncated Taylor series expansion.

$$
f(x_{n+1}, y_{n+1}) = f(x_n, y_n) + (x_{n+1} - x_n) \cdot \frac{\partial [f(x_n, y_n)]}{\partial x_n} + (y_{n+1} - y_n) \cdot \frac{\partial [f(x_n, y_n)]}{\partial y_n} + \varepsilon_r
\tag{3.78}
$$

The first order differentials can be replaced by a jacobian matrix $[J]$. These contain the set of derivatives of the Reynolds equation with respect to all the dependant variables. This is generally expressed as:

$$[J_n] = \frac{\partial f(x_n, y_n)}{\partial (x_n, y_n)}$$

(3.79)

In Reynolds equation the only term that is a multi variable function is pressure, P. Its evaluation is dependent on the four pressures surrounding it, as shown in Figure 3.4. The neighbouring nodes at $(i-1, j-1), (i-1, j+1), (i+1, j-1)$ and $(i+1, j+1)$ have been shown to have a relatively insignificant effect on pressure convergence, particularly when the extra computational burden is factored, (**Balakrishnan** (2002)).

Using only the 4 neighbouring nodes, a Gauss-Seidel iteration is used. Direct methods for inverting the jacobian matrix generally consume significant memory resources and have been proven to be lengthy and inefficient, whereas a number of authors have reported high efficiency and effectiveness for the solution of a non linear system of equations **Balakrishnan** (2002), **Jalali-Vahid** (2000).

3.6 Summary

Overall the calculation of the piston's dynamics is a *relatively* simple and well developed theory. For use with a single cylinder engine, *instantaneous* crank speed and cylinder pressure input data for a complete cycle are required as measured from the experimental setup (detailed in chapter 5). The effect of the changing piston position on the clearance values of the opposing skirt sides is discussed in chapter 5. The resulting load carried by viscous action is quantified separately and fed back into the controlling dynamics routines at the centre of the eventual routine. The outline of the transient routine is shown in Figure 3.5. Further details on the separate Reynolds and deflection exchange is shown in chapter 4. In addition to the solution routine at the centre of the methodology there are a number of pre-processing and data manipulation steps required as inputs to this model. The data flow between each of the different platforms and calculation algorithms toward the central solution algorithm is detailed in appendix B.
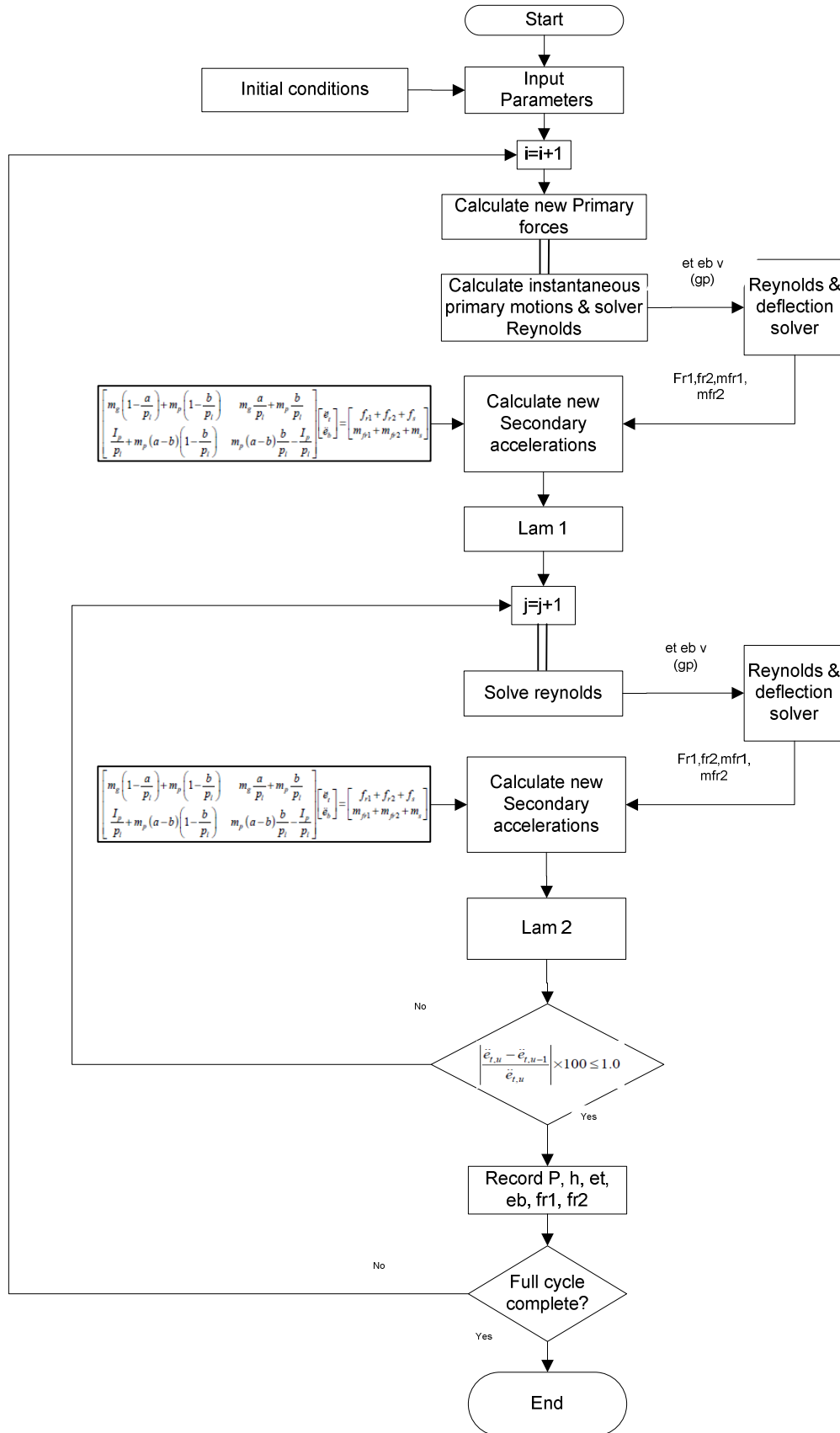
Figure 3.5 - Transient flow chart

Chapter 4.
Conjunction Geometry and flexibility

4.1 Overview and Introduction

In order to compute the solution of the piston's secondary motion, as discussed in Chapter 3, both moments and forces originating from the interactions between the liner and skirt must be calculated. This requires the consideration of both the thrust and anti – thrust side piston skirt actions. This chapter shows in detail how the conjunction geometry is formed with the various component inputs. The intricate manipulation of the stiffness matrices for direct, efficient, solution with the dynamics within Fortran is shown. Finally the formation of the film shapes for both the quasi-static and transient solution methodologies is given.

In basic terms, these two contacts are considered as *partially conforming*. This means that the contacting dimensions are not negligible compared to the principal radii of contact of the contiguous solids, as is the case for ball and rolling element bearings or a cam - follower pair. The contacting radii of solids are not close enough to cause a fully conforming contact, which is the case in a journal bearing; therefore partial conformance is due to the fact that one of the bodies has a concave radius in its radial plane.

The principal radii of the contacting bodies in the x-y plane are quite large. It is normal to assume an infinite radius for the bore and a parabolic profile for the piston skirt, in the first instance. These two assumptions are an excellent starting position for a basic analysis but they do not accurately take into account the changing operational shape and contributions of the separate deflection shapes.

This chapter details the initial shape of the piston skirt and liner. The role of deflection in the solution of the contact conjunction is detailed with it separate contributory components. The effects of normal contact load, in-cylinder pressure, thermal distortion and inertia on the piston shape are included in the calculation of the instantaneous conjunction shape.

4.2 Contact geometry and influencing parameters

4.2.1   Piston skirt

The modern piston skirt shape is manufactured to incorporate a barrel profile. The barrel profile is normally generated by a series of ellipses of differing ratios changing along the piston height defined by the major and minor ellipse geometry, as illustrated in figure 4.1. This graduated profile is included to ensure there is an entraining radius present when the piston expands that accounts for the differential thermal profile seen in operation. This is further explained in section 4.3.9.
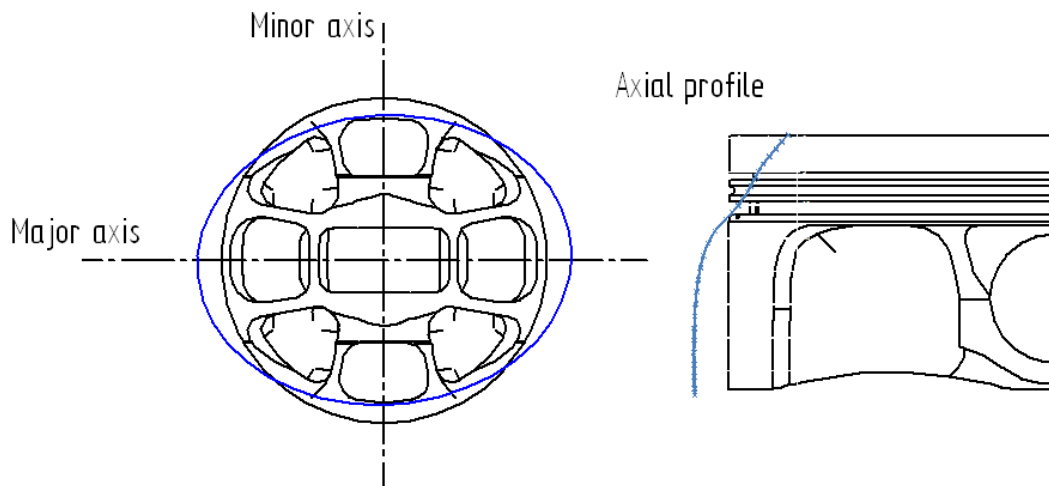
Figure 4.1 - Piston skirt geometry

Conventional OEM pistons (as seen on the right of Figure 4.2) rely on normal loads being spread circumferentially. The "double bridge" design on the left is more commonly seen in high performance race engines where weight rather than noise or lifespan is of primary importance. In this design the skirt side loads are directed perpendicular to the pin axis using the "bridges" to improve stiffness and reduce buckling in the perpendicular supports. This design change has been shown to reduce weight and thus performance without significantly increasing production costs. The analysis tools and methods of piston skirt shape calculation developed in this chapter are equally valid for both cases, though in the examples given and analyses performed, a double bridge design is used.

Figure 4.2 - Conventional piston types

The geometry of the piston drastically alters during use, affected by a number of different factors, all of which are of a transient nature. The main mechanical distortions on the piston are induced by pressures normal to the skirt surface, in cylinder combustion pressure and body inertia. Clearly the inputs to each of these are wholly dependent on the instantaneous operating conditions. Each of these modes of deflection is discussed in a separate section below. The thermal distortion drastically affects the global shape of the piston; again this is a transient phenomenon induced by the periodic heating and cooling of the chamber gasses. It is however very difficult to measure the changing temperature in order to include this as a transient phenomenon. Most analysis methods (**McClure**, (2007) and **Ning**, (2012)) limit this to a single thermally expanded case for a given condition and consider it to be thermally stable throughout the cycle. This technique has been shown to account for a large proportion of thermal growth.

4.2.2 Liner

Controlling the geometry of the cylinder liner is critical to the in-operation shape and overall operation. The mechanical forces that are imparted onto the liner throughout the cycle are typically of transient nature, including normal loading from the ring and skirt interfaces and the combustion gas pressure. These are dynamic by their nature and as such it is difficult to provide an analytic solution for their effects. The thermal distortion is again transient; its gross effect can be calculated by a single quasi static result or through the use of a hot honing manufacturing technique, a large portion of this effect can be removed. Finally, the fitment of the liner itself and the load applied by the fixing of a head distorts the liner geometry. This is wholly dependent on the setup and as such a single static contact FEA solution would produce a representative distortion, or equally measurements from the bottom end using a CMM can be performed (**Rahmani**, (2012) to give the resulting shape. Typically to overcome the effects of these load cases, a torque – plate or dummy head can be installed to induce the 4th order mechanical distortions prior to the honing process so as to produce a more cylindrical bore once assembled. This however is a costly exercise rarely performed on typical road cars.

4.3 Contact deformation

4.3.1 Classical consideration of contact deformation

The deformation induced by the normal loading on the skirt plays a crucial part in the calculation of the contact geometry and the effectiveness of the lubrication mechanism. The calculation of localised deflection has classically been achieved by the solution of the elasticity integral **Timoshenko** (1970) and **Hamrock** (1994).

$$\delta_{i,j} = \frac{2}{\pi E^{'}} \int_{-\tilde{a}}^{\tilde{a}} \int_{-\tilde{b}}^{\tilde{b}} \left\{ \frac{p_{k,l} dx_1 dy_1}{\left[\left(y - y_1 \right)^2 + \left(x - x_1 \right)^2 \right]^{1/2}} \right\} = \frac{2 p_{k,l}}{\pi E^{'}} D^{*}$$

(4.1)

For a rectangular contact area of $2\tilde{a}, 2\tilde{b}$, the influence coefficients are found as

$$D^* = \left(x+\tilde{b}\right)\ln\frac{\left(y+\tilde{a}\right)+\left[\left(y+\tilde{a}\right)^2+\left(x+\tilde{b}\right)^2\right]^{\frac{1}{2}}}{\left(y-\tilde{a}\right)+\left[\left(y-\tilde{a}\right)^2+\left(x+\tilde{b}\right)^2\right]^{\frac{1}{2}}} + \left(y+\tilde{a}\right)\ln\frac{\left(x+\tilde{b}\right)+\left[\left(y+\tilde{a}\right)^2+\left(x+\tilde{b}\right)^2\right]^{\frac{1}{2}}}{\left(x-\tilde{b}\right)+\left[\left(y+\tilde{a}\right)^2+\left(x-\tilde{b}\right)^2\right]^{\frac{1}{2}}}$$

$$+ \left(x-\tilde{b}\right)\ln\frac{\left(y-\tilde{a}\right)+\left[\left(y-\tilde{a}\right)^2+\left(x-\tilde{b}\right)^2\right]^{\frac{1}{2}}}{\left(y+\tilde{a}\right)+\left[\left(y+\tilde{a}\right)^2+\left(x-\tilde{b}\right)^2\right]^{\frac{1}{2}}} + \left(y-\tilde{a}\right)\ln\frac{\left(x-\tilde{b}\right)+\left[\left(y-\tilde{a}\right)^2+\left(x-\tilde{b}\right)^2\right]^{\frac{1}{2}}}{\left(x+\tilde{b}\right)+\left[\left(y-\tilde{a}\right)^2+\left(x+\tilde{b}\right)^2\right]^{\frac{1}{2}}}$$

$$(4.2)$$

Equation (4.2) is often used to evaluate the term $\dfrac{\partial h}{\partial p}$ within the discretised Reynolds equation (section 3.5). It is also used to correct for deflection and the adjustment within the elastic film equation. This is more commonly referred to as the *localised* deflection. This method, as described by **Hamrock** (1980), is for an isotropic and homogeneous perfectly elastic material. This approach is commonly used for hard EHL contacts, such as cam follower and gear teeth contacts, where deflections are of the order of 1µm and the global component geometry does not have an effect on the deflection response.

4.3.2 Application of the Finite Element Method on the component deflection calculations.

Much research over the past 6 years, especially **McClure** (2007) and **D'Agostino** (2006), has shown that piston skirt does not operate according to the above idealised behaviour and distortion magnitudes are much greater than those calculated using the elasticity integral.

Consideration of piston skirt flexibility in a lubricated contact dates back to the 80's when **Li** (1982) presented a method for evaluating the response of the skirt shape to a load at specific points, but it was limited by the relatively primitive computational resources available at the time. Both **Cheng** (1993) and **Ricardo** (1994) introduced relatively coarse piston surface grids, incorporating stiffness matrices extracted from commercial software. The resulting

matrices were of sufficiently small size that they could be directly inverted, giving the direct solution post inversion with very little computational effort. More recent developments have used more dense arrays, providing better resolution and have removed much of the profile coarseness seen with arrays of low density. The increase in array density produces a significant issue in terms of the computational time for the deflection solution.

To form a FE model, a given model volume with known material/physical properties is approximated by a number of interconnected discrete nodes. This process using an imported solid model is usually performed semi-automatically by the FE program. Each node created represents the finite volume immediately surrounding within the boundaries of other nodes and the model edges. A set of governing differential equations are created connecting all the discrete nodes in the computational domain. For models of real 3D bodies this domain is often complex and irregular in, rendering an exact solution unachievable. With the use of carefully designed models and precisely controlled meshing layouts this solution can be modified to achieve a suitable degree of accuracy.

A number of finite element types exist (in geometrical form; triangular, quadrilateral etc). However, they all have specific points, referred to as nodes, where the variable is to be explicitly calculated. The simplest type of solid element is a tetrahedron with 4 nodes – one on each vertex. This type of element is referred to as 'linear' or '1st order' and can be visualised as a flat faced tetrahedron with 4 nodes. A 'parabolic' or 2nd order variation introduces mid-nodes, totalling 10 nodes (Figure 4.3).

Typically, connectivity between elements involves shared nodal positions (external nodes) except for nodal points within elemental volumes, which have no connectivity. Boundary nodes lie on the approximate outer surface of the discretised volume and as such usually have no inter-element connectivity, except for contact analysis.
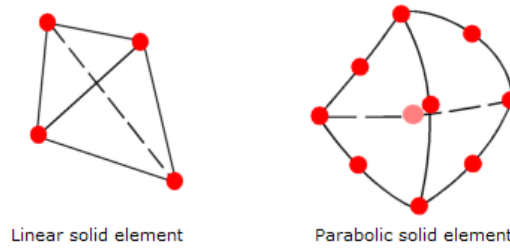
Figure 4.3 - Finite element types

A measure of the overall system complexity is the number of degrees of freedom (DOF). This is generally the number of elements in the solution and the number of values in the field variable. For a simple displacement analysis there would be 3 degrees of freedom x,y,z for each element.

For a linear analysis, such as the case of a statically loaded displacement, the procedure requires a number of decisions / user inputs prior to the automated solution:

- Definition of the geometric computational domain (i.e. component import)
- Model meshing: Definition of element type, geometric properties (overall size, geometric limits/tolerances, local density/refinement, seeding for mesh alignment / mesh efficiency) and the connectivity between the elements
- Inclusion of material properties for the elements
- Apply/define boundary conditions (physical constraints)
- Apply/define loadings such as forces, pressure, and temperature to nodal boundary positions.

In conventional applications the processing of solution is an automated process, most frequently performed by Nastran. Generation of a specific finite element solution for this problem is well outside the scope of this project; the importance of generating a procedure that can be actively linked to the design process is though fundamental. To achieve this, a direct interface with Nastran has been developed. The already well developed input procedure presents a number of problems for an integrated lubricated analysis.

1. Accurate passing of pressure distribution data between Reynolds and Nastran
2. Collation of solution platforms (Nastran and Fortran)

3. Frequent update of nodal force vectors

4. A suitably fast solution retaining an adequate level of accuracy.

Ensuring the correlation between the position of the finite element nodes and the nodes of the lubrication analyses is achieved by forcing the surface nodes on the skirt into the predefined rectangular pattern with nodal separation intervals matched to the Reynolds discretisation. 3D tetrahedral nodes are still employed but are manipulated accordingly, producing a pattern as shown in Figure 4.4. This nodal matching technique removes the need to utilise an uneven multi-grid transformation.

It is crucial that all of the nodes on the skirt surface are common to the models. Additional nodes, aside from the common nodes not used, would indicate false areas of zero load and thus a pressure discontinuity (**Ning** (2012)).
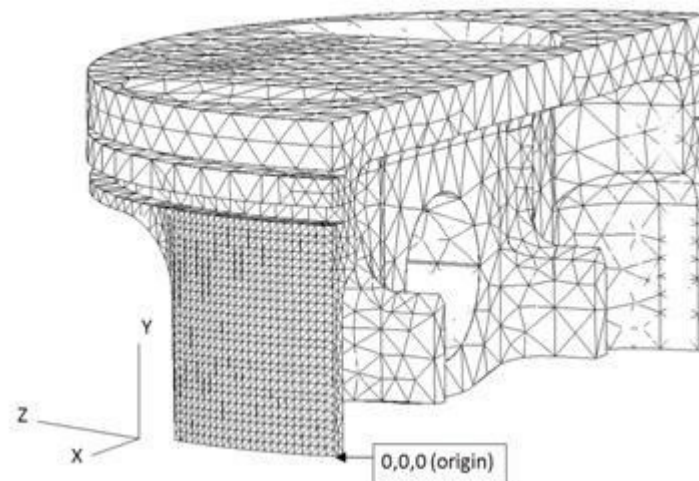
Figure 4.4 - Typical piston mesh

4.3.3   **Model boundary conditions and symmetry**

Appropriate constraint of the FE models is fundamental in ensuring the accuracy and validity of the deflection produced by the model. For a statically dependant solution to exist there must be an equal and opposite net force in each direction to all of the body forces applied for a solution to be calculated. For simple linear static cases this is achieved with a restriction to the pin bore axis (**McClure** (2007)). For load cases without a rigid constraint, the inertia

relief method can be employed. Inertia relief allows the inertia (accelerating mass) of the body to resist the forces applied. This method assumes that the structure is in a state of static equilibrium without direct boundary constraints; it does however result in a further addition of motion, most usually a secondary vector, which would need to be incorporated directly into the secondary dynamics, equation (3.31).

For a piston symmetrical in the x-y plane through the central axis, such as the one presented here for the Honda CRF engine, a symmetry condition can be drawn along the neutral skirt axis resulting in a significantly reduced computational effort. The symmetry boundary condition ensures there is no deflection across the face of the divide, i.e. the forces are equal and opposite, perpendicular to the symmetry plane. This is clearly the case for symmetrical pressure profiles on the crown and skirts. This assumption is only broken from a resulting asymmetric contact pressure profile, which is only likely to be produced from a small order bore distortion, twisting due to bearing clearances or connecting rod buckling/flexibility. This case is neglected at this stage as the effects are relatively small and the global phenomena are captured using the symmetric case without an additional computational burden

A symmetry boundary condition is also imposed on the liner FE model after dividing the component using the same plane co-ordinates used for the piston divide. The liner is modelled with an integral cylinder head, pressure is applied to the cylinder head to simulate the loading imparted by the securing head bolts. Fixed axial positioning of the head is imposed to account for the coupling of the head to the main engine block. Relative motion between the head and the liner is not permitted as this is not seen in normal use due to both the high normal load and co-efficient of friction between the two surfaces, (**Howell Smith** (2013)). Vertical constraint in the Y direction is applied to the underside of the flange mid-way, this simulates the contact seen with the liner carrier. For both the piston and Liner the boundary conditions are shown in isolation in appendix A.

In both models, the symmetry condition is limited to the flexibility calculations alone, for input into the elastic film equation the deflection result from both separate calculations is mirrored back to the full skirt contact width for use within Reynolds and in the boundary contact calculations. As such, the generated pressure profiles are symmetrical about the same axis and half the values of overall contact pressure can be used to calculate the body deflection from the half FE model.

4.3.4   Producing the models

The piston design for the Honda CRF engine, produced by the research sponsor Capricorn, was obtained and imported into the commercial FEA package MSC Patran. Square mesh seed of 1mm was laid on the skirt surface and a 3D tetrahedral mesh was generated for the half case. The pin bore surface nodes were constrained in the xyz directions and a symmetry boundary condition (as described above) was used as input to the split plane.

In the same manner as for the piston, the liner solid was imported into a separate simulation. A matching mesh seed was laid onto the varying skirt liner contact position along the axial height of the liner. The patch width was matched to the skirt width and nodal separation copied.

For a linear elastic solution, the stiffness matrix can be output from Nastran for the two separate models. The resulting stiffness matrices are symmetric and positive-definite **Zienkiewicz** (2000). The varying contact patch position is dealt with in a secondary processing algorithm detailed in section 4.3.5.

4.3.5   Solution within Fortran for normal load surface deflection, *(l_nor & p_nor)*

To allow for the frequent update of the nodal forces and input of the resulting deflections, a quick and efficient interface is required between the FE results and Reynolds solution algorithm within Fortran. To achieve this, a direct computation of the deflection within the Fortran environment is necessary in order to maintain computational efficiency. Nastran is able to output the sparse stiffness matrix used within the automated calculation. This can then be inspected and converted to a standard text file using matlab (**Danial**, (1994)). The general form of a set of linear equations is presented in equation (4.3).

$$[F] = [k][\delta] \tag{4.3}$$

By inverting k, the stiffness matrix;

$$[F][k]^{-1} = [\delta] \tag{4.4}$$

The direct inversion of k for problems such as the one presented (with around 40,000 - 100,000 DOF) is computationally very inefficient and not possible with the limited RAM currently available on a typical desktop computer, or even a moderately sized server computer. As such, a number of algorithms have been developed for the iterative solution of linear equations, which require much less computational effort (**Saad**, (2003)). The solution within the Fortran environment is performed using an iterative solver based on the preconditioned conjugate gradient (PCG) method (**Dias da Cunha and Hopkins**, (1994)). For a system of 40,000 DOF, which is typical for piston presented in figure 4.4, solution requires approximately 50 seconds on a modest desktop machine. This however still presents a significant computational burden as for a single quasi-static or transient time step many hundreds of iterations are required for convergence, for each spatial step within the time step a new deflection response would need to be calculated and the burden of the deflection calculation would dominate.

As the iterative calculation for δ from equation (4.4) produces a significant computational burden, a linear superposition method was introduced to reduce overall convergence time. To illustrate the methodology a simple example is presented.

Take the following two sets of linear equations in the form of equation (4.3):

$$
\begin{aligned}
2k_1 - 3k_2 &= 5 \\
4k_1 + 5k_2 &= -7
\end{aligned}
\qquad \text{and} \qquad
\begin{aligned}
\sqrt{2}k_1 + 3k_2 &= 16 \\
-5k_1 - 1k_2 &= 3
\end{aligned}
\qquad (4.5)
$$

The above equations produce the following matrices:

$$
\begin{array}{cc}
[A] & [G]
\end{array}
\qquad\qquad\qquad
\begin{array}{cc}
[B] & [H]
\end{array}
$$

$$
\begin{bmatrix} (2) & -(3) \\ (4) & +(5) \end{bmatrix}\begin{bmatrix} 5 \\ -7 \end{bmatrix}
\qquad \text{and} \qquad
\begin{bmatrix} (\sqrt{2}) & +(3) \\ -(5) & -(1) \end{bmatrix}\begin{bmatrix} 16 \\ 3 \end{bmatrix}
\qquad (4.6)
$$

The addition of these matrices yields: (which is the calculation performed when the loads are applied simultaneously in the FE solver)

$$[C] \qquad\qquad [i]$$

$$\begin{bmatrix} (2+\sqrt{2})-(3+3) \\ (4-5)+(5-1) \end{bmatrix}\begin{bmatrix} 5+16 \\ -7+3 \end{bmatrix} \tag{4.7}$$

Clearly, as these are linear equations the following can be performed with chosen scalars (which would represent a single scaled force):

$$2[A]+3[G]=2[B]+3[H] \tag{4.8}$$

Equally, when they are summated simultaneously they would produce the same result:

$$\begin{bmatrix} (4+3\sqrt{2})-(6+9) \\ (8-15)+(10-3) \end{bmatrix}\begin{bmatrix} 10+48 \\ -14+9 \end{bmatrix} \tag{4.9}$$

The above demonstrates the ability to separate the loadings and appropriate scaling depending on the actual application load. To apply this to the special case of the piston skirt, a set of pre-calculated deflection arrays is employed within the conjugate method, producing a solution in the form of half of equation (4.6).

For each nodal position, a unit load (Lu) is applied normal to the external surface and the response of all the surface nodes are recorded in the x and z directions. Applying this load for each nodal position in isolation sequentially allows for a five dimensional reduced array to be formed, $A(i,j,k,l,n)$ for both the liner and the skirt. Where i and j refer to the position of the load, k and l refer to the response node position and n is either 1 or 2 for the respective x or z deflection. A special case for the edge and corner nodes has been applied of $Lu/2$ and $Lu/4$, respectively, to account for the reduced nodal surface areas. This routine has been automated as a pre-processing algorithm within Fortran, using the PCG method described above.

A given conjunction pressure profile (P) can be discretised into an array of forces using the node separation lengths.

$$[F]=[P]\mathrm{dxdy} \tag{4.10}$$

Using array [A] in a series of 4 nested do loops allows for the scalar multiplication and addition for each of the separated [F] terms. This is performed in the following way for the x term:

$$[\delta_x] = \sum_{nxx}^{i=1}\sum_{nyy}^{j=1}\sum_{nxx}^{k=1}\sum_{myy}^{l=1}[\delta]_{k,l} + \left([A]_{i,j,k,l,1} \cdot \frac{F_{(i,j)}}{Lu}\right) \tag{4.11}$$

Similarly for the z deflections;

$$[\delta_z] = \sum_{nxx}^{i=1}\sum_{nyy}^{j=1}\sum_{nxx}^{k=1}\sum_{myy}^{l=1}[\delta]_{k,l} + \left([A]_{i,j,k,l,2} \cdot \frac{F_{(i,j)}}{Lu}\right) \tag{4.12}$$

This method reduces the storage requirement, typically the storage of the sparse matrix of the full model requires 160Mb and the reduced equivalent $[A]$ matrix only requires 40Mb for the Skirt. Clearly though the gains are greatest in terms of computational time. Each single calculation of equation (4.4) requires approximately 50 seconds, whereas the calculation using equations (4.11) and (4.12) requires only 10ms. However, this doesn't come without some computational cost, since the pre-processing step is rather time consuming, this needs to be performed only once for any given piston and liner nodal arrangement.

The variable alignment between the skirt and liner nodes requires an interpolation algorithm that varies for a given crank position and thus a varying piston Y displacement. Figure 4.5 shows the possible alignment issue seen when the bodies are frozen at a given time step.

Ignoring any misalignment in the Z direction as movement is assumed to be negligible as detailed in section 4.3.4 the shift can be corrected for in only the y direction. As shown in Figure 4.5 a miss alignment of Yc. Using a basic linear interpolation the following corrections are used for the forward and backward correction of liner input pressure and deflection.
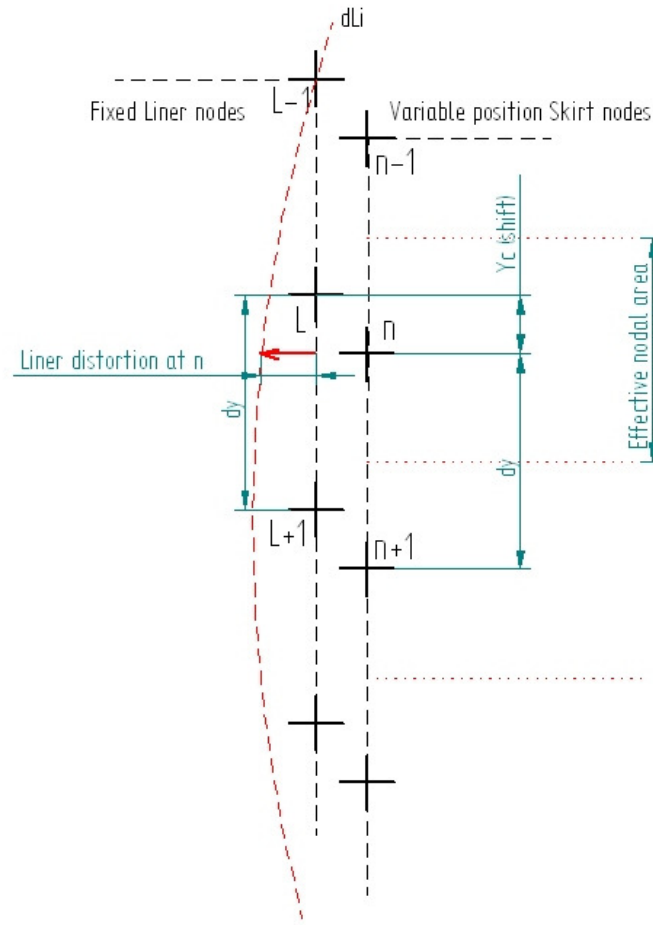
.

Figure 4.5 - Liner and piston nodal mis-alignment

$$F_L = (P_{n-1}Y_C d_x) + (P_n(\mathrm{dy} - Y_C)d_x) \tag{4.13}$$

$$\partial li_n = \left(\frac{\partial li_L - \partial li_{L+1}}{dy} \right) y_c + \partial li_{L+1} \tag{4.14}$$

4.3.6   Cylinder head loading, *(l_hd)*

As with any conventional engine a cylinder head is installed to seal the combustion chamber. A seal is created between the head and liner using a gasket conventionally. This sealing action requires a force across the face of the bodies. As a result of this, a force is imparted by the securing of the head, this is generally controlled by the precision application of torque through the clamping bolts. Figure 4.6 shows the deformation mode observed with this loading. It should be noted that as neither the load nor the profile alters significantly circumferentially, the deformation shape has insignificant circumferential variation either. This is a simplified analysis and as such does not include the 4th order "lobbing" effect often seen due to the uneven normal force seen relative to the bolt positions. It does though include the gross effect in compressing the liner which is the dominating component of liner distortion form head loading. To induce this loading a uniform pressure distribution of 180 bar, twice the maximum in-cylinder pressure, as per the advice of **Howell-Smith** (2013).
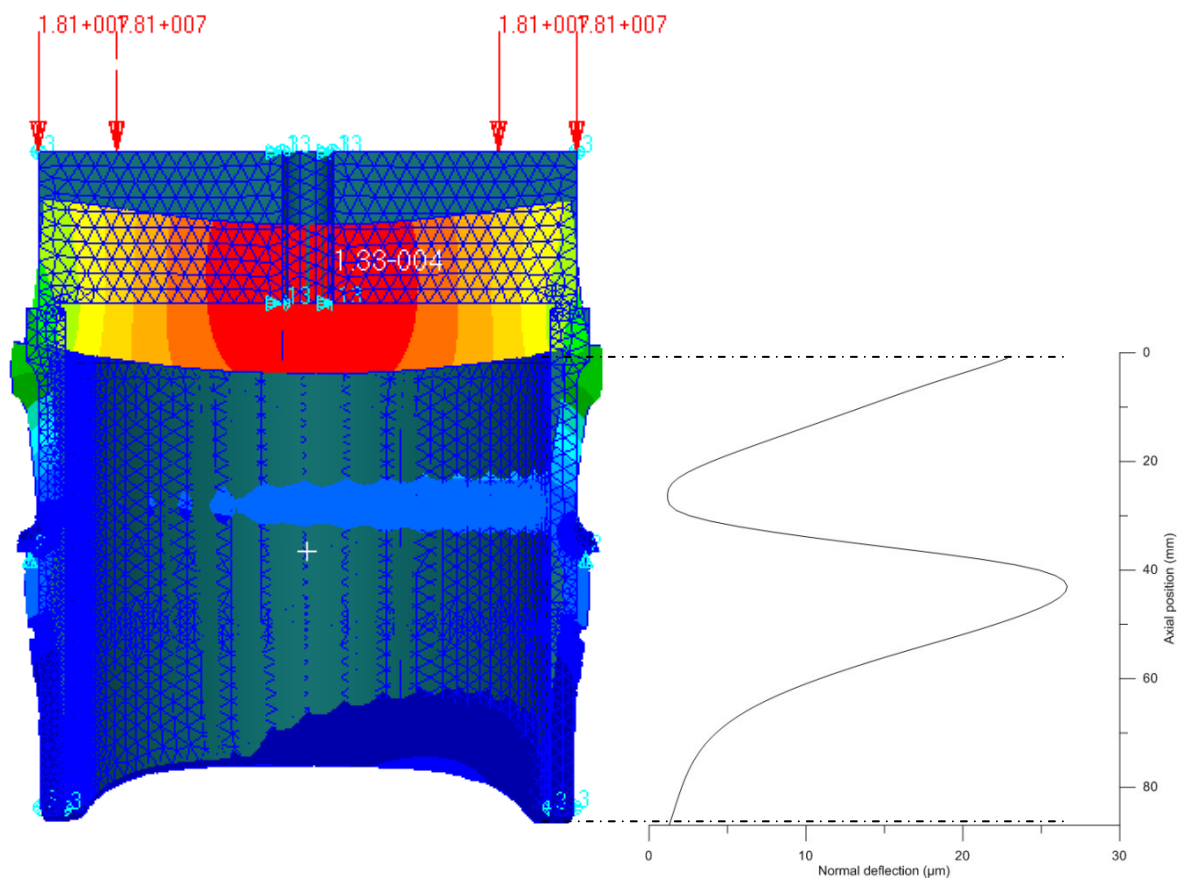

Figure 4.6 - Cylinder head loading deformation mode

4.3.7 Crown loading, *(p_cp)*

It is well understood that the combustion chamber pressure has a great effect on the contact geometry of the skirt (**Hoshikawa**, (2011)). More emphasis has been placed on this effect as the mass and structural stiffness of pistons have been reduced in the past years in an attempt to improve emissions and reduce noise, (**Mahle***, (2013))*. This direct effect of crown stiffness on friction and contact patch has been experimentally highlighted recently by **Hoshikawa** et al (2011).

Using the same FE model to produce the stiffness arrays, the crown loading is applied in a single static case on a half piston model. The reaction constraint is provided by the constraint of the pin bore surface in XYZ. This replicates a vertical reaction from the gudgeon pin – bore interface and provides rotational stability. As this load case is treated independently and the resulting deflection is linear, a direct proportionality between in cylinder pressure and skirt x-z deflections is drawn and used.

Figure 4.7 - Crown pressure effect on piston
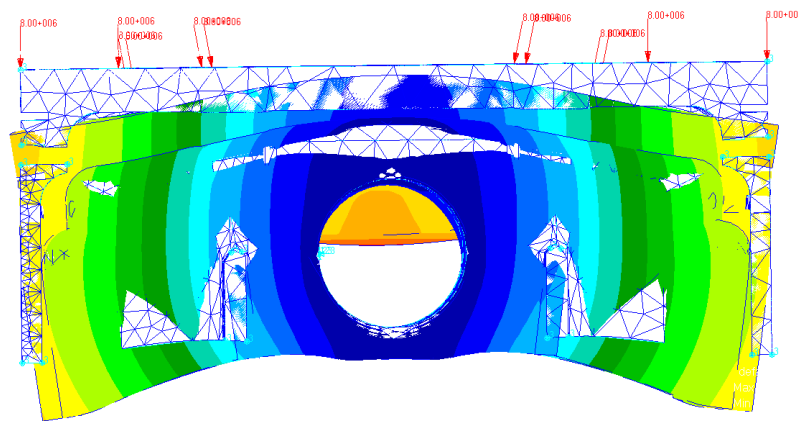
The case shown in Figure 4.7 is for the combustion pressure at 17° ATDC, 6250rpm Wide open throttle (WOT). The same analysis is performed for the smaller load case of 150° ATDC. Similar shape (only scaled) is observed and thus the crown deflection scalar, [ε_c], is devised. This allows for the fast calculation of skirt shape change with respect to cylinder pressure.

$$\partial s_{i,j} = Cp.\varepsilon_{ci,j} \qquad\qquad (4.15)$$

For clarification of the linear trend observed, solutions for three pressure cases have been created and for the same node sets the deflection and pressure have been plotted in Figure 4.8.
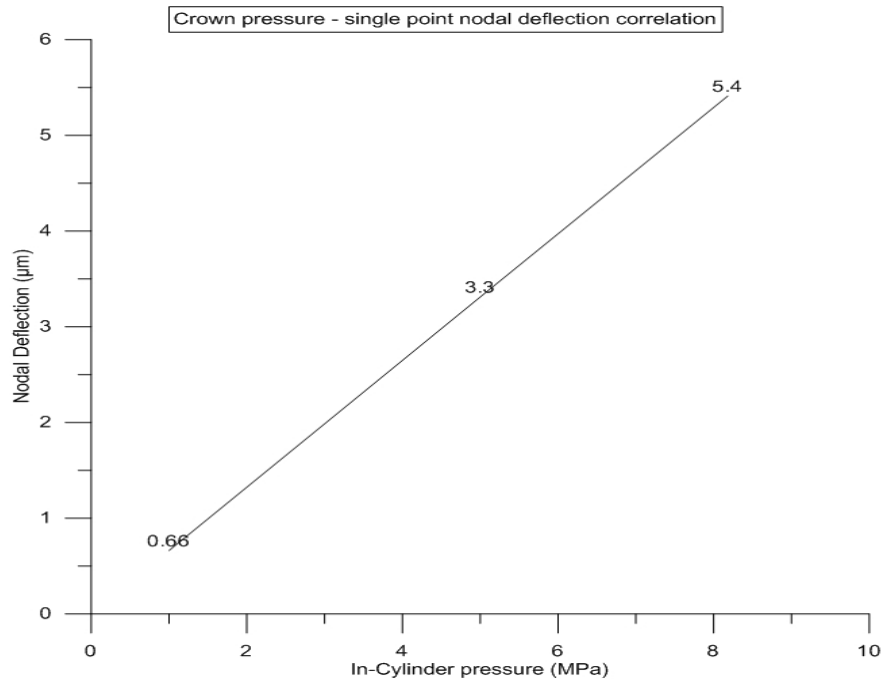
Figure 4.8 - Crown pressure distortion shape correlation

For the inclusion of the above, a skirt response shape is generated for a unit crown pressure loading. Using this response shape and scaling according to the cylinder pressure ratio, a linear solution for the response of the skirt nodes is generated. This analysis is based on the following assumptions and simplifications.

- The cylinder pressure acts evenly over the surface of the crown
- The deflection of the crown has a negligible effect on the application direction of the pressure
- The altering connecting rod angle resulting direction of constraint has a negligible effect on the constraint direction of the gudgeon axis.

4.3.8 Primary inertial, (*p_in*)

The effect of the inertial loading acts to bend the piston in the same manner as the crown loading, but with alternate directions. Using the same half model of as shown used in section 4.3.7, a number of sample inertial load cases with given acceleration have been solved using a linear solution. A shape array for the skirt is created for both the positive and negative directions of the primary acceleration. Using these shape arrays and a given primary acceleration magnitude, the resulting skirt shape change can be input to the elastic film equation, using the equations given in equation (4.16).

$$[\delta In] = \frac{\ddot{y}_{ca}}{\ddot{y}_{rp}}[\varepsilon ip] \quad \text{or} \quad [\delta In] = \frac{\ddot{y}_{ca}}{\ddot{y}_{rn}}[\varepsilon in] \tag{4.16}$$

4.3.9 Piston thermal distortion, (*p_th*)

The piston structure is subjected to a large thermal gradient resulting from elevated temperature on the upper crown surface due to the combustion. Once the experimentally verified temperature profile has been obtained, an thermal expansion can be calculated. Initially this temperature profile can be estimated within the FE environment. A standard approach for obtaining a full field temperature profile is by means of modifying the heat transfer coefficients and both the surface temperatures such that correlation with the experimental point data is achieved. Convective fluid heat transfer is the dominant mechanism of heat transfer, with Conductive heat transfer only occurring where there is boundary contact, typically only seen parts of the pin bore, ring – liner conjunction and skirt – liner conjunction at selected positions in the cycle. As mentioned previously, an instantaneous solution is beyond the scope of this project, the approach taken here follows a similar approach to that of **Abbes** (2004). This focused on the time average convective heat transfer coefficients. These values can be altered iteratively until the experimentally obtained point measurements agree with the values predicted in the thermal model. This approach has been successfully applied for the case of the CRF piston used here by **Howell-Smith** (2011); appendix A shows the derived boundary conditions calculated by Howell-Smith. Using the derived 3D temperature profile the thermal expansion can then be calculated using the

relevant material thermal expansion coefficient. This calculation is performed once for this analysis, the resulting thermally deformed skirt shape is then used as the base for the radial values used in equations (4.20) and (4.21).

For the examples shown here a 2d temperature profile as published by **Bosch** (2007) has been used for the target temperatures. As detailed in section 5.5.5 the precise acquisition of this 3d profile is beyond the scope of this research project.
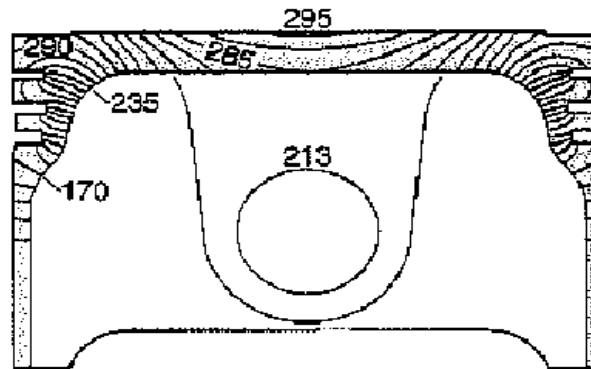

*Figure 4.9 - Temperature gradient within a spark ignition engine piston, **Bosch** (2007)*

4.3.10 Liner shape thermal distortion, *(lin)*

Thermal distortion has a significant effect on the principal diameter of the cylinder. The liner itself plays a crucial role in the dissipation of excess heat from the combustion chamber into the surrounding solids and into the water coolant system of the engine. Using a technique similar to that used in the calculation of thermal expansion for the piston explained in section 4.3.9 and in appendix A the 3D temperature profile of the liner can be modelled. The acquisition of in-cycle temperatures is significantly easier than for the case of the operating piston due to its static nature. The most frequently used technique is to use embedded thermocouples (Figure 5.12) with the wires routed out through specifically designed and sealed conduit routes.

Again there is a differential thermal expansion caused by the localised variation in liner temperature, this means the conjunctional geometry of the liner is also dependent on the piston position. In order to include this in the formation of the film shape, a series of arrays

have been formed for each of the angular increments along a given stroke of the cycle. The *lin* term in the film shape formation takes the form of a 3D array, *(i,ca,)*, where *i* represents the row and ca represents the nearest angular increment. The analysis does not consider a circumferential variation in diameter hence the dropping of the *j* direction; this retains the pressure symmetry assumption made in section 4.3.3.

Due to the limitation in results measured results a single uniform temperature on the internal has been used in order to perform a simple expansion. This boundary condition is shown in Appendix A.

4.4 Film shape formation

4.4.1   Quasi-static film shape formation

The quasi static analysis seeks to form a solution to the skirt – liner contact, it considers only the thermo-mechanical deformations observed on the piston, maintaining a fixed liner geometry in order to directly compare the piston design and the constituent effect of piston distortions of the contact. With this in mind the instantaneous film shape for the given x and z components is given by equations (4.17) and (4.18).

$$h(i, j)_x = lin(i, \text{j})_x - p\_th(i, j)_x - p\_in(i, j)_x - p\_cp(i, j)_x - p\_nor(i, j)_x \quad (4.17)$$

$$h(i, j)_z = lin(i, \text{j})_z - p\_th(i, j)_z - p\_in(i, j)_z - p\_cp(i, j)_z - p\_nor(i, j)_z \quad (4.18)$$

Typically these are updated as their boundary conditions change throughout the calculation, briefly summarised in Table 4.1.

Table 4.1 - Film shape variables for both Quasi static and transient analysis routines

Variable	Description	Update frequency
lin	Liner thermally distorted shape (radial value)	Constant, Piston position (Y) dependant
l_nor	Deflection due to normal load at conjunction (∂)	Spatial iteration, Y dependant
l_hd	Deflection due to head clamp loading (∂)	Constant, Y dependant
p_th	Thermally distorted skirt profile (radial)	Constant
p_in	Inertial deformation (∂)	Time step
p_cp	Crown pressure deformation (∂)	Time step
p_nor	Deflection due to normal load at conjunction (∂)	Spatial iteration

4.4.2 Transient film shape

The accurate calculation of the instantaneous film thickness is key to the operation of the transient routines. The resultant eccentricities measured at the top and bottom of the piston skirt (e_t & e_b) defining deviation from the centralised position, are combined with the axially aligned conjunction geomerty, *Ss,* to generate the film thickness. *Ss* is defined as;

$$Ss(i, j) = \sqrt{Ss(i, j)_x + Ss(i, j)_z} \tag{4.19}$$

Where;

$$
\begin{aligned}
Ss(i, j)_x = {} & lin(\mathrm{y}, i, \mathrm{j})_x + l\_nor(\mathrm{y}, i, j)_x + l\_hd(\mathrm{y}, i, j)_x \\
& - p\_th(i, j)_x - p\_in(i, j)_x - p\_cp(i, j)_x - p\_nor(i, j)_x
\end{aligned}
\tag{4.20}
$$

$$
\begin{aligned}
Ss(i, j)_z = {} & lin(\mathrm{y}, i, \mathrm{j})_z + l\_nor(\mathrm{y}, i, j)_z + l\_hd(\mathrm{y}, i, j)_z \\
& - p\_th(i, j)_z - p\_in(i, j)_z - p\_cp(i, j)_z - p\_nor(i, j)_z
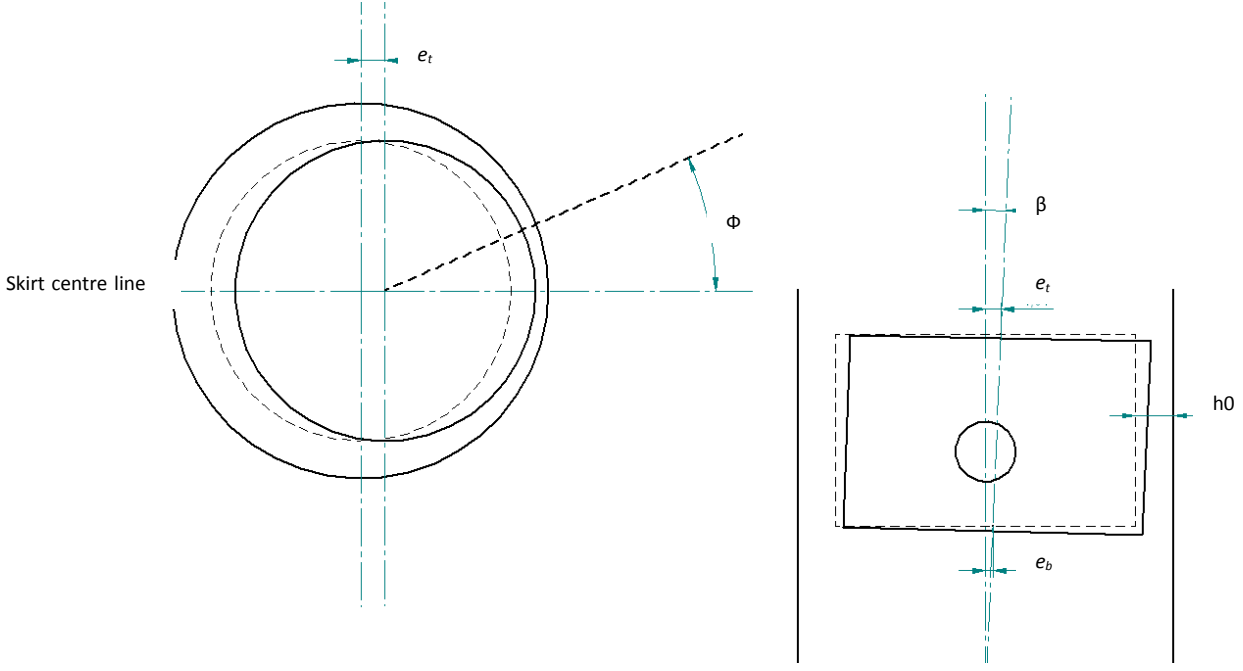\end{aligned}
\tag{4.21}
$$

Figure 4.10 - Transient film shape position reference

With reference to Figure 4.10, considering the centre line of the skirt, where $\Phi=0$, the difference due to the effect of offset on the thrust side becomes (where i represents the nodal increment in the y axis along the skirt):

$$c_o(i) = e_t - (i-1)\left(\frac{e_t - e_b}{nxx - 1}\right) \qquad (4.22)$$

This can be altered for the anti-thrust side;

$$c_o(i) = e_t - (i-1)\left(\frac{-e_t + e_b}{nxx - 1}\right) \qquad (4.23)$$

For each position on the circumference, the incremental change of Φ changes the value of differential clearance as;

$$d(i, j) = c_o(i)\cos\left(\left(\frac{nyy+1}{2} - j\right)\Delta\Phi\right) \qquad (4.24)$$

Where $\Delta\Phi$ is the angular increment for the given nodal separation in the nyy direction and j is the incremental nodal position.

Each time a new profile is calculated for a given computational step, it is normalised with respect to its minimum clearance, such that S_min = 0. Using this modified Ss and combining equations (4.19), (4.22) and (4.24) for the thrust side;

$$h(i, j) = Ss(i, j)_{ts} + h0 + \left\{ e_t - (i-1)\left(\frac{e_t - e_b}{nxx-1}\right)\cos\left(\left(\frac{nyy+1}{2} - j\right)\partial\Phi\right)\right\} \qquad (4.25)$$

Similarly using (4.19), (4.23) and (4.24) for the anti-thrust side;

$$h(i, j) = Ss(i, j)_{ats} + h0 + \left\{ -e_t - (i-1)\left(\frac{-e_t + e_b}{nxx-1}\right)\cos\left(\left(\frac{nyy+1}{2} - j\right)\partial\Phi\right)\right\} \qquad (4.26)$$

4.5 Summary

This chapter has detailed the complex piston skirt – liner conjunction shape. The piston's operation under load is determined by the 3D response of both the liner and piston to the boundary forces and thermal conditions seen. It is critical that these shapes and responses are returned accurately and without an excessive computational load to the calculation algorithms for lubrication and secondary motion. Methods have been developed to optimise the calculations based on the FEM, with innovative post processing routines the original techniques that are very expensive in terms of computational power have been made more efficient for iterative and repetitive calculations without loss in accuracy.

Each of the techniques shown and developed here is highly dependent on the data supplied to the individual model. The acquisition and processing of the boundary conditions for the specific engine used are developed in chapter 5.

5.1 Introduction

This chapter details the test bed setup and the engine used throughout the work. The selection of the instrumentation and modification of the some of the engine components for testing has been detailed. The test boundary conditions used throughout are given. Sample data acquired for input to the models has been shown alongside some of the 2D measured film thickness data sets.

As mentioned previously in chapters 3 and 4, a single cylinder motorbike engine has been used as the base engine for both the measurements and numerical predictions throughout this thesis. The chosen engine is Honda CRF 450R. This choice allows for conditions to be monitored at significant engine speeds, up to 12000rpm, yielding piston sliding speeds of up to 33m/s. Although it is still a naturally aspirated (NA) engine (as opposed to turbo or supercharged), it still exhibits a relatively high specific power output and torque of 41KW and 50Nm respectively. It is one of the highest performing NA engines widely available at over 90KW/L and 110Nm/L. Its single cylinder arrangement allows for the measurement of variables in isolation of any effects from other cylinders. As a single cylinder it also allows for system changes i.e. component alterations and data acquisitions, to be performed with greater ease and more economically than on a multi-cylinder engine.

Significant effort was expended on the understanding of engine operation, particularly under controlled test-bed conditions to ensure good test repeatability, which is crucial for trustworthy comparative parametric testing.

5.2 Test engine selection

The area of interest in this study is restricted to the in-cylinder region of the engine, specifically the piston skirt – liner conjunction. Due to the high cost of necessary instrumentation a single cylinder engine configuration is chosen. The key technical reasons for this engine choice are:

- Representative base parameters – bore, stroke, connecting rod length and fuel type representative of current and predicted future market OEM and motorsport technology.

- High speed and load capabilities – as this is a scientific study the data obtained should envelope all commercially available engines in speed and load characteristics

- Relatively low complexity – with fewer components comes less friction and less possibility for failure; although a high performance engine is required, a minimum component count enables faster disassembly and assembly.

- Replaceable barrels (as opposed to incorporated within the crankcase) - to allow for instrumented and modified barrels to be tested, preferably easily replaceable with a wet liner system as typical in motorsport applications.

- Water cooled – as some instrumentation is temperature sensitive; also this is a typical configuration in industry.

Engines of the type described in the above requirements are commercially available and commonly used in the motorbike sector. Off road motorcycles match these requirements exceptionally well. The motocross motorbike engines are high speed and load machines and their simplicity lends them well for the intended investigation.

Table 5.1 lists the specifications for the engine. Figure 5.1 shows the complete engine architecture. It can be seen that the operating speed is quite high with maximum power at 9000rpm (speeds of up to 12000rpm are possible). This would be the equivalent of a naturally aspirated 2l engine producing 183KW and 222Nm which is very close to the limit in both OEM and in the motorsport arena.

*Table 5.1 - Engine characteristics of Honda CRF450R (**Honda Motor Co**. (2002))*

Engine type	Water cooled 4-stroke, 4-valve single cylinder
Engine displacement	$449cm^3$
Bore & Stroke	96mm x 62.1mm
Compression ratio	11.5:1
Max quoted power [specific power]	41kW@9,000 rpm [91.31kW/dm^3]
Max quoted torque [specific torque]	49.8Nm@7,000 rpm [99.80Nm/dm^3]
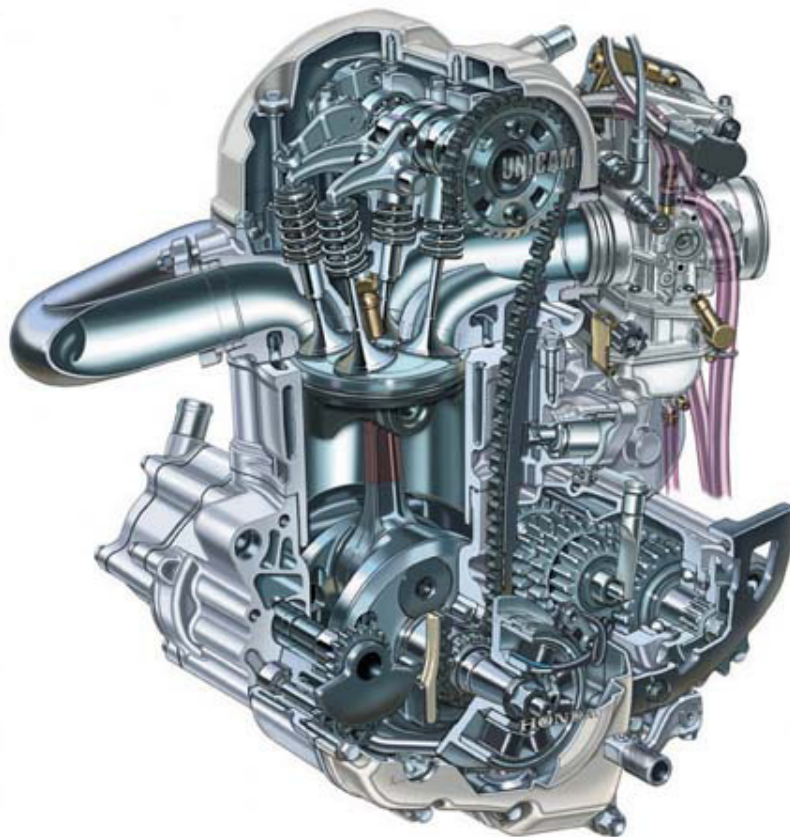
*Figure 5.1 - Cutaway of CRF450R engine (**Honda Motor Co**. (2002))*

As would be expected, in the operation of a stock engine for instrumentation and parametric study there are a few design issues with the Honda CRF450R that need modification before it can be used as intended.

- The cylinder block is a single unit incorporating the cylinder liner, oil channels, water cooling and chain tensioning system. This makes the modification process difficult and increases the costs of manufactured parts due to their complexity.

- The complex piston shape of the OEM part supplied by Honda is not easily characterised, modified and the CAD geometry is not available for simulation models

- The thin walled nature of the engine does not lend itself to constant assembly and disassembly. The latter coupled with the aluminium and magnesium non-inserted threaded parts, means that there will be a finite life for each test component, which adds significantly to testing costs.

5.3 Modified components

5.3.1   Liner and Cylinder block

The standard Honda incorporates a cast cylinder block which houses the cylinder liner (a mono-block arrangement, Figure 5.2), oil and water channels and chain enclosure with an integral tensioning system. This configuration required modification, as replacement of the liner and refitting is an expensive and time consuming operation. For the eventual inclusion of ultrasonic sensors the original mono-block left very little room for sensor positioning and connectivity.

Figure 5.2 - Original Honda CRF450R OEM cylinder block

Motorsport wet liner conversions were investigated and it was decided to manufacture the cylinder block from two separate components; a cylinder liner and holder, (Figure 5.3i & ii). This arrangement simplifies the geometry of the test part, reduces cost and also makes modelling easier as the liner is pinned in defined positions. The design and manufacture of this configuration was kindly performed and overseen by the project sponsor Capricorn Automotive.

Figure 5.3i & ii - new wet liner (left) and liner carrier block (right)

The new arrangement has identical oil and water system, pickup points and a chain tensioning system. It incorporates a nitrile o-ring seal to prevent ingression of coolant into the crankcase. Both top and bottom OEM specification gaskets are used in the assembly.

The liner and the piston (as detailed in section 4.2) are both manufactured from a high performance aluminium alloy, AA2618. This is an alloy commonly used throughout automotive and aerospace applications, **Luo** et al (2002). Both the piston and liner undergo a cyclic loading from the combustion pressures and dynamic contact loads throughout the cycle. The fatigue life is dramatically affected by the elevated temperature seen throughout the operation. This selected grade has been carefully chosen to account for the operational temperatures seen in both the liner and piston and ensures maintenance of sufficient strength through its expected lifespan.

5.3.2 Piston body

To facilitate simulation of the piston body under operation, the OEM Honda piston was deemed unsuitable for direct modification or use throughout for reasons discussed in section 5.2. As such, a new piston was developed to ensure all the required geometry and properties, as well as enabling ease of altering profiles, geometry, surface finishes and use of additional coatings. The designed piston maintained a similar mass, removing the need to rebalance the engine and maintained the same pin bore geometry, allowing the existing Honda connecting rod and integral crank to be used without any further modification.

The piston skirt geometry and manufactured barrel profile are further detailed in chapter 4. To achieve this geometry a method of single point turning has been used. The roughness and profile of the skirt surface in the axial direction is defined by the cutting tool geometry and the feed rate at which it moved down the axis, as would be expected of a conventional turning process. In general, modern pistons usually exhibit either industry standard waved pattern, incorporating the radius of the cutting tool, a reversed saw tooth profile or a '*smooth*' profile. For the tests and simulations performed here the smooth piston was used, reasons for which are detailed in section 5.5.4, ultrasonic measurement.

Clearly, an optically smooth profile is not created by this process. The profile used still has an element of waviness which is generated by the radius of the cutting tool and the spiral effect expected when traversing axially. Its effect in the case of the piston skirt used here is small. The length of the waves is approximately 50μm and the overall depth of these, including the surface roughness is approximately 1.75μm. It also features S_a value of 0.46μm (surface roughness average). Figure 5.4 shows a cut through the measured surface profile in the axial direction, illustrating these features. These are in any case much less significant than the roughness of the liner surface itself.
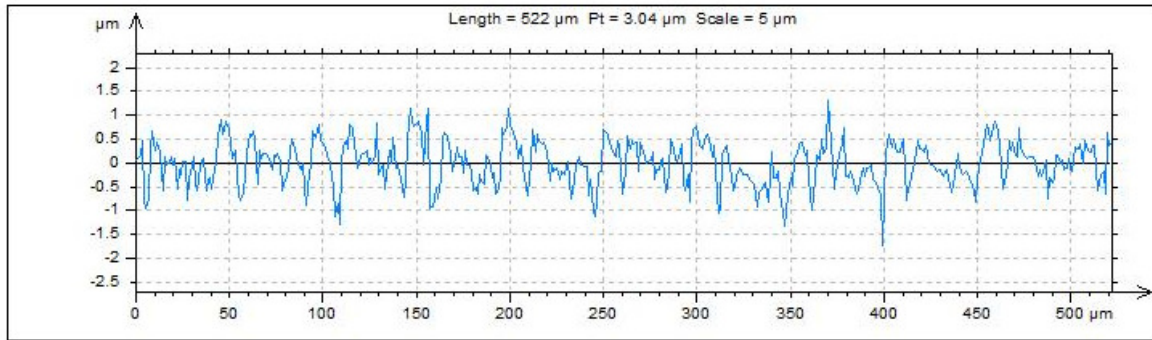
Figure 5.4 - Axial cut through the measured surface roughness

5.4 The engine Test-bed set up

The engine is mounted onto a specifically designed aluminium stand, which replicates the mounting locations that are used in the original motorbike, ensuring the engine structure is not stressed incorrectly, which can become a source of component distortions. This stand is attached to a very stiff structure via four anti-vibration rubber couplings in an attempt to isolate the gross vibrations. The output shaft of the gearbox is then axially aligned to the transient dynamometer. The assembled engine and dynamometer can be seen in Figure 5.5.
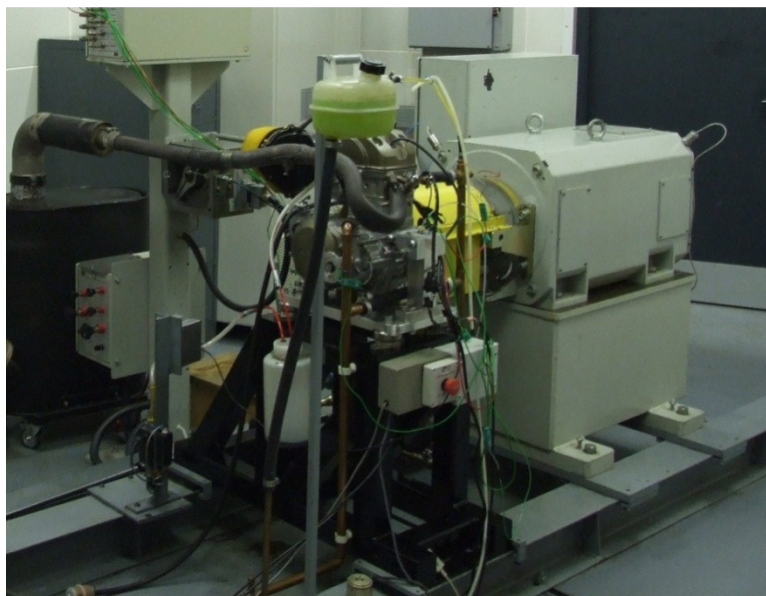

Figure 5.5 - Engine setup as installed with dynamometer

The transient dynamometer is an Oswald 250kW which is controlled by the installed Ricardo S3000/3345 system. The engine's throttle control is integrated into the Ricardo system and actuated by a standard cable operated throttle control unit. The test cell provides built-in provisions for cooling via a chilled high volume recirculation circuit with thermostatically controlled coolers, mounted outside the building. An air supply which is able to control the pressure in the test cell ensures that a slight negative pressure is maintained, ensuring the exhaust fumes are extracted and dumped to atmosphere. Throughout all tests the temperature, humidity and pressure are logged separately.

The engine water temperature is monitored by thermocouples and the pump is activated when a set temperature is reached and then turns off when the temperature falls below a pre-determined point.

The engine is started using the dynamometer, thus the kick-start pedal is removed. The gearbox is locked in second gear throughout. This gives a cumulative gear ratio of 4.026. Otherwise, the engine is built to OEM specifications for all tests.

The engine speed is monitored by a TTL 1024 point encoder manufactured by Hubner Berlin (HBM) (OG 90 DN 1024 TTL). The produced or absorbed (under motored condition) torque is measured by a HBM T10F torque flange attached to the dynamometer output shaft. Both the speed and torque outputs are input to the Ricardo monitoring and control system.

5.5 Standard instrumentation

The overall operation of the engine and the equipment involved is not the main focus of this thesis, nor do they constitute a significant portion of the work performed by the author. The standard instrumentation such as fuel and air supply and monitoring is not detailed here as it is not directly relevant to the output demands of this work. The instrumentation required in connection to input parameters of the models is detailed below.

5.5.1 Coolant water

The bulk water temperature is measured with a standard K-type thermocouple at the top hose point, where the coolant exits the engine to the cooling circuit and at the bottom of the hose point where the coolant enters the engine from the cooling circuit. These two temperatures are constantly monitored to regulate the flow rate through the engine; too high a differential and the block is susceptible to damage through thermal shock, too little the difference and inadequate cooling may take place resulting in localised hot spots or catastrophic failure. The top hose temperature is usually held to a target of 70°C, the direct control of this temperature represents the set point for the engine cooling loop, the secondary cooling loop is controlled to ensure this is met and thus the exit temperature maintains a suitable proportionality. Due to the relatively slow response times that thermocouples require (2-3s), the measurements taken are not suitable for acquisition on a crank angle or a cycle based time interval. As such for the duration of a test the mean water temperature will be used for any further processing.

5.5.2 Measurement of engine (crank) position

In order to make use of pressure and film thickness signals, the individual signals need to be recorded simultaneously with the crank angle position and speed, thus giving sufficient detail of the piston position, speed and acceleration for a given separate measurement. To achieve this, the crank position is monitored through a specifically made encoder that is mounted to the engine's balance shaft (coupled via a gear directly onto the crankshaft), Figure 5.6. It comprises of a 360 tooth encoder wheel and an optical reader that detects both 360 pulses and a single TDC pulse. These pulses are processed using a specifically designed piece of Labview software, allowing for the simultaneous sampling of up to 8 analogue channels using a National instruments (NI) BNC-2110 termination block and an NI PCMCIA DAQ card for connection to the main acquisition computer. In addition to this, using a fixed frequency input of 10 MHz (as opposed to the CPU clock), the time interval between pulses is measured and as such the crank speed can be derived for each defined crank angle position. Each of the measurements taken are made from/to 0°, which is defined as the TDC from the separate TDC pulse.
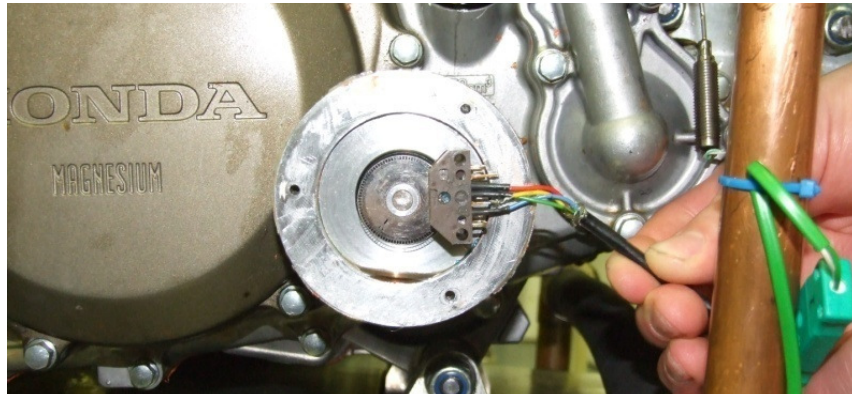
Figure 5.6 - Custom made encoder mounted to the side of engine

5.5.3   Measurement of cylinder pressure

A Kistler 6081A40 Probe with a 3 mm Sensor head, rated to 250 bar is used. It is a piezoelectric sensor utilising a quartz crystal to produce an electric charge proportional to the force/pressure applied. It is installed in the cylinder head in a stainless steel sleeve with the tip of the sensor mounted flush with the cylinder head. As the sleeve of the sensor penetrates through the cylinder head's cooling jacket it negates the requirement for a dedicated jacket or specific water cooled sensor. The sensitivity has been shown to remain constant up to a range of 350°C, but the bulk temperature of the sensor is unlikely to approach this during normal operation with this configuration. Finally, the sensor is connected to a Kistler charge amplifier which is in turn connected to the National Instruments data acquisition system mentioned above.

5.5.4   Ultrasonic film thickness measurement

As described in the literature review, there are various methods for measuring the film thickness between the ring or piston skirt and the liner. There is only one known method though that can be implemented unobtrusively without interfering with the film. The ultrasonic technique was developed for this purpose at the University of Sheffield, who are part of the Encyclopaedic project consortium.

The film thickness measurement of the piston skirt conjunction is crucial for the validation of the numerical models generated throughout this project. It is also critical that film thickness values can be recorded over a number of positions over the skirt-liner conjunction during operation, thus giving validation of the operational conjunction shape, as well as the instantaneous positional film thickness.

The system is composed of a piezoelectric sensor that is mounted onto the cylinder liner with the use of strain gauge adhesive and pulsed at a rapid rise rate with narrow duration and high voltage "top-hat" signal. This signal makes the piezoelectric crystal oscillating at the pulse frequency and sends an ultrasonic wave through the material in its path. When the ultrasonic wave strikes a boundary between materials acoustically different, a portion of the energy is transmitted while the remainder is reflected. The term reflection coefficient, R_f , that gives the relative amplitudes of transmitted and reflected waves can be written as follows for a perfectly bonded interface:

$$R_f = \frac{Z_{s1} - Z_{s2}}{Z_{s1} + Z_{s2}}$$

(5.1)

Where Z_{s1} and Z_{s2} are the acoustic impedances of the boundary materials. For the case of a thin layer $(h << \lambda)$ present between the two bounding materials, **Tattersall** (1973) modelled the situation as a complex, quasi-static spring model in which the layer stiffness, K, is a function of the layer properties.

$$R_f = \frac{(Z_{s1} - Z_{s2}) + i2\pi f_u \left(\dfrac{Z_{s1} Z_{s2}}{K} \right)}{(Z_{s1} + Z_{s2}) + i2\pi f_u \left(\dfrac{Z_{s1} Z_{s2}}{K} \right)}$$

(5.2)

Where, f_u is the frequency of the ultrasonic wave. **Dwyer-Joyce** et al (2003) identified that the layer stiffness for a thin fluid layer would be governed by its thickness and compressibility. For the situation of identical boundary materials $(Z_{s1} = Z_{s2} = Z)$ equation

(5.3) can be used to relate film thickness to reflection coefficient, given the fluid layer acoustic velocity, c_s, and density, ρ.

$$h = \frac{2\rho c_s^2}{\omega Z} \sqrt{\frac{R_f^2}{1 - R_f^2}}$$

(5.3)

The crystals used are standard ultrasonic parking sensors that are bought off the shelf as 0.2 mm thickness and 7 mm diameter discs. These are cut to the required size. Once the crystals are cut they are fixed to the liner with the use of two part strain gauge adhesive ensuring the thickness of adhesive is as uniform as possible and extremely thin (in the order of 0.01-0.02 mm). Wires are then soldered directly to the back of the sensor, which is then encapsulated in Araldite to protect from coolant ingression and to provide mechanical stability, Figure 5.7.
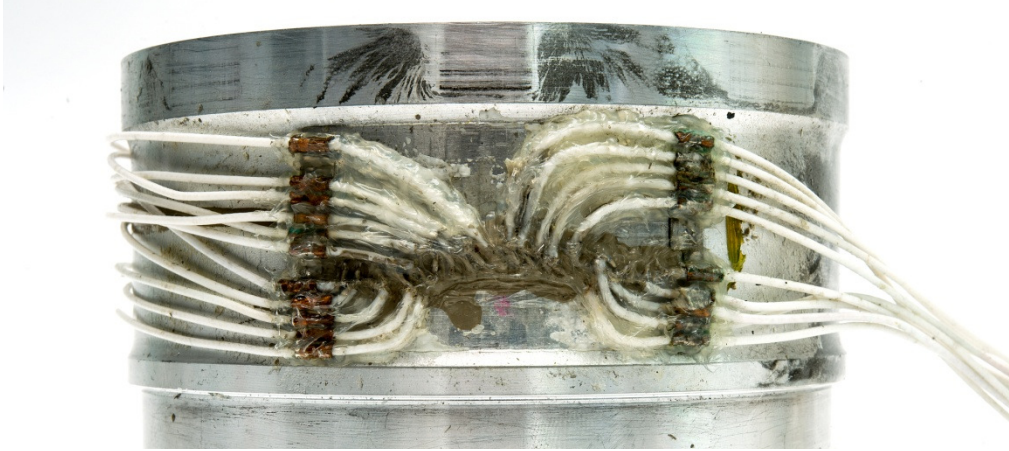
Figure 5.7 - Ultrasonic sensor installation and insulation

In order to measure both a conjunction shape, as well as positional values, an array of sensors is used. The sensors use a modified liner carrier block, featuring a window cut into the side and are sealed appropriately around the wires. This is displayed schematically in Figure 5.9.
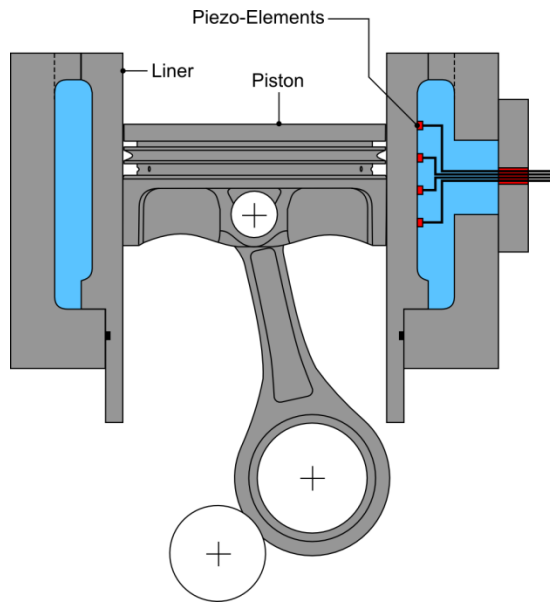

Figure 5.9 - *Schematic view of US sensor installation*

Figure 5.8 - *Installed sensors*

Two different configurations of sensor positioning have been employed. The first uses an axial line of 3 sensors shown, positioned on the liner, (Figure 5.11). The second giving an array of 21 sensors, as shown in Figure 5.10 is referenced to the geometry of the piston skirt. Clearly though, their axial alignment is dependent on the absolute piston position.

Since the instrumentation requires such a significant amount of implementation time, fewer sensors were used on the first test as a demonstration of capability. This first test ensured that the method of sensor adhesion, insulation and the wire conduit routes were durable enough to survive the conditions encountered during engine operation.

In order to ensure accurate measurement, the film thickness needs to be relatively constant over the area of the ultrasonic patch. The industrial standard surface exhibits a profile variation of up to 9 μm over a length of 0.2 mm. If such a rough profile was to be used, a de-convolution algorithm would need to be integrated into the signal processing procedure, adding further sources of error and uncertainty to the results

As such a relatively *smooth* profile is used, as described in section 5.3.2, with surface roughness amplitude of 1.7 μm over a length of 50 μm. Therefore, a surface of this type does not necessitate a convolution correction.
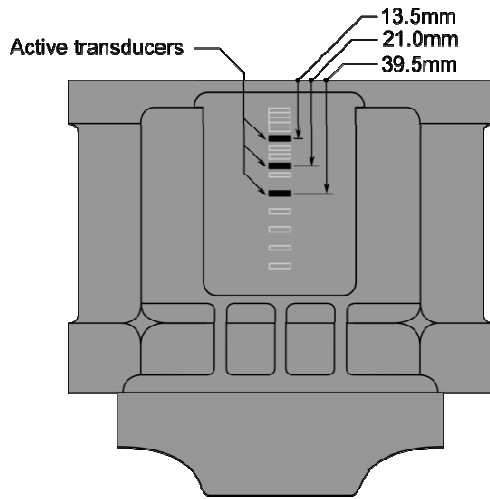

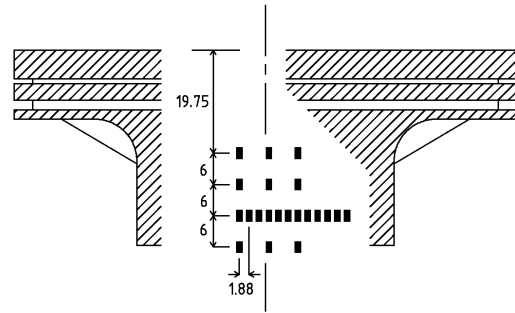*Figure 5.11 - Axial sensor positioning*   *Figure 5.10 - Array of installed sensors*

During testing, ultrasonic pulses at 10MHz were projected towards the liner-skirt interface. The pulses were generated and received using a PC mounted ultrasonic pulse receiver at a rate of 80kPulse/s and were digitised at 100MSamples/s. The reflected pulses were windowed and stored in a hard disk drive with a measure of crank position obtained from the crank encoder signal. A remotely operated multiplexer was used to switch between the active elements. Each element was pulsed for a period of 2s before switching to the next. A total of between 70 and 120 engine cycles were captured over the typical engine speeds tested.

The spectral content of the reflected pulses was extracted using the Fast Fourier Transform (FFT) and reflection coefficient obtained by normalising the measured spectral content with that from a reference pulse. The term reference pulse refers to the condition of total internal reflection of the ultrasound pulse. This essentially occurs when a gaseous interface is present at the liner surface. The reference condition was obtained during periods when the piston was positioned away from the location of the sensor. By continually updating the reference, temperature induced transducer drifts could be eliminated. The measured reflection coefficient was then used to calculate film thickness according to equation (5.3).The results

compared (shown in chapter 6 and 7) are in terms of mean film thickness and a calculated standard deviation for each measurement from the 70-120 measurements recorded.

5.5.5   Oil film temperature

The viscosity of engine oil decreases exponentially with increasing temperature, equation (3.49). Therefore, the operational temperature as an input to the lubrication model is critical to the overall accuracy and validity of the predictions. In addition to the lubrication models, the ultrasonic system relies on knowledge of the speed of sound in all substrates so that the time of flight and wave distortion can be calculated. The speed of sound in engine oil varies significantly with a change in the lubricant density; therefore, knowledge of temperature is required for the oil within the conjunction.

Actual conjunction oil temperature measurement is difficult to be conducted and as such it has not been directly performed here. General measurement of operational temperatures is an already well developed area of research, as such there are a variety of methods available. Most commonly temperature sensors, either thermocouples or thermistors are sealed into drilled cavities allowing for the recording of bulk temperatures close to the critical interfaces. Transferring the signal from these sensors out is a far more demanding task.

For the liner a series of thermocouples were embedded in 0.8 mm from the internal surface and wired out using the modified liner carrier block. A total of 7 were installed and positioned as shown in Figure 5.12 and Figure 5.13.

Figure 5.13 - Thermocouple positions

Figure 5.12 - Installed thermocouples

These sensors are sampled throughout the engine running and allow the position of steady state to be identified once each of the recorded measurements shows a flattened trend. This position can be *mapped* to the other engine operating conditions (speed, load, oil & water tempreature) and used as a reference point for other comparable tests. Unfortunately due to the space requirements needed for instrumentation and conduit routing this cannot be recorded simultaneously with ultrasonic film thickness measurements.

Clearly the conjunction tempreature could be a function of the two adjoining surfaces. Aquisition of the piston tempreature profile is a much more difficult task due to the speeds and accelerations seen by the piston throughout operation. It can be achieved by direct wiring with the use of a grasshopper linkage (**Priest**, (2006)) or hard wired along the connecting rod with an articulating junction (**Ladommatos**, (2005)). Methods employing the use of telemetry, on board piston storage and intermittent electromagnetic transfer have all been employed previously with varying levels of success.

A crucial part of the design of a sensory system is the effect it has on the operation of the original configuration. Bulky sensory equipment may influence the oil flow from the cooling jets, or the surfaces to which the sensors are bonded to affect the heat transfer co-efficient. Any increase in mass will have an effect on the operational dynamics of the system and as such should be kept to an absolute minimum.

Thermally reactive paints have been employed in a various high temperature applications, such as turbine blades and brake callipers. Cases where this method has been successful are generally where a gentle surrounding environment is present. Factors including hydrocarbon content and high speed fluid impact are detrimental to the operation and survival of the paint. Paints do have the advantage of being relatively non-intrusive; they have a small effect on the heat surface, heat transfer co-efficient and do not disturb the regular oil flow to the surface. Accurate calibration is achievable over 10 minute intervals in controlled temperatures. This stable state is not apparent in the piston due to the periodic quenching of the crown underside from the oil jet. Thus, any results are time averaged over the controlled period.

The averaged operational temperature can also be obtained from the residual hardness of the bulk material. This looks at the hardness at various points on a dissected piston that has been subjected to 20+ hours of continuous use. This can be cross calibrated against the oven controlled test pieces to give an average operational temperature over the cycle. This is

widely performed throughout industry; recently it has been documented by **Howell-Smith** (2011). Unfortunately the design, manufacture and commissioning of a system capable of accurately and reliably recording the transient three dimensional temperature profile of the piston is beyond the realm of this project.

5.6 Test results

5.6.1   Controlled boundary conditions

As discussed and already illustrated in this chapter it is not possible to perform a single test to record each of the parameters required, as such a number of benchmark tests have been performed. The most fragile and time consuming piece of instrumentation to setup is by far the ultrasonic sensors. Two data sets have been selected from these results to ensure that the boundary conditions are consistent throughout with each of the pairs of readings summarised in Table 5.2 (load and thermal conditions are presented).

Table 5.2 - Test speed and temperature set points

Speed	**4250**	**6250**	**rpm**
Throttle position	90	90	*%*
Top hose water temp	70	80	^{o}C
Bulk oil temp	104	110	^{o}C

5.6.2   Speed and pressure

Using the crank based encoder and the in-cylinder pressure transducer as described in section 5.5.2 and 5.5.3 enables simultaneous pressure and speed to be recorded with respect to crank angle. Figure 5.14 and Figure 5.15 show the recorded pressures for the boundary conditions stipulated in Table 5.2 and at two respective speeds.
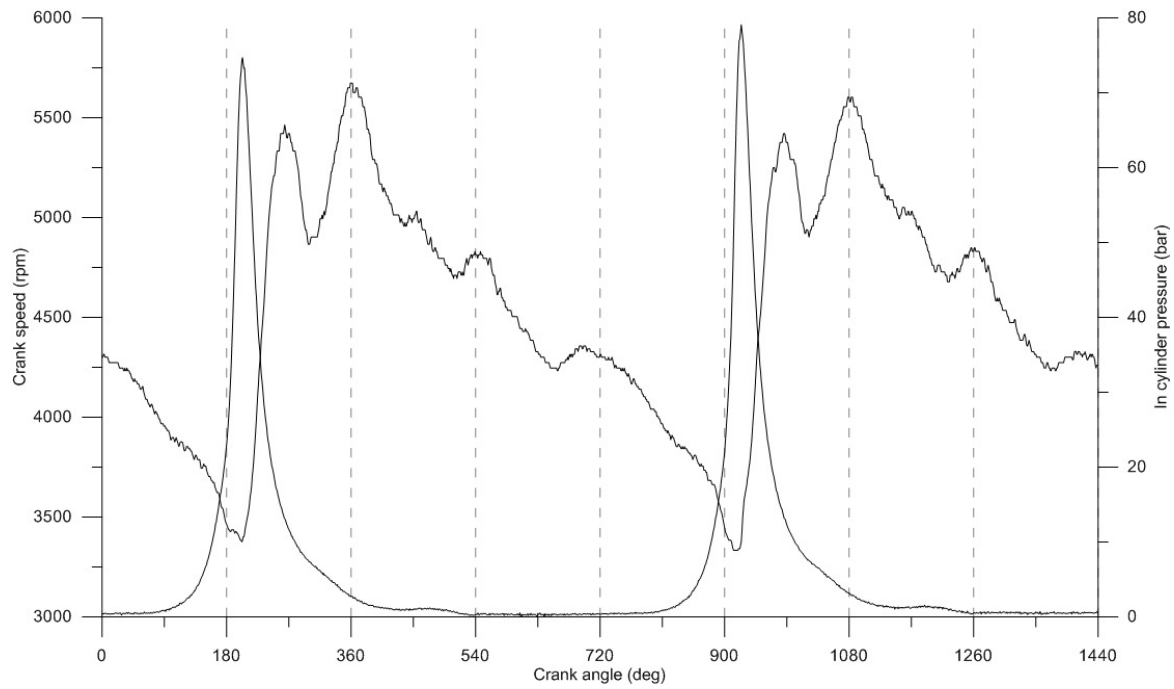
Figure 5.14 - 4250rpm, 90% throttle, cranks speed and pressure plot
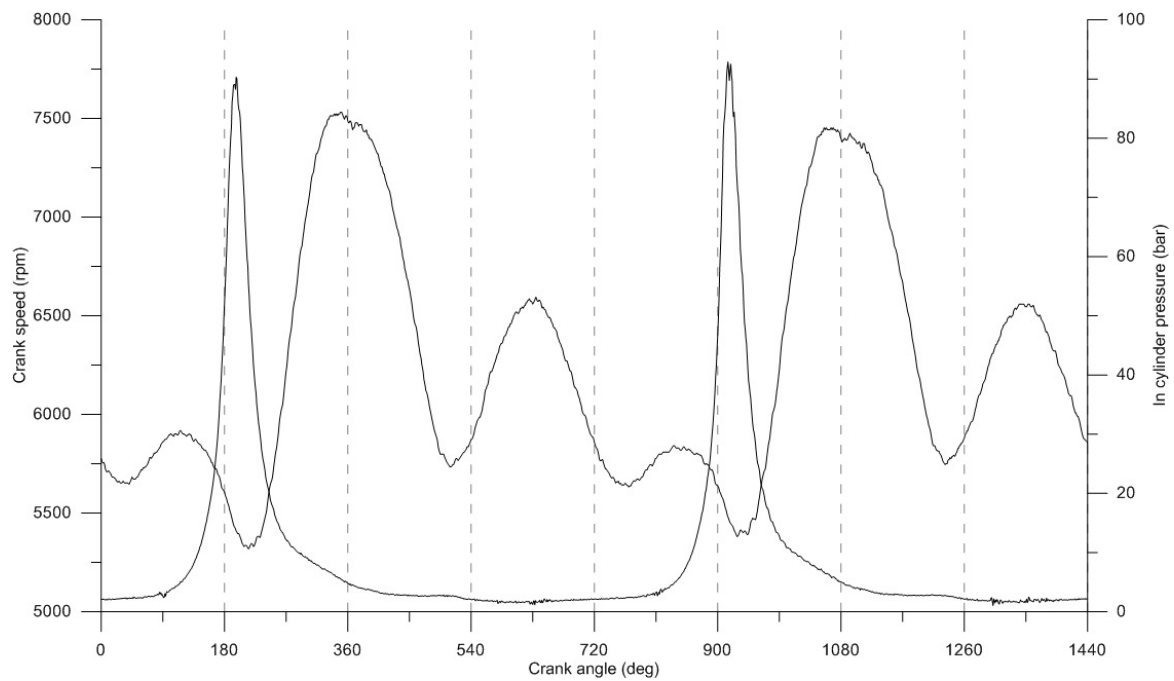

Figure 5.15 - 6250rpm, 90% Throttle, crank speed and pressure plot

As would be expected from a single cylinder engine with a relatively small flywheel, its speed varies dramatically throughout the cycle and hence alters the piston's primary motion from the nominal speed cases. This phenomenon is discussed and described further in chapter 7.

5.6.3   Liner temperature

Using the liner with thermocouples arranged as shown in section 5.5.5 for the two conditions described, the positional temperatures were measured and recorded. To ensure they were at steady state, transient observations were made to ensure that the variation was sufficiently small enough to be considered stable. This sample plot for the case of the engine speed of 4250 rpm can be observed in Figure 5.16.
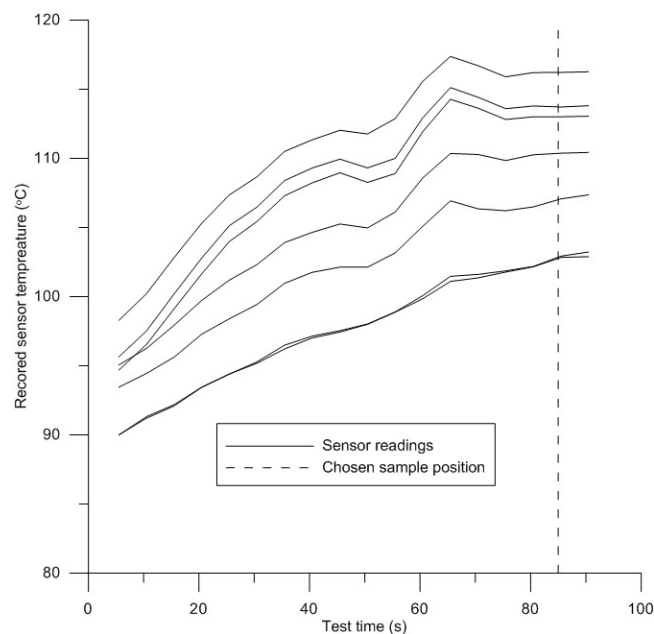
Figure 5.16 - Liner warm up and steady state identification

After 85s at the fixed load and speed, with stabilised coolant tempreatures, each of the sensors had achieved stability at the prescribed load set point, therefore these were used as the prescribed axial temperatures. Figure 5.17 shows the resulting temperature profile recorded for the two load set points. As expected, the higher load speed case exhibiting a higher water temperature during operation sees a higher average liner wall temperature.
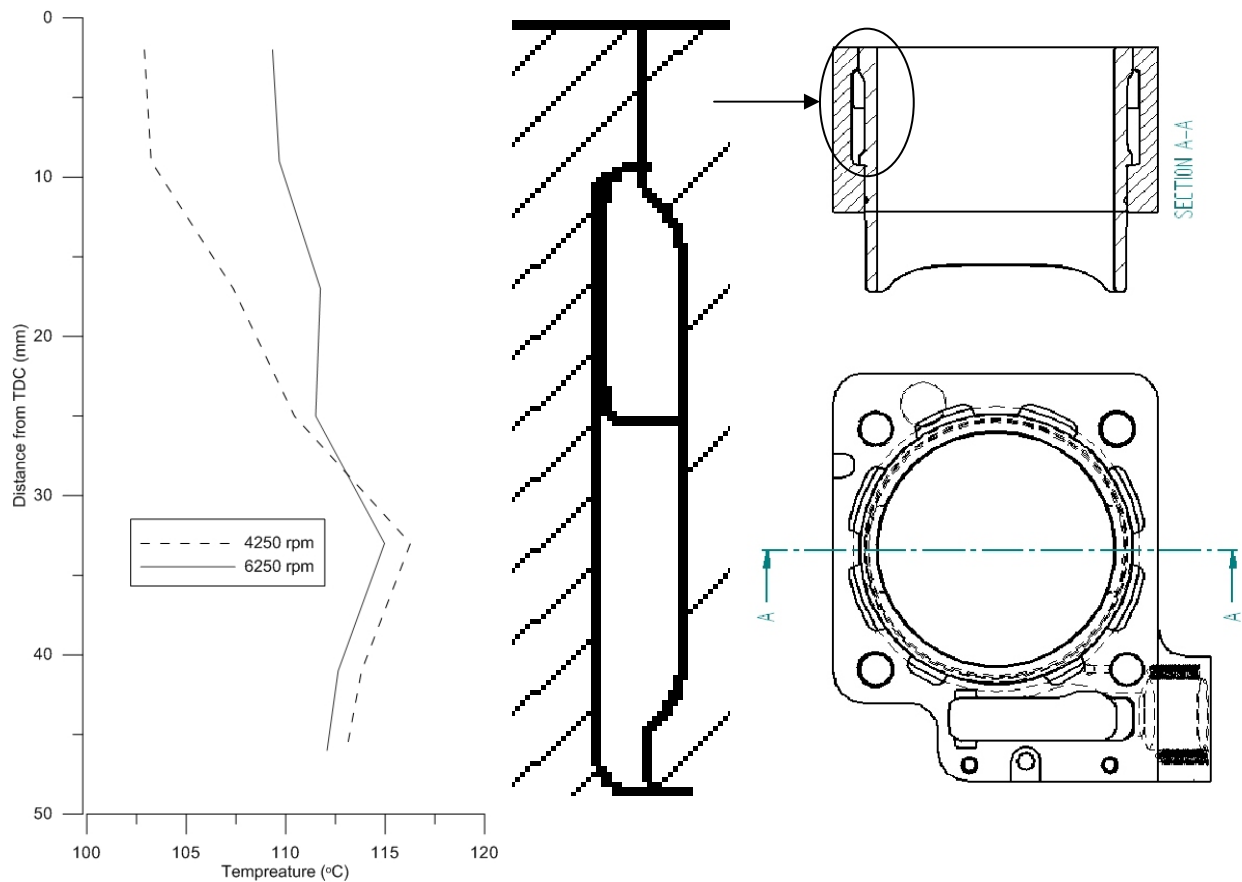
Figure 5.17 - Steady state liner temperature profiles

The profile observed contradicts the normal assumption of temperature reduction moving down from TDC, the simple logic being the uppermost sections of the liner is in contact with the hot combustion gasses for a longer period of time. The use of the new wet liner and modified carrier block to facilitate the required wiring alters the coolant water flow and thus the thermal profile. The current cooling loop within the test cell is controlled to a low flow rate high temperature differential, as opposed to a higher flow rate and lower temperature differential more commonly employed. Unfortunately the flow and differential used was necessitated by the limited variability of the test cell services. The coolant water enters through the supply at the bottom of the head and exits at the top. With the modified liner carrier used the top of the liner has a much greater contact area with the coolant water than the OEM cylinder barrel (shown in Figure 5.2). As such the effective cooling is greater in the

case of the modified liner and carrier. The results obtained are representative for the temperature of the conjunction from which Ultrasonic measurements are performed. The limited axial distribution of these yields an incomplete data set so its use in section 4.3.10 for the liner thermal expansion is not possible. As discussed also discussed in section 4.3.10 the mean temperature data provided here is used to derive a uniform expansion for the calculation of the *lin* array within the formation of film thickness equations.

5.6.4   Lubricant film thickness

By pulsing the 21 sensors sequentially as described in section 5.5.4 the film thickness values and shape over the conjunctional area can be measured during the combustion stroke. The values are obtained on the thrust side for crank angles of approximately 23° and 65° ATDC. This is limited due to the static positioning of the sensors. The hardware used limits the measurement range up to the value of approximately 20µm, which is also the approximate limit of a realistic fluid film formation within the conjunction. Due to the uncertainty of the temperature of the lubricant in the conjunction the mean average of the liner temperatures recorded in section 5.6.3 is used to calculate the lubricant density and thus the speed of sound within it. The detailed result comparison of film thickness measurement with prediction is discussed and shown in chapters 6 and 7. Figure 5.18 shows the "sweep" of the positional values returned by the denser row of circumferential sensors as the piston skirt traverses past them. It shows the positions at which the minimum film thickness values are recorded. These correlate approximately with the sections of increased structural stiffness on the skirt. It is worth noting that this shape is as the result of a compounded number of factors; as time and crank angle alter during measurements, thus the contact load, piston tilt, relative line stiffness and deflection do also as detailed throughout chapter 4 and later shown in chapters 6 and 7.
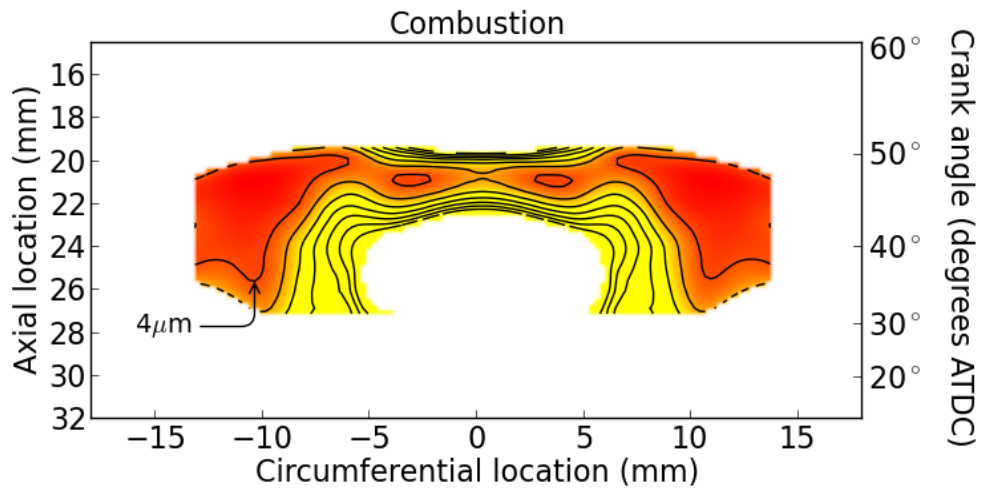
Figure 5.18 - Sensor readings through the combustion stroke as piston passes

5.7 Summary

This chapter has detailed the methods of data acquisition and the experimental setup used throughout the testing runs. It is crucial that the input boundary conditions to the numerical predictions have adequate precision so as to make an accurate and valid comparison. It is also equally crucial that any predictions made within the numerical routines are adequately validated. In order to achieve this, a novel method developed by partners in Sheffield University as part of the collaborative Encyclopaedic project has been outlined and applied here. The results of this experimental work are compared to the numerical analysis in great detail in chapter 6 and 7.

Chapter 6.
Quasi static approach

6.1 Introduction

This chapter presents the simplified analysis of the skirt liner conjunction without the complex tilting motion of the piston or the flexibility of the liner. A number of pertinent positions are simulated using a simple load balance. The results from which are compared with a ultrasonic film thickness measurements for two specific positions. For a fixed speed, variable load data set the contact conditions are analysed and the contact condition, Iso-viscous elastic, is identified.

Chapter 4 detailed in-depth the lubrication model and the calculation of both the primary and secondary motions of the piston. Numerous researchers have shown the application of single position (quasi-static analysis at a given crank angle) calculations, including **McClure** (2009), **Balakrishnan** (2002) and **Offner** (2000). Quasi-static analysis can quickly provide an approximate description of the contact using boundary conditions derived from kinematic relationships. Clearly, the use of such boundary conditions limits the full application of the Reynolds equation (under transient conditions), which includes the effect of squeeze film term (lubricant time history). In areas where significant relative sliding motion is present the Couette flow term within Reynolds equation is dominant (i.e. the lubricant entraining motion). As this is known and can be measured from the derived primary motion, a quasi-static analysis can be performed where modest sliding speeds are predicted. This generally limits the analysis to all areas aside from the dead centres, where it has been shown that the squeeze term dominates as the pistons speed diminishes. However, a quasi-static analysis can provide a series of snapshots in terms of approximated contact conditions and indicative conjunctional behaviour. Thus, it represents a computationally efficient approach to the analysis of the lubricated piston skirt – liner conjunction. In the cases presented here only the piston skirt stiffness is modelled so as to illustrate the effects of the 3D stiffness variation observed on the skirt surface.

6.2 Simulation conditions

In this chapter a number of positions are considered and compared, representing some of the harshest conditions in terms of film thickness and load. Additional positions are evaluated that allow for direct comparison with measured film thickness values. The results in terms of conjunction load, pressures and film thickness are of interest in the development and improvement of the contact conditions. Chapter 5 detailed the acquisition of the significant operation conditions; using these, the following sets of boundary conditions are formed. The boundary conditions required and their use is detailed in Table 6.1.

Table 6.1 - Required input boundary conditions

Boundary condition	Use
Cylinder pressure	Crown bending and resulting deformation
Net lateral force	Defines load carrying demand
Conjunction temperature	Lubricant viscosity and density
Piston acceleration	Primary inertial deformation

For the case of the engine speed of 6250rpm with a fixed throttle position of 90% the in-cylinder pressure and instantaneous crank speed were recorded, as detailed in section 5.5. The raw data for the 4 strokes are presented in Figure 6.1. The cyclic repeatability of the measurements is demonstrated in this figure, showing two complete 4-stroke cycles.
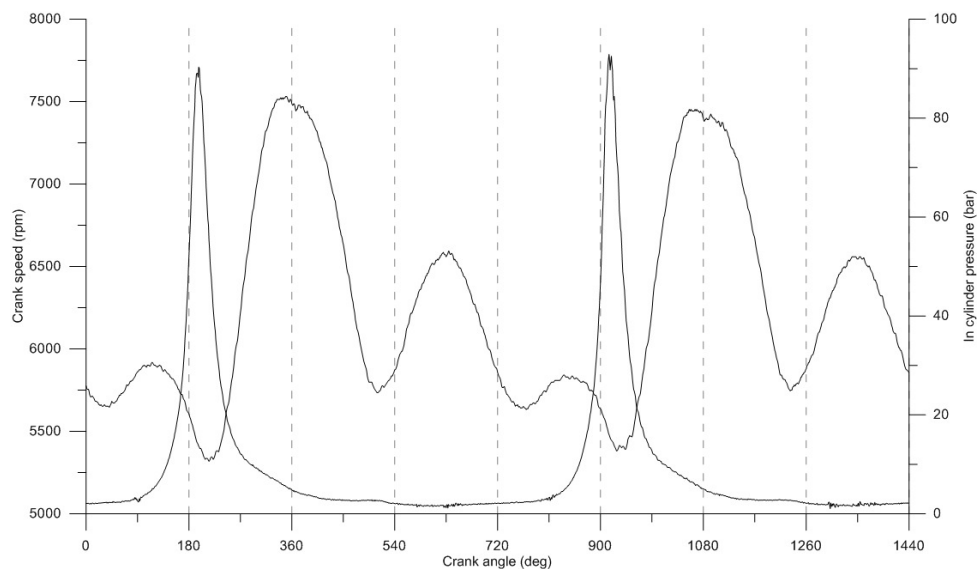
Figure 6.1 - Recorded engine speed and in-cylinder pressure (6250 rpm)

Using the derivations of primary motion from section 3.2 (equations (3.13) and (3.18)) the instantaneous piston sliding speed and acceleration can be derived for the variable speed cycle. The instantaneous lateral force can be derived using equation (6.1).

$$Fs = \left((P_{cy} \pi r_p^{\,2}) + (m_g + m_p) \ddot{x}_p \right) \tan \phi \qquad (6.1)$$

Using these two sets of equations, Figure 6.2 is generated, showing the instantaneous sliding speed plotted with the net side skirt side force. For clarity, a positive value for side force indicates loading on the thrust side. A positive value for sliding speed is observed in the downward strokes.
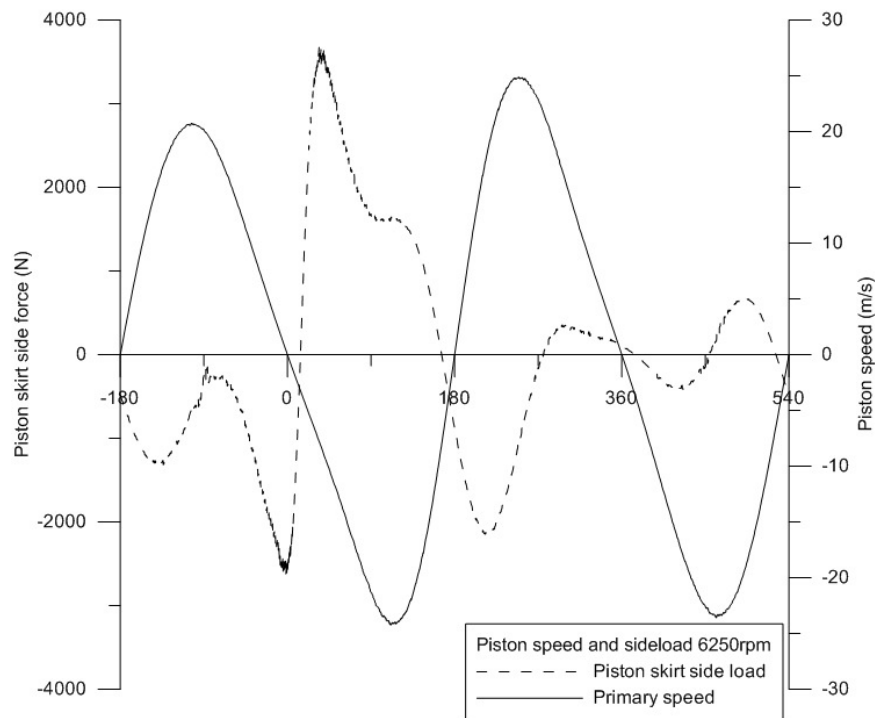
Figure 6.2 - Instantaneous side load and piston sliding speed

Considering the loaded thrust side during the combustion stroke a series of pertinent positions are selected for quasi-static analysis (Maximum combustion pressure, side load and two positions where measure film data is available). These positions are detailed in Table 6.2. The side force and primary speed are from Figure 6.2, the acceleration is calculated using

equation (3.18) and the in cylinder pressure is from the experimental data presented in Figure 6.1.

Table 6.2 - Selected simulation positions

Angle (^{o})	Force (N)	Speed (m/s)	Acceleration (m/s^2)	Cylinder Pressure (bar)
17	926.17	-3.92	-8003.67	90.33
34	3674.70	-7.76	-7828.64	58.35
41	3578.62	-9.40	-7828.64	44.31
53	3015.87	-12.16	-7530.29	28.81

The starting shape of the piston, subjected to gross thermal distortion is fixed throughout the analysis using the thermal expansion detailed in section 4.3.9. The lubricant temperature within the conjunction is fixed at 120°C. This is calculated using a mean liner temperature derived from the measurements shown in Figure 5.17.

6.3 Simulation results

6.3.1   At 17° ATDC – Maximum combustion pressure

The converged lubricant pressure profile for this position is shown in Figure 6.3.
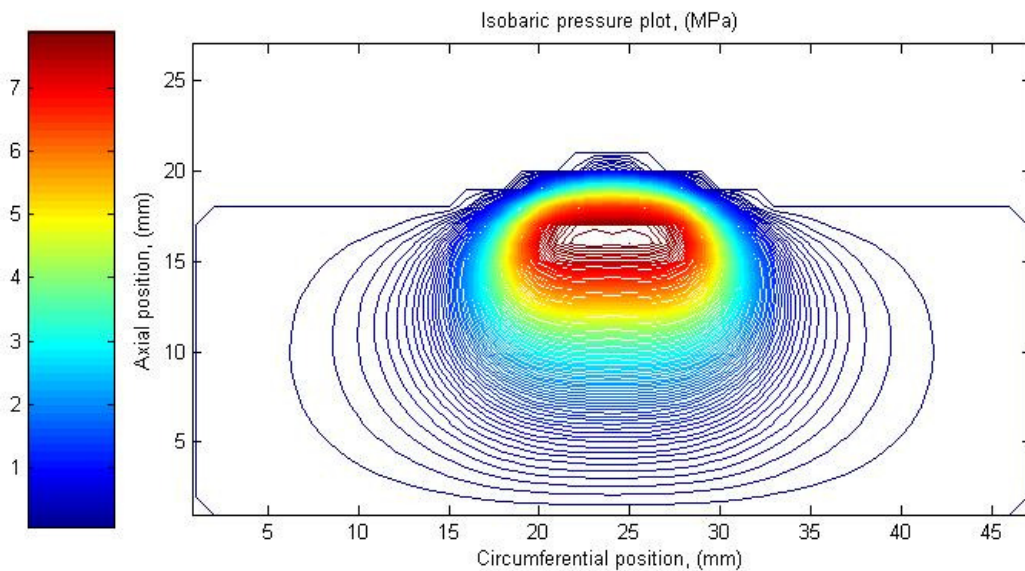
Figure 6.3 - Pressure profile for 17° ATDC in the combustion stroke for 6250rpm

This result exhibits a peak pressure of 7.95MPa, centred at 17mm from the skirt base. The overall contact load is relatively small at 926N, but with a reasonable sliding speed of 4m/s, ensuring the use of only the Couette flow term being valid. The pressure distribution is the highest around the central axis of the skirt, thus indicating little occurring deflection that would induce a greater circumferential conformability, spreading the load outwards. This observation is backed by the plot of film thickness displayed in Figure 6.4.
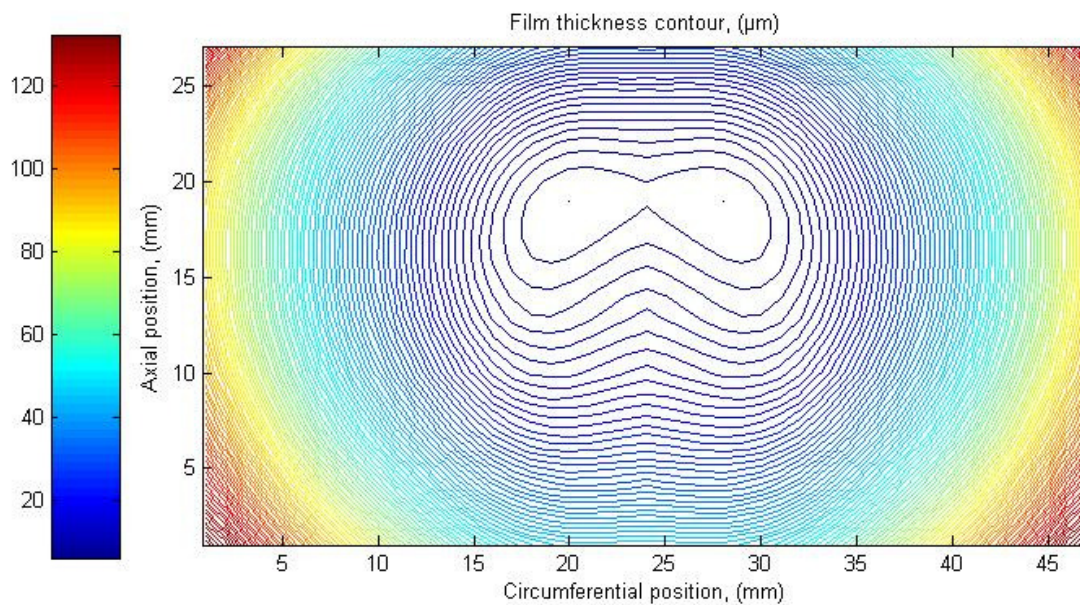
Figure 6.4 - Film thickness profile for 17° ATDC in the combustion stroke for 6250rpm

The in-cylinder pressure has its greatest effect on the skirt shape in this position and the mode of deflection observed in Figure 4.7 is at its most exaggerated position. This mode acts to move the position of maximum skirt radius towards the piston crown as the bottom edge of the skirt is forced away from contact with the liner. This effect is the most significant contributor to the shift of maximum radial value upwards toward the exit of the contact at the top of the skirt. This lightly loaded contact produces a minimum film thickness of 5.2µm.

6.3.2 At 34° ATDC – Maximum side load

At 34 ^{o} crank angle position the side force reaches its largest value of 3674N. This results in a peak pressure of 20.7MPa, centred approximately 7mm from the top of the skirt. The pressure profile is displayed in Figure 6.5. This pressure profile indicates a significant circumferential load spreading, when compared with the pressure profile displayed in

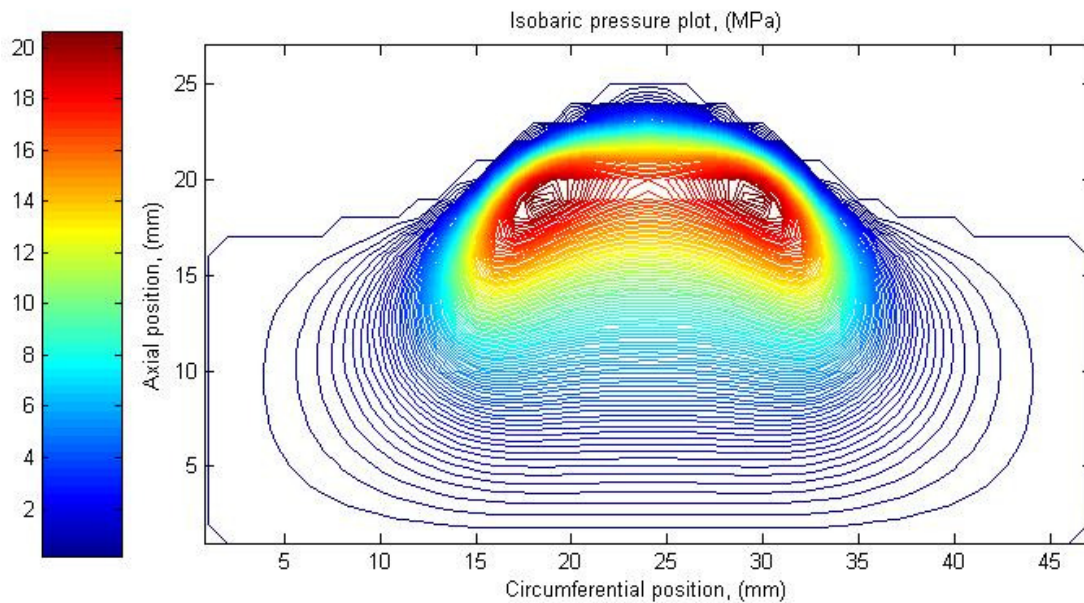Figure *6.3* for the lower loaded case of 17° crank angle position.

Figure 6.5 - Pressure profile for 34° ATDC in the combustion stroke for 6250rpm

The film thickness contour displayed below in Figure 6.6 exhibits a minimum value of 4.1µm. Although the load is significantly higher a proportional decrease is not expected in minimum film thickness as the contact is not wholly hydrodynamic, as discussed later in this chapter.
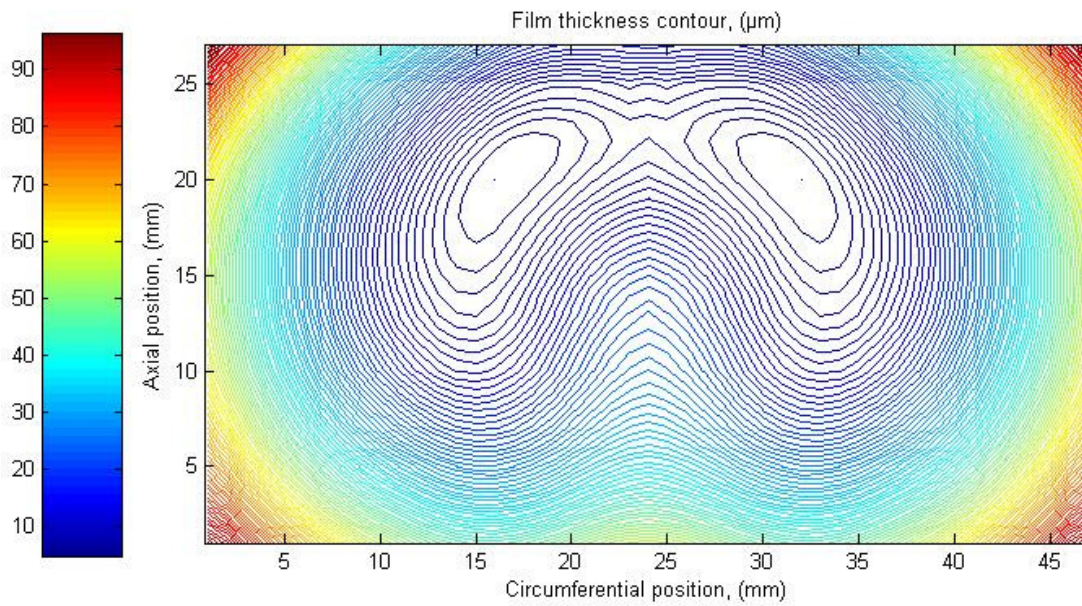
Figure 6.6 - Film thickness profile for 34° ATDC in the combustion stroke for 6250rpm

6.3.3   At 41° ATDC

At 41°ATDC in the combustion stroke there is a reduced contact load of 3578N and a modest sliding speed of 9.4m/s. Although this position does not represent an extreme condition it does represent the highest loaded position for which lubricant film thickness data has been recorded.

As expected, the generated pressures are still significant, reaching a peak of 18.8MPa. The shape of the pressure profile is similar to the previous case at 34° crank angle, but it is centred slightly closer to the bottom edge of the piston skirt because of the reduced effect of the in-cylinder induced deflections and the lower overall contact load.
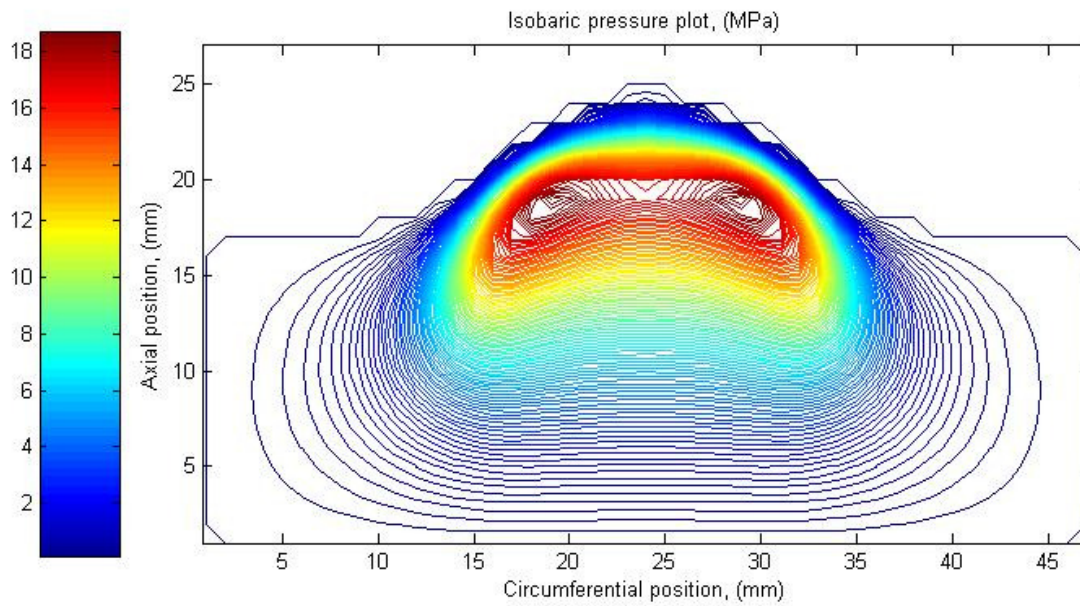
Figure 6.7 - Pressure profile for 41° ATDC in the combustion stroke for 6250rpm

The minimum film is only slightly increased from the previous step with a value of 5.0 µm. This slight increase is as the result of two mechanisms. The load carrying capacity of the lubricant is improved because of the increased sliding speed and thus a greater resulting pressure magnitude from the Couette term within Reynolds equation. The latter, coupled with the reduced side load results in an increase in the minimum film thickness. The observed 3D shape of the film thickness is not visually any different in terms of operating characteristics than that shown in Figure 6.6 and as such it is not shown.

Using the rows of sensors as arranged in Figure 5.10 the following circumferential cut profiles display a comparison between the recorded and predicted values of film thickness for this position.
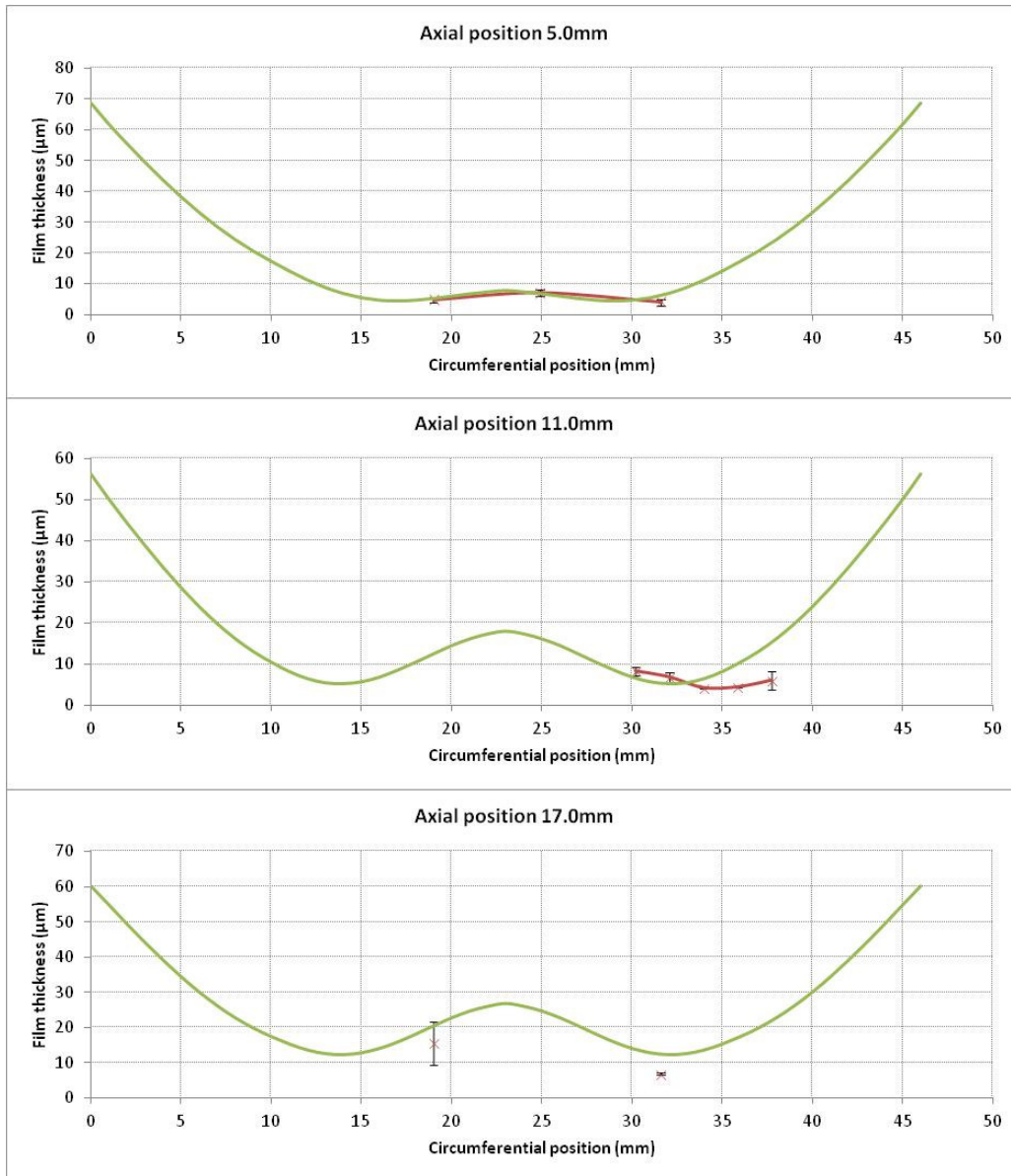
Figure 6.8 - Film thickness comparison for 41° ATDC

At 5.0 mm from the top of the skirt the comparison shows a very good agreement in terms of both the film thickness and the observed film shape. Moving down the skirt where the row of 8 sensors monitors the conjunction, this agreement is good in terms of film thickness, but the positions of greatest conformability are at a different circumferential position. Finally, the 2 sensors monitoring the lowest position of the skirt show relatively good agreement in terms of shape though the film thickness is smaller for the case of the recorded measurements by approximately 4µm. The centre sensor reading of the 3 sensors used is missing, most likely

due to the magnitude of the film measured being beyond the range of the ultrasonic measurement equipment.

6.3.4   At 53$^\text{o}$ ATDC

The final considered position is at 53$^\text{o}$ ATDC. This measurement is included showing a different set of observed measurement positions. The load seen at this position is 3015N, coupled with an increased piston speed of 12.2m/s. As expected the minimum film thickness has increased for this position, now predicting a value of 7.3µm.
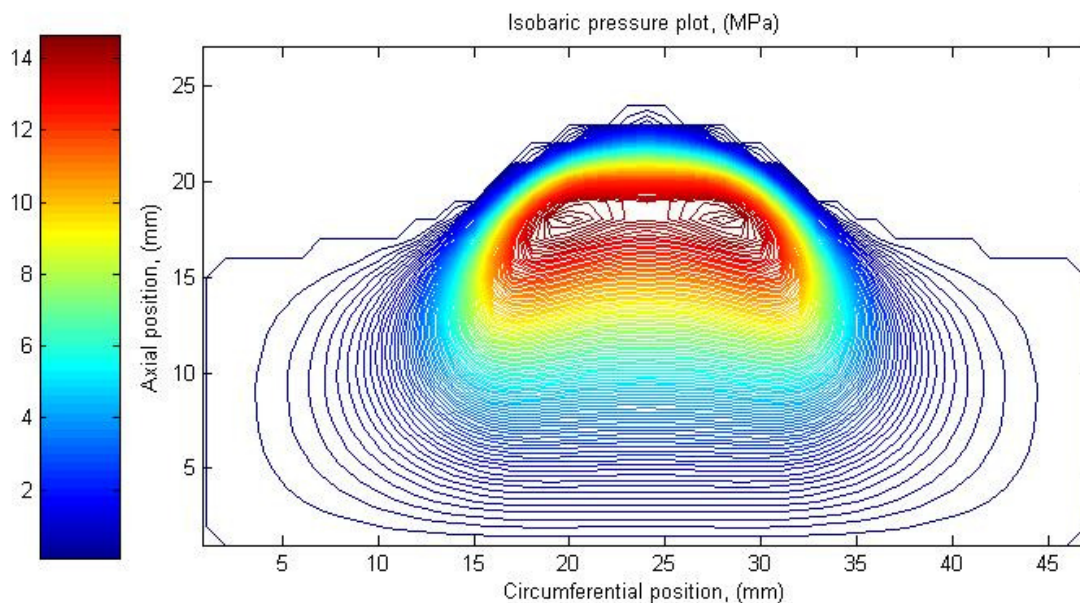
Figure 6.9 - Pressure profile for 53$^\text{o}$ ATDC in the combustion stroke for 6250rpm

Between this position and the previously predicted position at 41$^\text{o}$ ATDC there is a noticeable alteration on both pressure domain shape and position. The circumferential spread of the profile is reduced and it is centred closer to the bottom of the skirt. These two phenomena are attributable to the previously mentioned mechanism of film shape alteration, thought to be as the result of the combined effect of reduced bending through crown loading and the overall reduction of conjunction load.

In a similar manner to the results presented in Figure 6.8 the comparison of film thickness measurements and predictions are shown for a series of circumferential lines in Figure 6.10.
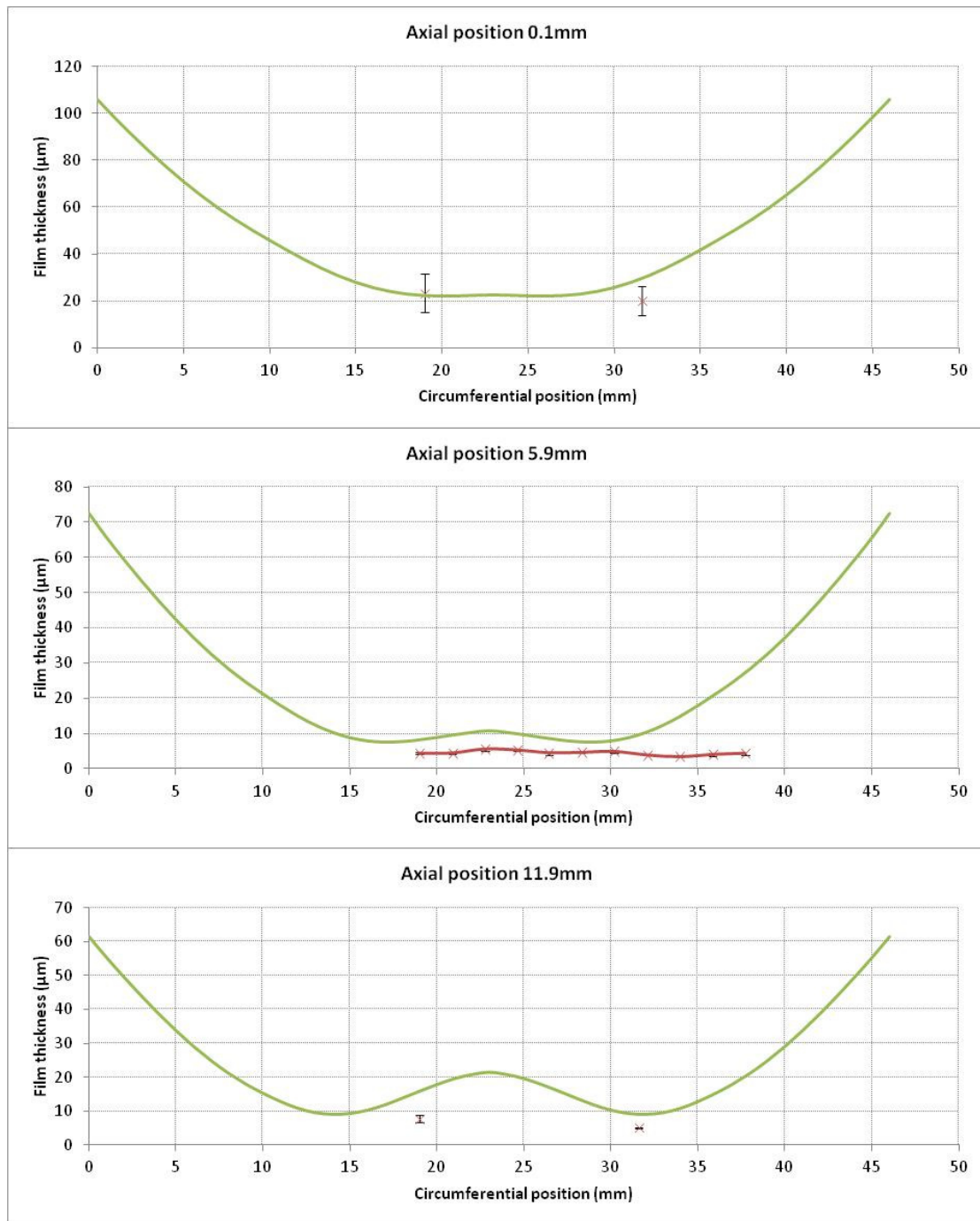
Figure 6.10 - Pressure profile for 53° ATDC in the combustion stroke for 6250rpm

The observed positions of film thickness measurements by the three sets of sensors have moved towards the top of the piston skirt as the piston moves in the down stroke. The very top of the skirt is observed and shows good agreement in terms of magnitude and shape.

Little circumferential distortion is observed at this axial position. Moving down the conjunction where the row of 8 sensors observes the conjunction there is a discrepancy in terms of both magnitude and distribution between the predicted and measured results. This is also observed as one progresses toward the lowest measured position. This discrepancy could be down to a number of variables not considered within the quasi-static analysis, such as any piston tilt angle induced by its secondary dynamics and the relative change in shape of the liner through its mechanical distortion.

6.4 Components of deflection

Considering only the components of skirt distortion in the analysis allows for the isolation of their effects and identification of phenomena attributable to each case. Through this chapter and up to this point the effects of normal distortion and in-cylinder pressure induced distortions have been discussed qualitatively, but with little quantitative comparison. For the predicted case at 41° ATDC the three mechanical distortion components are compared.

The normal deflection resulting from the generated conjunctional pressure distribution is presented in Figure 6.11. This profile illustrates the increased stiffness around the internal piston bracing and towards its crown. It is this mechanism that aids the improvement in circumferential conformability, as well as an increase in the entrainment wedge to the contact.
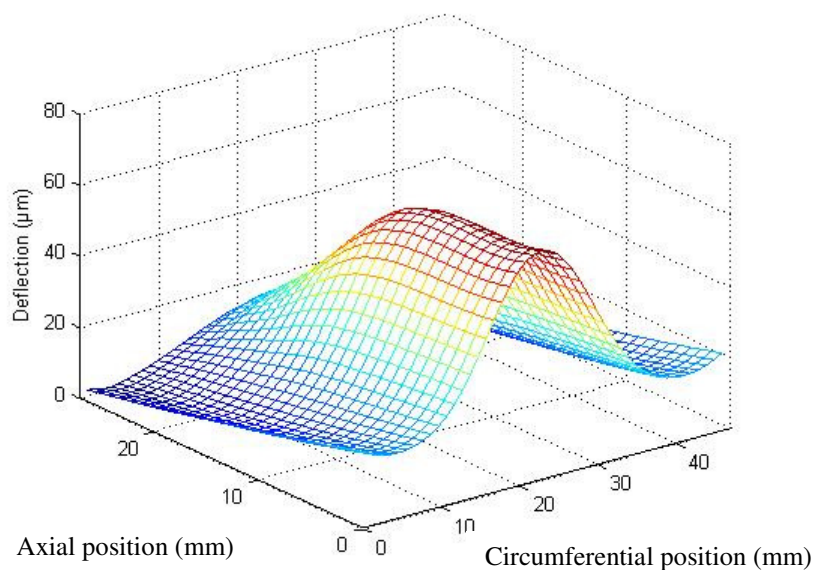

Figure 6.11 - Conjunction pressure induced skirt deformations

The in-cylinder induced skirt deflection (presented in Figure 6.12) always presents the same shape, its scaled magnitude is altered by the magnitude of the in-cylinder pressure, as defined by equation (4.15). At this position the crown pressure is moderate at only 44bar. This produces a maximum value of deflection at the bottom of the skirt of 15.7µm. For the highest pressure case as simulated at 17° ATDC, this maximum deflection would be more significant at 32µm.
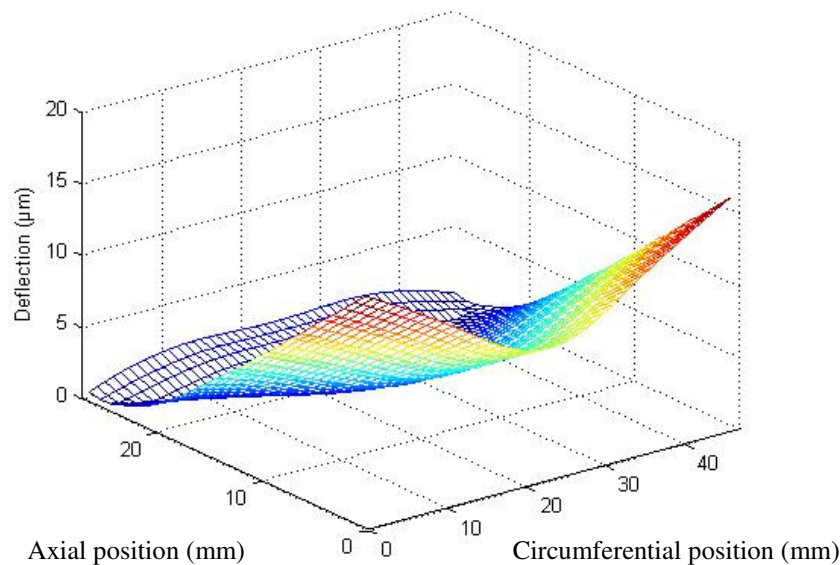

Figure 6.12 - In-cylinder pressure induced skirt deformations

The final component of mechanical distortion is originated from the inertial loading. This contribution is presented in Figure 6.13. For this specific position its contribution is an order of magnitude less that the contribution of the in-cylinder pressure induced deformation. Even at its greatest value the deflection observed at the bottom of the skirt is only 6µm.

These three examples have demonstrated the differing effect of the mechanical distortions, the significant factor in controlling the circumferential conformability produced by the deflection resulting from the normal load. This combined effect of normal and in-cylinder pressure induced deflections is greatest when a significant load is applied. The magnitude of the deflections from these two mechanisms is more significant by an order of magnitude than that due to inertial-induced piston bending at high speed. Inertia has a more significant effect on the profile shape at reversals. Approaching BDC will act to improve the inlet wedge

shape, but has a detrimental effect when the direction of motion reverses. At TDC the sign of the acceleration switches, approaching TDC will have positive effect on the entrance radius but detrimental as the direction switches and the piston progresses down the bore away from TDC. It should be noted, particularly in the combustion stroke as one moves away from TDC the detrimental effect of inertia is counteracted by the more significant effect of the in-cylinder pressure. Thus, it can be concluded that even though the effect of inertial deformation is small it is generally not considered detrimental to the operation of the liner-skirt conjunction in this modularised approach.
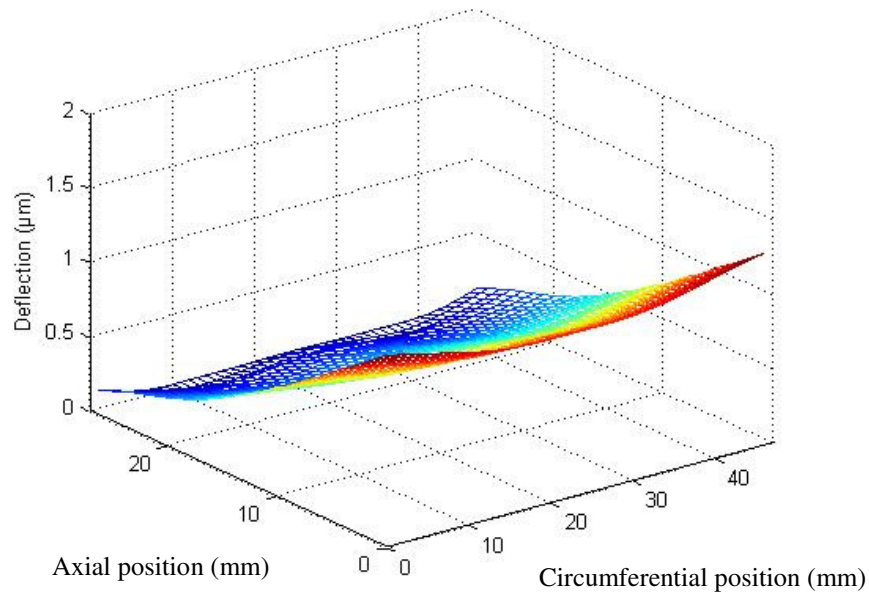
Figure 6.13 - Inertial force induced skirt deformation

6.5 Contact classification

The use of a quasi static analysis allows for the analysis of the direct effect of load on the contact conditions and the isolated effect of contact stiffness on the resulting lubrication of the contact. To do this the characteristics of both purely hydrodynamic lubrication and classical elastohydrodynamic contacts are used.

A relationship between the minimum film thickness (h), contact stiffness (k) and overall load (W) may be assumed in the form: where k represents the contact stiffness non-linearity

$$h \propto kW^a \qquad (6.2)$$

By plotting the load against film in a sample case with a sliding speed of 8.0 m/s, the above shape function is observed, as displayed in Figure 6.14. It should be noted that the 'bumps' in the curve presented are due to the changing nodal position of the identified minimum film thickness. These can be removed by interpolation or palliated by a finer grid mesh. Nevertheless, the phenomenon is adequately illustrated.
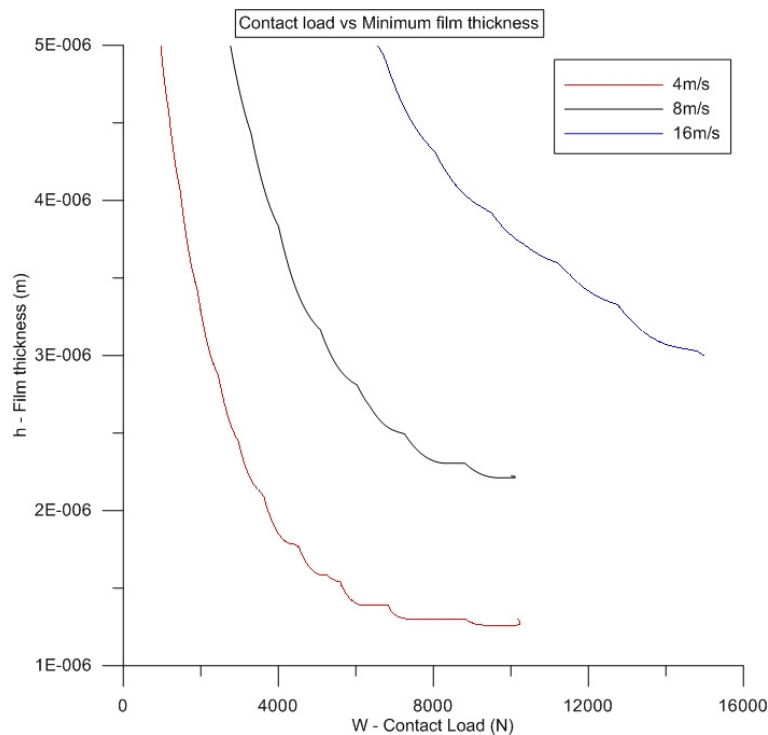
Figure 6.14 - Contact load vs film thickness for a series of fixed speeds

For a hydrodynamic line contact condition equation (6.3) is used to calculate the film thickness (**Gohar and Rahnejat**, (2008)).

$$h = \frac{2bU\eta_0 R}{W} \tag{6.3}$$

Therefore, also considering equation (6.2), one can put the film thickness in the form:

$$h = \frac{2bU\eta_0 R}{W} \propto kW^{-1} \tag{6.4}$$

This shows that the line contact film thickness is inversely proportional to the overall supported load. This proof though is for a counterformal contact. Considering a fully conforming hydrodynamic contact, such as a journal bearing (the other extreme as fully conforming), equation (6.5) describes the formation of the film thickness profile.

$$h = c(1 + \varepsilon \cos \varphi) \tag{6.5}$$

For the position of minimum film thickness $\varphi = \pi$, thus equation (6.6) is formed for the position of minimum film thickness as:

$$h = c(1 - \varepsilon) \tag{6.6}$$

Where ε is defined as the eccentricity ratio. Although a function of a number of parameters, it increases with increasing load and thus a diminishing film is observed. The two examples for the case of conformal and counterformal hydrodynamic contact show that, as expected, the film thickness decreases as load increases in hydrodynamic contacts, almost proportionally. From equation (6.2) with some manipulation;

$$\log h \propto \log k + a \log W \tag{6.7}$$

One can draw the best straight line between $\ln h$ (ordinate) and $\ln W$ (abscissa) using the least square method to show the best linear fit to this (Figure 6.15).
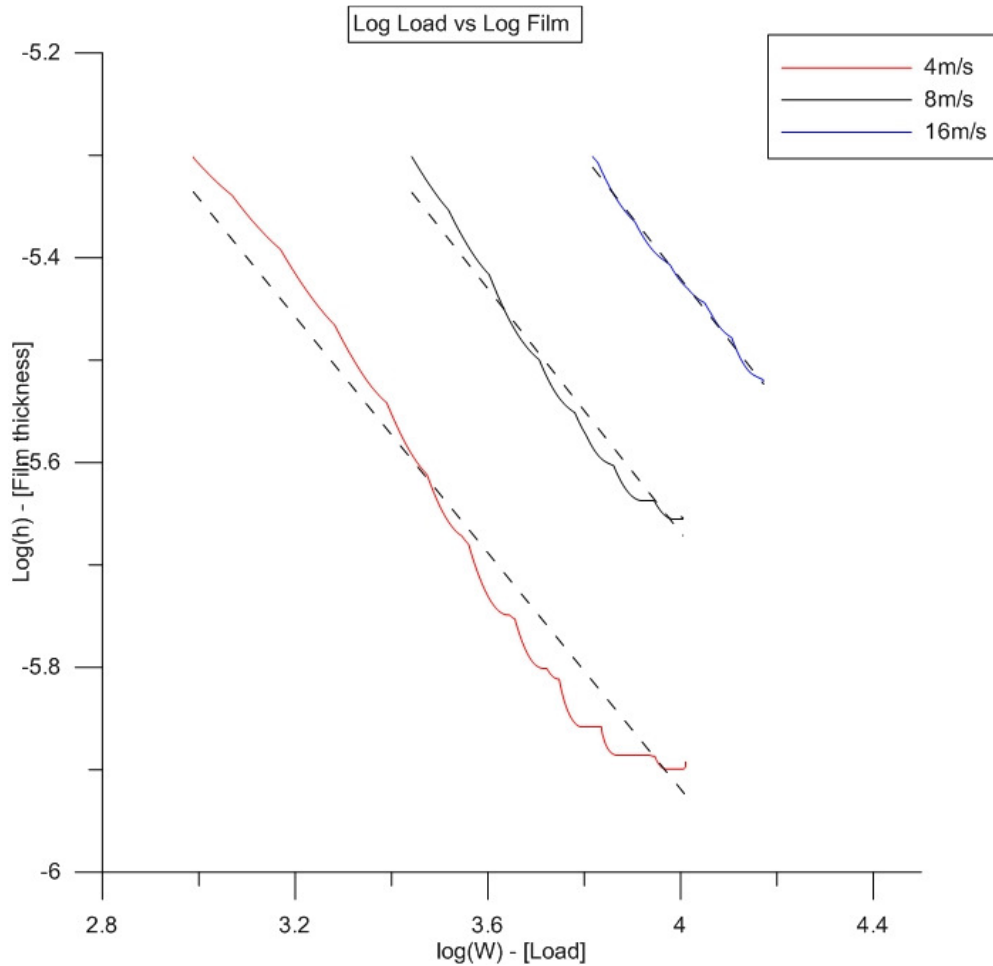

Figure 6.15 - Log Film vs Log Load for the three fixed speeds

The general equation for a straight line is given as:

$$y = mx + C \qquad\qquad (6.8)$$

The linear fit, shown in Figure 6.15 , shows a value of -0.59 for m and -3.29 for C for the central speed case of 8m/s. For the higher and lower speed cases, the value of m varies very slightly (due to the fluctuations observed as the position of minimum film moves between nodes). The intercept, C, differs for each case, since they have a varying contact stiffness due

to the changing film thickness as a function of the lubricant's entraining speed for which a pressure profile is formed.

The slope of these lines is the tangent of the angle that they make with the +ve $\ln W$ axis, which corresponds to the exponent in equation (6.7). The obtuse angle formed with the +ve $\ln W$ axis shows the inverse proportionality of film thickness with load, which is expected of all lubricated contacts to certain extent. For EHL cases, the film is almost insensitive to load. Therefore $a = m = \tan\theta_s$. For a perfect hydrodynamic line contact is should be expected that $a = -1$ in order to maintain the inverse proportionality as predicted by equation (6.4) and (6.6). For EHL contacts where a piezo-viscous elastic condition is satisfied it would be expected that $\ln a = -1$, or for elliptical contacts, $a \approx -\dfrac{1}{12} \rightarrow 0$ **Gohar** and **Rahnejat** (2008), (which shows that the minimum film thickness is insensitive to load, which is one of the key characteristics of an EHL contact. It has been shown that for a soft EHL contact (iso-viscous elastic) that a ranges between approximately -0.3 and -0.2, (**Karaszkiewicz**, (1998)) this is slightly sensitive to load as the pressures within the lubricant are not significant enough to reach the point of lubricant incompressibility. These pressures in a soft contact are often kept small due to the low contact stiffness of the conjunctional bodies. This theory and analysis agrees with the conditions observed in the results shown here with a value of -0.59, thus showing a contact that is operating in an iso-viscous elastic regime of lubrication. This is re-affirmed when one considers the reaction of the lubricant viscosity in terms of the generated pressures. Considering Barus law:

$$\eta = \eta_0 \exp(\alpha p) \qquad (6.9)$$

A typical mean pressure (constrained by the zero pressure isobar) has been calculated to be approximately 4.0Mpa, typical values for α are in the order of $1e^{-8}$, thus the product is of the order of $4.e^{-2}$. When taking the exponential of this product a value ≈ 1, thus the lubricant is classified as iso-viscous.

Since the intercept in the vertical axis is now known using equation (6.8) an approximation for the contact stiffness can be calculated as $C = \ln k$. So k becomes $k = \exp C$. Using equation (6.2) and considering that $k = \dfrac{\partial W}{\partial h}$ yields equation (6.10).

$$K = \frac{1}{a}\left(\frac{1}{k}\right)^{\frac{1}{a}} h^{\left(\frac{1}{a}-1\right)}$$

(6.10)

Using the m value of -0.59 and the C value of -3.29 from the best fit line shown in Figure 6.15 for 8.0 m/s a plot of effective conjunction stiffness vs film thickness can be made. This is shown in Figure 6.16.
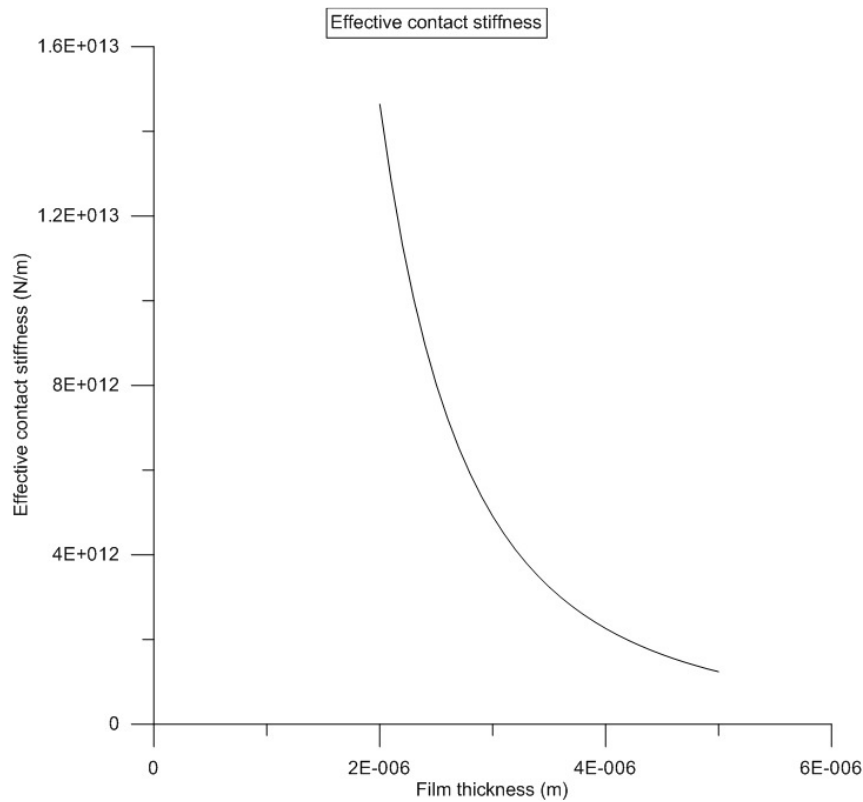
Figure 6.16 - Effective contact stiffness

It can be observed that contact stiffness increases with reduced film thickness. In general the contact stiffness may be viewed as having two components in series; one due to the effective

stiffness of the contiguous surfaces and the other as the result of load carrying capacity of the lubricant film. This serial arrangement leads to an equivalent contact stiffness as the addition of their reciprocals; i.e. $\dfrac{1}{k_e} = \dfrac{1}{k_s} + \dfrac{1}{k_l}$, where the subscripts e, s and l denote "equivalent", "solid" and "lubricant" respectively. Because of the reciprocal relationship, clearly the governing equivalent stiffness tends to be the lower of the two contributions. Therefore, for a light-to-moderately loaded hydrodynamic contact, the dominant stiffness is that of the lubricant (iso-viscous rigid). All highly loaded concentrated contacts, such as in rolling element bearings, meshing gear teeth and cam-follower pairs, the regime of lubrication is often elastohydrodynamic (viscous-elastic). The lubricant is often become an amorphous solid in the contacting region and its behaviour is incompressible. Therefore, the stiffness of the adjacent solid is lower than the lubricant. These conditions almost tend to Hertzian contact mechanics. In all other cases (iso-viscous, elastic), both stiffness contributions; solid surfaces and lubricant contribute to the equivalent stiffness to a certain extent. Figure 6.16 suggests that as the film thickness is reduced the stiffness has increased. For purely hydrodynamic case, this trend would not be seen, as a thicker film has a greater load carrying capacity, thus stiffness. The explanation is that small changes in film thickness tend to increase its density, thus its "degree of amorphous structure". Hence, the stiffness of the solid bodies become gradually more important, leading to iso-viscous elastic conditions. Therefore, an important conclusion of this study is that the thermo-elastic behaviour of in situ piston significantly alters the contact stiffness, which is not included in many analyses such as those of **Knoll and Peeken** (1982)**, Balakrishnan et al** (2005) and others. Those, who have included thermo-elastic deformation, such as **McClure** (2007) and **Bai** (2012) have not included the analysis of effect contact stiffness variation along the piston skirt under lubricated condition.

6.6 Conclusions

This chapter has presented the fundamentals of the skirt –liner conjunction; it has described some of the harshest loading conditions in the combustion cycle. The simplified analysis technique produces realistic results within an acceptable computational time; each of the separate simulations takes approximately two minutes on a typical desktop computer.

The multi-variable 3D motion of the piston assembly and the effect of liner distortion have not been included in the solution technique. Clearly the results thereof are not wholly representative of the real conjunction, but, they do offer a tool for use in the direct analysis of the pistons lubricated response to a series of mechanical loadings.

The analysis of the piston skirts response to load and the resulting derivation of effective conjunction stiffness highlights the tribological operation of the conjunction. It has been shown that the regime of lubrication is iso-viscous elastic, or as commonly referred to it operated by means of *soft EHL.*

Chapter 7.
Transient Tribo-dynamics

7.1 Introduction

This chapter combines the methodologies presented on lubrication and dynamics from Chapter 3, the geometry and flexibility of the bodies from Chapter 4 and the experimental measurements from Chapter 5. This approach results in a transient tribo-dynamic analysis of piston skirt-liner contact subjected to *in situ* thermo-elastic distortion. It also provides experimental validation of the developed analytical and numerical methods in this thesis. Results are compared in terms of dynamic reaction forces, contact pressures, solid body responses and film thickness for a pair of engine operating conditions.

7.2 Principal resulting dynamics

7.2.1   Engine speed of 4250rpm 90% throttle

The input data in terms of engine speed and in-cylinder pressures, obtained and discussed in section 5.6, represent the starting point for the analysis. These are used as input data for the calculation of the primary motion kinematics, also within both the equation of motion (3.31) and as loading for the calculation of piston crown deformation. The raw input data from section 5.6 are shown in Figure 7.1 for the engine speed of 4250rpm.
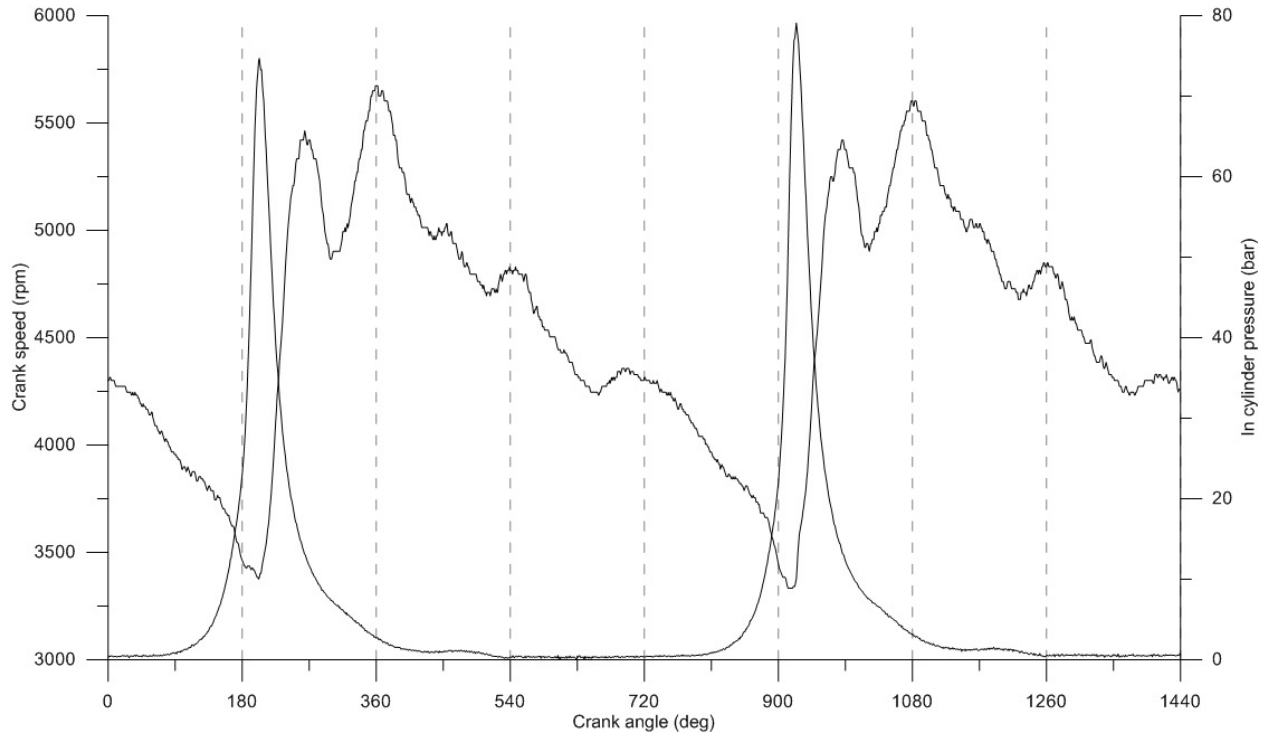
Figure 7.1 - Raw input data for 4250 rpm case

Using the equations formulated in section 3.2 the following piston motions were derived and used throughout the calculations for positional alignment between the liner – piston compliance matrices equation (4.14), entraining velocity calculation equation (3.69) and the inertial deformation of the piston equation (4.16). These are displayed in Figure 7.2.
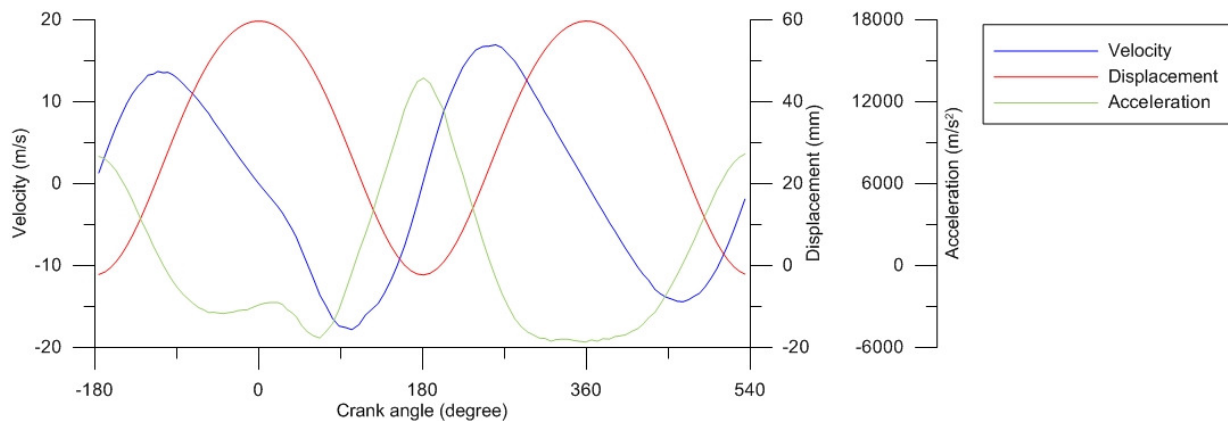

Figure 7.2 - Derived primary motions for 4250 rpm

The 4-stroke simulation results presented throughout this chapter are from simulations performed over 1440° of crank angle rotation. This equates to two complete 4-stroke process cycles. This selected simulation length ensures that dynamic stability is achieved within the numerical integrator and removes the errant results at the beginning of the simulation. Cyclic symmetry is normally achieved by the second simulated cycle; as such the second cycle results are presented throughout this chapter. In the results shown, the 0° crank angle represents TDC position in transition between the compression and combustion stroke, so simulation conditions commence at -180° for compression, followed by the combustion, exhaust and intake strokes.

Using the same thermal boundary condition data as in section 0, the converged results in terms of piston displacement at its top (e_{t}) and bottom (e_{b}) positions, as shown in Figure 3.2, are presented below in Figure 7.3.
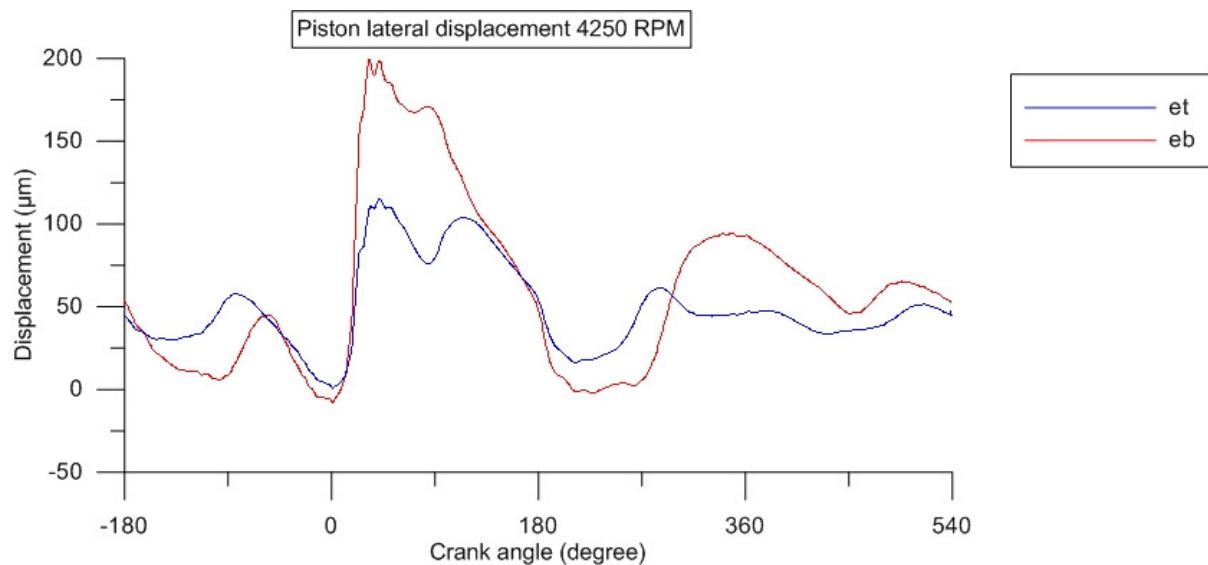
Figure 7.3 - Piston lateral displacements at 4250rpm

The minimum clearance observed when the thermally deformed liner and piston are axially aligned is 18µm. Clearly, given the magnitudes displayed in Figure 7.3, the distortion components must play a significant part in constraining the piston secondary motion. The initial conditions take the thermally deformed curvature of the piston skirt and place it with

axial alignment within the fixed coordinates of a static, thermally deformed liner. The initial clearances at e_t and e_b are 39 and 60 µm, respectively, under this initial configuration.

From Figure 7.3 it is not directly clear as to which direction the piston's translation would occur due to the initial e_t and e_b clearances. After subtracting the initial clearances at both e_t and e_b, any positive displacement indicates motion towards the thrust side and any negative value represents motion towards the anti-thrust side. Figure 7.4 and Figure 7.5 show the separation of the e_t and e_b values and compare the deflection contributions on both the thrust and anti-thrust sides. A negative value of either translation represents a shift towards, or deflection at, the anti–thrust side. It should also be noted that these are taken along a cut of the centre axis of the piston. Therefore, they only partially demonstrate the deflection contributions of the conformal bodies.
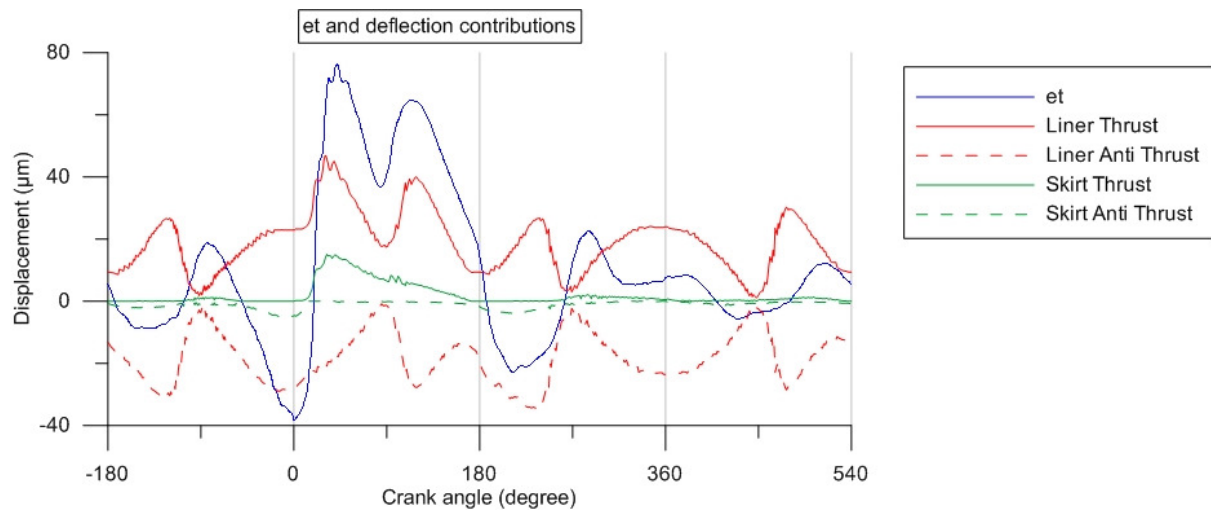
Figure 7.4 - e_t displacement and deflection contributions
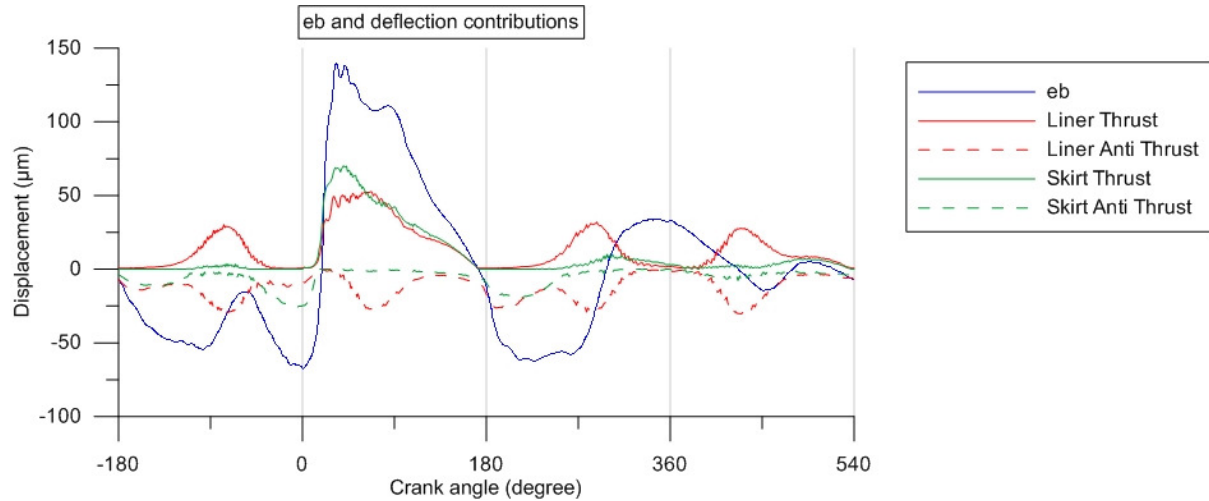
Figure 7.5 - e_b displacement and deflection contributions

Figure 4.6 shows a double barrelled deformation due to the torque loading of the head. This mode of deformation and its effect can be observed in both sets of presented results. With reference to Figure 7.4, this effect can be observed in the relative shape symmetry between the deflections on both the thrust and anti-thrust sides. The difference in magnitude of the deflections observed between the two opposing thrust sides, particularly in the combustion stroke, originates from the localised normal loading. In the second half of the combustion stroke, 90-180°, the e_t motion follows the shape of the liner distortion, whereas through the same position of the stroke the e_b position rides over a more stable and flat portion of the liner, thus not experiencing the same degree of offset. The combined effect of the two induces a clockwise tilting motion, concentrating the contact towards the bottom of the skirt. The relatively low conjunctional stiffness between the bottom of the skirt and the liner through these positions is unable to support/generate the significant pressures required to sustain the side load. As a result the contact position shifts in the direction of the crown where a greater conjunctional stiffness is able to support the required pressures. In these positions the greater conjunctional stiffness is as the result of combined additional stiffness contributed by the skirt crown towards the top of the skirt and a thicker section of the liner there. Although this may not be completely clear from Figure 7.4 and *Figure 7.5* the phenomena is made clearer later in this chapter.

Although the effect of liner distortion on the secondary motion is most prevalent during the combustion stroke, the same behaviour is also observed in the other three engine strokes in

both the thrust and anti-thrust directions. This behaviour and its effect on the pressure distributions is discussed in more detail using a number of 3D pressure profiles in and below Figure 7.19.

The magnitude and angular distribution of the combustion pressure are the most significant forcing mechanisms on the piston assembly and as such have a significant effect on the system dynamics. Figure 7.6 shows the input combustion pressure and the resulting maximum hydrodynamic pressures, side (contact) force and clearance at the thrust side.
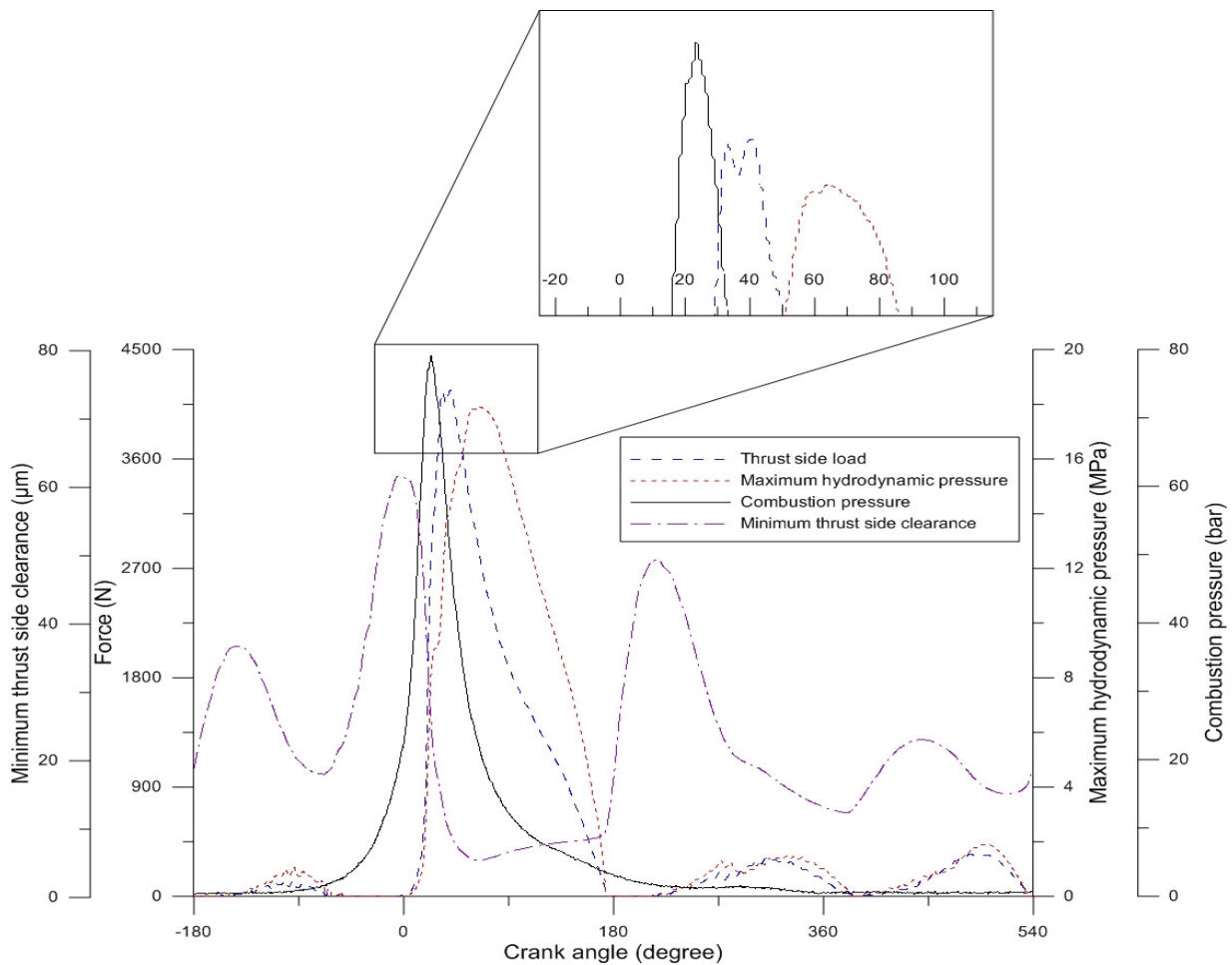
Figure 7.6 - Combustion pressure, contact pressure, side force and minimum clearance for 4250 rpm

There is a noticeable phase shift between the maximum applied combustion pressure and the resulting side load generated at the thrust side. As discussed in chapter 5, the CRF exhibits an offset crank; the logic behind its inclusion being two-fold. Often a positive pin offset or crank

offset are included so as to ensure the adherence of the piston to the thrust side throughout the combustion stroke. This reduces the magnitude of impact as the piston shifts from the ATS to TS, usually around 0° crank angle (TDC). This motion is induced in order to attenuate the noise generated through the piston slap phenomenon. However, this provision comes at a cost. A less vertical connecting rod angle through combustion increases the side loads (and thus friction) at the piston and reduces the instantaneous torque generated at the crank through the combustion stroke. The contrary is observed in the setup studied where a negative crank offset is employed, yielding an increased torque output and reduced side load when compared with a zero offset case. Clearly, the downside would be in terms of the slap noise noted after the TDC, though as this is a race engine, raw performance is more desirable as opposed to NVH refinement. The piston slap in the case presented here could be noticed at approximately 20°, where there is a rapid lateral shift between the anti- thrust and thrust side. This is seen above in the motion of e_t and e_b, as they cross the position of neutral alignment.

7.2.2 Engine speed of 6250rpm 90% throttle

A second higher speed case is detailed below. Its inclusion is intended to illustrate the effect of changing engine speed, an increase in combustion pressure magnitude and the position of maximum pressure occurrence. Hence, a direct comparison can be made between the two speed cases in terms of operational characteristics. The increase in pressure and difference in the peak combustion pressure position is seen when the speeds and cylinder pressures are compared on a single plot, as shown in Figure 7.7.
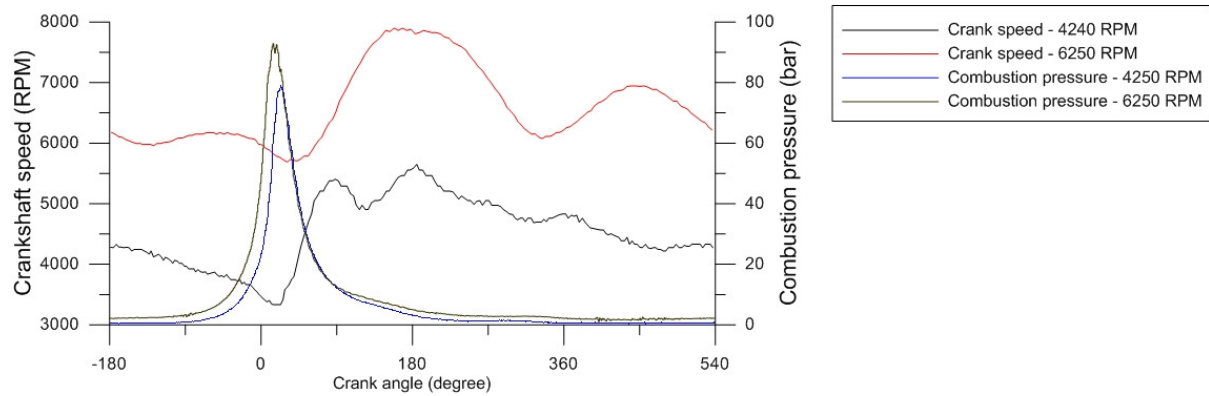
Figure 7.7 - Crank speed and in-cylinder pressure compared for 4250 rpm and 6250rpm

As expected, between the two cases there is an increase in maximum in-cylinder pressure. The position of the peak combustion pressure tends toward the TDC. This is a result of the advanced ignition, this allows sufficient time for the flame to propagate within the stroke time duration. This characteristic is well understood and critical in ensuring adequate combustion and thermodynamic efficiency.

With attention diverted to the crank speed, in both test cases the speed was controlled to the average nominal value quoted for both cases. It can be clearly seen that the speed varies significantly from this nominal value in both tests and a drop in speed is observed through the compression stroke. As the engine is a single cylinder configuration and with a relatively low rotational inertia, a portion of the rotational momentum is noticeably absorbed in order to overcome the work requirement of the compression stroke. Through the combustion stroke the engine rapidly accelerates to its maximum crank speed. The irregularities or variance in speed dips are most likely due to the dynamometer control. However, direct monitoring of these is well outside the scope of the project. Of greater importance is the actual speed variation experienced in the specific test cases for which the presented methodology suffices.

Figure 7.8 presents the combination of instantaneous in-cylinder pressure, side force on the thrust side and the lubricated thrust side parameter of maximum hydrodynamic pressure and minimum film thickness, in the same format as in Figure 7.6. Compared with Figure 7.6 there is a more prevalent "double peak" in the hydrodynamic response in the combustion stroke. It presents a similar offset in the maximum combustion pressure, thrust side load and maximum conjunction pressure. When inspecting equation (3.29) with the consideration of a negative crank offset, a lag between the maximum combustion pressure and the thrust side load is

presented. As discussed later on in this chapter, the generation of hydrodynamic pressure and its distribution and magnitude is a function of a number of variables, including conjunction flexibility, lubricant entrainment speed, secondary dynamics and lubricant rheology. Hence, a simple explanation is not possible for this offset.
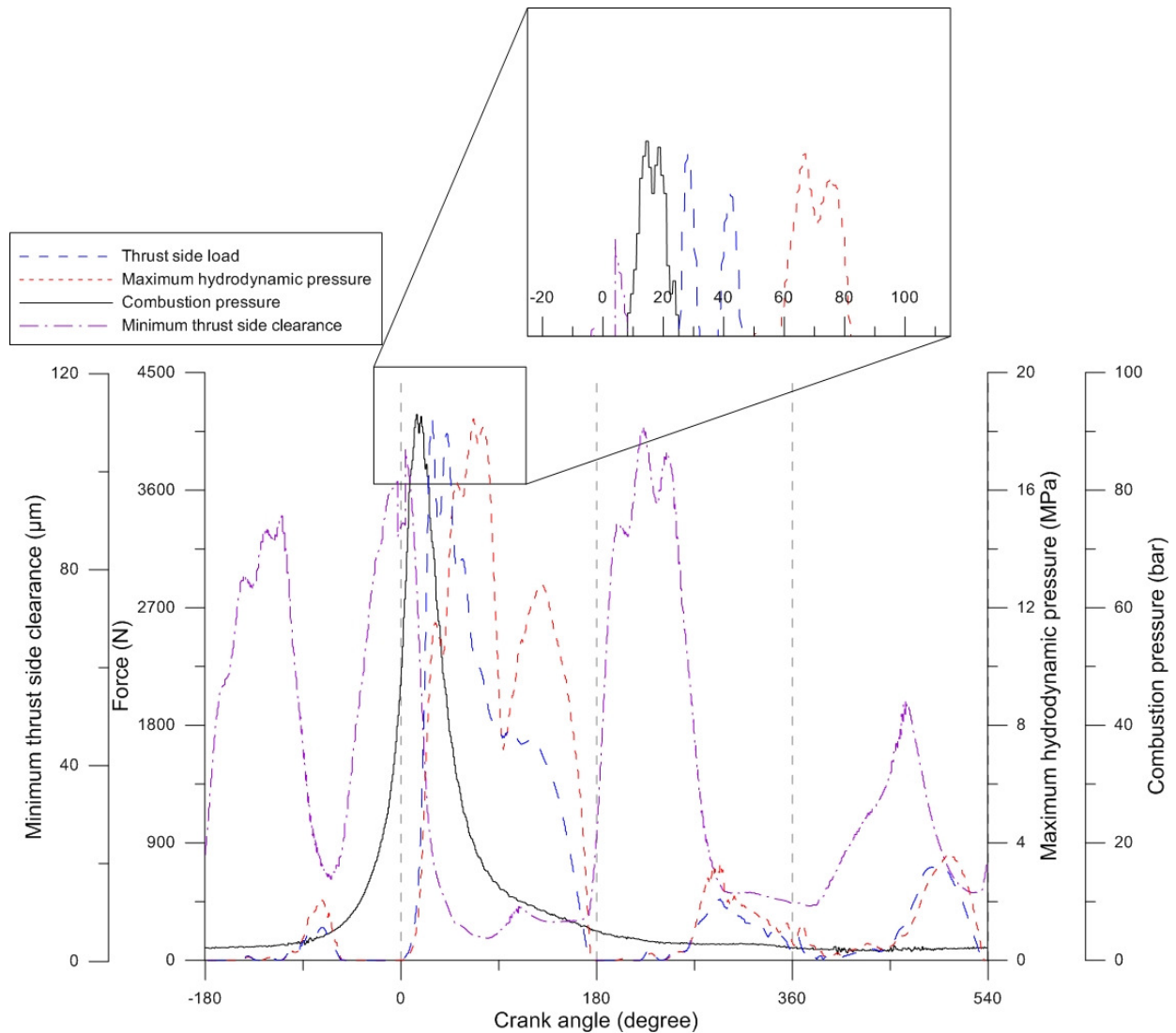

Figure 7.8 - Combustion pressure, contact pressure, side force and minimum clearance for 6250 rpn

Figure 7.8 illustrates the overall cyclic events, but lacks the detail in the combustion stroke. This isolated stroke is shown compared side by side for the two load cases presented in Figure 7.9 and Figure 7.10.
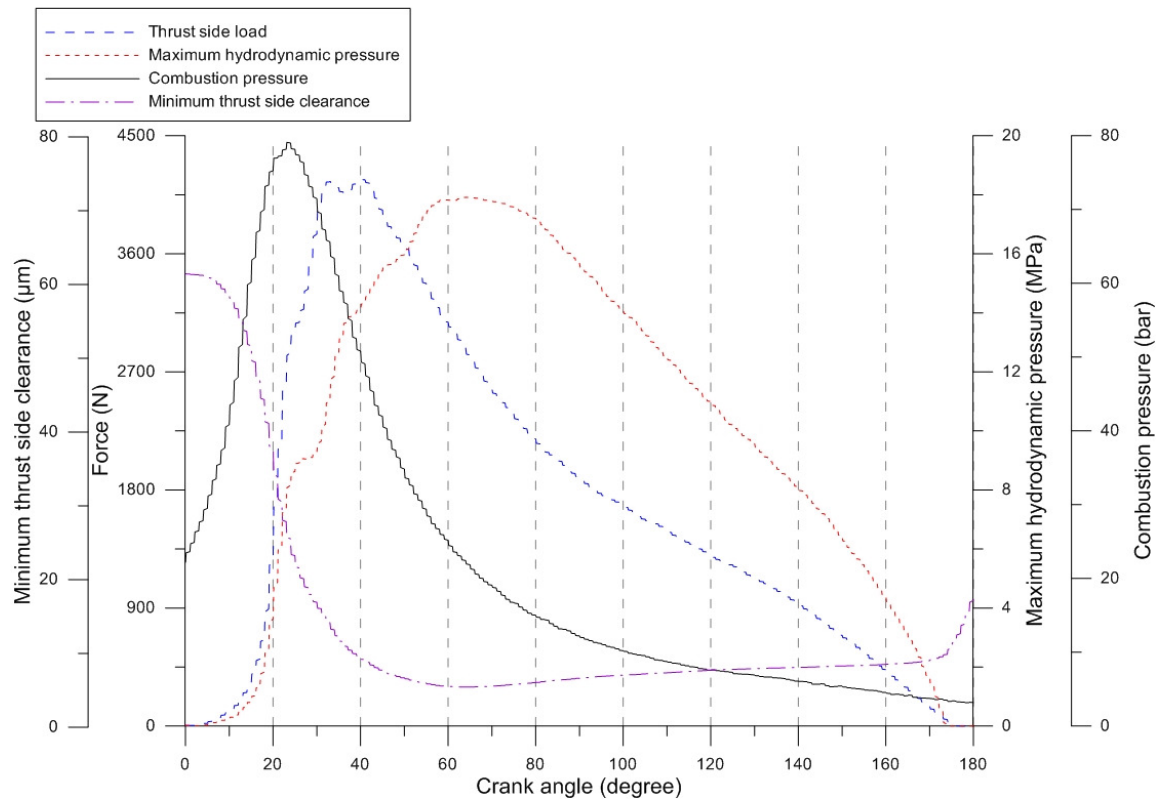
Figure 7.9 - Analysis through combustion stroke, 4250rpm
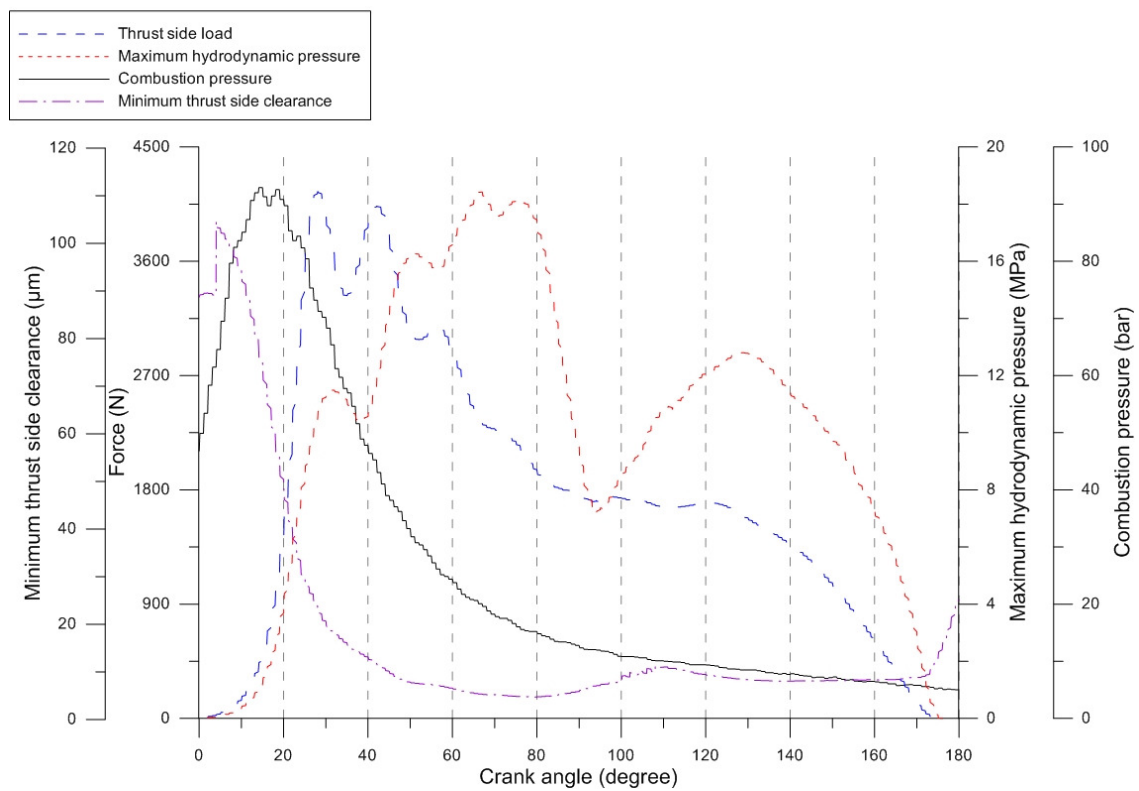
Figure 7.10 - Analysis through combustion stroke, 6250rpm

The initial difference between the two plots is the prevalent double peak in the maximum contact pressure. This can be attributed to a number of influential parameters. The tilting motion of e_t exhibits a similar characteristic in terms of following the available space made by the distorted liner shape. The position of maximum pressure tends to the top portion of the skirt, though at the higher engine speed case the side load is of greater magnitude in the second half of the combustion stroke. The force in the second half of the combustion stroke is a combination of two increasing variables. The residual in-cylinder pressure is greater, though only slightly. The component of force due to resolved primary inertial acceleration is much more significant. The difference in this force can be observed by a comparison between Figure 7.11 and Figure 7.12 for the piston inertial force.
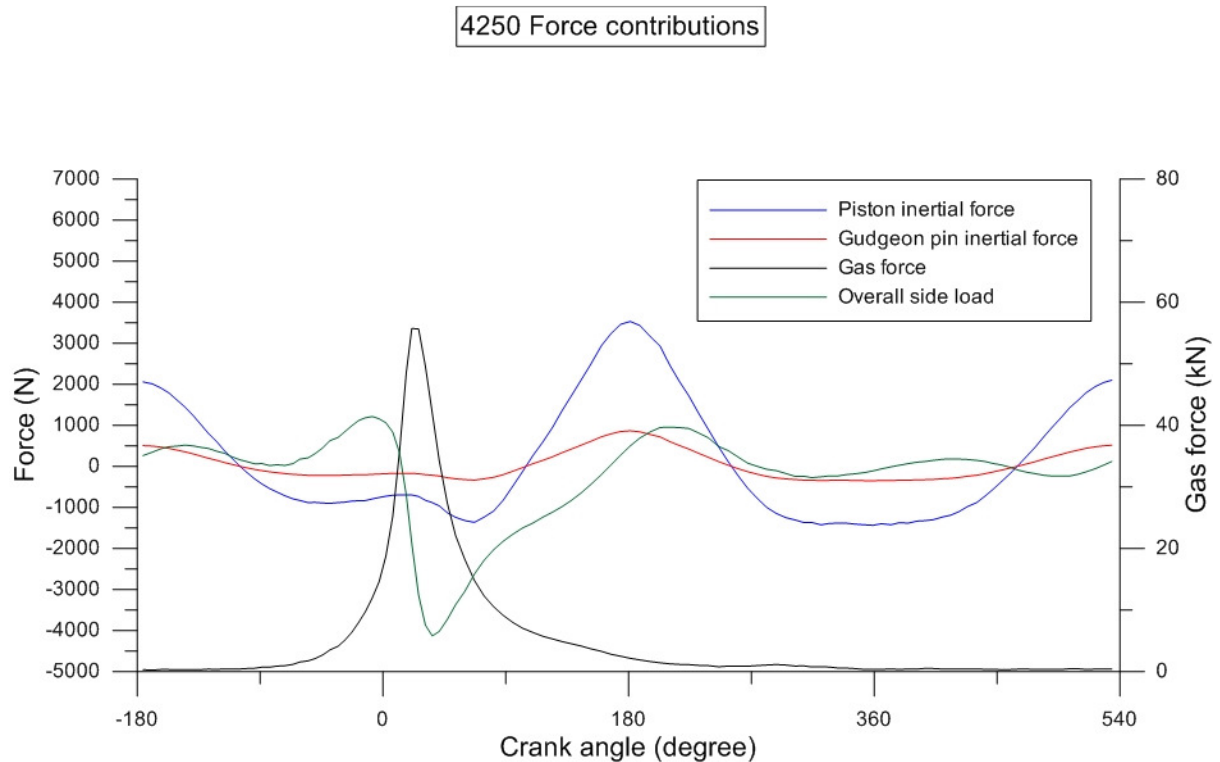
Figure 7.11 - Force comparisons 4250 rpm
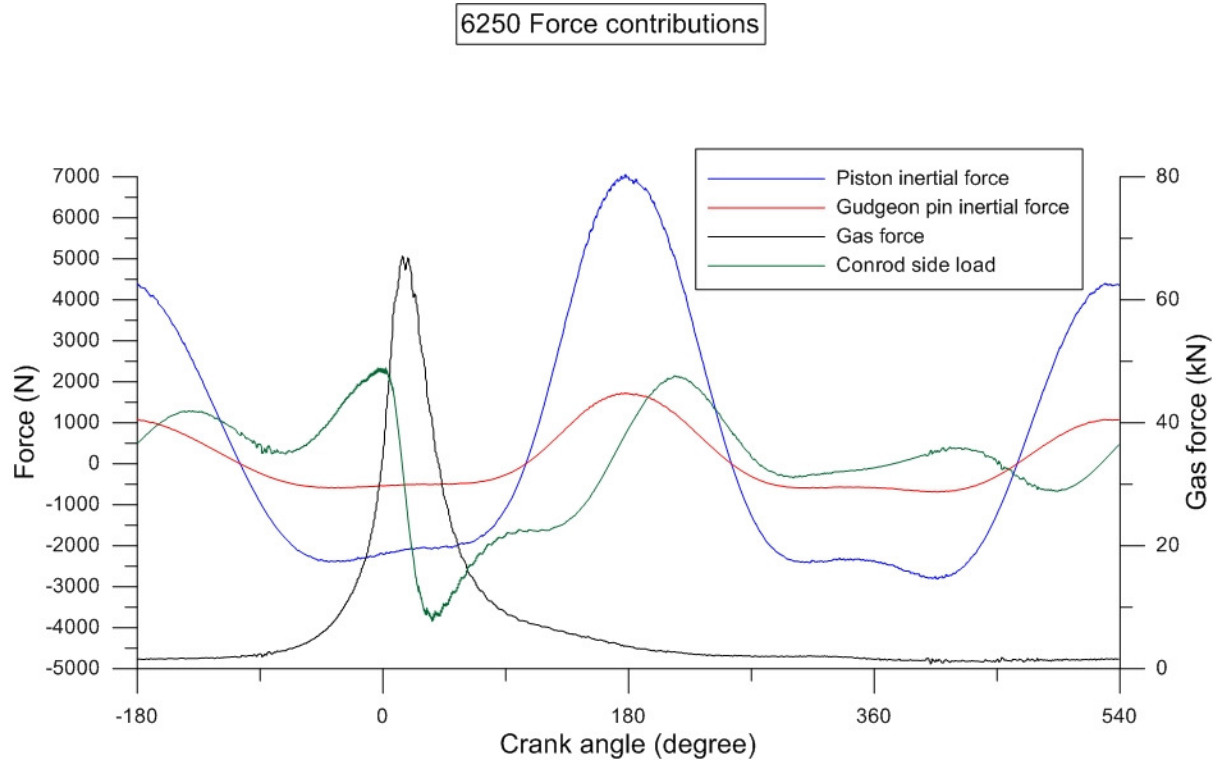
Figure 7.12 - Force comparisons 6250 rpm

The analysis of displacements e_t and e_b for the second engine speed case begins to highlight the difference between the dynamics of the two different sets of operational conditions. The maximum deflection in this case during the combustion stroke is much more pronounced (higher speed, thus higher inertial loading). These are shown for ease of comparison in Figure 7.13. The additional side load force towards the end of the combustion stroke is apparent in the drop observed at the bottom of the skirt. The e_t displacement follows very similar characteristics in terms of both magnitude and trend. At the bottom of the skirt, e_b maintains larger displacement between the 90° and 180° crank angles, which is the likely consequence of the second pressure peak in the combustion stroke observed in the 6250 rpm case.
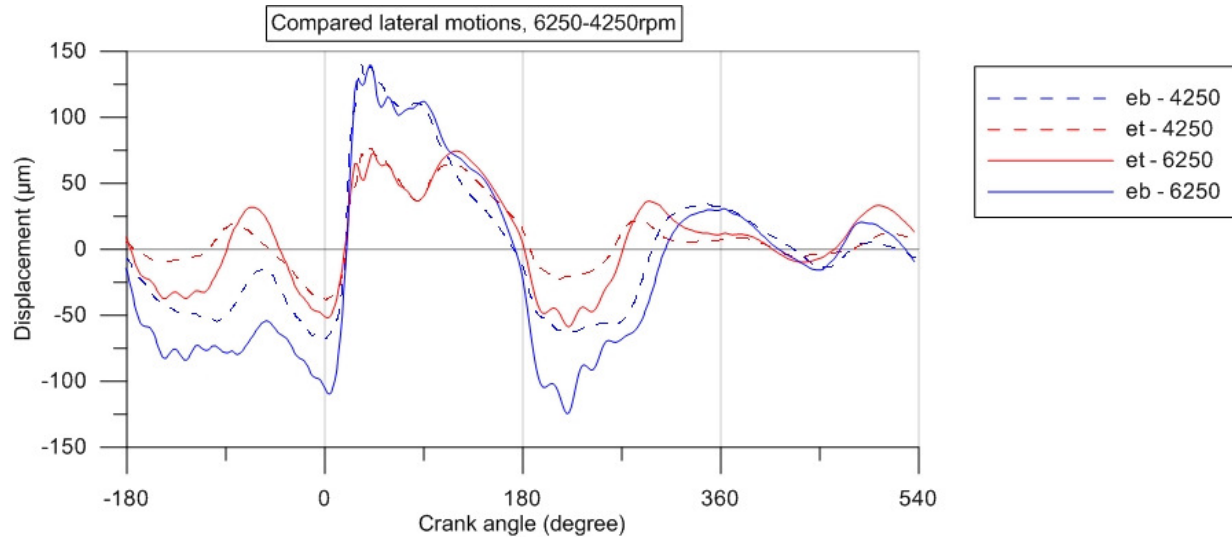
Figure 7.13 - Lateral displacements at 6250rpm compared with those at 4250rpm

Looking in detail at the deflection contributions compared with the varying lateral displacements, a similar trend is indicated between the two speed cases. Again the lateral displacements follow the freedom defined by the respective distortions in order to generate sufficient conjunction pressures, as would be expected.
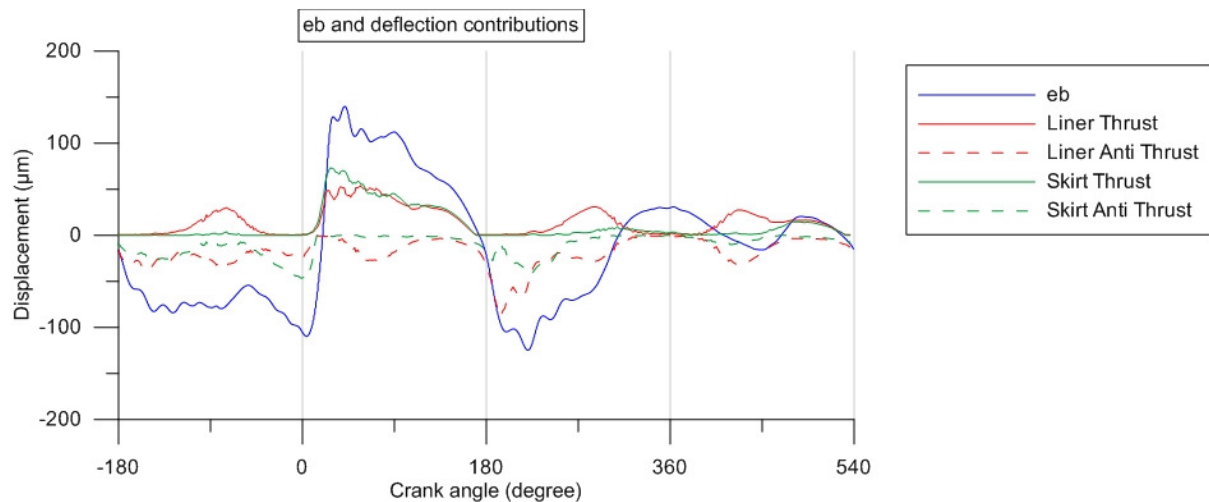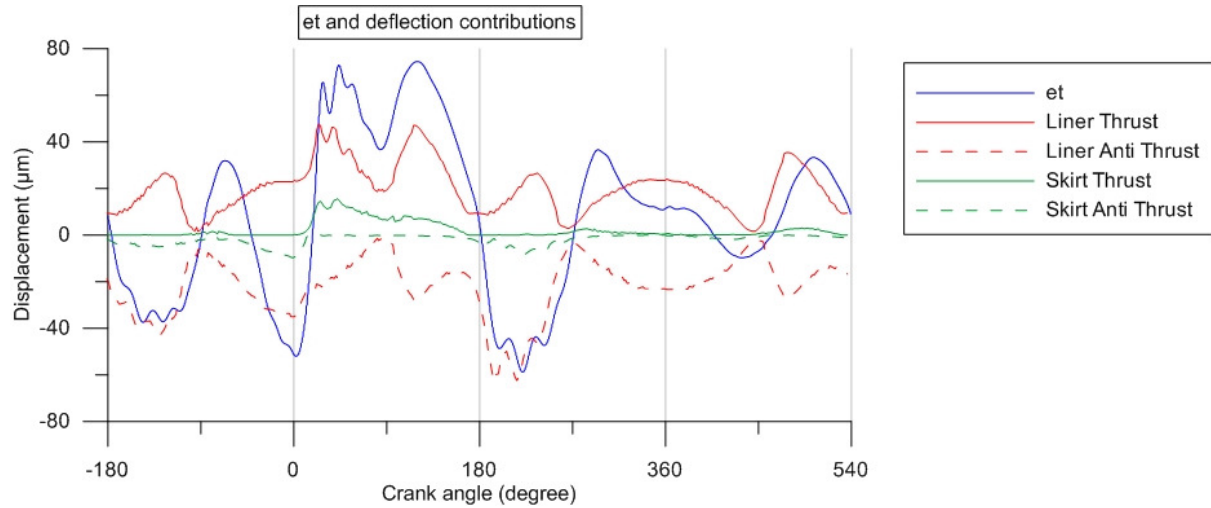

Figure 7.14 - e_b displacement and deflection contributions, 6250rpm

Figure 7.15 - e_t displacement and deflection contributions, 6250rpm

It is observed that during the compression and exhaust strokes there is a more pronounced deflection at the bottom of the skirt, thus inducing a tilting motion of the piston, which is more exaggerated at these positions. This is clearly observed in Figure 7.16 when comparing the tilt for the two speed cases.
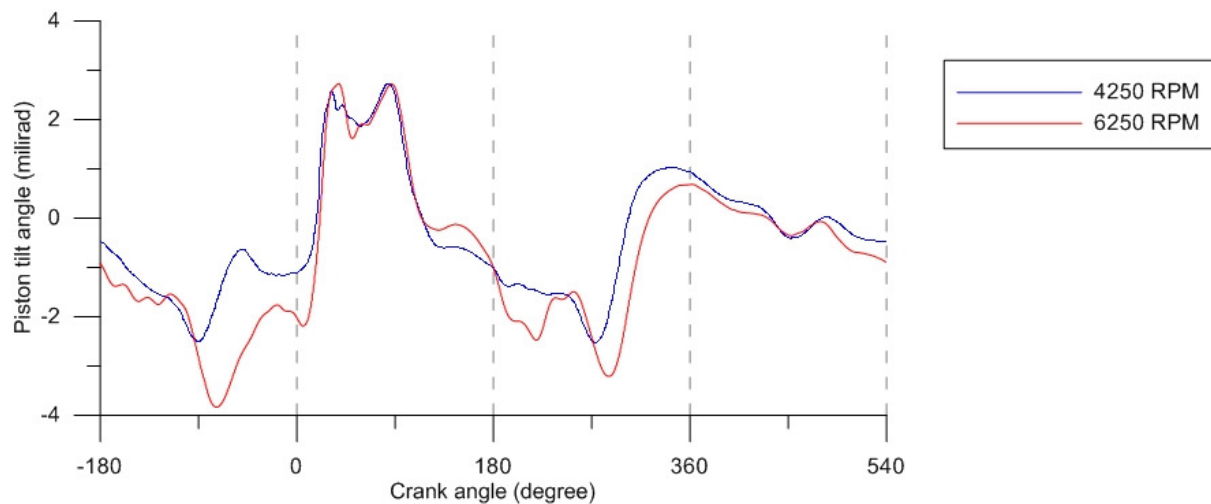

Figure 7.16 - Tilt angle comparison

In the case of the compression stroke a significant change in e_b is observed. By comparing Figure 7.14 and Figure 7.15 it can be seen that the comparison of the increased and compounded effects of deflection from both the liner and skirt bottom have induced this

increased angular change. For the case of the exhaust stroke a separate phenomenon is observed. In this case e_t has produced the most significant change. Since the top portion of the skirt is significantly stiffer than its bottom edge it plays a less significant role. The liner distortion through the top of the stroke is much more significant, thus the difference between the two speed cases. This exhibits a significant increase in the contribution of deflection.

Observations of deflection are very much indicative of conjunctional pressure profiles, but ultimately with such significant deflections apparent, they act to partially dictate the formation of a lubricant film and the contact patch. The variance of stiffness through the bodies modulates the allowable pressures generated in certain areas between the surfaces through differing portions of the cycles. Figure 7.17 shows the trend of stiffness variation along the centreline of the two bodies moving axially. The deflection response of the nodes along the central axis of both bodies to a unit force applied normally to each node in isolation is plotted. The skirt response is similar to that of a simply supported beam, as would be expected by applying the force further away from the anchor points of the skirt. The liner on the other hand is a less simple case; its constraint is over multiple positions (as it has been described in more detail in section 0). It exhibits stiffness proportional to its varying section thickness. Since its axial alignment is constrained along its top surface, there is a general trend of decreasing stiffness as moving down the height of the liner. The effect of increased localised stiffness is seen in particular at the bottom of the cooled section, where the raised sealing face is present. Previous studies using these components have highlighted the effects of this localised region of raised stiffness. Observations of localised pressure increase and tilting around this region have been commented upon in a recent thesis by **Howell-Smith** (2011).
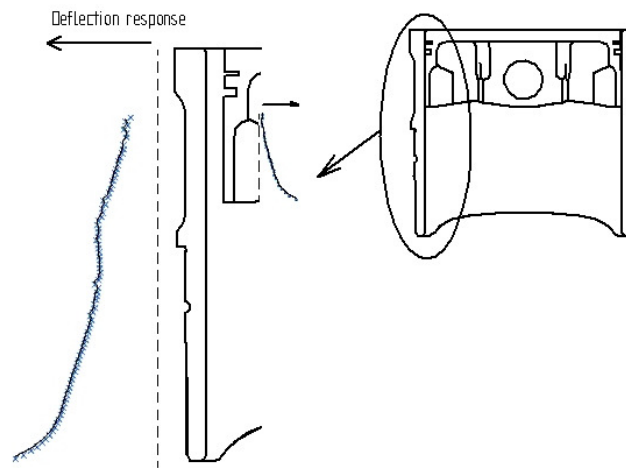
Figure 7.17 - Component response to normal load (axial cross section)

The effect of the combined stiffness variation on the magnitude of generated pressures and position have been discussed and identified above in Figure 7.9 and Figure 7.10 , though the phenomena and its illustration are limited to one-dimensional comparison. Figure 7.19 shows the combustion stroke in detail for the case of 6250 rpm engine speed. The positions of the piston are shown, alongside a diagrammatic representation for the instantaneous rotational and translational directions and the instantaneous side bias. The key to this small diagram is shown briefly in Figure 7.18. The position of the diagram also changes, moving to the direction of the side to which there is a piston adhering bias. The LHS of each of the data sets presents the thrust side. In the case where a pressure distribution is not presented, no lubricant film is likely to form because of a diverging gap or the overall force contribution from the associated side is less than 1N.
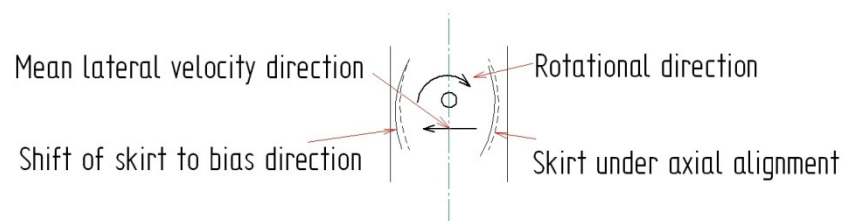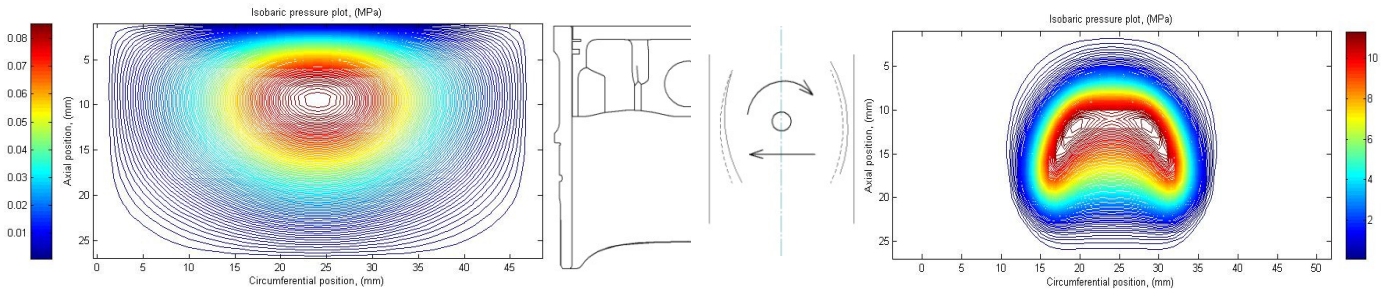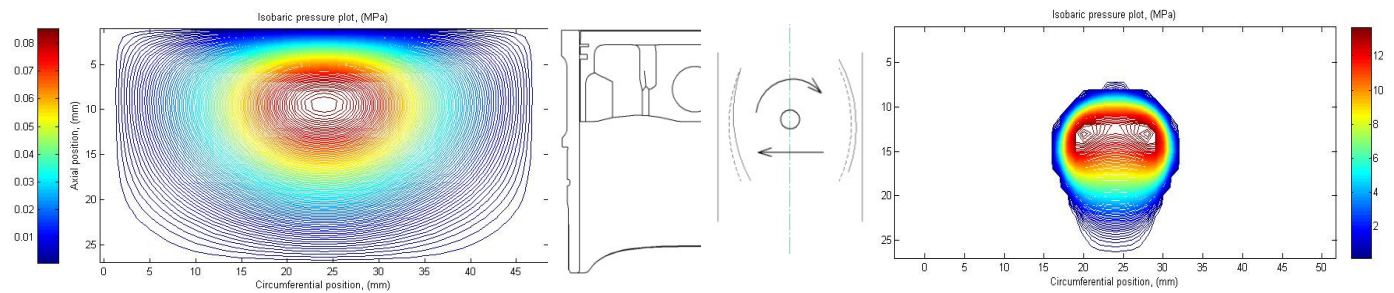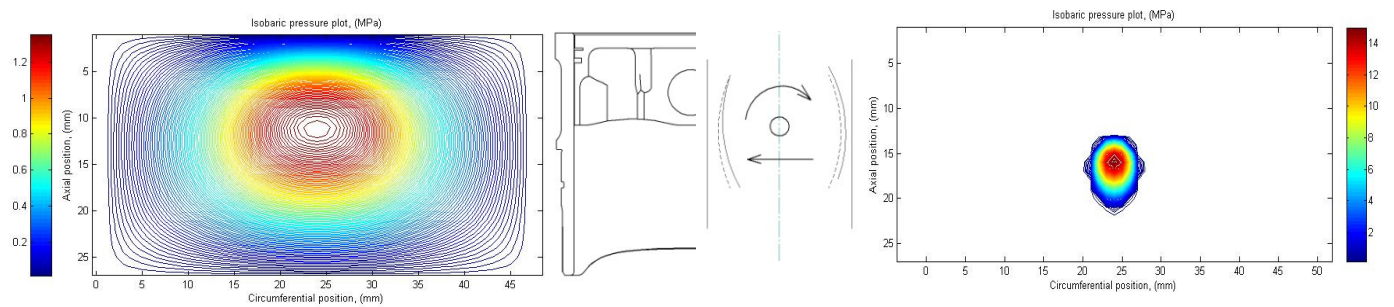

Figure 7.18 - Motion diagram explanation

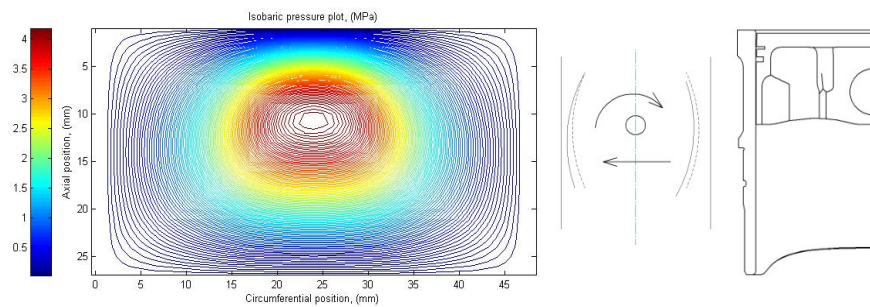5° – Speed 1.2m/s, FThrust 54.0N, FAnti 2426.7N
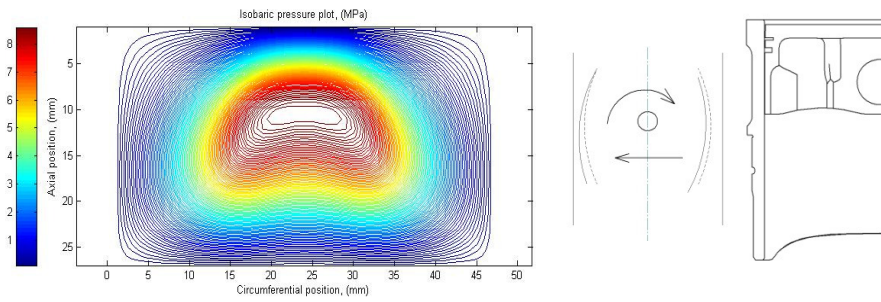

10° – Speed 1.2m/s, FThrust 54.0N, FAnti 2426.7N

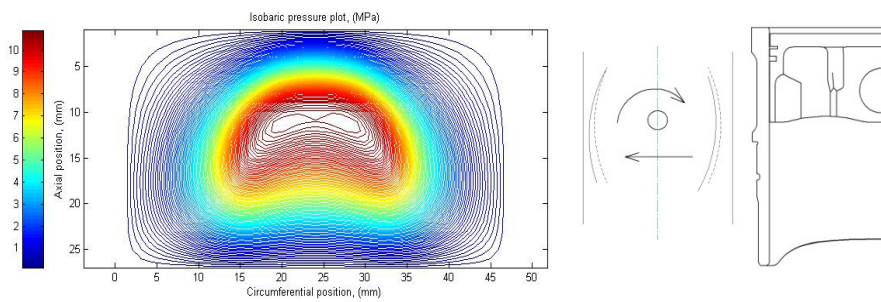15° – Speed 3.5m/s, FThrust 452.7N, FAnti 408.3N (Maximum in cylinder pressure)
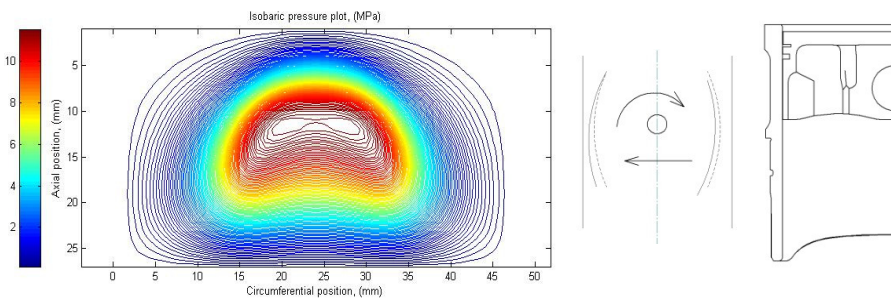

20° – Speed 4.6m/s, FThrust 1264.6N, FAnti 0N
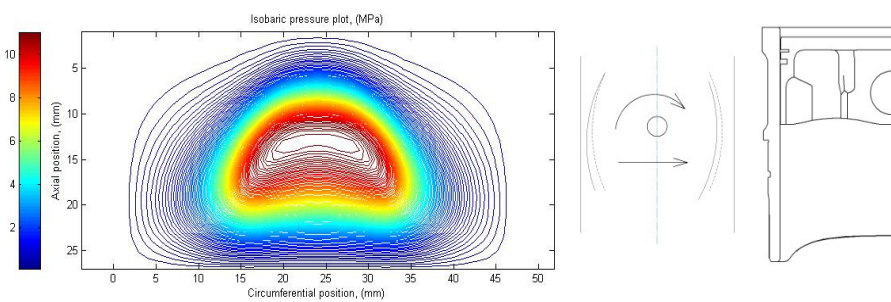
25 $^{\text{o}}$ – Speed 5.7m/s, FThrust 3192.3N

28 $^{\text{o}}$ – Speed 6.4m/s, FThrust 4075.7N (Maximum side load)

30 $^{\text{o}}$ – Speed 6.8m/s, FThrust 4018.9N

35 $^{\text{o}}$ – Speed 8.0m/s, FThrust 3119.7N

40 ^{o} – Speed 9.2m/s, FThrust 3618.8N
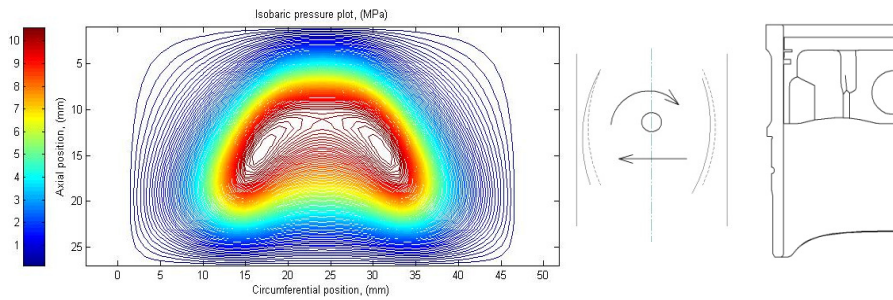
50 ^{o} – Speed 11.5m/s, FThrust 2916.8N
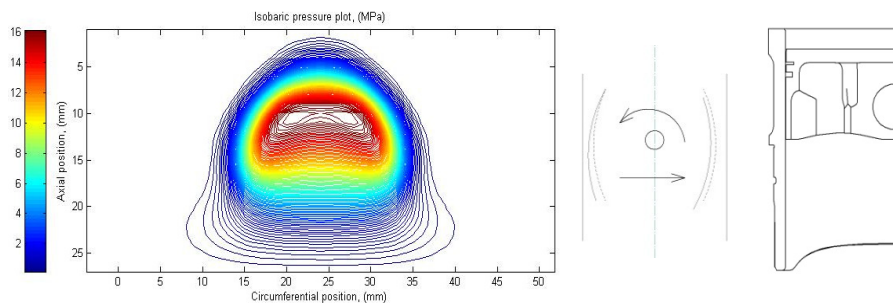
60 ^{o} – Speed 13.9m/s, FThrust 2786.0N
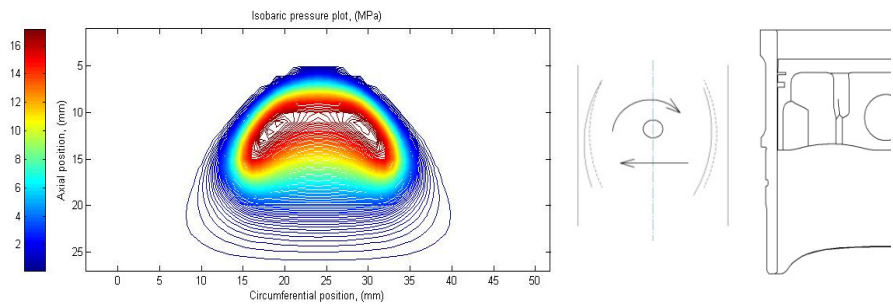
66 ^{o} – Speed 15.5m/s, FThrust 2305.8N (Maximum hydrodynamic pressure)
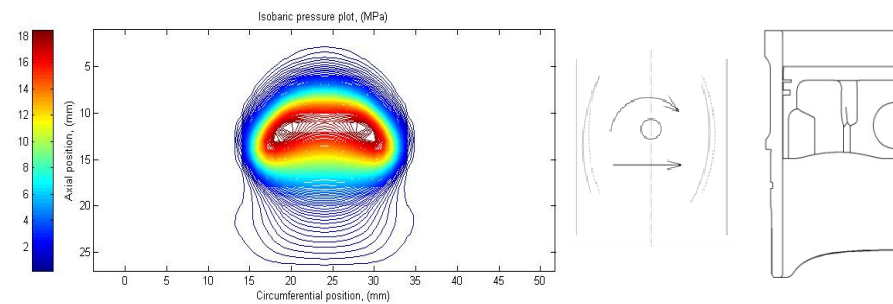
70 $^{\circ}$ – Speed 16.5m/s, FThrust 2180.2N
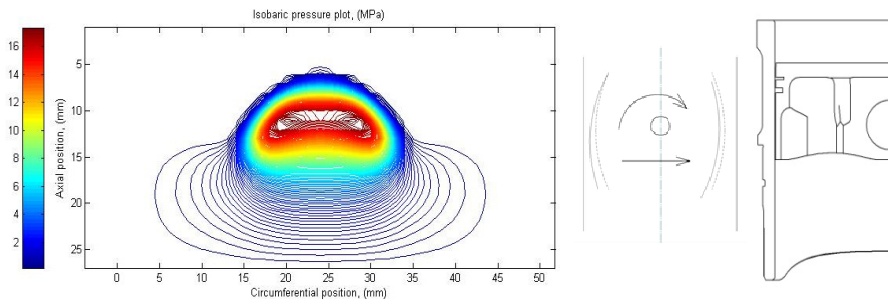
80 $^{\circ}$ – Speed 19.0m/s, FThrust 1878.9N (Minimum film thickness)
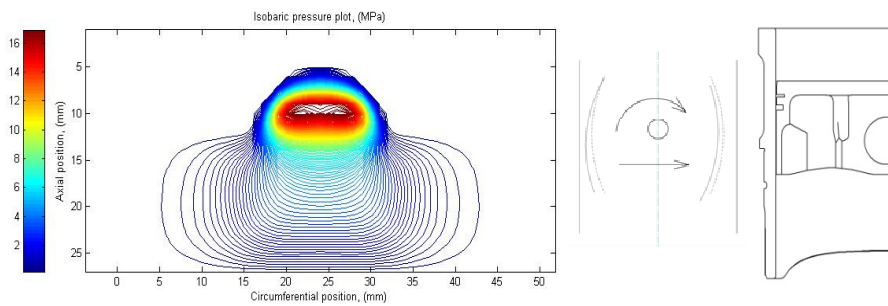
90 $^{\circ}$ – Speed 21.3m/s, FThrust 1705.2N
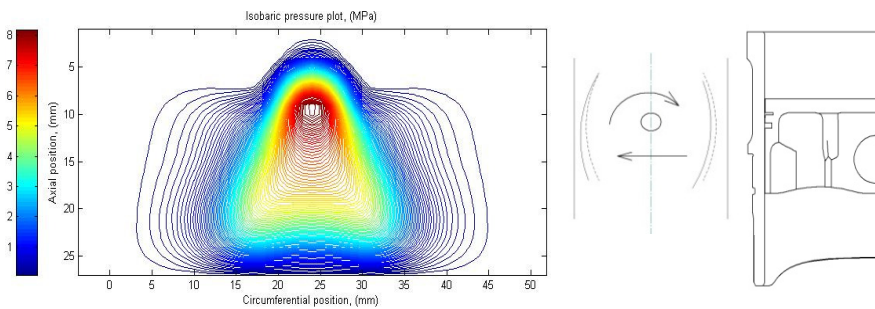
100 $^{\circ}$ – Speed 23.0m/s, FThrust 1729.2N, FAnti 50.0N
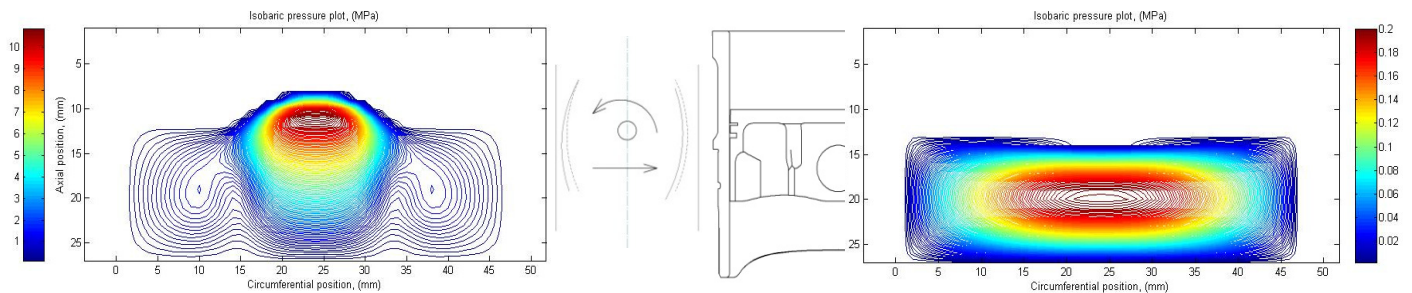
110 ^{o} – Speed 24.0m/s, FThrust 1640.9N, FAnti 42.6N
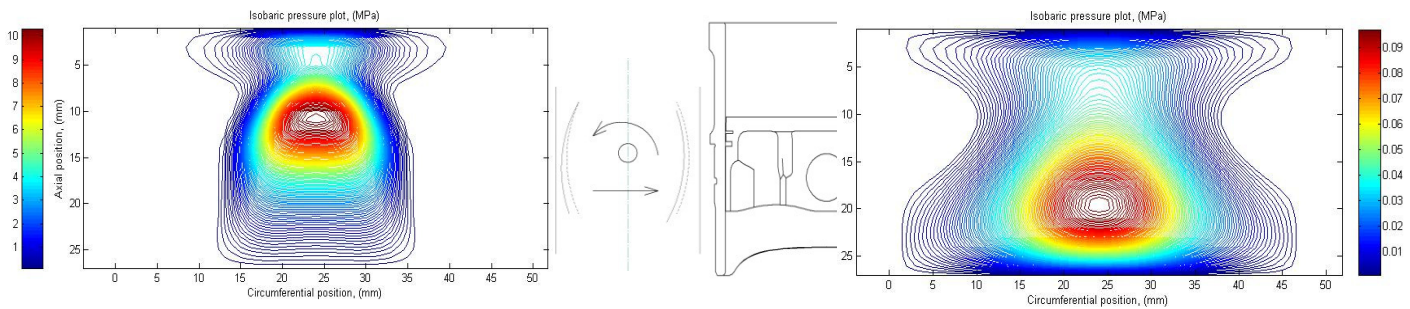
120 ^{o} – Speed 23.9m/s, FThrust 1662.5N, FAnti 77.7N
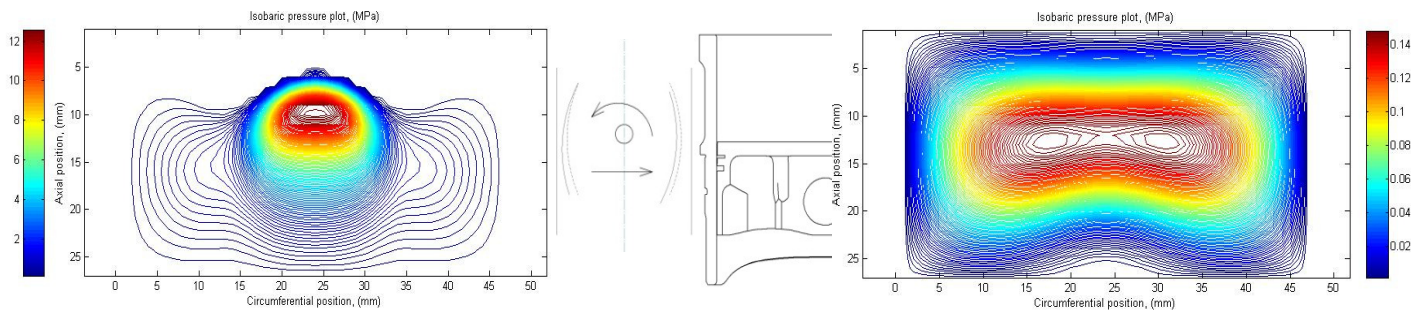
140 ^{o} – Speed 19.9m/s, FThrust 1370.3N, FAnti 69.0N
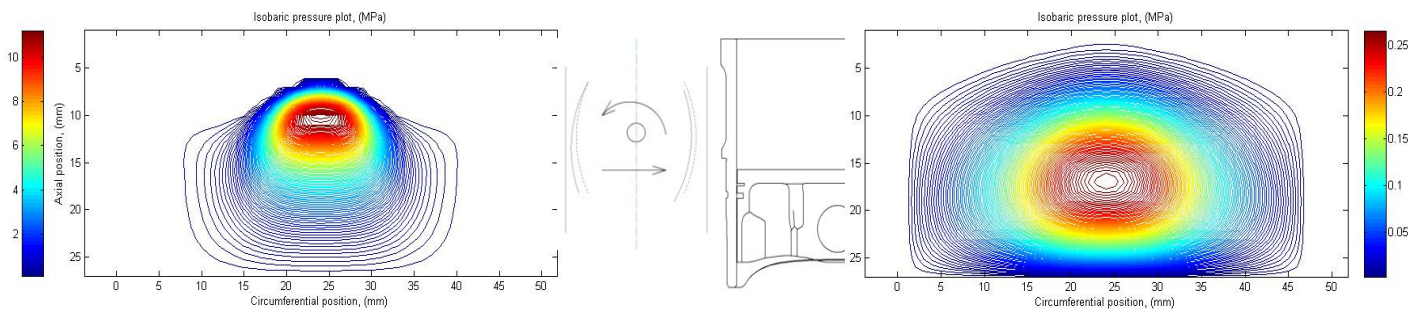
160 ^{o} – Speed 11.3m/s, FThrust 629.0N, FAnti 232.2N
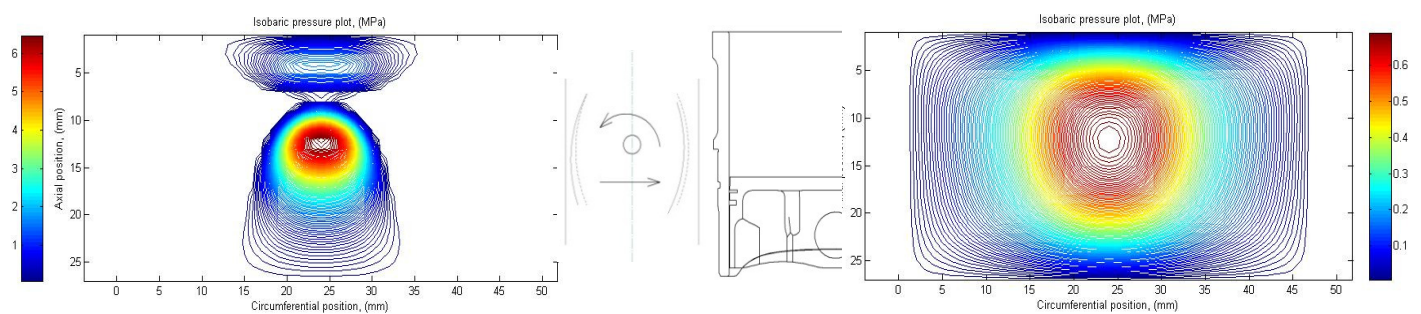
170 ^{o} – Speed 5.8m/s, FThrust 145.6N, FAnti 377.5N
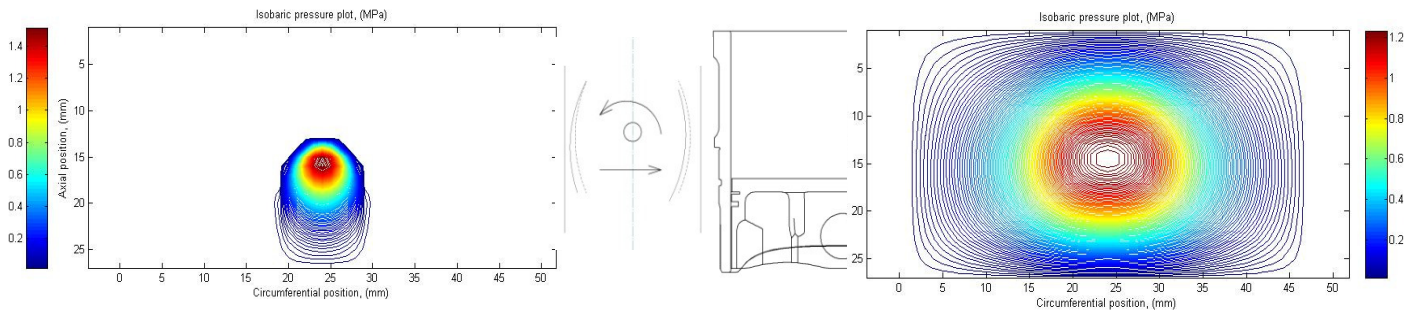
180 ^{o} – Speed 0.0m/s, FThrust 0N, FAnti 627.8N
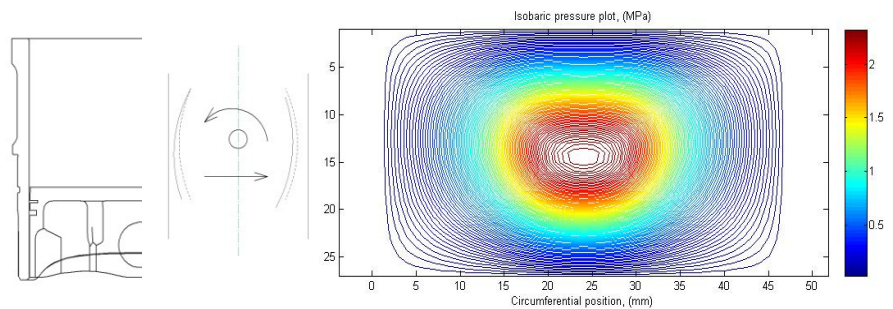
Figure 7.19 – Two dimensional pressure generation through the combustion stroke

In position interval 5-15° the net side load is on the ATS; meaning that adherence to the ATS is maintained from the end of the compressions stroke. The contact is, however, tending towards the thrust side and a clockwise tilt is evident. This can be observed in the shifting of the central position of the pressure profiles on both piston sides.

Between 15-20° significant load is transferred from the ATS to the TS and moderate pressures are generated on the thrust side. Through these first few positions relatively little axial movement is evident, as such little differences are observed in the structural stiffness of the liner within the contact patch. A clockwise tilt can been observed, preceding this transfer of bias from the bottom edge, leading to a TS contact patch under the rapid shift observed. It can be concluded that the more flexible bottom edge acts to dampen the secondary motion of the piston and reduces the magnitude of the generated pressures, confining them in the region of 4MPa.

At 28° crank angle the maximum side load is observed at 4075.7N, significant clockwise rotation has occurred. As in the previous time steps the bottom edge is led into the contact patch. The less stiff bottom section of the piston deforms and ensures that an entraining radius is still present. Therefore, the minimum film thickness in Figure 7.10 is still sufficient at approximately 12µm. The increased stiffness towards the top of the skirt effectively supports the load, though the increased stiffness circumferentially provided by the vertical braces acts to form the classical 'horse shoe' shape observed and reported by other researchers (**Bai** 2012).

From 28° to 35° the side load decreases, thus the pressure profile moves back towards the bottom of the skirt as a reduced stiffness is sufficient to support the reducing side load.

At 35° the side load starts to increase again toward a lower secondary peak, as expected in an opposite manner to the movement of pressure under a decreasing load. The pressure profile begins to move towards the crown again. This is observed up to the position of approximately 50° where the second peak in side load is observed.

Progressing towards 60° the side load diminishes, although the tilt still acts in the clockwise direction. This increasing clockwise tilt is permitted by the additional clearance the mechanical distortion of the liner has created, particularly in the positions that e_t occupies. The clearance created by the mechanical distortion at the 60° position begins to reduce, a clockwise tilting motion is observed though its angular velocity is reduced. The entraining motion increases significantly as it is approaching its maximum value at 90°. These features combined with the reduced conjunctional stiffness of the liner act to produce a sharper entrainment profile and thus generate a high pressure towards the top of the piston skirt. This is at its most exaggerated combination in comparison to the side load at 66°, thus producing the maximum pressure.

As one moves closer to mid span and the maximum primary axial sliding speed of the piston, the liner undergoes a significant variation in its stiffness. Through the stroke up to this point the stiffness has been decreasing gradually. As shown above in Figure 7.17 the sectional thickness increases and thus the relative change in stiffness is reduced. This effect, coupled with the mechanical buckling of the piston, being at its lowest around its centre support, results in the liner having a pronounced effect on piston's dynamics. At 70°-80° it is observed that the bottom portion of the piston bears a greater load than the preceding positions. This

comes as result of this localised increased stiffness observed on the liner. Between 80° and 90° the pressure build-up towards the bottom end of the skirt increases significantly, coupled with a clockwise rotation, indicating that a larger entraining radius (wedge angle) has been made between the two contiguous surfaces.

From 90° to 100° the piston's rotational motion shifts in an anti-clockwise direction. The majority of the contact pressure is developed over the sections of the piston skirt with highest stiffness.. The observation of altering rotational directions around the point of varying stiffness in the liner agrees with the observations made by **Howell-Smith** (2011). The change between 90° and 100° is also at the bottom of the valley between the two pressure peaks. This secondary peak in pressure has been previously identified as an effect of the increased primary inertia as the piston begins to decrease its velocity in the approach to the BDC reversal. At 100° the pressure distribution is mostly supported by the bottom of the skirt, the result of this being an anti-clockwise rotation, which results in the generation of a pressure distribution within the ATS at the skirt bottom. The pressures are quite small with magnitudes of approximately 100 kPa. The lateral motion is beginning to shift the side biased towards the ATS. This anti-clockwise tilting motion continues for the remainder of the stroke.

This continued anti-clockwise tilt centres the significant TS side load towards the top of the skirt. This load carrying mode occurs without any significant distortion of the lower skirt to ensure adequate entrainment. Finally one can observe the side load shift towards the ATS, with significant lateral displacement, showing an insignificant contribution from the TS.

7.3 Contact conformability

The piston skirt to liner conjunction is often referred to as a conforming or partially conforming contact. As it has been illustrated in section 7.2, the deflection and secondary motion of the opposing bodies has a significant effect on the position and shape of the contact footprint and thus, the isobaric plot. The conventional categorisation and measurement of conformability between a concave and a convex body is classified by the ratio of radii, r/R. The contact is deemed more conforming as the value of r/R tends to unity. The LHS of Figure 7.20 shows this in the classical, partially conforming contact.
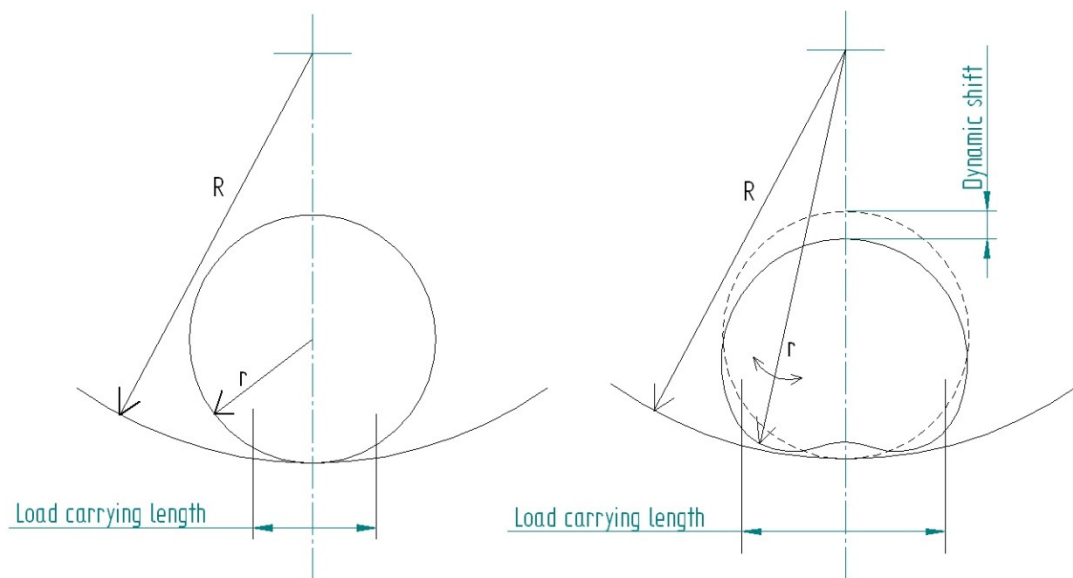
Figure 7.20 - Geometry of conformability

The RHS of Figure 7.20 shows the effect of both the shift in position and the gross mechanical deformation. Using this simple ratio of r/R for this case would result in a smaller conformability ratio. The difference in approximate load carrying footprint is highlighted between these two cases, showing an improvement in the globally deformed case, thus an increase in conformability is observed.

In the special case presented throughout this chapter, the conformability alters through two coupled mechanisms. The deflection of both bodies coupled with the axial offset has a significant effect on the relative shape and position of the contacting surfaces. Therefore, a

fixed axial position is used as the centre reference for both bodies, which allows for the incremental conformance to be calculated at each nodal position. In order to give a measure of the overall line conformability, a mean conformability value is calculated using equation (7.1).

$$\sum^{j=1,24} \frac{r_p{}'_{(j)}}{R_{L(j)}} \qquad (7.1)$$

where:

$$r_p{}'_{(j)} = r_{p(j)} + c_o(i)\cos\left(\left(\frac{nyy+1}{2} - j\right)\Delta\Phi\right) \qquad (7.2)$$

The definition of $c_o(i)$ comes from equation (4.22) or (4.23) for the respective thrust or anti-thrust side contacts.

For the higher load case of 6250rpm engine speed the conformability has been calculated throughout the four engine strokes on the thrust side for a series of axial positions, highlighting the varying conformance and how this changes with contact deformation.
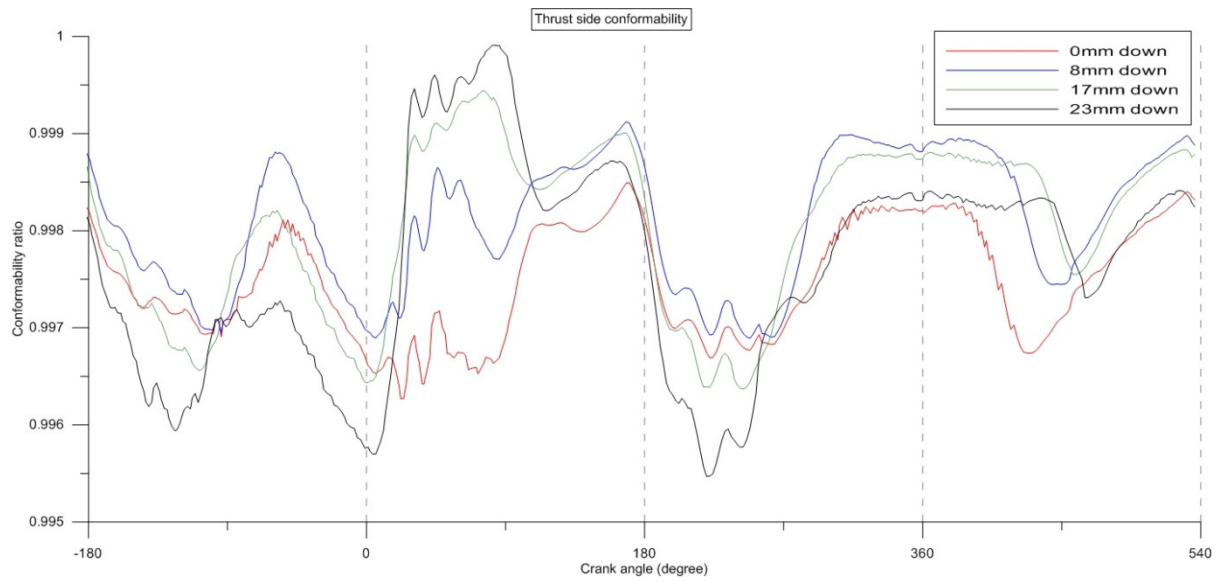
Figure 7.21 - Thrust side mean conformability
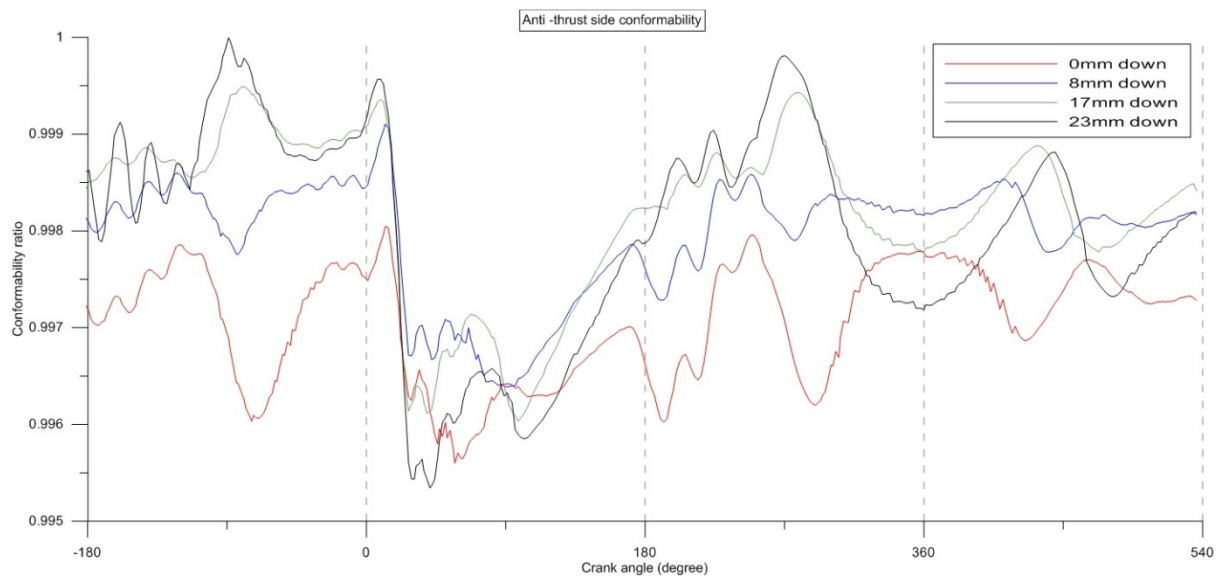
Figure 7.22 - Anti-thrust side mean conformability
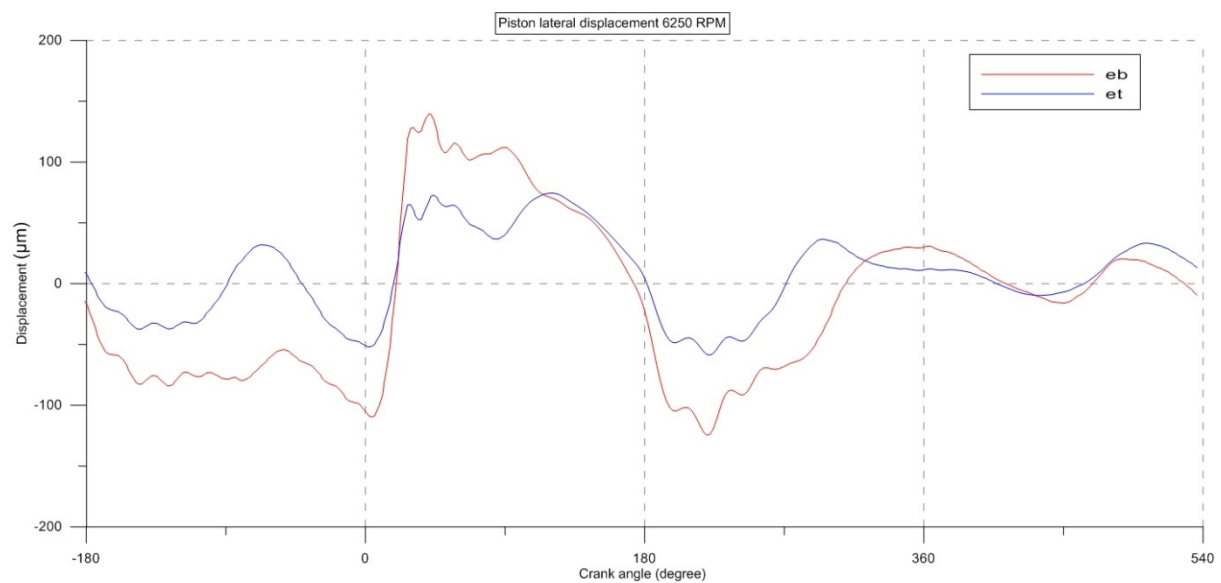
Figure 7.23 - Reference piston displacements 6250 rpm

The use of the three differing axial positions shows the partial effect of the varying skirt stiffness, progressively reducing from the top of the skirt downwards. This, however, only goes part of the way to explain the significant differences in conformability. The radius of the liner alters significantly throughout the stroke and as such it will affect the r/R ratio; again this only goes part way to explain the variance. The conformability change is a function of a

great number of separate variables aside from the stiffness of the two shapes. As highlighted earlier in the chapter the shape and positions of the deformation of the two bodies has a significant effect, almost dictating the secondary dynamics of the piston. The inputs to these deformations are the instantaneous forces and pressures applied to the piston, for which the shape and magnitude are traced back to the deformation characteristics of the contiguous contacting solids. It can be clearly seen that this is a multi-variant problem.

Figure 7.21 shows the mean conformability on the thrust side of the piston skirt. An interesting region of operation is the combustion stroke, where the most significant changes in forces, pressures and shifts in secondary motions are observed. The bottom region of the piston skirt has a more variable compliance spatially (shown in Figure 7.21); 23mm down the skirt the conformability shows the largest variability. In its initial undeformed condition, the bottom of the piston exhibits the lowest radius and thus in comparison with a perfect cylinder it would yield the lowest r/R ratio. The bottom of the skirt is also the area of lowest stiffness, being the furthest from the structural support provided by the crown and equidistant between the two vertical structural supporting braces. Thus, under load this position is able to conform with the greatest ease. Both of these combine to give this axial position the greatest circumferential conformability range under load.

7.4 Film thickness analysis and verification

Both the input primary motion and resulting secondary motion have been analysed in great detail through this chapter. Little quantitative detail has been given on the film thickness behaviour, other than through the minimum film thickness. The interaction between the observed pressure distributions and the instantaneous film thickness profiles is relatively simple to predict, given one of the two profiles. However, it is crucially important to validate the results of the simulations. For the case of 6250 rpm the validation is presented for the combustion stroke of the 4-stroke engine cycle through means of comparison between measured and predicted film thickness values. For the measurement of the instantaneous film thickness, ultrasonic sensors are employed, as detailed in section 5.5.4.

Due to the intrinsic difficulties of the experimental measurement of film thickness under high speed transient conditions, the data available are not necessarily for the pertinent crankshaft

locations detailed in the two-dimensional pressure analysis of section 7.2.2. Due to limitations in the location of the ultrasonic sensors because of the liner's complex geometry, the sensors can only monitor between 17° and 69° of the combustion stroke; therefore, not all the three-dimensional profile would be visible. A balance had to be struck between the number of sensor positions and the resolution of the observed film shape profile. Hence, only the thrust side was instrumented in an attempt to measure the three dimensional film thickness profile of the liner – skirt conjunction, in an attempt to capture the combination of the effect of the secondary piston dynamics and surface distortions instantaneously on the film thickness. Furthermore, the methodology and equipment used for the ultrasonic measurements only yield reliable data for film thickness values in the order of 0-20µm. This range was, therefore, most ideally suited to the measurement of the anticipated thrust side film thickness values.

After exhaustive data processing, it was found that the largest amount of data successfully collected was between 41° and 66° crank-angle locations for the case of the engine speed of 6250 rpm in the combustion stroke. The following plots present the comparison; the contour plot highlights the shape of the predicted film thickness and shows the magnitude of instantaneous minimum film thickness. As the piston moves through its stroke, the relative observation point between each sensor row and the skirt shifts, i.e. the axial position relative to the top of the piston skirt is detailed with the positional measured film thickness values. The measured film thickness and standard deviation of the measurement, obtained over approximately 70 measurements, are displayed along a series of circumferential cuts where the readings were present. Over the contour plot the position of these circumferential cuts is shown, where a row of sensors are present but have not recorded any values. The cut line is shown but not labelled.

41º ATDC in Combustion stroke
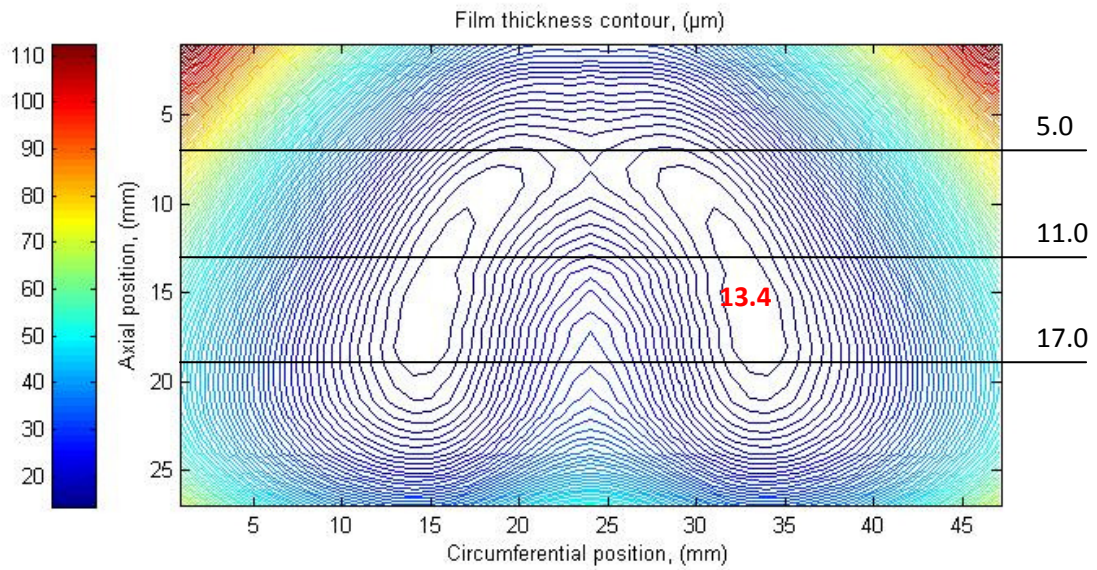
Figure 7.24 - Film thickness contour 6250rpm 41º ATDC
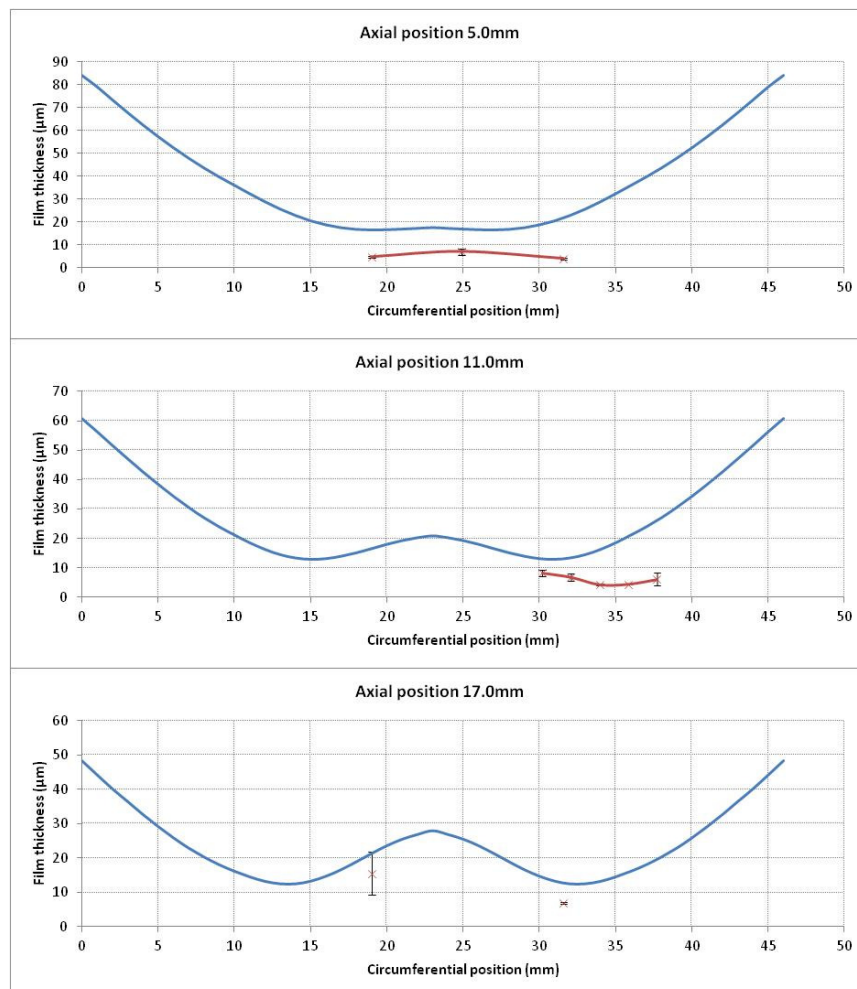
Figure 7.25 - Film thickness comparisons for 6250rpm at 41º ATDC

At 41° the contact load between the liner and skirt is 3771N with a sliding speed of 9.4m/s. In Figure 7.25 each of the 3 rows of sensors functioning monitor a film thickness in the range of 5-15µm. The minimum film thickness recorded is 4µm, 5mm from the top of the skirt, whereas the minimum film thickness predicted is greater at approximately 14µm.

Moving towards the bottom of the skirt at 17.0mm, greater agreement is noted between measurements and numerical predictions. The centre sensor of the 3 was unable to perform a measurement, most likely because a film thickness beyond its measurable range of 0-20µm was encountered. This would agree with the value predicted for this region at 28µm. The two sensors with recorded measurements show good agreement, both being only 3-4µm from the predicted values, but they also reflect the shape of the conjunction geometry qualitatively. From the central row at 11.0mm, of 8 sensors present only 5 yielded results. Although the magnitude of the difference between predicted and measured values is in the range of 3-15µm, the shape of the contact is similar, indicating that the most conforming contact occurs at approximately 9mm from the centre line of the conjunction.

45° ATDC in the Combustion stroke
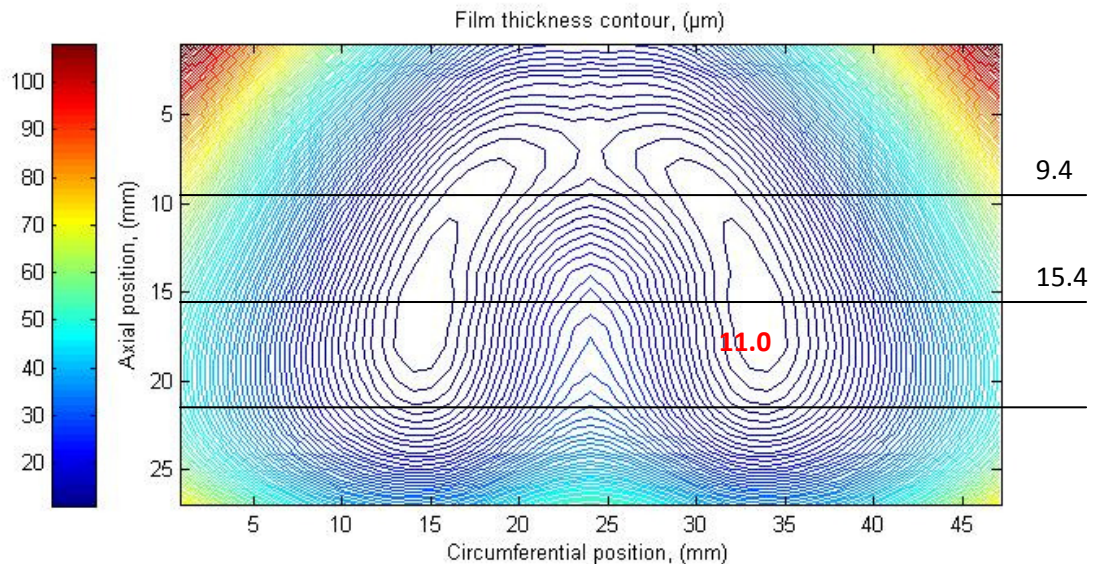
Figure 7.26 - Film thickness contour for 6250rpm at 45° ATDC
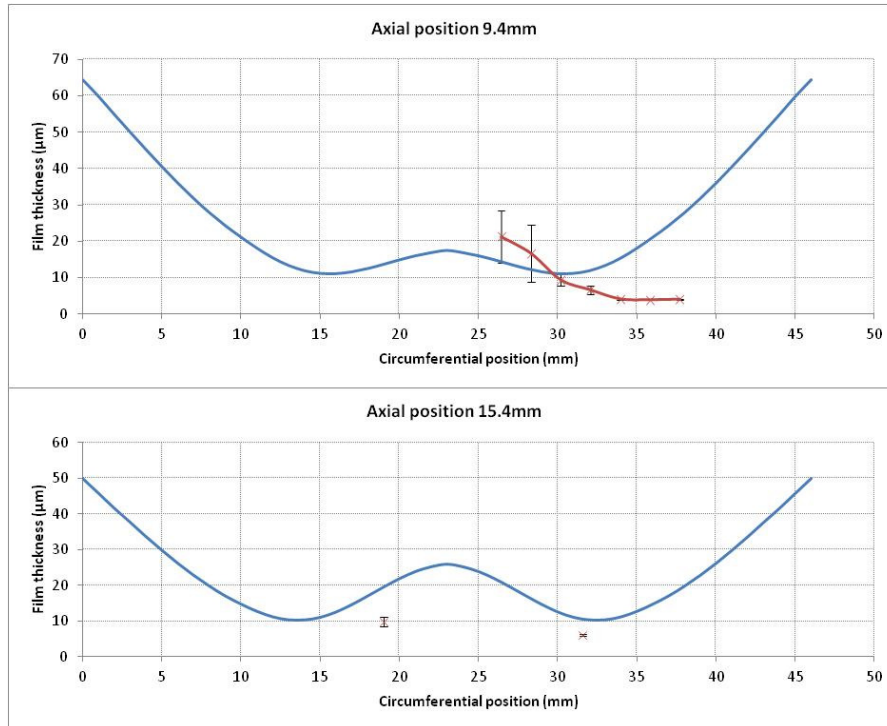
Figure 7.27 - Film thickness comparisons for 6250rpm at 45° ATDC

For the second comparison shown in Figure 7.27, the crank position of 45° was used. At this location there is a thrust side load of 3714N and a sliding speed of 10.3m/s. This position is a lower loaded case than the previous one. However, the maximum hydrodynamic pressure is increased here. As discussed in sections 7.2.1 and 7.2.2 this is as the result of both the increased entrainment speed and the shift of the pressure distribution. The pressure distribution has spread out in the circumferential direction, as a partial result of the distribution being centred closer to the bottom of the skirt due to the clockwise rotation observed. Prediction of relative change is supported by the difference observed in the film thickness measurements recorded. Both the observed positions have moved up along the conjunction, towards a stiffer portion of the piston skirt. For the uppermost reading in Figure 7.27 at 9.4mm from the skirt top, the measured film thickness is thicker compared with that at the 5 mm case at 41°, (Figure 7.25). This change, although not directly comparable due to differing position, load and speed is likely to be as the result of a pair of actions. As one moves towards the piston crown from the maximum skirt radius, the radius of the piston reduces, yielding a larger gap. Between the time steps 41°- 45° there is also a significant clockwise tilt observed which would further act to increase this effective clearance. The

difference in terms of magnitude of the film thickness values recorded is better than in the previous case, with a small difference of approximately 3µm.

The second denser row of sensors at 15.4mm initially shows a greater number of sensors operating within their range; 7 of these sensors in total, as opposed to 5 in the previous case, monitoring a film thickness within their measurement range. The measurements observed show a greater range of between 4 and 21µm, though for the higher readings the range and standard deviation of the results is greater. This yields a standard deviation of almost 50% of the measured value. The indicated mode of deflection agrees with the predicted results, although in a similar pattern to the previous compared case, the contact conformability is at its greatest, approximately at 4mm from the predicted data. The range and magnitude of the readings presented are reassuringly similar.

49° ATDC in the Combustion stroke
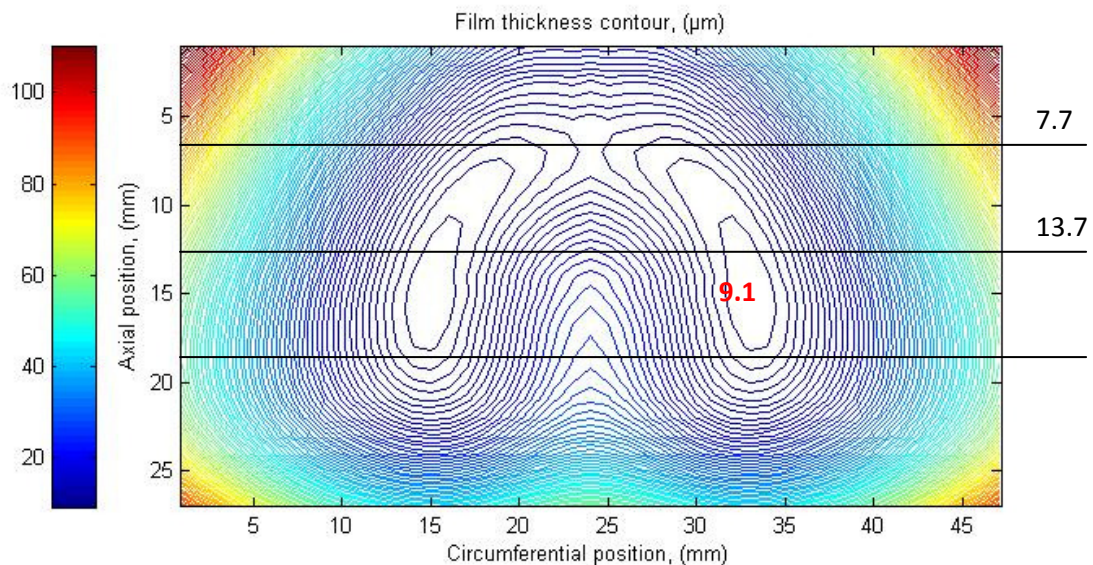
Figure 7.28 - Film thickness contour 6250rpm at 49° ATDC
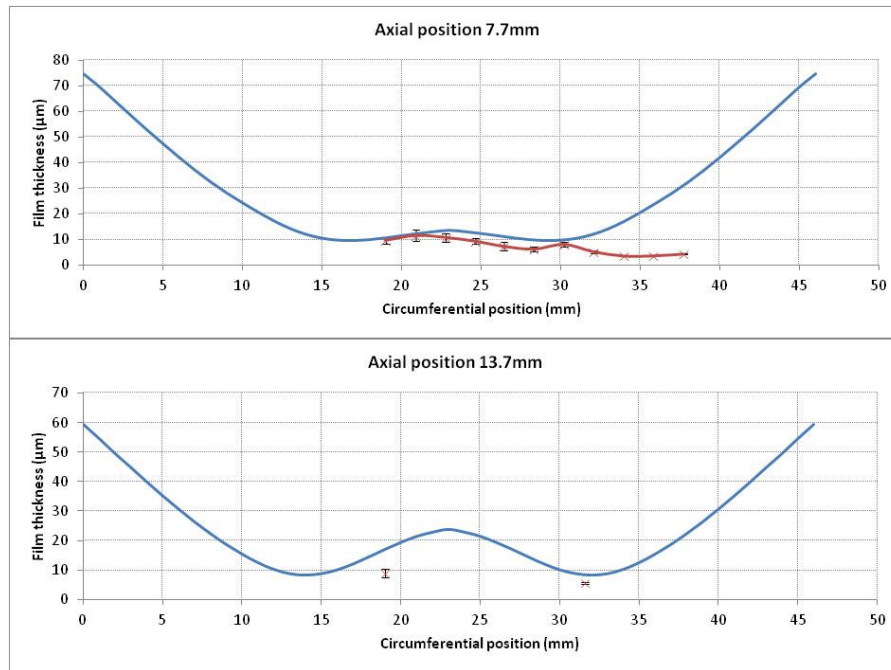
Figure 7.29 - Film thickness comparisons for 6250rpm at 49° ATDC

Moving on to the crank angle position of 49°, shown in Figure 7.28, the side load has decreased again to a value of 3039N and the sliding speed is 11.3m/s. Now the dense row of sensors monitors the uppermost recorded values at 7.7mm (Figure 7.29), a region of increased stiffness (as opposed to the previous measurement position). In the section of the contact showing the greatest predicted conformability (18-30mm) the comparison of film thickness measurement and prediction is very close, most showing the predictions to be within 1-2µm of the measured values. Progressing outwards toward the 38mm location the comparison begins to diverge, with the recorded measurements showing a much greater degree of conformability than those predicted.

The second sets of recorded values at 13.7mm partially agree with those predicted. The second measured point at 32mm is within 2µm of the predicted values. The first measured point at 19mm is further away from the predicted value of 15 µm but it does agree qualitatively with the increasing gap provided by the conjunctional thermo-elastic deformation.

53° ATDC in the Combustion stroke
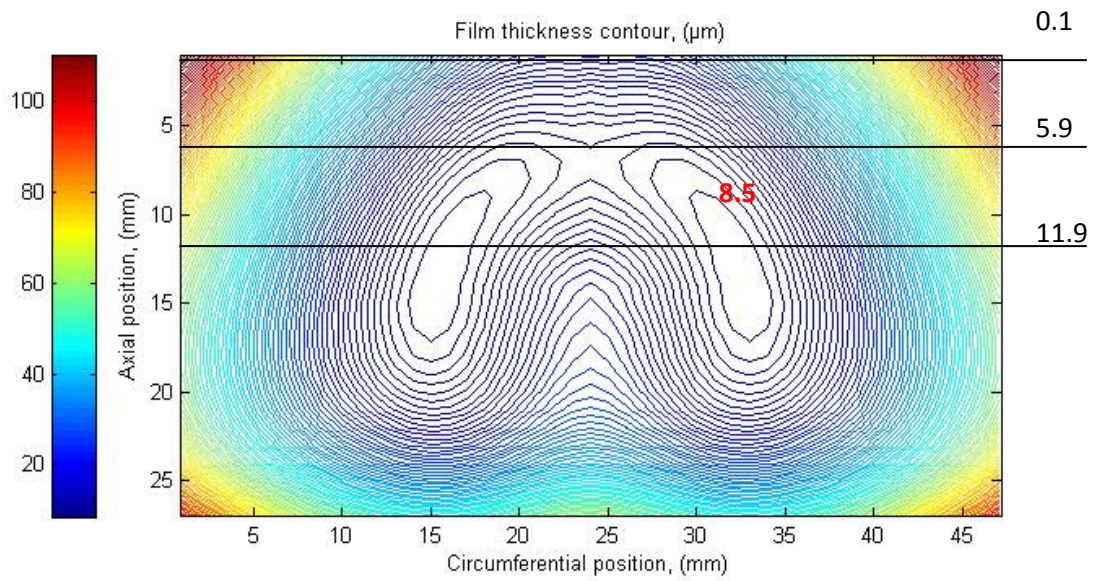
Figure 7.30 - Film thickness contour 6250rpm at 53° ATDC
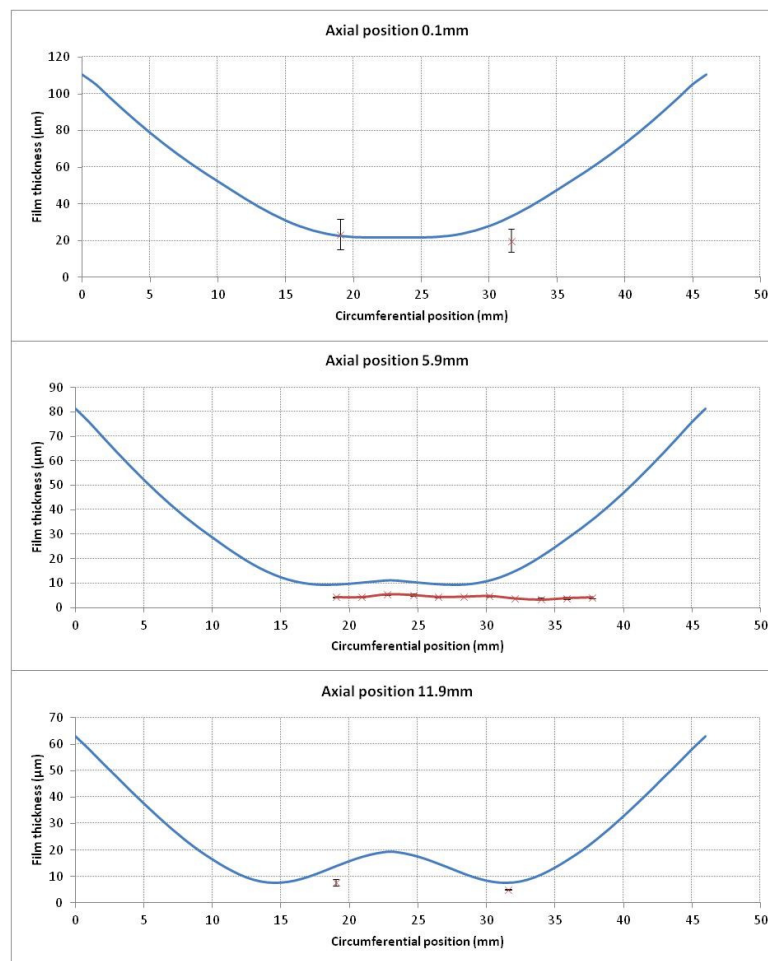
Figure 7.31 - Film thickness comparisons for 6250rpm at 53° ATDC

The uppermost row of three sensors at 0.1mm from the top of the skirt measure values within an acceptable deviation from those predicted for the two positions (Figure 7.31). Their absence from the previous measurement position of 49° and inclusion now is likely due to the reduction in the present film at these locations. This is consistent with the predictions in the observed positions. The two readings at 0.1mm from the top of the skirt align exceptionally well with the predicted values in this circumferential cut. The dense row of sensors observes the conjunction at 5.9mm from the top of the skirt. They show a more uniformly conforming conjunction patch between 19 and 38mm. For the first part the predicted conformability shape agrees well with the measurements, but in a similar fashion to the dense row comparison at 49° the comparison diverges. The results are at the limit of what can be considered a good comparison with the values differing by up to 5µm. The final pair of readings at 11.9mm down the skirt show good agreement again in terms of conformability shape; the absolute film thickness magnitude is comparable with only a 2-3µm difference observed between predictions and measurements.

64° ATDC in the Combustion stroke
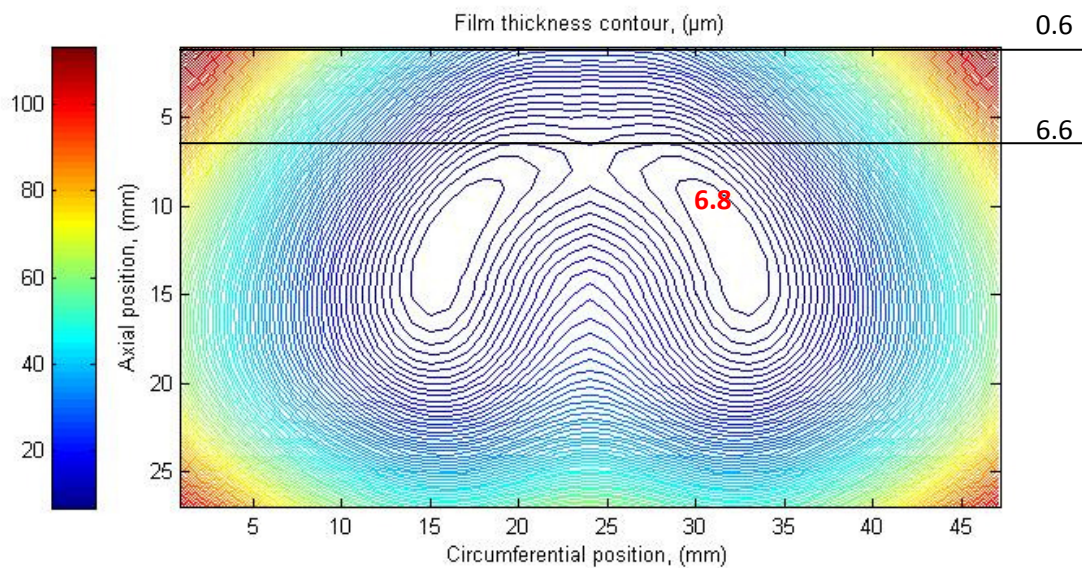
Figure 7.32 - Film thickness contour 6250rpm at 64° ATDC
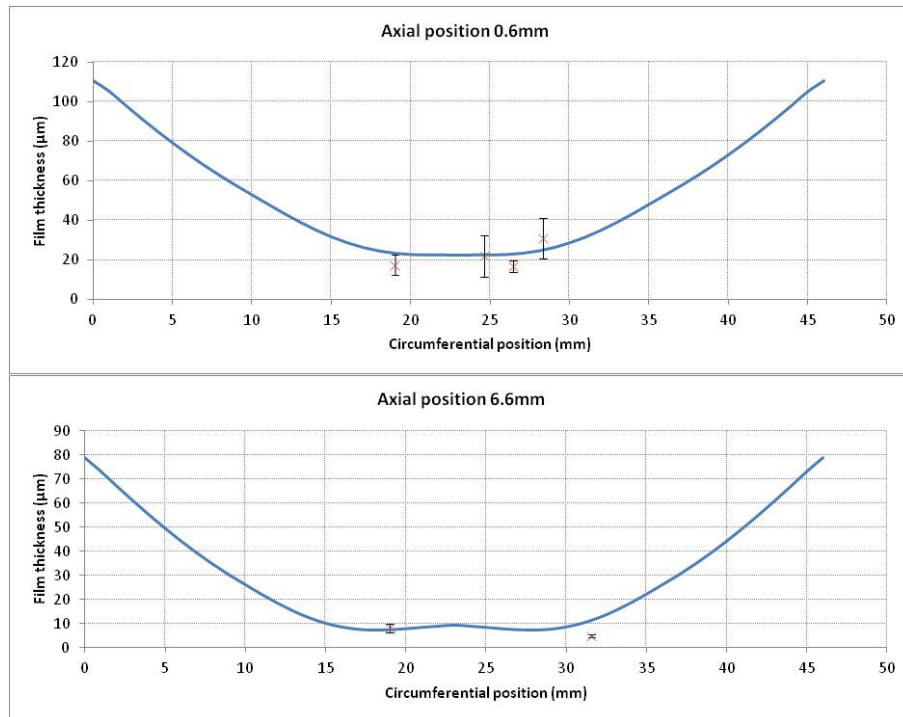
Figure 7.33 - Film thickness comparisons for 6250rpm at 64º ATDC

At 64° crank angle position the upper 3 sensors are located over the ring pack and as such no readings are acquired, whilst the dense row of sensors observe the very top edge of the skirt, (0.6mm) as shown in Figure 7.33. Their readings are at the very limit of their measurement range, achievable by the ultrasonic instrumentation and, therefore, the variability and accuracy of the readings may be considered as rather poor as indicated by the standard deviation of the recorded results. The absence of readings beyond 28mm indicates the clearance/film to be outside the measurement range. This agrees with the prediction of films in the region of 30-47mm circumferentially, all in the range of 30-110µm

7.5   Transient analysis summary and conclusions

This chapter has detailed a great number of the operational parameters critical for adequate and stable operation of the piston skirt – liner conjunction. The two separate speed cases highlight the overall effect with increasing engine speed, component inertia, in-cylinder pressure and mean conjunctional sliding speed. It has also been shown that the overall contribution of three dimensional distortion has a significant, and partially controlling, effect

on the secondary piston dynamics and thus, the resulting conjunction shapes and pressure profiles.

The comparison with film thickness measurements has brought a degree of certainty to the predictions and calculation methodology. The discrepancies between the predicted and measured values do offer a possible insight into the limitations of both the solution methodology and the input criteria, such as *in situ* geometry. Although much of the comparison between film thickness predictions and measurements show relatively good agreement, there is a trend in both the shape and film thickness variation. Firstly, the measured values are, in most cases, lower than those predicted. Secondly, the measured film shapes imply much more conformal contacts with the areas of low film thickness spreading into a much wider circumferential region. Initially a lower film thickness would indicate a lower viscosity of the lubricant present, which could be as the result of a higher than expected realistic conjunction temperature. The observation of increased circumferential conformability agrees with this, a lower value of lubricant would require a more conforming conjunction in order to carry the required hydrodynamic reaction force. This hypothesis cannot be simply confirmed by employing a lower lubricant viscosity, as the calibrated measurement of film thickness is dependent on the lubricant's acoustic properties. By considering the calculation of oil film thickness from its basic formulation (5.3) it can be seen that the oil film thickness measurement is proportional to the oil density and acoustic velocity. $h \propto \rho c^2$; the acoustic velocity is also a function of the density, thus yielding $h \propto \rho^3$. Very simply put, the film thickness predicted for a common pressure but with a hotter lubricant is $h \propto (\ln T)^{-1}$. These two proportionalities show that it is not a simple case of modifying the viscosity to achieve a match as it is a highly non-linear interaction between the two.

There are other limitations in both the predictive and measurement methodologies that add uncertainty to the validity of some comparisons made throughout. Oil supply and availability is assumed to yield a fully flooded inlet conjunction at all times. In the Honda CRF engine used for this analysis the oil is made available to the liner/skirt contact through a combination of the two most common supply mechanisms. It is both splash fed from the partially immersed crank and supplied directly using an oil jet aimed toward the underside of the piston. Aside from oil supply to the conjunction, the oil jet also acts to cool the underside of the piston crown and supply lubricant to the gudgeon pin/piston conjunction. The

combination of these two mechanisms gives good confidence of reasonable oil availability to the skirt/liner conjunction but only in the combustion and intake strokes. The issue of oil availability in the compression and exhaust strokes is a much more complicated, which has not been discussed or quantified in this work, as such only the highly loaded combustion stroke has been analysed in greater detail.

The consideration of bore shape has been included but only in a limited sense. The gross mechanical distortion due to contact skirt reaction force and a basic head loading have been included. However, the thermal distortion has been limited to a single uniformly expanded case. Additional modes of deflection were discussed in section 4.3 but have not been included in the analysis due to the limited boundary data available or the excessive computational demands. These modes of distortion include the differential thermal expansion, in-cylinder pressure and non-uniform cylinder head clamping. These combined would have an effect on the contact conformability and the available free translational space.

The limited approach used to determine the nominal bore diameter using the uniform thermal distribution illustrates the modes of deflection but does not necessarily simulate the true operating 'clearance'. The observations in terms of secondary motion and the mechanical deformation bring into question the accuracy of the nominal of nominal clearance predicted in an engine configuration using a bore and piston as flexible as presented in the case here. In the case investigated here the cumulative deflection outweighs the observed nominal clearance by an order of magnitude under operation, as such the nominal clearance acts to accentuate the secondary motion and increase the lateral momentum, further loading the conjunction under translation. Additionally, the excessive clearances observed at the anti-thrust side under thrust side loading would almost certainly lead to oil film rupture with increasing gaps in a manner that an inlet meniscus may not be formed. When the anti-thrust side is reloaded towards the end of the combustion stroke there would be an absence of a coherent film; as the load is transferred back to the anti-thrust side, the sliding speed is diminished and as such the squeezing of a lubricant film is the reliant mode of load carrying. Thus, without a coherent film in place the likelihood of surface contact would significantly increase.

Again the approach limitations have been created as a result of the uncertainty in the instantaneous 3D temperature profiles of both the piston and the liner.

Chapter 8.
Overall conclusions & suggestions for further work

8.1 Conclusion

Historically, simulations of piston skirt lubrication and the derived secondary motion have been achieved using rigid body dynamics solutions. Recent research and the significant improvement in computational power, particularly over the past decade, have facilitated the advancement of elastic tribological conjunction simulations. Even with the current developments in computational resources, the recent work in this research uses multi-grid operators with reduced statically dependant flexibility models. This approach has highlighted the interaction between the flexible liner and piston skirt and the effect of the tribological conjunction formed between the two surfaces. It has been shown that the detailed structural design is critical in controlling the formation of lubricated pressure distributions. Through the years, the geometry of the piston – crank mechanism has been used to manipulate the secondary motion of the piston. Some geometrical changes, such as an offset gudgeon pin, have been implemented to induce secondary motion but reduce the NVH effect. With the concentration focused on raw performance, the inclusion of an offset crank avoids the effect of significant side load at reversals, as such this does not force significant loads to be supported by the squeezing action of the lubricant.

Solving the combined conjunction flexibility and lubrication provided a solution for the conjunction geometry. Crucially a comparison and validation has been made with the ultrasonic recorded measurements. The comparison process is though not a completely separate line of research, the alignment of sensors with the regions of predicted film thickness minima aided the final result correlation. This comparison showed a good level of agreement between predicted and measured values of film thickness. The degree of conformability varied across some of the measurements, as alluded to in chapter 7. Although the simulation process is thorough, there is still a multitude of uncertainties present in the prediction methodology. These uncertainties can be classified in two types; solid and lubricant state errors. The solid errors and inaccuracies originate from the uncertainty in the boundary conditions, Additional modes of distortion on the liner induced by un-even head clamping

loads, in cylinder pressure and differential thermal expansion have not been incorporated in to the analysis. The true instantaneous and variable 3D temperature profile of the piston has been excluded from this analysis due to the difficulties encountered in such measurements. The accurate response of the lubricant to changes in pressure and temperature are well understood and characterised by the industrial partners, again the input boundary conditions to these calculations contain a level of uncertainty. As with the solid boundary constraints, the temperature field within the variable conjunction contains a level of uncertainty. Since the response of the lubricant to temperature is exponential, the potential for gross inaccuracies is significant. The significance of the oil availability in the contact has not been considered. It has been assumed that during down strokes there is a free and generous supply of lubricant on the surface of the liner. In the upward strokes the oil can only be supplied by the reservoir formed between the mouth of the contact and the oil control ring. Finally the formation of a coherent fluid film between two surfaces is limited by the separation distance between the two and the meniscus force present in the given lubricant state. The rupturing of the film at a certain separation and reformation has not been included, as the mapping of the lubricants response has not been available.

8.2 Achievement of aims

The project set out to develop fundamental knowledge surrounding the piston skirt – liner conjunction. The effects of realistic high contact loads and piston sliding speeds for fired engine on the transient operational characteristics of the piston have been detailed throughout.

More specifically, the research aimed to ensure the predictive tools were sufficiently validated with accurate representative measurements. This overall aim has been achieved through detailed comparisons with measured oil film thickness results. The variable operational parameters of the engine and their effects on the behaviour of the conjunction have been ascertained.

Finally, an important aim was to combine flexible multi-body dynamics with the transient tribological analysis of the piston – liner conjunction. This has been achieved and the effects of global thermo-elastic distortion of the body structures on the dynamics of the piston assembly were ascertained.

8.3 Contributions to knowledge

There are various contributions to knowledge in this thesis. These are:

- A numerical methodology is developed, which is multi-scale, multi-physics in nature. This incorporates rigid body inertial dynamics of the piston in its primary axial motion and secondary lateral and tilting motion (relatively large displacement dynamics). It also includes thermo-elastic deformation of the piston skirt (in sub-millimetre scale), as well as micro-scale lubricant film formation. The methodology incorporates physics of inertial dynamics, structural dynamics, thermal analysis, contact mechanics and lubrication. A comprehensive solution, such as this under transient conditions has not hitherto been reported in literature.

- The thesis reports on combined numerical and experimental investigations, which for the case of piston skirt-liner conjunction is rather unique and shows reasonably good conformance between the experimental measurements of film thickness and numerical predictions. This is an approach, which further highlights the underlying multi-physics nature of the problem and leads to fundamental understanding of conjunctional behaviour, an approach not reported in literature thus far.

- The thesis also contributes to knowledge and technological advance in terms of piston skirt technology for high speed and contact loads, which occur in high performance race engines. Furthermore, significant effort is expended in data acquisition and retrieval from very confined spaces and large volume signal processing at engine speeds not reported by others.

8.4 Suggestions for future

A number of areas for further work are suggested that can extend or improve upon the approach undertaken in this thesis. These suggestions concern experimental investigations, as well as numerical analysis.

- Clearly, increasing the number of ultrasonic film thickness measuring sensors would yield a better measurement resolution. This would yield a more accurate representation of the oil film thickness contour, thus the conjunctional shape at any instant of time. Miniaturisation of sensor size would also improve the spatial resolution of a measurement array of these. Smaller sensors will also provide a smaller divergence of the emitted ultrasonic wave, which essentially propagates in a conic form. An increase in the number of sensing arrays, however, would represent a significant challenge in terms of large volume signal processing and data manipulation. Furthermore, complex wiring in very confined spaces would pose another challenge.

- Accurate representation of temperature gradient along the piston skirt and the cylinder liner is essential for more precise predictive analysis, as described below. However, arrays of thermocouple tapping or more advantageously miniature light weight thermistors need to be attached to the outer surface of the liner and the inner cavity surface of the piston skirt. Provisions have to be made to route the data stream from these remote locations to data acquisition and processing systems. In practice grass-hopper links or telemetric methods have been used in such cases. However, at high speeds encountered in the developed set up there may be significant difficulties with telemetric devices. Additionally, use of grass-hopper link is probably inappropriate for light weight high speed engine piston assemblies such as that of the Honda CRF 450R, because the dynamics of piston-crank system would be significantly affected.

With respect to numerical analysis, the most pertinent potential improvements may be:

- Although lubricant temperature is adjusted with respect to the average liner surface temperature, the approach undertaken is otherwise "isothermal" in nature. Contact thermal analysis involves either the solution of energy equation or a somewhat simplified control volume instantaneous thermal balance approach, such as that reported by **Morris** et al (2013b). They show that the temperature of the lubricant rises at the inlet to the conjunction by heat convection from the bounding surfaces into the lubricant. Subsequently, the temperature of the lubricant further increases due to its shear in transit through the contact. Ultimately at any instant of contact, the temperature of the lubricant is slightly above that of the moving surface (i.e. the piston skirt surface), which is in turn higher than that of the stationery surface (i.e. the liner). This means that in turn the lubricant film takes some of the heat away by convection, with the remaining heat conducted away by the solid surfaces. The proportion between these depends upon the film thickness. It is, therefore, quite clear that simple average measure for surface temperature is not adequate to fully represent the thermal balance in the contact, which would affect the thermo-elastic distortion of the solids as well. Deviations in measured and predicted conformity in chapters 6 and 7 are indications of this anomaly.

- The differences noted in the conformity in some of the comparative work between numerical predictions and measured data may also be due to bore out of roundness, which is considered to be a perfect right circular cylinder. Furthermore, it is assumed that any emerging clearance would be filled with a film of lubricant as a flooded inlet is considered for all contacts on the thrust and anti-thrust side. This is not always true of tribological contacts as a relatively large gap may not be conducive to formation of a meniscus of lubricant as a bridge between the contiguous surfaces. Equally well, the measurements indicate the presence of films in all diverging gaps, which may be filled with lubricant vapour or liberated gas from the solution due to cavitation. Therefore, enhanced numerical analysis may be used to include the effects of starvation and cavitation.

References

Abbes, M.T., Maspeyrot, P., Bounif, A. and **Frene, J.** (2004) A thermo-mechanical model of a direct injection diesel engine piston. *Proc. IMechE, Part D: J. Automobile Engineering*, **218**, p395-409

ACEA, European automotive manufacturers association, http://www.acea.be/index.php/news/news_detail/cost_effectiveness_must_guide_progress/

Baker, C.E., Theodossiades, S., Rahnejat, H. and **Fitzsimons, B**. (2012) Influence of in-plane dynamics of thin compression rings on friction in internal combustion engines. Transactions of the ASME, Vol. 134 Article 092801-1,11

Bai, D.(2012) Modeling piston skirt lubrication in internal combustion engines. *PHD Thesis*, Massachusetts institute of technology

Balakrishnan S (2002) Transient elastohydrodynamic analysis of piston skirt lubricated contact under combined axial, lateral and tilting motion *PhD Thesis* Loughborough University, Loughborough, UK

Balakrishnan, Howell-Smith, and **Rahnejat,** (2005). Investigation of reciprocating conformal contact of piston skirt-to-surface modified cylinder liner in high performance engines. *Proc. IMechE, Part C: J. Mechanical Engineering Science*, **219**(11), 1235–1247. DOI: 10.1243/095440605X32147.

Barus, C. (1893) **"**Isothermals, Isopiestics and Isometrics relative to Viscosity". *American Journal of Science*, Volume 45, p87.

Betts, H. (1997): Offset piston pins in reverse rotation engines. *The Edge*, Engine-tech Inc, Texas, November

Blau P.J., Qu J. (2004) Laser Surface Texturing of Lubricated Ceramic Parts, *FY 2004 Progress Report on Heavy Vehicle Propulsion Materials, pp. 123-128, URL: http://www1.eere.energy.gov/vehiclesandfuels/pdfs/hv_propulsion_04/4k_blau-laser.pdf*

Blok, **H**. (1965): Inverse problems in hydrodynamic lubrication and design directions for lubricated flexible surfaces. *Proceedings of the International Symposium on Lubrication and Wear*, D. Mester and B. Sternlicht (eds.,), McCutchan, Berkeley, p1-151

Bosch (2007): Automotive Handbook, 7th Edition, John Wiley and Sons

Brown M.A., **McCann, H.** and **Thompson, D.M.** (1993): Characterization of the oil film behaviour between the liner and piston of a heavy duty diesel engine. Tribological Insights and Performance Characteristics of Modern Engine Lubricants, SAE/SP-93/996/932784

Cameron, B.,(1952) Hydrodynamic lubrication of rotating discs in pure sliding. A new type of film formation. J. Inst. Petrol. 37, p. 332, 1951: AMR 5.

Courtney-Pratt, J.S. and **Tudor G.K.** (1946) An analysis of the lubrication between the piston-rings and cylinder wall of a running engine. *Proc IMechE* **155** p293-299

Crouch, R.F., and **Cameron, A.** (1961) Viscosity-temperature equations for lubricants. Journal of institute of petroleum, Volume 47, p307-313

D'Agostino,V. (2006) Optimised EHL piston dynamics computer code, AITC-AIT 2006 international conference on Tribology

Danial (1994),From Nastran to Matlab, Weblink; http://danial.org/op4/

De La Cruz, M. (2011), The influence of transient thermo-elastohydrodynamic conjunctions on automotive transmission rattle, PhD Thesis, Loughborough University

De La Cruz, M, Chong, W.W.F., Theodorescu, M., Theodossiades, S. and **Rahnejat, H.** "Transient mixed thermo-elastohydrodynamic lubrication in multi-speed transmissions", *Tribology international* **49**, 17-29

Dell, R, and Rand, D, (2004), Clean Energy, *The Royal Society of Chemistry*, Cambridge, UK

Dias da Cunha R and Hopkins T (1994) PIM 1.1 — The parallel iterative method package for systems of linear equations user's guide — Fortran 77 version Technical Report Computing Laboratory, University of Kent at Canterbury, Kent, UK

Dow, T. A., Schiele, C. A. and **Stockwell, R. D.** (1983) "Technique for experimental evaluation of piston-ring/cylinder film thickness". *J. Lubr. Technol.* **105** pp 353.

Dowson, D. and **Higginson**, G.R. (1959): "A numerical solution to the elastohydrodynamic problem". *Journal of Mechanical Eng. Science*, Part 1, Volume 6.+

Dowson, D., Higginson, G.R., and **Whittaker, A.V.** (1962): Elastohydrodynamic lubrication: a survey of isothermal solutions. *Journal of Mechanical Eng. Science*, Volume 4

Dowson, D (1968) History of Tribology, (Professional engineering publishing) Second edition, (1998) ISBN 1 86058 070 X

Dowson, D., **Taylor, C.M.** and **Godet, C.M.** (1983): Tribology of Reciprocating Engines. *9th Leeds-Lyon Symposium on Tribology* (Butterworth, Oxford), p 348

Dursunkaya, Z. and Keribar, R. (1992). Simulation of secondary dynamics of articulated and conventional piston assemblies. *SAE Paper No.* 920484

Dwyer-Joyce, T., Drinkwater, B.W. and **Donohoe, C.J**., (2003) The measurement of lubricant-film thickness using ultrasound. *Proc R. Soc. Lond. Ser. A: Math. Phys. Eng. Sci.* **459**(2032), p957-976

Dwyer-Joyce, R.S., Green, D.A., Harper, P., Lewis, R., Balakrishnan, S. King, P.D., Rahnejat, H. and **Howell-Smith, S.** (2006), The Measurement of Liner Piston Skirt Oil Film Thickness by an Ultrasonic Means. *SAE paper No* 2006-01-0648

Ertel, A.M. and Grubin, A.N. (1949): Investigation of Scientific and industrial research. Book 30, Central Scientific Research Institute for Technology and Mechanical Engineering, Moscow

Etsion, I. "Surface texturing for in-cylinder friction reduction", in Rahnejat, H. (Ed.), Tribology and dynamics of engine and powertrain, 2010, Woodhead Publishing, Cambridge, UK, ISBN 978-1-84569-361-9

Evans H.P., Snidle R.W., (1982) The elastohydrodynamic lubrication of point contact at heavy loads. *Proc. R. Soc. Lond. A* **382** no.1782 p183-199

Federal Mogul, MTZ 05/2012 Volume 73, Piston Ring coating reduces gasoline engine friction

Furuhama, S. and **Sumi, T. A**. (1961) "A dynamic theory of piston ring lubrication, 3rd report: measurement of oil film thickness". *Bull JSME* 4(16) p744.

Garcia-Atance F, Smith, G.E.H and **Sherrington, I**.(2013) "A high-Precision, High-speed system for measuring instantaneous lubricant film thickness profiles. WTC conference 2013 Torino, Italy September 8-13th.

Gatcombe E.K., (1945) "Lubrication characteristics of involute spur gears-a theoretical investigation" *Trans. ASME* **67** (1945), p177-188.

Gohar and Rahnejat (2008) "Fundamentals of Tribology", Imperial College Press. ISBN 13 978-1-84816-184-9.

Greenwood, J. A. and **Tripp** (1970), J. H. The contact of two nominally flat rough surfaces. *Proc. Instn mech. Engrs*, **185**, p625-633.

Grimble, D (2009) Ultra-thin film Tribology of elastomeric seals in pressurised metered dose inhalers, PHD thesis, Loughborough

Grubin, A.N. and Vinogradova, I.E (1949): Investigation of scientific and industrial Research. Book 30, Central Scientific Research Institute for Technology and Mechanical Engineering, Moscow.

Guzzomi, A. L., Hesterman (2008) D. C., and Stone, B. J. Variable inertia effects of an engine including piston friction and crank/gudgeon pin offset. *Proc. IMechE, Part D: J. Automobile Engineering* , **222**, p397–412.

Hamrock, B. J. (1980): Film Thickness for different regimes of fluid-film lubrication. NASA Technical Memorandum 81550

Hamrock, B. J. (1994): Fundamentals of fluid film lubrication, McGraw-Hill

Hartfield-Wünsch, S.E., Tung, S.C. and **Rivard, C.J.** (1993): Development of bench wear test for the evaluation of engine cylinder components and the correlation with engine test results. Tribological Insights and Performance Characteristics of Modern Engine Lubricants, SAE/SP-93/996/932693

Hertz, **H**. (1896): Miscellaneous papers by H. Hertz. Eds. Jones and Schott, Macmillan London, p146-162

Heywood, **J. B.**, (1988) "Internal combustion engine fundamentals". McGraw-Hill Higher Education; ISBN-10: 0071004998.

Honda Motor Company (2002): Owners Manual, CRF450R, Part number 69MEB510 00X69-MEB-6101

Hoshikawa, J., Kiminari, K., Miyamoto, K. and **Higashi, H**. (2011). A study of friction reduction by 'soft skirt' piston. *SAE paper No* 2011-01-2120

Howell-Smith, **S J** (2010/2013) Private communication

Howell-Smith, S.J (2011) Tribological optimisation of internal combustion engine piston-bore conjunction through surface modification, PhD Thesis

Jalali-Vahid, D. (2000): Transient analysis of isothermal elastohydrodynamic point contact. PhD thesis, University of Bradford.

Johnson, K.L.(1985):Contact Mechanics. Cambridge University Press, ISBN 0521- 34796-3

Kerr (1995) Cylinder systems, the basics. AE Goetze

King, J. (2007) Review of low-carbon cars Part I: the potential for CO2 reduction. HMSO, October 2007.

Knoll, G.D. and **Peeken, H.J.** (1982): Hydrodynamic lubrication of piston skirts. *Transaction of the ASME*, Volume 104, p504-509

Ladommatos, N., Xian, Z. and **Zhao, H**. (2004) The effect of piston bowl temperature on diesel exhaust emissions, *Proc.ImechE, Part D: Journal of Automobile Engineering* 2005 p219-371

Li, D.F., Rhode, S.M. and **Ezzat, H.A.** (1981): An automotive piston lubrication model. *ASLE Transaction,* **26**, p151-160

Liu, K., Xie, Y.B. and **Gui, C.L.** (1998): A comprehensive study of the friction and dynamic motion of the piston assembly. *Proc. Institution of Mechanical Engineers Part J,* **212**, p221-226

Luo, W., Yan, M., Zhu, W.Z. and Cantor, B. (2002): An experimental study on the melt spinning of AA2618 alloy, *Journal of Materials Science* **37**, p2685-2691

Ma, M.T., Smith, E.H and Sherrington, I. (1995a): Three dimensional analysis of piston ring lubrication, Part 1: Modelling. *Proc. Institution of Mechanical Engineers Part J*, **209**, p1-14

Ma, M.T., Smith, E.H and Sherrington, I. (1995b): Three dimensional analysis of piston ring lubrication, Part 2: Modelling. *Proc. Institution of Mechanical Engineers Part J*, **209**, p15-27

Mahle (2013), Piston technology for modern combustion engines, Online.

http://www.mahle.com/C1256F7900537A47/vwContentByKey/W29BDBWJ144STULEN/$FILE/EN_01_MAHLE_Piston%20technology.pdf – retrieved 08/11/2013

McClure, F (2007) Numerical modelling of piston secondary motion and skirt lubrication in internal combustion engines, PhD thesis, Massachusetts institute of technology.

McFadden, P.D and **Turnbull, S.R**., (2011) Dynamic analysis of piston secondary motion in an internal combustion engine under non-lubricated and fully flooded lubricated conditions. *Proc. ImechE Part C*, **225,** p2575-2585

Meldahl A. (1941) Contribution to the theory of the lubrication of gears and of the stressing of the lubricated flanks of gear teeth. *Brown Boveri Rev*. 28 11, p374.

Morris, N., De la Cruz, M., Rahmani, R., Leighton, M., Rahnejat, H. and **King, P.** (2013a). A numerical and experimental approach in understanding the performance of textured surfaces in sliding contacts. WTC conference 2013 Torino, Italy September 8-13th.

Morris, N., Rahmani, R., Rahnejat, H., King, P.D. and **Fitzsimmons, B.** (2013b) "Tribology of piston compression ring conjunction under transient thermal mixed regime of lubrication" *Tribology international*, **59**, p248-258

Muskhelishvili, N.I (1963): Some Basic Problems of the Mathematical Theory of Elasticity: Fundamental Equations, Plane Theory of Elasticity, Torsion, and Bending, 4th corr. and augm. ed. Groningen: P. Noordhoff

Newmark, N., M., (1959): A method of computation for structural dynamics. *Transactions of ASME, Journal of Engineering, Mechanical Division*, **85** EM3 p67-94

Newton, I. (1674): Mathematical principles of natural philosophy. Lib. II, Sec. II, London

Ning, L., Meng, X. and **Xie, Y**. (2012). Incorporation of deformation in a lubrication analysis for automotive piston skirt-liner system, *Proc. ImechE Part J,* **227**(6), p654-670

Notay, R.S., Priest, M. Fox, M.F and **Coy, R.C** (2013) Influence of lubricant degradation on measured piston ring film thickness in a fired gasoline reciprocating engine, WTC conference 2013 Torino, Italy September 8-13th.

O'Connor, A (2008) Tata nano – world cheapest new car is unveiled in India, The Times, January 11th 2008, http://www.thetimes.co.uk/tto/life/fashion/mensstyle/article1761748.ece, Retrieved, October 2013.

Oh, K.P, Li, C. H. and **Goenka, P. K.** (1987): Elastohydrodynamic lubrication of piston skirts. *ASME Journal of Tribology,* **109**, p356-362

Offner, G and Priebsch, H. H. (2000): Elastic body contact simulation for predicting piston slap induced noise in an ic engine. In multi-body dynamics; Monitoring and simulation techniques – II, ISBN 1 86058 258 3

Otto (1877) Improvement in gas motor engines, US pat 194047

Patir. N & Cheng,H (1978) An average flow model for determining effects of three dimensional roughness on partial hydrodynamic lubrication, *Trans ASME journal of lubrication technology,* **100**, p12-16

Paul, B. and **Hashemi, J** (1979): Numerical determination of contact pressures between closely conforming wheels and rails. *Technical Report No. 8*, Federal Railroad Administration Washington

Peppler W., (1936) Untersuchungen uberdie Druckubertragung bei belasteten und geschmierten umlaufenden achsparallelen Zylindem. In: *Maschinenelemente-TatungAachen* **42**, VDI, Berlin (1935), p1936.

Petrusevich A.I (1951) "Fundamental conclusions from the contact hydrodynamic theory of lubrication". *Izo. Akad. Nauk SSSR OTN 2*, p209.

Priest, **M** (2006) Reducing automotive friction through Tribology, Internal Leeds seminar

Ragot P. and **Rebbert M.** (2007): Investigations of crank offset and it's influences on piston and piston ring friction behaviour based on simulation and testing. *SAE international* (SP-2073) Detroit, Michigan (2007-01-1248)

Rahnejat, H. (1998): Multi-Body Dynamics; Vehicles, Machines and Mechanisms, John Wiley & Sons, ISBN 10 1-84816-184-0

Rahnejat, H. (1984): Influence of Vibration on Oil Film in Concentrated Contacts. PhD. Thesis, Imperial College of Science and Technology, University of London

Rahnejat, H., Balakrishnan, S., King, P. D., and **Howell-Smith, S.** (2006) In-cylinder friction reduction using a surface finish optimization technique. *Proc. IMechE, Part D: J. Automobile Engineering*, **220**, p1309–1318.

Rahmani, R. (2008) An investigation into analysis and optimisation of textures slider bearing with application in piston-ring/cylinder liner contact. PhD Thesis, Anglia Ruskin

Rahmani, R., Theodossiades, S., Rahnejat, H. and **Fitzsimons, S**. (2012) Transient elastohydrodynamic lubrication of rough new or worn piston compression conjunction with an out-of-round cylinder bore. *Proc. ImechE part J,* **226**(4). p284-305

Reynolds, O. (1886): On the theory of lubrication and its application to Mr. Beauchamp Tower's experiments, including and experimental determination of the viscosity of olive oil. *Transaction of Royal Society, London*, **177**, p157-234.

Ricardo, Dursunkaya, Z (1994) A model of piston secondary motion and Elastohydrodynamic skirt lubrication, *Journal of Tribology*, **116**, p777-785

Roelands, C.H., (1966): Correlational Aspects of the Viscosity-Temperature-Pressure Relationship of Lubricating Oils, O.P. Books Program, University Microfilm, Ann Arbor, Michigan

Ronen, A. Etsion, I. Kligerman, Y. (2001) Friction reducing surface texturing in reciprocating automotive components. *Tribology Transactions*, **44**, No 3 p359-366

Saad, P., Kamo, L., Mekari, M., Bryzik, W., Wong, V., Dmitrichenko, N., and **Mnatsakanov, R.** (2007) Modelling and measurement of tribological parameters between piston rings and liner in a turbocharged diesel engine. *SAE paper No* 2007-01-1440.

Saad, Y (2003). Iterative methods for sparse linear systems, Second edition ISBN 9780898715347

Sommerfeld, A. (1904). "Simplified Deduction of the Field and the Forces of An Electron Moving in Any Given Way". Akad. van Wetensch. te Amsterdam 13. (English translation 7, 346 (1905)).

Stachowaik, G.W., and **Batchelor, A.W**., (2001) Engineering Tribology, Second edition ISBN 0-7506-7304-4

Stribeck, R. (1901) "Kugellager fur beliebige belastungen". *Z. Ver. Deutsche Ing.*, **45**, p73-125.

Suhara, T., Ato, S., Takaguchi, M. And Furuhama, S. et al (1997), Friction and lubrication characteristics of piston pin boss bearings of an automotive engine, *SAE paper No* 970840

Szabo,B and **Lee,G** (1969) Derivation of stiffness matrices for problems in plane elasticity by Galerkin's method, *Int.J. Numerical methods in engineering*. **1.** p301-310

Tamminen, J., Sandstrom, C-E., and Andersson, P. (2006) "Influence of load on the tribological conditions in piston ring and cylinder liner contacts in a medium-speed diesel engine". *Tribology International*. **39**. p1643-1652.

Tattersall, H. G., (1973): The ultrasonic pulse-echo technique as applied to adhesion testing, *Journal of Physics D: Applied Physics*, **6**, p819

Timoshenko, S.P. and **Goodier, J.N**.(1970): Theory of Elasticity. McGraw Hill, New York

Tower, B. (1883): First Report on Friction Experiments (Friction of Lubricated Bearings). *Institution of Mechanical Engineers Part J*, p632-659

Usher A.P. (1970): A History of Mechanical Inventions, Harvard University Press, p135

VW (2010) Online price list, retrieved April 2010 http://www.volkswagen.co.uk

Wing, R. D., and **Saunders, O**. (1972): Oil film temperature and thickness measurements on the piston-rings of a diesel engine. *Proc. of the IMechE*.**186**. p1–9.

Zhu, D. HU, Y and **Cheng H. S.** (1993) A numerical analysis for piston skirts in mixed lubrication Part II: Deformation considerations, *Journal of Tribology*. **115.** p125-133

Zienkiewicz, O.C. and **Taylor, R.L.** (2000): The finite element method Vol. 1, 5th Ed., Butterworth Heinnemann, Oxford, ISBN 0750651601
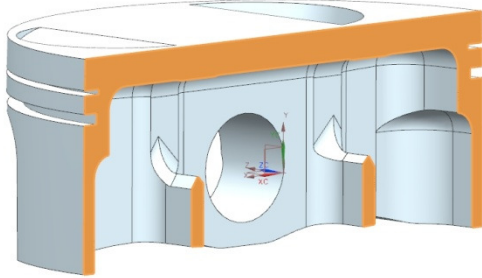
Piston mirror boundary

Due to the symmetry of geometry and loads the *Z* direction across the highlighted planes was constrained to zero translation, (1,1,0)
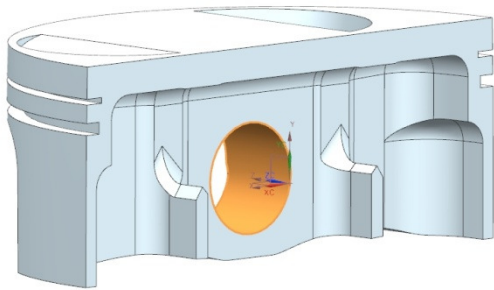
Pin Bore constraint

For static stability all the nodes lying on the highlighted surface were constrained (0,0,0)
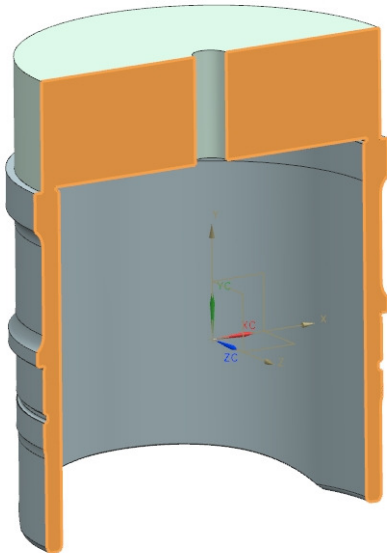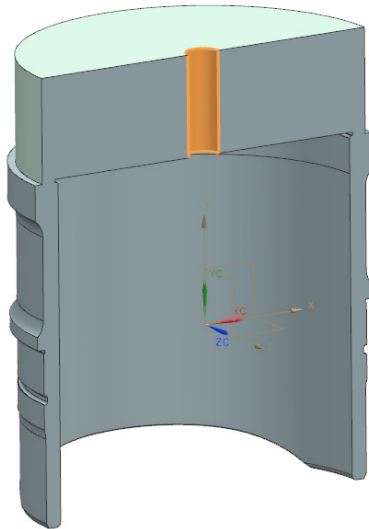

Liner Mirror boundary

Due to the symmetry of geometry and loads the *Z* direction across the highlighted planes was constrained to zero deflection
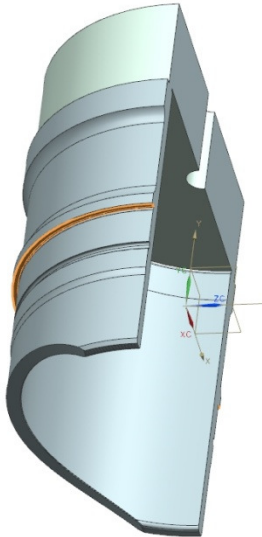
Mid height support flange

The mid height support flange surface is constrained such that no translation of the surface nodes is permitted normal fto the surface in the y direction (1,0,1).

Head location

The location of the dummy cylinder head is fixed in the XZ directions. This replicates the axial location provided by the head bolts and the friction between the head and liner.
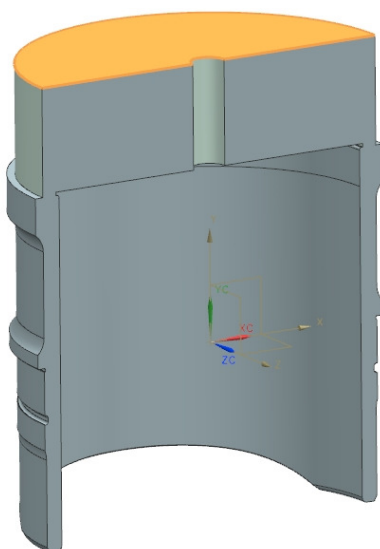
Cylinder head clamping load

The clamping load of the cylinder head is applied over the surface of the dummy head.

This section details the thermal boundary conditions used in order to generate the thermally distorted profiles discussed in section 4.3.9. Any surfaces not detailed on the models below were considered as perfectly insulated. The thermal boundary co-efficients and bulk temperatures have been derived by **Howell Smith** (2011) so as to generate a thermal profile on the piston similar to that of **Bosch** (2007).
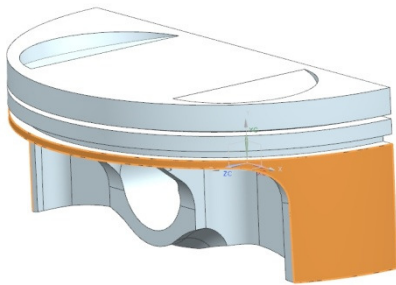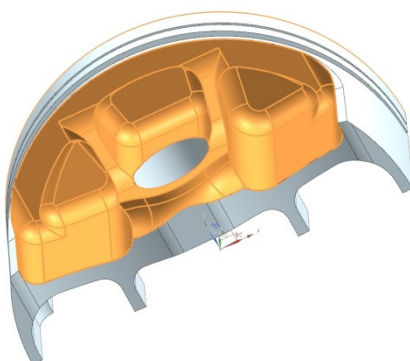

Piston Skirts & 3rd land

Convection, Temp $(157^{o}C)$ $4500Wm^{-2}K^{-1}$
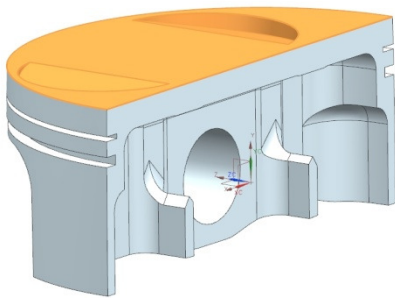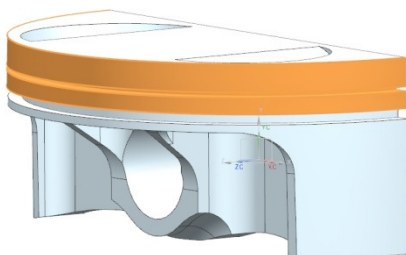

Piston Top surface

Convection, Temp $(627^{o}C)$ $1600Wm^{-2}K^{-1}$

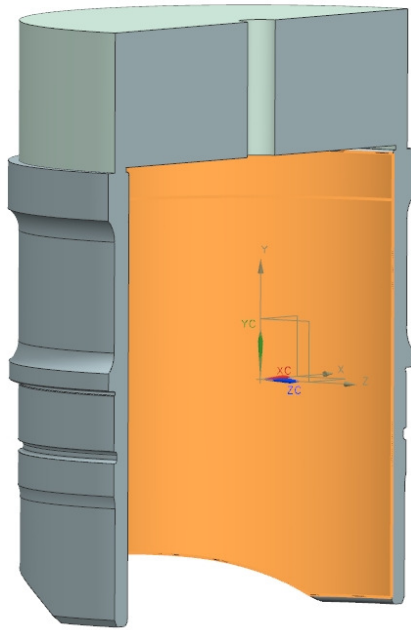**Underside of piston**

Convection, Temp $(157^{o}C)$ $2500Wm^{-2}K^{-1}$

Ring pack of piston including groves
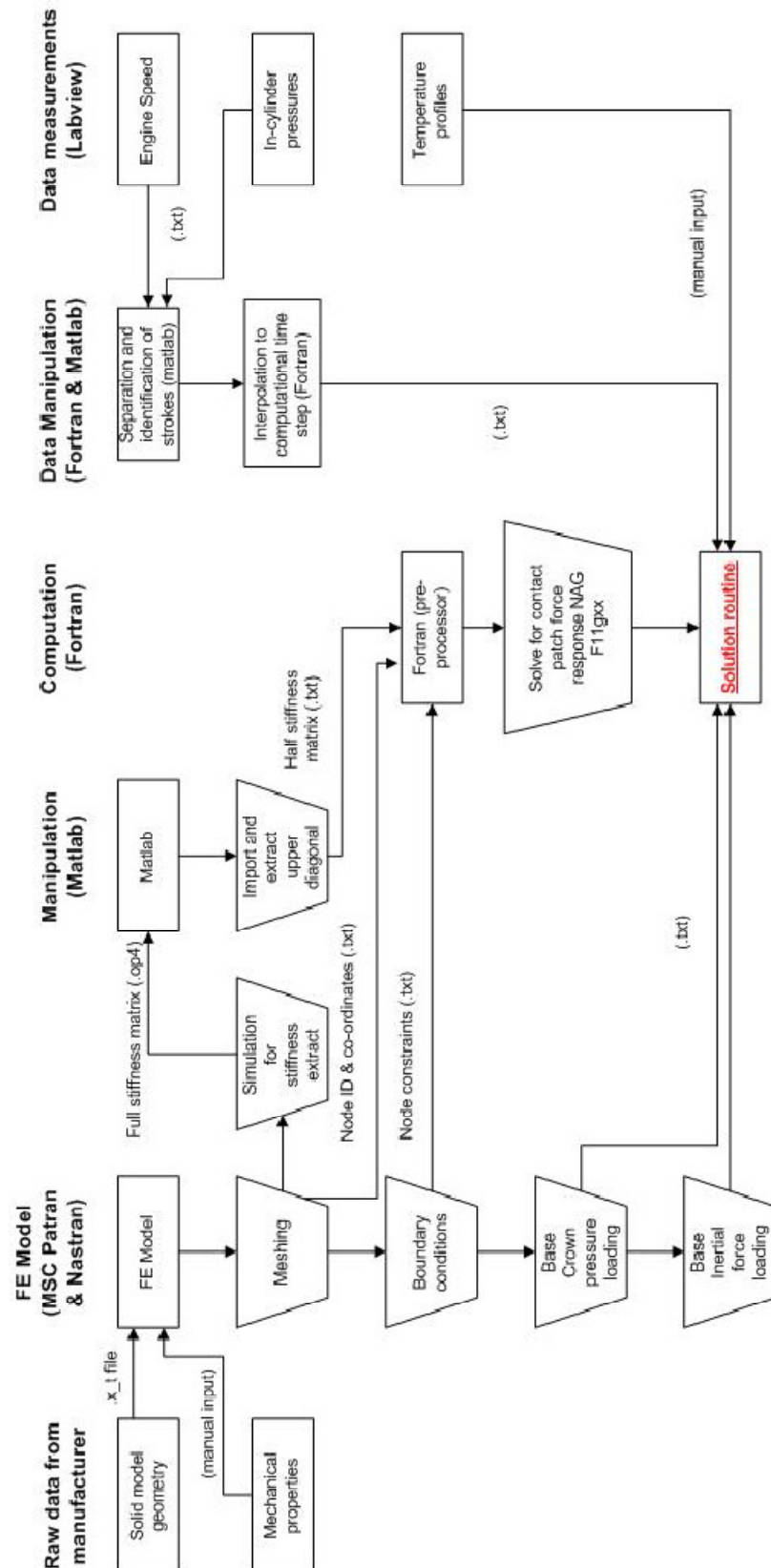
Convection, Temp $(157^{o}C)$ $2000Wm^{-2}K^{-1}$

Liner internal temperature

The internal face set to the mean recorded temperature of 120°C

The following pages reprint the publications made by the author in scientific peer reviewed journals:

1. **LITTLEFAIR, B**. ... et al 2013. Transient tribo-dynamics of thermo-elastic compliant high-performance piston skirts, Tribology Letters, DOI 10.1007/s11249-013-0243-6

2. **LITTLEFAIR, B**. ... et al 2013. Lubrication of a flexible piston skirt conjunction subjected to thermo-elastic deformation: A combined numerical and experimental investigation. ImechE part J, DOI: 10.1177/1350650113499555

The following papers were presented at International conferences:

3. **LITTLEFAIR, B**....et al., 2011. Tribology of piston skirt conjunction. IN: 3rd European Conference on Tribology (ECOTRIB 2011) and 4th Vienna International Conference on Nano-Technology (Viennano '11), Vienna and Wiener Neustadt, 7-9th Jun, 7pp.

4. **LITTLEFAIR, B.** ... et al., 2012. Assessment of thermo-structural effects on EHL piston skirt lubrication. IN: Proceedings of the ASME 2012 Internal Combustion Engine Division Spring Technical Conference (ICES 2012), 6 - 9 May, Torino, Italy.

5. **LITTLEFAIR, B** ... et al, "Comparison of calculated skirt friction with isolated-driven floating liner force measurements" 15th Nordic symposium on Tribology 12-15 June 2012 Trondheim

6. **LITTLEFAIR, B.** ... et al "Film thickness measurements and predictions of a flexible piston skirt", World Tribology congress 2013, Torino, Italy September 8-13th 2013